

CONTRIBUTIONS TO ELECTROCARDIOGRAPHIC SCIENCE

A thesis
presented for the Degree of
Doctor of Philosophy in Electrical Engineering
in the
University of Canterbury,
Christchurch, New Zealand.

by
P. J. BONES

University of Canterbury

1981

ABSTRACT

This thesis reports original theoretical and experimental studies related to the measurement and interpretation of the electrical activity of the heart. The relevant literature and clinical practice are reviewed at length.

Part I is a review of the science of electrocardiography. Included in the review are the electrophysiology of the heart, the potential theory which relates the electrocardiogram (E.C.G.) to its source, the various schemes used to measure and interpret the E.C.G. and the use of computer modelling to aid in E.C.G. interpretation.

The effects of body shape and internal conductivity inhomogeneities on the E.C.G. are studied by means of a computer model. A simple form of the model has a piecewise homogeneous interior with spherical boundaries and a surface admittance is invoked to model changes in the surface shape. An extended form of the model allows the boundaries to be irregular and it is solved by means of an integral equation and the extended boundary condition. Representative numerical results are presented, illustrating the practical utility of the model. The sensitivity of the E.C.G. to certain types of inhomogeneity and surface shape changes is established.

An experimental study, supported by a computer model based on the techniques outlined above, of the non-invasive detection of the signals from the ventricular specialised conduction system is reported. Thirty-five subjects were studied using a measurement system with a frequency response extending from 0.1 Hz to 500 Hz (-3 dB points) and using a pair of chest electrodes (similar to Lead C1). Signal averaging was performed on groups of approximately 50 beats, using the onset of the QRS wave as a timing reference. The signals were detected with certainty in 85% of the subjects studied. The typical measured signal waveform is remarkably similar to that predicted by the aforementioned computer modelling technique. Two features are identified: an initial positive deflection (which probably represents the initial activation of the bundle of His) and a notch approximately 10 msec later (which may represent the passage of the activation into the bundle branches).

PREFACE

In 1972, while completing the final year of my Bachelor of Engineering degree, I had cause to complete an essay assignment in control theory. I chose to base my essay on the design of a heart pacemaker adapted to the physiological demands of the body, in a similar manner to the heart's own pacemaker. While I have not carried this idea further, my literature research for the essay introduced me to the fields of biomedical engineering and cardiac medicine and has now, some years later, led to the preparation of this thesis. In the interim I completed two years postgraduate (graduate, in North American terminology) study for my Master of Engineering (M.E.) degree, and I have been employed for six years by the North Canterbury Hospital Board as a biomedical engineer in the Department of Cardiology, The Princess Margaret Hospital, Christchurch.

My postgraduate study for the M.E. was supervised by Dr Basil Kerdelmelidis and (while Dr Kerdelmelidis was on leave) Dr Fred Cady. I worked on the design and construction of a special-purpose calculator for estimating the fraction of blood ejected from the heart during each beat. Some means of making this calculation from two-dimensional X-ray projections had been sought by members of the Department of Cardiology at The Princess Margaret Hospital. Through the success of this project and the recognition that there was work aplenty in the Department for a biomedical engineer, I was offered a position on the permanent hospital staff. I am pleased to report that my prototype calculator has operated without fault ever since it was put into service!

During my first two years in the hospital I gained valuable experience in medical instrumentation and in the application of the digital computer to physiological signal analysis. In particular I developed a computer-based vectorcardiography system, instrumentation for measuring the signals from electrode catheters positioned within the heart and a system for analysing heart rhythms from electrocardiograms. Throughout this period I worked closely with Dr Hamid Ikram, Consultant Cardiologist.

Early in 1977, I enrolled for the degree of Doctor of Philosophy in Electrical Engineering under the supervision of Professor Richard Bates at the University of Canterbury. Dr Ikram was co-opted as my

associate supervisor. The then Head of the Department of Cardiology, Dr David Hay, was instrumental in getting the administrative details sorted out with the support of Professor Donald Beaven, Professor of Medicine, University of Otago (Christchurch Clinical School).

The original outline for my Ph.D. project covered a broad area under the general heading of "electrocardiography". As is common with such projects, I explored the subject in general before focussing on several particular aspects. For the first twelve months, I concentrated on an extensive literature survey and on understanding the theory of electrocardiography. I presented a preliminary paper entitled "Towards an inverse solution for electrocardiography" at the 1978 Australasian Conference on Physical Sciences in Medicine, which was held in Melbourne. In this context, an inverse solution is a characterization of the heart source from the electrocardiographic potential field measured on the body surface. By this time, Professor Bates and I had decided that one of the major difficulties in finding the inverse solution is allowing for the effects of the variation of the conductivity throughout the body and the irregular shape of the body. We felt that the effects of the inhomogeneities and surface shape were not sufficiently well understood and therefore I concentrated on the development of the two computer models presented in Chapters 5 and 6. A grant was received from the National Heart Foundation of New Zealand to assist in this work.

At the same time as working on the computer modelling, I was helping to measure and analyse the signals from electrode catheters in patients with abnormal heart rhythms. Using catheters to measure electrical signals from inside the heart is clearly a risky procedure, so considerable interest was aroused by early reports in the literature of a method of detecting some of the signals from the electrocardiogram without invading the body. There were some obvious inadequacies in the reported studies so I embarked on a modelling and experimental investigation aimed at establishing the nature of the signals. The study was carried out during 1979 and the early part of 1980 and I presented the results at "BIO-ENG 80" (20th Conference of the Biological Engineering Society, 1980) in London. This work, which is reported in Chapter 7, was assisted by another grant from the Heart Foundation of New Zealand for an F.M. tape recorder and other instrumentation.

I did originally plan to investigate a third aspect of electrocardiography - a model for the properties of the heart tissues as they relate to the heart rhythm. I did not have enough time to do this but I am pleased to report that another of Professor Bates' Ph.D. students, Mr Rick Millane, has developed a very useful computer model (Millane *et al.*, 1980) which he will soon be discussing at length in his thesis (Electrical Engineering Department, University of Canterbury).

My thesis is comprised of two parts. Part I (Chapters 1 to 4) is a review of the science of electrocardiography and it provides a detailed background for the original work presented in Part II. In Chapter 1 the aspects of physiology which are relevant to the rest of the thesis are reviewed. The aspects covered are the excitation of cardiac cells, the anatomy of the heart and the relationship of the electrocardiogram to the activation of the heart. The chapter concludes with a brief review of the electrocardiographic changes which are associated with common disorders of the heart.

The relationship of the electrocardiogram to the activation of the heart is formulated in terms of potential theory in Chapter 2 and the inverse solution is discussed. It is readily shown that there is no unique inverse solution so the interpretation of the electrocardiogram must rely to some extent on a *a priori* knowledge about the source, commonly the assumption of an "equivalent heart generator".

The practical schemes in use for measuring and interpreting the electrocardiogram are reviewed in Chapter 3. These are the standard 12-lead scheme (used almost universally throughout the world), orthogonal lead schemes (vectorcardiograms) and schemes which utilise the whole body surface field.

Chapter 4 is a review of the use of modelling in electrocardiography and thus provides the background to the work presented in Chapters 5 and 6. A simple model for the field of a bundle of Purkinje fibres is developed and it is shown to closely resemble the field of a current dipole. Models for the excitation of the heart as a whole and for the effects of the body surface and internal inhomogeneities are also reviewed.

Part II of my thesis covers my original computational and experimental work. In Chapter 5 a simple model is presented to study the effects of the body surface shape and internal conductivity

inhomogeneities. The surface field is found for a specified source and "body". The body is represented by a piecewise homogeneous conducting region with spherical internal and outer boundary surfaces. The potential throughout the model is represented by a series of analytic functions. Although the outer surface is spherical, the effects of irregular surface shapes are evaluated by incorporating a theoretical device known as "surface admittance" on the outer surface. A number of examples of the application of the model are presented. A two-dimensional model of a "limb" is also presented to show that the surface admittance technique is applicable even to sharp changes in the body surface. The limb model results are checked by conformal mapping.

In Chapter 6 the model is extended to incorporate irregular internal and outer surfaces. The potential field is again represented by a series of analytic functions but an integral equation is invoked to solve for the surface field. A number of examples of applying this model to test the effects of internal inhomogeneities are presented. The model is also used to predict the type of signal which should be measured by the methods reported in Chapter 7.

In Chapter 7, I present an experimental study of the non-invasive detection of signals from the specialised conducting tissues of the heart. These signals are normally only detected by electrode catheters, as mentioned above. The chapter commences with a brief review of the state-of-the-art. The instrumentation and methods I used are then described in detail. My results indicate that the signals are certainly measurable in most subjects although interference from the P wave and skeletal muscle activation restricts the amount of information which can be obtained. Two features are identified in the measured signal waveform.

Finally, in Chapter 8, I make a number of conclusions and suggestions for future work. I intend to carry out some of the suggested work myself.

The following papers have been prepared during the course of this work:

1. Bones, P.J., H. Ikram and R.H.T. Bates. Towards an inverse solution for electrocardiography. Australasian Physical Sciences in Medicine, 1: 47, 1978.
- Also (Abstract) New Zealand Medical Journal, 89: 276, 1979.

2. Bones, P.J. and R.H.T. Bates. Computational assessment of electrocardiographic measurement sensitivity. Accepted for publication in Medical and Biological Engineering and Computing.
3. Bones, P.J., H. Ikram, A.H. Maslowski and R.H.T. Bates. Signals from the ventricular specialized conduction system in man. I) Modelling the His bundle electrogram; II) Non-invasive measurements. Submitted to Cardiovascular Research.
- Also (Abstract) Proceedings of the 20th Conference of the Biological Engineering Society, London, 1980.
4. Bones, P.J. Non-invasive detection of signals from the specialized conduction system of the heart. New Zealand Medical Physics and Bio-Medical Engineering, 7: 5, 1980.
- Also (Abstract) New Zealand Medical Journal, 91: 363, 1980.

In addition, I have presented the work reported herein at the following meetings:

1. Annual Scientific Meeting of the Cardiac Society of Australia and New Zealand, Christchurch, 1978.
2. 18th Conference on Physical Sciences in Medicine and Biology, Australasian College of Physical Scientists in Medicine, Melbourne, Australia, 1978.
3. Annual meeting of the New Zealand Medical Physics and Bio-Medical Engineering Association, Dunedin, New Zealand, 1979.
4. New Zealand Branch Meeting of the Cardiac Society of Australia and New Zealand, Rotorua, New Zealand, 1979.
5. BIO-ENG 80, 20th Conference of the Biological Engineering Society, London, 1980.
6. 20th Conference on Physical Sciences in Medicine and Biology, Australasian College of Physical Scientists in Medicine, Christchurch, 1980.

CONTENTS

	Page
ABSTRACT	i
PREFACE	ii
 PART I. REVIEW OF ELECTROCARDIOGRAPHIC SCIENCE 	
CHAPTER 1. CARDIAC ELECTROPHYSIOLOGY	1
1.1 The cardiac cell	1
1.2 Cardiac anatomy	8
1.3 The electrocardiogram	15
1.4 Cardiac pathology	30
CHAPTER 2. THE APPLICATION OF POTENTIAL THEORY TO ELECTROCARDIOGRAPHY	37
2.1 Formulation	37
2.2 The inverse solution	47
CHAPTER 3. ELECTROCARDIOGRAPHIC MEASUREMENT SCHEMES	65
3.1 The standard 12-lead E.C.G.	66
3.2 Orthogonal lead schemes	80
3.3 Measurement of the total body surface field	87
CHAPTER 4. MODELLING	93
4.1 Modelling the cardiac generator	94
4.2 Modelling the surrounding tissues	107
 PART II. COMPUTATIONAL AND EXPERIMENTAL RESULTS 	
CHAPTER 5. SIMPLE MODEL (SURFACE ADMITTANCE)	117
5.1 Details of the model	118
5.2 Applications of the simple model	124
5.3 Two-dimensional study of a sharp boundary change	138
5.4 Discussion	150

	Page
CHAPTER 6. EXTENDED MODEL (INTEGRAL EQUATION)	153
6.1 Details of the extended model	153
6.2 Applications of the extended model	160
6.3 Modelling the field produced by the ventricular specialised conduction system	170
6.4 Discussion	181
CHAPTER 7. NON-INVASIVE MEASUREMENT OF SIGNALS FROM THE VENTRICULAR SPECIALISED CONDUCTION SYSTEM	185
7.1 Review	185
7.2 Methods	192
7.3 Results	202
7.4 Discussion	208
CHAPTER 8. CONCLUSIONS AND SUGGESTIONS FOR FUTURE WORK	211
8.1 Modelling the source of the E.C.G.	211
8.2 Modelling the effect of the body surface	213
8.3 Modelling the effect of internal inhomogeneities	214
8.4 Non-invasive detection of the activation of the V.S.C.S. (NID)	215
ACKNOWLEDGEMENTS	217
REFERENCES	219
APPENDICES	237

PART I

REVIEW OF ELECTROCARDIOGRAPHIC SCIENCE

CHAPTER 1

CARDIAC ELECTROPHYSIOLOGY

1.1 THE CARDIAC CELL

All of the cells that make up the atrial muscle, ventricular muscle and specialised conduction tissues of the heart are excitable. The cardiac cells exhibit some of the characteristics of nerve cells and skeletal muscle cells, as well as some characteristics not shared by these other excitable cells.

Some fibrous and inexcitable tissue is also found in the heart, connecting the atrial and ventricular muscular chambers together and providing support for the cardiac valves. The only electrophysiological role of this fibrous tissue is to prevent propagation of the cardiac activation impulse between the excitable atrial and ventricular tissues. The properties of this fibrous tissue need not be considered further.

Cardiac excitable cells are bounded by a thin (approximately 80 Å thick) plasma membrane. The membrane has a large number of internal folds so that the total surface area of membrane may be many times the area of the cell periphery. The large surface area aids in the exchange of ions between the relatively small internal cell volume and the outside. The flow of ions, particularly Na^+ , K^+ and Ca^{++} , across the plasma membrane is the basis of the excitatory properties of the cardiac cells. Electrically the excitation process is manifest in the cardiac action potential, the voltage measured across the membrane during excitation. The membrane voltage of a cell in the resting state is approximately -90 mV measured inside relative to outside. It is thus polarised in the resting state. During activation the membrane rapidly depolarises to a membrane voltage near zero. The cell remains in the activated state for approximately 300 msec, during which time contraction occurs, before it spontaneously repolarises to the resting state. Some cardiac cells exhibit the property of spontaneous depolarisation, i.e. the propensity for becoming the heart's pacemaker (cf. §1.1.2). All cardiac cells, once activated (either by external stimulation or spontaneously), are refractory (unable to be reactivated) until repolarisation occurs.

§1.1.1 Resting transmembrane voltage

The Nernst equation (Coraboeuf, 1978) relates the equilibrium voltage across a membrane to the intracellular and extracellular concentrations of any given type of ion. Table 1.1 lists the concentrations of the important ions in cardiac tissue. The equilibrium voltage for potassium ions calculated from the Nernst equation is approximately equal to the measured resting membrane voltage of cardiac cells. It is concluded therefore that the resting voltage is primarily due to the dominant permeability of the cell membrane to potassium. However, a change in the relative concentrations of intracellular and extracellular potassium ions does not alter the voltage by the amount predicted by the Nernst equation (Coraboeuf, 1978). The cell membrane appears therefore to be significantly permeable to ions other than potassium during the resting period and this property varies from tissue to tissue within the heart (West, 1972). Furthermore, the effective concentration of ions may differ from the mean concentration because of interactions between ions and the sequestering of ions in the narrow clefts between cells.

TABLE 1.1 Concentrations of the important ions in the intracellular and extracellular regions of the cardiac tissue (from Guyton, 1971).

Ion	Valency	Concentrations		Nernst voltage mV
		Intracellular milliosmols/l of H ₂ O	Extracellular milliosmols/l of H ₂ O	
Sodium, Na ⁺	1	10	137	69
Potassium, K ⁺	1	141	4.7	-90
Calcium, Ca ⁺⁺	2	0	2.4	-
Chlorine, Cl ⁻	-1	4	112.7	-88

§1.1.2 Activation and contraction

Cardiac cell activation is accompanied by a sudden change in the membrane permeability to certain ions, principally Na⁺ and Ca⁺⁺. A cardiac action potential and the corresponding pattern of membrane ionic exchange is shown in Figure 1.1. A large amount of experimental evidence suggests that a rapid influx of Na⁺ ions is responsible for the initial rapid phase

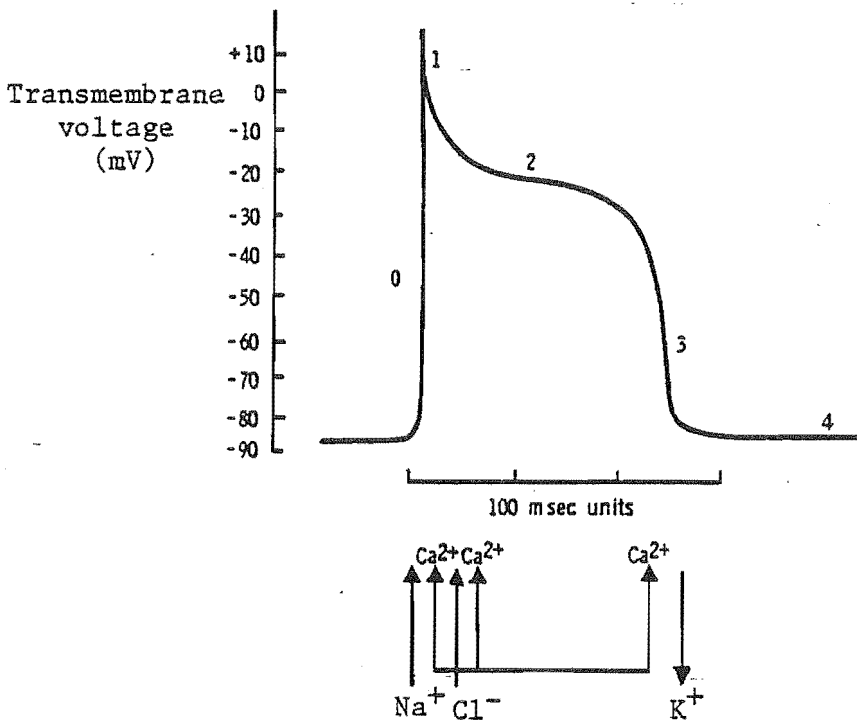


Figure 1.1 The transmembrane action potential of a cardiac cell and the membrane ionic currents (from Naylor and Krikler, 1975).

of depolarisation (phase 0 in Figure 1.1) and a secondary inward current, mainly carried by Ca^{++} ions, is responsible for the plateau of the cardiac action potential (Coraboeuf, 1978). The process of repolarisation is less well understood. It appears likely that a flow of Cl^- ions into the cell soon after depolarisation contributes to the initial repolarisation phase (phase 1 in Figure 1.1) (Coraboeuf, 1978). At least two currents involving K^+ ions have been identified and it is generally accepted that they are responsible for the final phase of repolarisation (Krikler and Goodwin, 1975; Coraboeuf, 1978).

The ionic currents discussed above are present to some degree in all cardiac excitable tissues but considerable variation exists in the precise nature of the currents and of the cardiac action potential exhibited. In particular, mention must be made of the pacemaker cells. An important feature of the action potential of the pacemaker cells is a slow depolarisation during phase 4 (see Figure 1.2) instead of the steady resting voltage found in non-pacemaking cells (West, 1972). When the membrane depolarises to a critical threshold voltage, an action potential is initiated. A progressive decrease in membrane permeability to potassium is the likely mechanism for phase 4 depolarisation and it may be controlled by the intracellular concentration of Ca^{++} ions (Coraboeuf, 1978). Both the rate of phase 4 depolarisation and the initial polarisation level affect the frequency at which pacemaker cells fire.

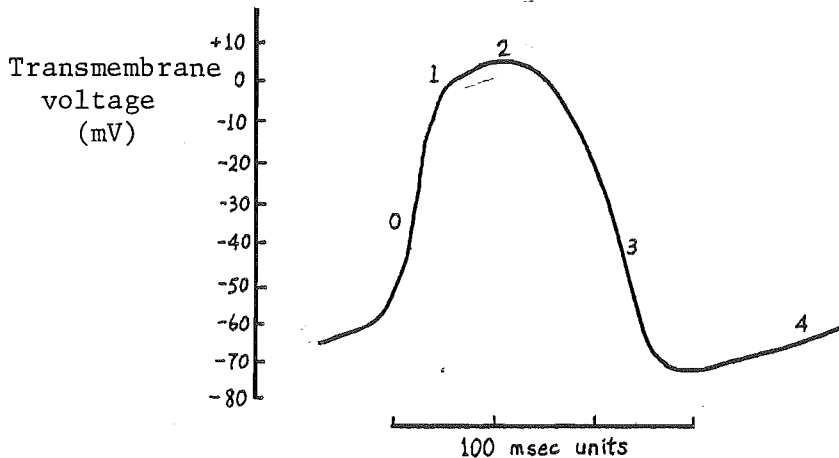


Figure 1.2 The transmembrane action potential of a cardiac pacemaker cell (from Coraboeuf, 1978).

The shape of the action potential of pacemaker cells also differs from that of other cells in that phase 0 is less rapid and the sharp positive peak between phases 0 and 1 may be missing (see Figure 1.2).

The electrical activation of cardiac cells is accompanied by the mechanical contraction of muscle filaments within the cells. The transition from the diastolic (resting) state to the systolic (active) state in these muscle filaments is triggered by a sudden increase in the intracellular availability of Ca^{++} ions (Naylor and Krikler, 1975). Conversely, a reduction in intracellular Ca^{++} ion availability is responsible for the return to the diastolic state. The purpose of the prolonged plateau phase of the cardiac action potential, during which Ca^{++} ions enter the cells (see Figure 1.1), is clearly to allow sufficient time for a cardiac chamber to eject its contents into the next part of the circulation. It is likely that some Ca^{++} ions are released from internal cellular stores to assist in the contraction. The current theories on the mechanism of muscle contraction and the role of calcium therein are described by Langer and Brady (1974). Some specialisation in the mechanical properties of cells is evident from tissue to tissue in the heart. For example, the cells of the Purkinje fibres, which appear to be specialised for rapid impulse propagation, have been found to contain relatively few muscle filaments (Langer and Brady, 1974, Chapter 1; James and Sherf, 1978) compared to the ventricular muscle cells.

The energy required to maintain the ionic gradients across the cell membrane and to power the mechanical contractions, is obtained from the hydrolysis of adenosine triphosphate (ATP). This complex compound is

formed from the metabolism of glucose and fatty acids supplied to the heart tissues by the coronary blood circulation (Olson, 1962). An enzyme based on ATP and located in the cell membrane supplies the energy for what has become known as the "sodium-potassium pump". This pump acts to push Na^+ ions out of the cell and pull K^+ ions into the cell to maintain the respective resting intracellular and extracellular concentrations (see Table 1.1). Most of the energy liberated by ATP hydrolysis is channelled into mechanical work via the contractile process. Olson (1962) reviews the mechanical energy utilisation in cardiac cells.

§1.1.3 Intercellular coupling

Cardiac cells, like many other types of cells, are coupled electrically by nexuses, which are small areas where the membranes of adjacent cells are in close apposition. Each nexus is crossed by a network of extremely fine tubules which are likely to form a permeable channel between the interiors of adjacent cells (Coraboeuf, 1978). There is some suggestion that the nexuses provide a low resistance path for current which is probably carried by K^+ ions. A simple equivalent circuit for the electrical coupling between two cells is shown in Figure 1.3. The excitation of cell 1 causes the internal potential to change to the depolarised state so that current flows through the nexus (elements R_N and C_N in Figure 1.3) into the (polarised) interior of cell 2. Provided R_N is small compared to the transmembrane resistance R_{m2} , the potential in cell 2 is raised sufficiently to initiate depolarisation.

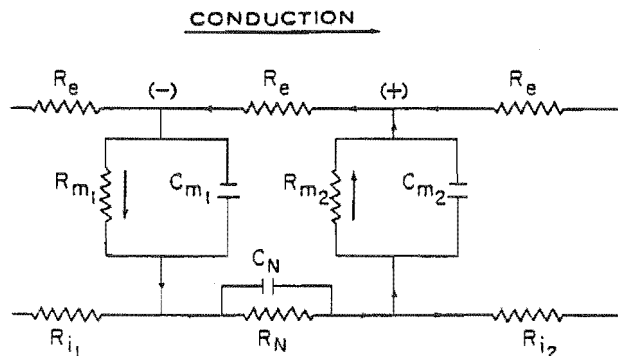


Figure 1.3 A simple equivalent circuit for the electrical coupling between two cells (cf. Langer and Brady, 1974, Chapter 5).

Freygang and Trauntwein (1970) derive a time constant for the coupling in Purkinje fibres of approximately 60 μ sec and note that C_N should be small because of the small size of the nexuses. The properties of the nexus may play an important role in controlling the speed of conduction in specialised tissues such as the atrioventricular node.

Mechanical coupling of the cardiac cells is achieved by further regions of close apposition of membranes known as intercalated disks, which are thought to have a relatively high electrical resistance (Coraboeuf, 1978). Cell-to-cell mechanical coupling is of course vital to convert the individual contractions of millions of cells into a concerted muscular contraction. The majority of cardiac cells are specialised for contraction and are normally 20 to 30 μ m in diameter and 100 μ m in length. The muscle filaments are arranged longitudinally within the cells with are attached end-to-end by the intercalated disks. However, each disk is divided into a number of offset segments to form an interlocking join (Langer and Brady, 1974, Chapter 1). The nexuses appear in the longitudinal sections between disk sections so that each cell may be electrically coupled to several others at each end. The interlocking nature of the joins in cardiac muscle may explain why the direction of the action potential propagation has been observed to be different than the longitudinal axis within a region of cells (Casella and Taccardi, 1965).

§1.1.4 Cellular electrical measurements

The direct recording of transmembrane voltages in cardiac cells was made practical by the introduction of the "ultramicroelectrode" in 1949. This electrode is constructed by pulling a fine glass tube with heat applied until the luminal diameter is less than 1 μ m. A suitable solution, typically 3 Molar potassium chloride, is used to provide conduction from the fine tip to a metal electrode inserted in the other end. Micromanipulators are necessary to position the tip of one microelectrode inside a cell and a second in the extracellular space to measure the transmembrane voltage. A floating version of the microelectrode was later developed to allow measurements to be made on muscle cells while contractions were occurring.

The impedance of a typical microelectrode is in the range of 10 $M\Omega$ to 100 $M\Omega$ depending on the tip size and filling solution concentration (Geddes, 1972). The input impedance of the differential amplifier used to measure the transmembrane voltage must therefore be extremely high if significant inaccuracies are not to occur due to the voltage across the

electrodes. The electrode potential at the metal/solution interface and the tip capacitance must also be considered in the design of instrumentation and experiments. Geddes (1972) has published an exhaustive treatise on the properties of microelectrodes and has reviewed their method of construction.

Apart from their use in direct measurement of the transmembrane voltage, microelectrodes have been used extensively in methods directed at measuring ionic conductances in cardiac cell membranes. These methods are all of the voltage clamp type. One version of the voltage clamp is shown in Figure 1.4.

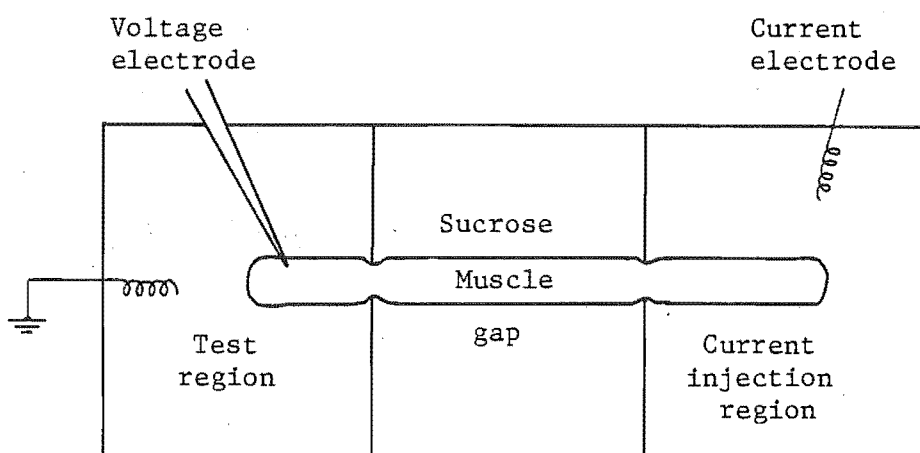


Figure 1.4 An example of a voltage clamp experiment (cf. Fozzard and Beeler, 1975).

A small section of cardiac tissue approximately 4 mm in length is mounted within a three-compartment chamber. Two close-fitting rubber diaphragms isolate the centre compartment in which the tissue is bathed in a high resistance sucrose solution. The end compartments are filled with a (conducting) physiological salt solution. In one end compartment a microelectrode is positioned to monitor the intracellular potential relative to an external electrode. A further external electrode in the other end compartment supplies current to the preparation to clamp the transmembrane voltage at a preset level. It is therefore a negative feedback circuit. The sucrose gap, if properly applied, prevents any of the feedback current flowing in the extracellular space so that this

current represents only the flow of ions across the membranes in the compartment with the microelectrode. Ionic conductances at steady-state voltages and in response to step changes may be measured with the technique. Fozzard and Beeler (1975) give a detailed account of the uses and limitations of the voltage clamp in cardiac electrophysiology. Coraboeuf (1978) points out a further limitation, yet despite this criticism the voltage clamp is the means by which all knowledge of excitable cell membranes has been gained since Hodgkin and Huxley's (1952) classic experiments on the squid giant axon.

Recently a new technique of monitoring cell membrane voltage has been developed. It uses voltage sensitive dyes (cf. Hartline, 1979). These dyes, which are the subject of intensive pharmacological research, allow the transmembrane voltage of single cells or whole arrays of cells to be measured optically, without recourse to electrodes. Two types of dyes have been successfully used. The first, or "slow", type permeate the cell membranes in response to changes in voltage in much the same way as the ionic solutions involved in cell processes. Intracellular potential changes may be inferred from changes in the absorption of applied light (or changes in fluorescence) of the order of 0.04 dB/mV. The second type of dyes - i.e. the "fast" dyes - have the property that their molecules, when within membranes, turn in direct response to the electric field intensity and can follow changes in microseconds. The changes in absorption and fluorescence are much smaller with the fast dyes (of the order of 4×10^{-4} dB/mV) than with the slow dyes but are still detectable. Non-toxic dyes suitable for *in vivo* and *in vitro* studies of actional potential formation and propagation have only been developed recently, but it appears likely that their use will become widespread in cardiac electrophysiological research.

1.2 CARDIAC ANATOMY

This section reviews the cardiac anatomy from an electrophysiological viewpoint and describes the properties of the tissues. Emphasis is given to aspects which are relevant to later chapters. For a more complete coverage of the subject see Spach and Barr (1976), James (1978) and James and Sherf (1978). Note that "conduction" is often used in the electrophysiological context to mean propagation rather than the passage of electric current. It is used sparingly here in this sense to comply with common usage. The cardiac tissues are presented in three subsections: the atria (including

the S-A node), the atrioventricular (A-V) conduction system and the ventricles. Each subsection contains, in order, a description of the function, the anatomical features and the electrophysiological properties of the tissues concerned. Some terms which are used throughout are defined here. They are myocardium (cardiac muscle), endocardium (inner surface of the myocardium), epicardium (outer surface of the myocardium), septum (wall separating chambers), anterior (towards front), posterior (towards back), superior (above) and inferior (below).

§1.2.1 Atria

The atrial chambers of the heart provide a "priming" action for the main ventricular pumps by contracting shortly before the ventricles. By this means some of the blood contained in the atria is ejected through the A-V valves to increase the volume of blood in the ventricles by about 20%. This additional stretching (preloading) of the muscle filaments within ventricular cells aids in their contraction by the Frank-Starling mechanism (Olson, 1960). While life cannot be sustained by atrial contraction alone, correct operation of the atria contributes significantly to the overall efficient circulation of the blood.

Embedded within the atrial tissue is the sino-atrial (S-A) node which normally provides the pacemaking impulses to the heart by spontaneous depolarisation. These impulses propagate through the atrial myocardium to the A-V conduction system and thereby to the ventricular myocardium. The time taken for impulses to propagate throughout is dependent to some extent on the frequency of pacemaking so that maximum efficiency of pumping is maintained. The timing of the mechanical contractions is entirely determined by the timing of the pacemaking impulses.

The simplest representation of the anatomy of the total atrial myocardium (both right and left atria plus atrial septum) is a hemisphere with a central partition formed by the septum (Scher, 1976). Figure 1.5 shows an exploded view of the components of the heart. The walls of the atria (cf. Figure 1.5a) are thin (ranging from 0.5 mm to 4 mm in thickness) and comprise many bundles of muscle fibres bound together by connective tissue. Several large blood vessels open into each of the atria. The superior vena cava and inferior vena cava return blood from the venous side of the systemic circulation to the right atrium and the coronary sinus drains the coronary circulation (the blood supply to the myocardium itself) into the same chamber. Four or five pulmonary veins

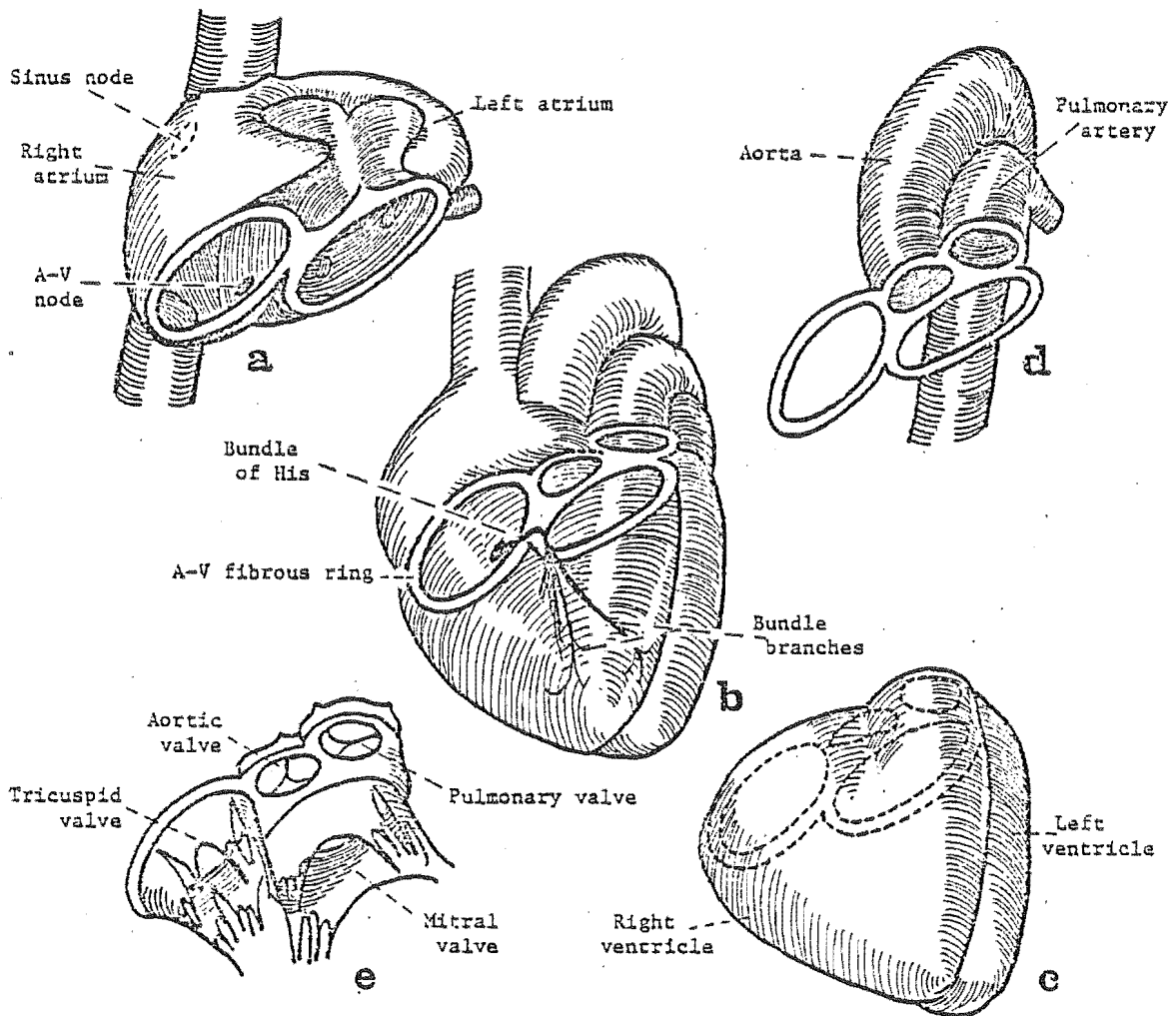


Figure 1.5 The anatomy of the heart including the specialised conduction tissues. a) Atrial myocardium, b) assembled heart, c) ventricular myocardium, d) great vessels, and e) valves (from Rushmer, 1970).

return oxygenated blood from the pulmonary circulation into the left atrium. The atrial and ventricular myocardium is mechanically connected by the fibrous A-V ring (Figure 1.5b) which also supports the four cardiac valves (cf. Figure 1.5e).

The sino-atrial (S-A), or sinus, node is an oval-shaped region of tissue measuring about 15×5×1.5 mm which lies at the junction between the superior vena cava and the right atrium (Kulbertus and Demoulin, 1975). The cells of the S-A node are small and contain relatively few muscle filaments. Microelectrode studies of experimental preparations confirm that some of the cells within the S-A node exhibit the slow diastolic depolarisation associated with pacemaker cells (Sano, 1976; James, 1978).

Transitional cells which connect pacemaker cells to the atrial myocardial cells are also reported (James and Sherf, 1978; Kulbertus and Demoulin, 1975). Their role is unclear although they may form the basis of the "nodal protection" from externally generated impulses which is reported in clinical studies (cf. Schamroth, 1971). The region containing the S-A node is rich in nerve endings, indicating that neural influences on the function of the node are strong (Kulbertus and Demoulin, 1975). The nerves are both of the sympathetic type (which tend to increase heart rate) and the parasympathetic type (which tend to decrease heart rate). The node also has its own blood supply in the form of an artery which originates either from the right coronary artery (65% of subjects) or the left circumflex artery (35%), both of which are main coronary arteries (James, 1978). The S-A nodal artery passes directly through the node so that the node essentially forms part of the arterial wall (Kulbertus and Demoulin, 1975). This suggests that a functional relationship may exist between a mechanical pulse in the artery (causing the arterial wall and node to stretch) and impulse generation in the node. Indeed James (1978) reports successful synchronisation of S-A nodal impulses with mechanical pulsations in dog hearts. However, a useful role for such a feedback mechanism has yet to be established.

A large research effort has been directed at establishing the precise nature of impulse propagation from the S-A node along the atrial myocardium to the A-V node, which is situated near the base of the right atrium (cf. Figure 1.5a). It is generally agreed that the majority of cells in the atrial myocardium are specialised for muscular contraction but some Purkinje cells, specialised for impulse propagation, have been found (Kulbertus and Demoulin, 1975; James, 1978). A number of investigators have reported the existence of three preferential pathways linking the two nodes (Sano, 1976). Although it is possible that these pathways represent an organised conduction system in the manner of the A-V conduction system described below, it appears more likely that the pathways follow the broad bands of atrial muscle which are delineated by the various orifices in the right atrium (Kulbertus and Demoulin, 1975). Because both nodes are in right atrial tissue the right atrium is excited shortly before the left atrium and the impulse reaches the A-V node well before the atrial activation is complete (Scher, 1976).

§1.2.2 Atrio-ventricular conduction system

The A-V conduction system controls the coupling of excitation from the atrial myocardium to the ventricular myocardium. It consists of the A-V node, the common bundle of His (which penetrates the fibrous A-V ring) and the bundle branches (the fine ramifications of which spread over most of the ventricular endocardium). Figure 1.5b shows the approximate relationship of the A-V conduction system to other cardiac structures. After receiving the excitory impulse from the atrial tissue, the A-V node delays its propagation further in the system to allow time for the atrial contraction to move blood into the ventricles. Then the impulse is distributed rapidly and widely to the ventricular muscle via the bundle of His and bundle branches, which are collectively described herein as the ventricular specialised conduction system (V.S.C.S.). The nearly simultaneous delivery of the impulse over much of the ventricular endocardium ensures a synchronous contraction and an efficient pumping action.

Under conditions of physiological stress or malfunction of the atrial activation, the refractory properties of the A-V node play a vital role in the protection of the ventricular myocardium from dangerously high rates of impulse repetition. If the atrial impulses fail to occur or to propagate to the ventricles at least 40 times per minute, then subsidiary pacemaking cells within the A-V conduction system usually spontaneously depolarise to maintain ventricular function at a level sufficient to sustain life.

The A-V node is approximately 5-10 mm in length and 3 mm wide. It is located at the base of the right atrium between the opening of the coronary sinus and the fibrous tissue supporting the tricuspid valve (cf. Figure 1.5e). The common bundle of His connects directly to the A-V node. It first runs forward and leftward along the fibrous tissue at the top of the interventricular septum and then penetrates downward and splits into bundles down either side of the septum (see Figure 1.5b). The "penetrating" portion of the bundle of His is close to the aortic and mitral valves (Kulbertus and Demoulin, 1975). Although the bundle branches are classically described as "left" and "right", the structure of the former is now known to be considerably more complex than this simple description might indicate. The right bundle branch remains a discrete bundle for most of its length, takes a downward and forward direction in the interventricular septum and makes its first functional contact with

the myocardium near the base of the (right) anterior papillary muscle (Kulbertus and Demoulin, 1975). Other fibres of the branch are spread over much of the endocardial surface of the right ventricle. The left bundle starts as a virtual sheet of fibres running slightly forward and down with a width of between 6 mm and 10 mm (Kulbertus and Demoulin, 1975). Some controversy exists over the nature of the rest of the left bundle branch. Rosenbaum (1970) suggests that the left bundle is functionally divided into two divisions (anterior and posterior) which link to the myocardium in the vicinity of the (left) anterior and posterior papillary muscles, respectively. This classification has been accepted for clinical diagnosis (cf. Shamroth, 1971), but studies of the histology (Kulbertus and Demoulin, 1975) and the excitation sequence (Durrer *et al.*, 1970) indicate that the left bundle divisions are more complex and varied.

The recognition of the importance of the A-V node in the maintenance of cardiac rhythm has inspired many studies into its electrophysiology and histology. However, the mechanism of propagation delay within the node and the site of subsidiary pacemaker activity remain unproven. James and Sherf (1978) report the presence in the A-V node of pacemaker cells, transition cells, Purkinje cells and ordinary myocardial cells. Sano (1976) reports that the node appears to have several layers of differing properties and he advances several possible theories for the propagation delay. Several workers propose the existence of longitudinal dissociation in the node (and possibly in the bundle of His) which may be responsible for some of the node's properties. Innervation of the A-V node is less extensive than that of the S-A node and the nerves appear to be of the parasympathetic type (James, 1978).

The histology and electrophysiology of the V.S.C.S. are less contentious than those of the A-V node. The majority of cells in the bundle of His and bundle branches are Purkinje cells, formed into fibres and larger than those found in the A-V node (James, 1978; Sano, 1976). Impulse propagation in the V.S.C.S. is fast (1 - 1.5 m/sec) and is generally believed to be uniform (Sano, 1976). Little is known to date about the end connections of the fibres in the bundle branches to the endocardium, largely because of the difficulty of finding such junctions. Sano (1976) reports that only an insignificant delay (less than 1 msec) was measured for normal impulse propagation from a Purkinje fibre to the adjoining myocardial cells.

§1.2.3 Ventricles

The ventricles provide the main propulsion for blood in the circulation. The left ventricle pumps out into the high pressure systemic circulation and therefore has a thick wall (approximately 15 mm thick). The right ventricle on the other hand pumps blood through the pulmonary circulation at much lower pressure and has a correspondingly thinner wall (approximately 4 mm). The interventricular septum is slightly thicker than either wall. The anatomical location of the ventricles is not strictly "left" and "right". The left ventricular wall and interventricular septum form a roughly elliptical chamber with the major axis (from A-V fibrous ring to apex) oriented forward, downward and leftward. The right ventricular chamber is quite flattened and positioned forward and rightward of the left ventricle (cf. Figure 1.5c). Blood enters the ventricles from the atria via the A-V valves (mitral and tricuspid) during diastole and is ejected out through the aortic and pulmonary valves during systole (cf. Figure 1.5). Papillary muscles within the ventricles provide support to the three leaflets of the tricuspid valve and the two leaflets of the mitral valve (cf. Figure 1.5e).

Ventricular myocardial cells are primarily specialised for mechanical contraction. They are arranged in interleaving sheets of fibres through which the activation spreads with little regard to fibre orientation. Studies with multi-electrode needles (Durrer *et al.*, 1970; Scher, 1976) have allowed three dimensional plots of impulse propagation to be made for the ventricular walls. The average velocity of the depolarisation propagation through the myocardium is about 0.4 m/sec, although velocities as high as 1 m/sec have been recorded for propagation along the endocardial surface (Scher, 1976). Activation in the ventricular myocardium generally propagates from the endocardium (where the Purkinje fibres of the bundle branches terminate) to the epicardium. Earliest activation is on the left side of the septum, followed shortly afterwards by the right side of the septum and regions of the endocardium near the apex of the left ventricle (Durrer *et al.*, 1970; Scher, 1976). The last regions of the ventricular myocardium to be activated are towards the fibrous A-V ring and activation is complete after 80 msec. The sequence of activation is described in more detail in the next section in relation to the generation of the electrocardiogram.

1.3 THE ELECTROCARDIOGRAM

The electrocardiogram (E.C.G.) is the time-varying potential field produced on the body surface by the electrophysiological activity of the heart. The E.C.G. is measured as the differential voltage between two electrodes (or sets of electrodes) on the body surface. In this section the E.C.G. of a normal healthy adult is described. In §1.3.1 a simple explanation for the origin of the E.C.G. is presented as an introduction (Chapter 2 includes a complete treatment of the origin of the E.C.G.). The time sequence of the major features of the E.C.G. is described in §1.3.2. In §1.3.3, §1.3.4 and §1.3.5 the nature of the body surface field is discussed for the P, QRS and T waves, respectively. The effects on the E.C.G. of normal physiological activities are summarised in §1.3.6. Finally, the method of intracardiac electrocardiography is reviewed in §1.3.7.

§1.3.1 The origin of the E.C.G.

The tissues within the heart and most of those surrounding the heart conduct electric current (cf. Table 2.2 for typical conductivities of the tissues). While cardiac tissue is being activated, some cells in the tissue are in the depolarised state while some are in the (resting) polarised state (cf. §1.1.2). An electric field is therefore impressed on the surrounding tissues by the region of tissue depolarising. The impressed electric field (which can equivalently be described as an impressed current source - cf. §2.1.3) causes current to flow in the tissues surrounding the heart and therefore causes the electric potential to vary over the body surface. Similarly, when tissues are repolarising, an impressed electric field is set up which causes the potential to vary over the body surface. When no tissues within the heart are depolarising or repolarising, no surface potential field appears (assuming the tissues are purely resistive - cf. §2.1.1).

Consider the activation of the strip of cardiac tissue illustrated in Figure 1.6. The depolarisation wavefront is proceeding from right to left. The impressed electric field is directed from the depolarised cells towards the polarised cells, i.e. in the direction of the propagation. The current in the surrounding tissue flows from the front of the advancing depolarisation wavefront to the rear of the wavefront. Since this current flow is passive, the potential of the region ahead of

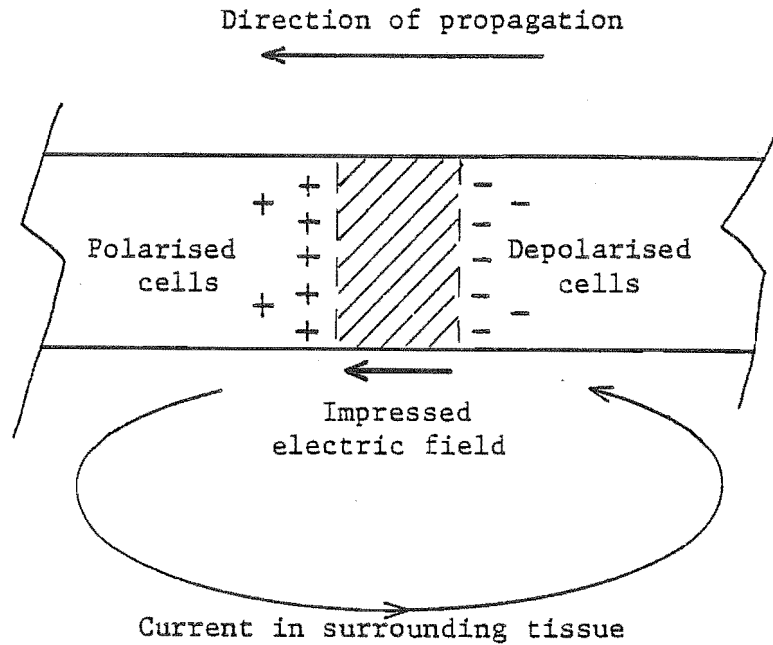


Figure 1.6 Illustration of the origin of the E.C.G.: the activation of a strip of cardiac tissue.

the wavefront must be greater than the potential behind the wavefront. Therefore the propagation of the depolarisation along this strip causes the potential to be greater on the region of the body surface ahead of the wavefront than on the region behind. The propagation of repolarisation produces a field of the opposite polarity. The structures of the heart are made up of very many strips of tissue, so the total E.C.G. is the sum of the fields produced by all of the strips (assuming linearity of the tissue properties - cf. §2.1.1). This simple explanation of the origin of the E.C.G. neglects the effects of the inhomogeneities in conductivity throughout the heart and the torso and the effects of the shape of the torso surface, but it provides an introduction to the remainder of this chapter.

§1.3.2 The time sequence of the E.C.G.

Three major features are observed in the E.C.G. of a typical healthy adult. The P wave is caused by the depolarisation of the atrial myocardium. The QRS wave is caused by the depolarisation of the ventricular myocardium. The T wave is caused by the repolarisation of the ventricular myocardium. In sinus rhythm, the S-A node initiates each heartbeat by delivering a pacemaking impulse to the surrounding atrial myocardium. From the atrial myocardium the impulse propagates through

the A-V conducting system to the ventricular myocardium. The lower part of Figure 1.7 illustrates one typical heartbeat of the E.C.G. The three major features appear in the order of P, QRS and T. The shapes of the waves are dependent on the positions chosen for the measuring electrodes.

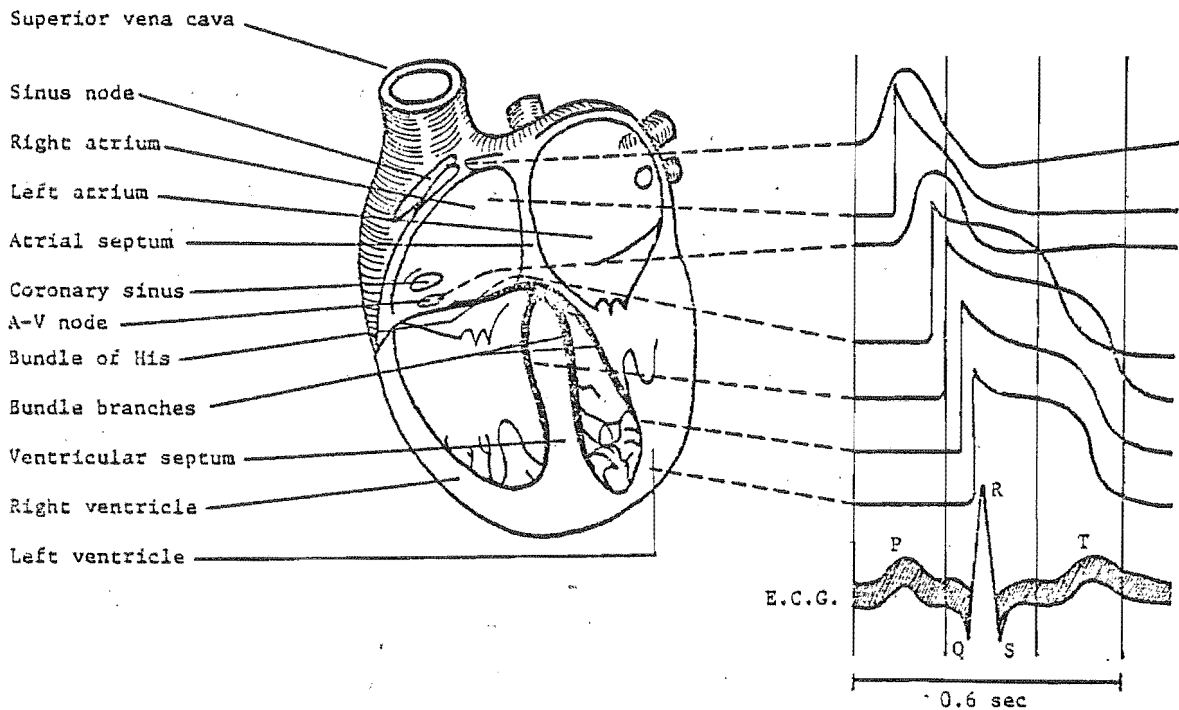


Figure 1.7 The time sequence of the activation of the heart and of the E.C.G. (from Spach and Barr, 1976).

The relationship of the time sequence of the activation of various tissues to the time sequence of the E.C.G. is approximately represented in Figure 1.7, and Table 1.2 contains a summary of the typical values for the properties of the tissues which relate to timing.

TABLE 1.2 A summary of the resting electrophysiological properties of the heart for the normal adult population (Scher, 1976; Curry, 1975; Pipberger et al., 1967; von der Groeben, 1967; Peuch, 1975; Lister et al., 1965; Wyndham et al., 1978).

Tissue	Conduction velocity m/sec	Conduction time msec	Intrinsic pacemaker rate beats/min
Sinoatrial node	0.05(?)	40-150	60-80
Atrial myocardium	0.8	100 (S-A to A-V node = 30-55)	-
A-V node	0.05	50-100	-
Ventricular specialised conduction system (V.S.C.S.)	2.0	35-55	40
Ventricular myocardium	0.4	80	-

Initial spontaneous depolarisation occurs in pacemaker cells within the S-A node to initiate a beat. The onset of the P wave occurs as soon as sufficient cells, of the S-A node and the surrounding atrial myocardium, are actively depolarising to generate a measurable signal at the body surface. Thereafter the P wave lasts for the time it takes the impulse to depolarise all the atrial myocardium, about 100 msec (see Table 1.2).

The anatomical relationship of the A-V node to the S-A node (and possibly the influence of preferential inter-nodal pathways) is such that the excitory impulse enters the A-V node approximately 50 msec after the onset of the P wave. Note that the A-V conduction system is therefore activated well before the end of the P wave. The time taken for the impulse to reach the bundle of His is highly variable as may be seen in Table 1.2. This variability is both from normal subject to normal subject and under autonomic nervous control and other influences in the same subject (Lister et al., 1965). The wide normal range for the interval between the onset of the P wave and the onset of the QRS wave (120-200 msec) also reflects the variability of the A-V nodal transmission. The time taken for the impulse to traverse the V.S.C.S. (known as the 'H-V' interval), however, shows a relatively small variation between normal subjects (see Table 1.2) and is virtually constant for any given subject (Curry, 1975). The period between the end of the P wave and the onset of

the QRS wave has classically been assumed to include no signals since none is discernible with the standard E.C.G. recording equipment. However, there is clearly some electrophysiological activity occurring continuously during the P-Q period. Chapter 7 reports on the successful detection of very small signals arising from the V.S.C.S. activity during this period. Atrial repolarisation is also likely to commence during this period (Spach *et al.*, 1979a; Brorson and Olsson, 1976).

The depolarisation of the ventricular myocardium takes approximately 80 msec, which is therefore the duration of the QRS wave. This relatively short time for the large bulk of muscle is facilitated by the nature of the connections of the V.S.C.S. to the myocardium. The large number of cells depolarising at any one time instant accounts for the large amplitude of the QRS wave.

The duration of cardiac action potentials measured from cells of the ventricular myocardium shows significant variation anatomically (Burgess, 1972). This, coupled with the prolonged nature of the repolarisation process (*cf.* Figure 1.1), causes the T wave to be considerably longer in duration than the QRS wave and lower in amplitude. The Q-T interval (used in making certain diagnoses - *cf.* Section 1.4) is defined as the time from the onset of the QRS wave to the end of the T wave and has a normal range of 300-420 msec (Goldman, 1976). A late component of repolarisation, called the U wave, is also often observed.

§1.3.3 The P wave

Activation of the atrial tissue in normal sinus rhythm begins in the region of the S-A node and proceeds with approximately uniform velocity over the atrial myocardium (Durrer *et al.*, 1970). Since the S-A node is positioned in the upper right atrium, the net direction of the spread of depolarisation (in an upright human) is downward and leftward. The surface potential field during the atrial depolarisation shows a corresponding maximum low down on the left side of the chest and a minimum near the right shoulder (*cf.* Taccardi *et al.*, 1976; Mirvis, 1980). Data from one of a very few studies published of body surface potential during atrial depolarisation and repolarisation is shown in Figure 1.8 (from Taccardi *et al.*, 1976). In Figure 1.8a the surface field at an instant near the mid point of the P wave is shown. Late in the P wave the net direction of depolarisation is directed more leftward (Taccardi *et al.*, 1976). The apparent reason is that the right atrial

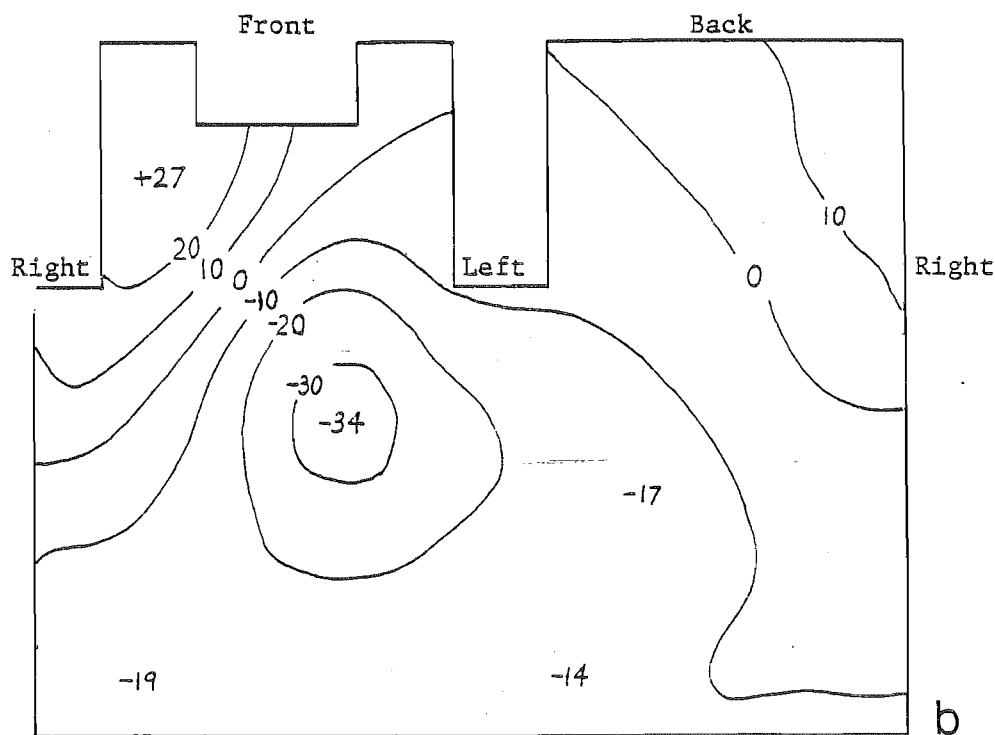
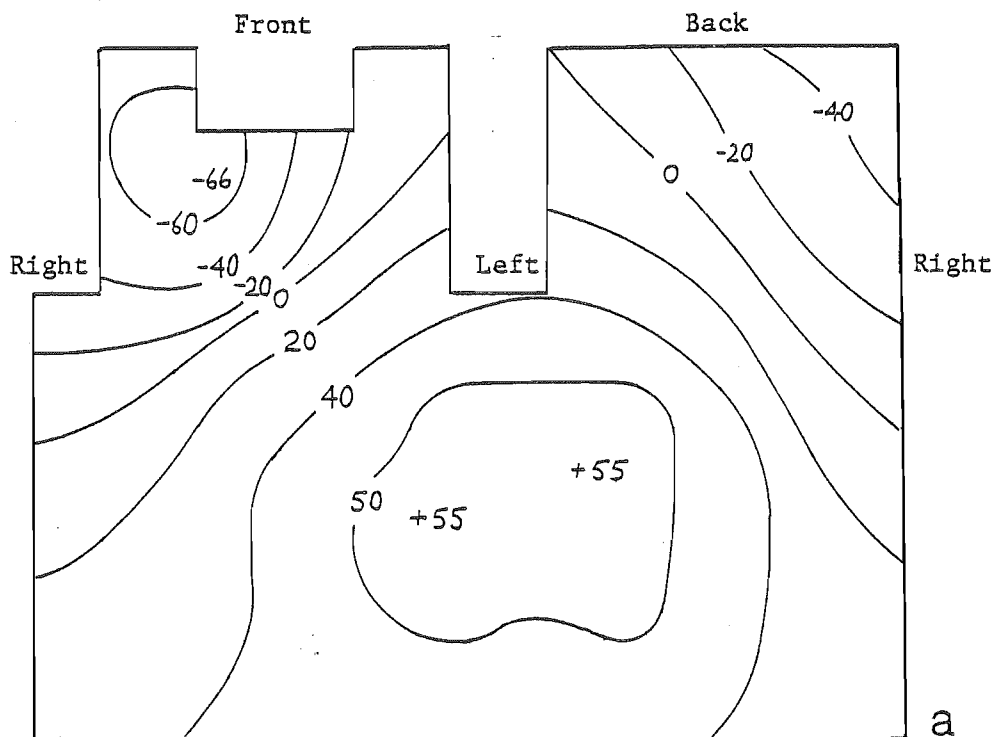
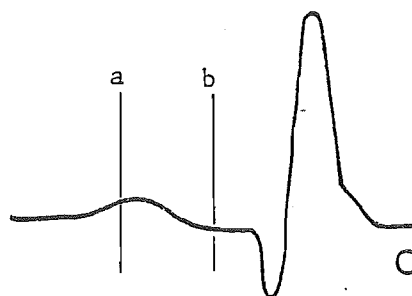


Figure 1.8 The body surface E.C.G. potential field associated with a) atrial depolarisation (P wave), b) atrial repolarisation at the times indicated in c). Lines of constant potential are plotted, the units are microvolts (from Taccardi et al., 1976).



activation is complete by this time leaving only some of the left atrial tissue to be activated. Durrer's data (1970) supports the view that the last one third (approximately) of the P wave duration is caused by left atrial activation alone. The P wave shows a slow variation with time (compared to the QRS wave) although higher frequency components are observable with high-gain low-noise instrumentation (Golden *et al.*, 1973; Selvester and Pearson, 1971).

In Figure 1.8b the surface field during the P-Q interval is shown (Taccardi *et al.*, 1976). The field is similar to that during atrial depolarisation, but lower in amplitude and reversed in polarity. Taccardi *et al.* (1976) conclude that the atrial repolarisation spreads through the atrial myocardium in approximately the same sequence as does the depolarisation. The study of Spach *et al.* (1969) on dogs supports this view.

The peak-to-peak amplitude of the P wave, in healthy subjects, is reported to have a mean of 120 μ V and a standard deviation of 30 μ V (von der Groeben *et al.*, 1968). The large variation is probably mainly caused by the variation in the thickness of the atrial myocardium and in the heart and torso size (cf. Lepschkin, 1976c).

§1.3.4 The QRS wave

A number of investigators have studied the spread of depolarisation through the ventricular myocardium and the resulting surface potential field of the QRS wave of the E.C.G. The work of Durrer *et al.* (1970) on the sequence of ventricular depolarisation has become virtually the "industry standard" for those carrying out model studies of the E.C.G. (see for example Solomon and Selvester, 1971; Kulbertus and Demoulin, 1975; Salu and Marcus, 1976). The earliest depolarisation, according to Durrer *et al.* (1970), occurs on the endocardium, particularly on the left side of the interventricular septum near the base of the (left) anterior papillary muscle. Approximately 10 msec later depolarisation occurs in the part of the endocardium of the right ventricle near the base of the (right) anterior papillary muscle. The depolarisation proceeds from the endocardium to the epicardium in both of the ventricles. After approximately 30 msec the converging wavefronts meet and extinguish in the interventricular septum. At about the same time, the depolarisation wavefront first reaches the left and right ventricular epicardium in regions approximately midway between the A-V fibrous ring and the ventricular apex. At 45 msec (approximately) the activation of the

apical region is complete. The only remaining portion of the myocardium, near the A-V ring, is depolarised from low to high with activation complete by 80 msec.

The QRS surface field is a less simple function of time and position than the P wave. Diagrams of typical potential fields for the QRS wave are reproduced in Figure 1.9 from Taccardi *et al.* (1976). For descriptive purposes the wave may be divided in time into the early (Q), mid (R) and late (S) ventricular activation. During the early activation the potential gradient on the chest is directed to the right, reflecting the dominance of the left-to-right depolarisation in the septum (Figure 1.9a). The amplitude of the surface field at this time is low (of the order of 0.4 mV peak-to-peak) because relatively few of the myocardial cells are actively depolarising. During the middle period of the QRS wave a large number of cells are depolarising at any instant so the maximum amplitude of the surface potential (of the order of 3 mV peak-to-peak) is recorded at this time (the R wave). The potential gradient on the chest region is correspondingly high (Figure 1.9b). The depolarisation wavefront encompasses both ventricles with a net direction of activation from the A-V ring to the apex and a leftward bias due to the larger bulk of the myocardium on the left and the orientation of the heart in the thorax. Thus the surface field exhibits a maximum at the lower left chest and a minimum at the middle chest (cf. Figure 1.9b). During late ventricular activation (S) the number of cells depolarising at any instant is small and decreasing with time. A low amplitude surface field is observed (Figure 1.9c) with a net direction from front to back as the last regions of the ventricular myocardium depolarise.

In common with the other features of the E.C.G., the QRS wave varies significantly between normal healthy subjects (see §1.3.6 for a discussion of the effects of normal physiological changes). Besozzi *et al.* (1973) report that late in the QRS, while all adults have a positive maximum on the lower back, approximately half have a second maximum on the upper right chest (cf. Figure 1.9c). The maximum peak-to-peak amplitude of the E.C.G. field during the QRS wave is of the order of 3.6 mV (Taccardi *et al.*, 1976), but, to my knowledge, no data on the variability of the body surface field amplitude appears in the literature. There is, however, ample data on the variability of the QRS wave measured by standard lead systems (cf. Pipberger *et al.*, 1967; von der Groeben *et al.*, 1968; Simonson, 1961). Von der Groeben *et al.* (1968) report that the

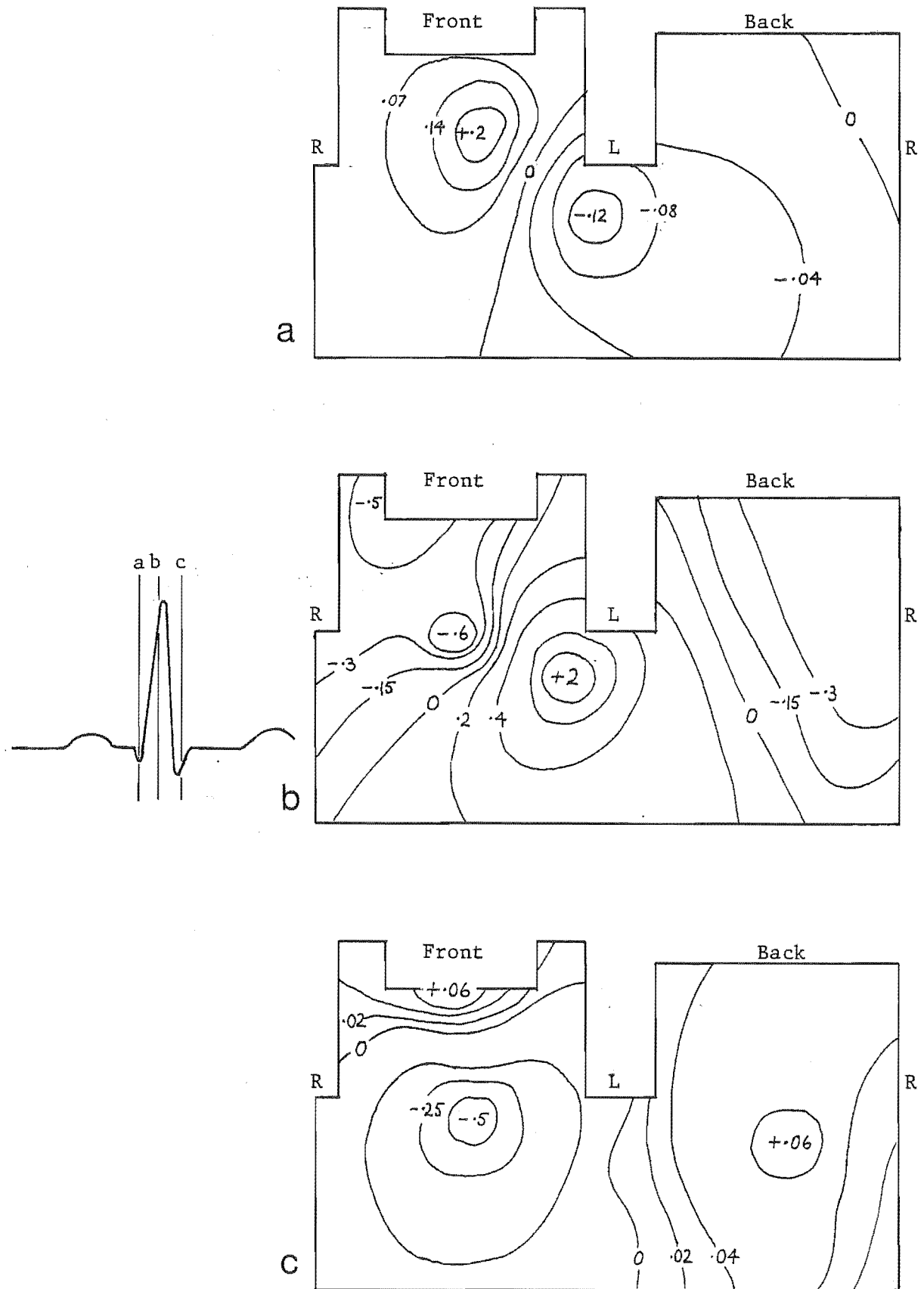


Figure 1.9 The body surface potential field during the ventricular activation (QRS wave), illustrating a) early, b) mid and c) late activation. The units are millivolts (from Taccardi et al., 1976).

QRS wave (measured by an orthogonal lead system - cf. Section 3.2) has a maximum amplitude of 1.91 ± 0.49 mV (mean \pm standard estimate of error) at the age of 20 and 1.35 ± 0.41 mV at the age of 50.

§1.3.5 The T wave (U wave)

The T wave of the E.C.G. is produced by the repolarisation of the ventricular myocardium. It seems likely that repolarisation is largely a passive process, so that it does not propagate through the myocardium in the way that depolarisation does. However, the entire ventricular myocardium does not repolarise simultaneously, so that it is still appropriate, in the electrocardiographic sense, to talk of a "spread of repolarisation". Studies of the variation of refractoriness (cf. Burgess, 1972; Lipeschkin, 1976a) indicate that the length of the action potential is greatest in the endocardial layers of the ventricular myocardium and least in the epicardial layers. It is likely, therefore, that the earliest repolarisation occurs near the epicardium and then spreads inwards towards the endocardium (Lipeschkin, 1976a). An apex-to-A-V ring progression of repolarisation also appears likely (Lipeschkin, 1976a), although it is not clear if this is again due to a variation in the length of the action potential or simply a result of the variation in the time of depolarisation.

Figure 1.10, again reproduced from the excellent review of Taccardi *et al.* (1976), shows typical body surface potential fields for two instants during ventricular repolarisation. The net direction of the spread of repolarisation from the apex towards the A-V ring generates a surface field very similar in shape to that of the mid point of the QRS (cf. Figure 1.10b and Figure 1.9b). The polarity of the field is the same for the QRS and T waves since the direction of propagation and the polarity of the impressed electric field are both reversed in the latter. The smaller T wave amplitude and its slow and smooth variation with time reflect both the distributed nature of the repolarisation process and the smaller ionic membrane currents involved. In contrast to the thin sheet of cells which are depolarising at any one time during the QRS, the majority of ventricular myocardial cells are undergoing slow repolarisation towards the middle of the T wave.

The U wave is reported to have a similar surface field to the T wave with only minor differences (Spach *et al.*, 1979a; Lipeschkin, 1976b). Several theories are advanced for the origin of the U wave. One is that

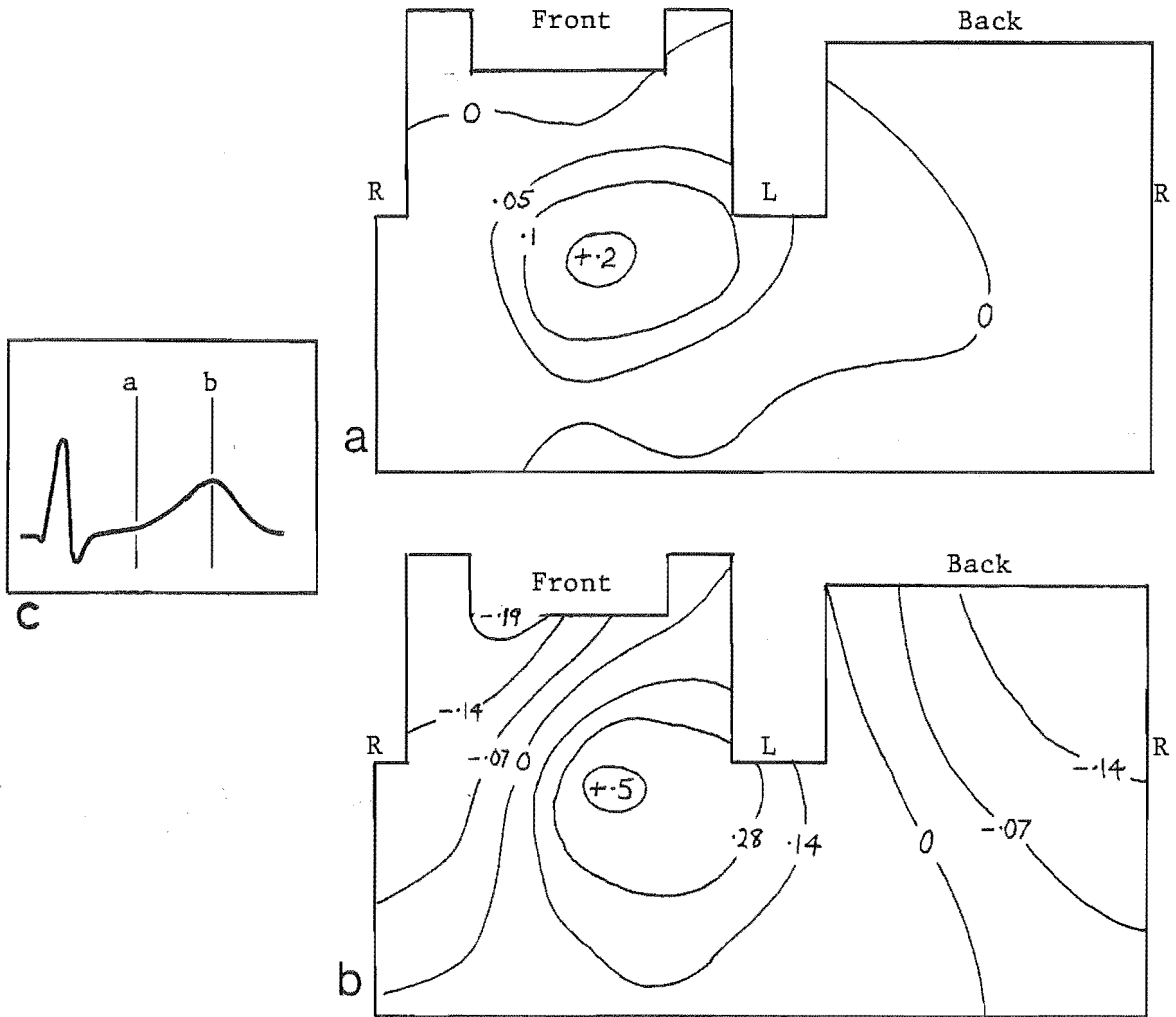


Figure 1.10 The body surface E.C.G. field during the T wave at the times indicated in c) (from Taccardi *et al.*, 1976). The units are millivolts.

it results from a prolonged and very slow component of repolarisation observed in some ventricular myocardial cells. Another theory is that it is caused by the repolarisation of the V.S.C.S. Lepschkin (1976b) has made a thorough review of the subject.

The T wave is reported to have a relatively consistent spatial distribution among normal healthy subjects (Taccardi *et al.*, 1976). However, during the earliest part of the T wave (cf. Figure 1.10a), Taccardi *et al.* (1976) report that in 75% of subjects the potential minimum occurs on the lower torso, while in the remaining 25% the minimum occurs on the upper right chest. The maximum amplitude of the T wave (measured by an orthogonal lead system) is 0.55 ± 0.19 mV at the age of 20 and 0.44 ± 0.16 mV at the age of 50 (von der Groeben *et al.* 1968).

§1.3.6 The effects on the E.C.G. of normal physiological changes

Table 1.3 is a summary of the effects on the E.C.G. which are caused by normal physiological changes and which are divided into three categories in the table. The first category is the effect on the peak-to-peak surface potential amplitude. The second is the effect on the spatial orientation of the field. The third category in the table is the effect on the temporal relationships between the features of the E.C.G. Most of the data presented in Table 1.3 is based on recordings made with standard E.C.G. lead systems (cf. Chapter 3) rather than on measurements of the entire body surface field.

The effects of respiration on the E.C.G. are of particular relevance to the results presented in §5.2.1. Very little data is available on the changes in the P wave which occur with respiration. Ruttkay-Nedecky (1976) reports that an increase in the amplitude of the P wave with deep inspiration was observed in a small group of subjects. Respiratory changes to the QRS and T waves have received more attention. Body surface field data was obtained by Flaherty *et al.* (1967) from seven children. At the mid point of the QRS, they demonstrate movement of the potential maximum from the lower left chest to the lower left back on inspiration. There is a corresponding slight movement of the potential minimum downward in the mid chest region (cf. Figure 1.9b). A study of 60 normal adults using a vectorcardiography lead system (Ruttkay-Nedecky, 1976) shows similar results. Both authors report a decrease in the overall QRS wave amplitude with inspiration. The T wave field orientation, as measured by the vectorcardiography system (Ruttkay-Nedecky, 1976), rotates forward during deep inspiration (cf. Figure 1.10).

A number of reasons have been suggested for the mechanism of the effects of respiration on the electrocardiographic field (cf. Ruttkay-Nedecky, 1976). One theory (popular with cardiologists) is that the lowering of the diaphragm during inspiration and the corresponding slight rotation in the heart's orientation effect the E.C.G. Other changes also occur in the chest with respiration, however. They include an increase in the thoracic dimensions, an increase in the lung volume and a decrease in the lung conductivity (Ruttkay-Nedecky, 1976). The different response to respiration reported for the QRS and T waves would seem to indicate that changes in the electrophysiology of the myocardium may also be involved. The model described in Chapter 5 is applied to test three of the possible mechanisms and the results are presented in §5.2.1.

Table 1.3 The effects on the E.C.G. of normal physiological changes.

Influence	Amplitude	Orientation	Temporal	References
Increase in age (adult)	Decrease in QRS and T	—	Small increase in P duration. Increase in P-Q interval.	Pipberger <i>et al.</i> , 1967
Increase in body size (adult)	Decrease in QRS	Upward and forward deflection of QRS	—	Pipberger <i>et al.</i> , 1967
Chest configuration - increase of ratio of depth to width	Decrease in QRS	Slight upward and forward deflection of QRS	—	Pipberger <i>et al.</i> , 1967
Respiration - effect of deep inspiration	Increase in P. Decrease in QRS and T.	QRS deflected downward and backward. T deflected forward	Sinus rate increases (sinus arrhythmia).	Ruttkay-Nedecky, 1976 Flaherty <i>et al.</i> , 1967 Moore and Spear, 1976
Exercise	Increase in P. Decrease in T.	—	Increase in sinus rate (in proportion to oxygen demand). Decrease in P-Q and S-T intervals. Decrease in the QRS duration.	Lister <i>et al.</i> , 1965 Moore and Spear, 1976 Simonson, 1961 Blackburn, 1969
Valsalva maneuver	Decrease in T in some subjects.	—	Increase in sinus rate during breath hold, decrease after.	Simonson, 1961

There are temporal changes in the E.C.G. with respiration as well as spatial changes. The principal of these is sinus arrhythmia, which occurs in most healthy subjects. During inspiration the heart rate transiently increases, then it decreases during expiration. While the total deviation of the rate varies considerably from subject to subject, it decreases with increasing age and it increases with the level of respiratory movements (Marriot and Myerburg, 1978). Sinus arrhythmia is apparently due to an alteration in parasympathetic nervous activity transferred from the central respiratory mechanisms to the sinus node (Marriot and Myerburg, 1978). This nervous activity is also transmitted to the A-V node, with the result that the A-V nodal impulse conduction time fluctuates slightly in phase with respiration (Moore and Spear, 1976). During inspiration the A-V nodal conduction time (and thus the P-Q interval of the E.C.G.) decreases. Both these temporal effects of respiration were used in the study of the non-invasive detection of signals from the V.S.C.S. presented in Chapter 7.

§1.3.7 Intracardiac electrocardiography

The importance of the diagnosis and treatment of cardiac arrhythmias has led to the development of a technique of monitoring the excitation of the heart tissues which supplements the E.C.G. This technique is known as intracardiac electrocardiography and involves the positioning of one or more electrode catheters within the heart. The technique is clearly invasive and therefore is usually restricted to the investigation of patients in whom there is strong evidence of an abnormality. Catheters are normally positioned only in the right-sided chambers of the heart, so that access may be gained via peripheral veins (entry via the higher pressure arteries is considerably more dangerous). Each catheter has two or more platinum electrodes near its tip, spaced at about 1 cm intervals. When the electrodes are connected to a suitable amplifier (cf. Curry, 1975), activity in tissues close to the tip is recorded (cf. Section 6.3). An external pulse generator may be attached to an electrode catheter to carry out tests of the response of the heart to pacing at different rates or to programmed sequences of pulses (cf. Curry, 1975).

Figure 1.11a illustrates the sites commonly used for catheters within the right atrium, right ventricle and coronary sinus. The high right atrial (HRA) catheter is positioned as near as possible to the S-A node to record the earliest activation of the atrial myocardium in sinus rhythm. Comparing the signals from the lower right atrial (LRA) position

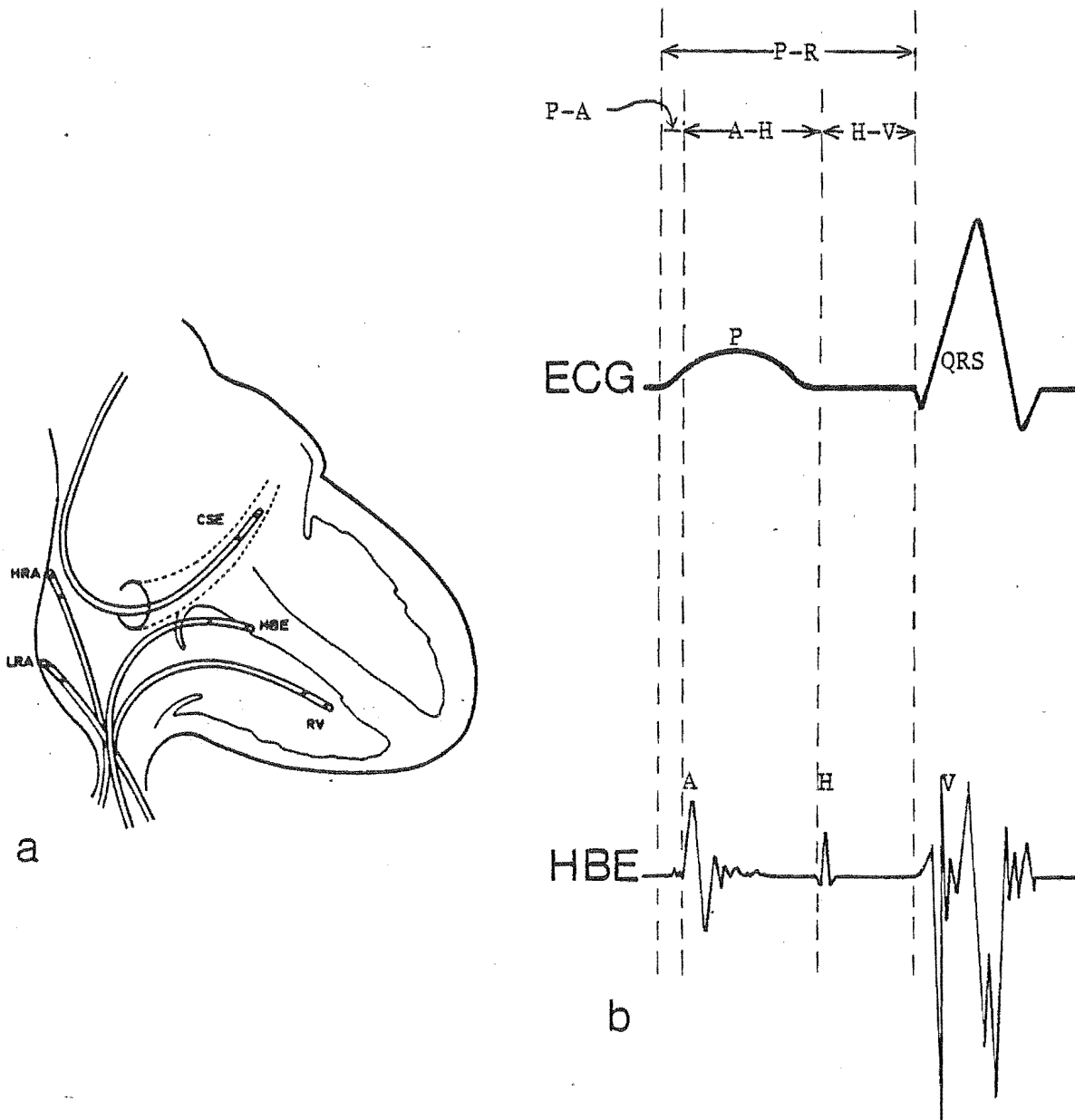


Figure 1.11 a) Catheter electrode positions normally used for intracardiac recording. HRA = high right atrium; LRA = lower right atrium; HBE = His bundle lead; RV = right ventricle; CSE = coronary sinus electrode representing, indirectly, left atrial and left ventricular sites.
b) A typical intracardiac recording from the vicinity of the His bundle with an E.C.G. for comparison (from Curry, 1975).

and the coronary sinus (CSE) position allows the determination of the direction of the atrial activation. The catheter position which is common to all intracardiac electrocardiography is in the vicinity of the common bundle of His (HBE). A typical recording from the HBE catheter is depicted in Figure 1.11b along with an E.C.G. for comparison.

The labels A, H and V are commonly associated with the atrial activation, His bundle activation and ventricular activation, respectively. The normal intervals between these events can be read from Table 1.2. The final catheter position shown in Figure 1.11a is within the right ventricular chamber (RV) and is commonly used to directly pace the ventricular myocardium.

Two excellent reviews of the methods of intracardiac electrocardiography are Curry (1975) and Narula (1975).

1.4 CARDIAC PATHOLOGY

A vast amount of published material is available on the causes and electrocardiographic manifestations of cardiac disorders (see, for instance, Hurst, 1978; Braunwald, 1980). The purpose of this section is to introduce several aspects of cardiac pathology with relevance to later chapters, particularly abnormal heart rhythms - arrhythmias. These aspects of cardiac pathology have been loosely divided into five subsections. The first three of these (covering infarction and ischaemia, electrolyte disturbances and hypertrophy) are only a brief introduction - the reader is referred to Hurst (1978) and Braunwald (1980) for more detail. Arrhythmias are split into two subsections, those caused by disorders of impulse production and those caused by disorders of impulse conduction.

§1.4.1 Infarction and ischaemia

Myocardial infarction is the death of a region of the myocardium as a result of the interruption of an adequate blood supply to the region. The most common cause of myocardial infarction is coronary artery disease, in which the vital coronary arteries become reduced in internal diameter by the build up of fatty and (in advanced states) calcified deposits. Infarcted muscle loses its contractile properties permanently and is eventually replaced by fibrous tissue. The occurrence of infarction is therefore extremely serious, especially if left ventricular myocardium is involved, and frequently it is fatal. Myocardial ischaemia is a transient inadequacy of the blood supply to the myocardium. Often the occurrence of ischaemia, with its symptoms of chest pain and E.C.G. changes, is an indication of coronary artery disease and may forewarn a myocardial infarction. Ischaemia also occurs directly before infarction and in regions of myocardium which eventually recover around an infarction.

At the cellular level, a number of changes occur as a result of myocardial infarction. In the acute phase (that is within the first few hours after the onset of infarction) cells in the affected area have a decreased resting membrane voltage of approximately -70 mV (Castellanos and Myerburg, 1978). As a result (assuming the infarction is occurring in the ventricular myocardium) an impressed electric field exists during ventricular diastole, directed from the affected region to the surrounding unaffected myocardium. This is the so-called "current-of-injury" (Schamroth, 1975). Its effect on the E.C.G. is to produce a diastolic field on the body surface with a potential minimum located in the area above the region undergoing infarction. An E.C.G. lead recorded from this region will show an apparent raising of the potential during the S-T interval (cf. Figure 1.7) relative to the rest of the signal (this is S-T elevation). A few hours after the onset of infarction the cells in the centre of the region begin to die. These dead cells no longer undergo depolarisation so the wave of depolarisation deflects around the infarction as it moves through the myocardium. As a result, the surface electrocardiographic field is often substantially altered from normal (or at least from its pre-infarction form) (Boineau et al., 1968). If the endocardium is involved (particularly in regions normally excited early during ventricular activation) the early portion of the QRS will be modified with areas of negative potential appearing on the surface above the infarcted myocardium (Boineau et al., 1968; Castellanos and Myerburg, 1978). With the standard E.C.G. measurement techniques this is manifest in the appearance of abnormally large Q waves in leads positioned over the infarction.

The current-of-injury mentioned above occurs in cells which are temporarily ischaemic as well as those becoming infarcted. The blood supply to the endocardium of the ventricles is less extensive than that to the epicardium, so ischaemia of the endocardium occurs more readily than ischaemia of the epicardium. The resulting electrocardiographic field during ventricular diastole, therefore, has areas of positive potential over ischaemic regions. These often appear on standard ECG leads as S-T depression (Schamroth, 1975). The repolarisation of myocardial cells is also altered by ischaemia. The repolarisation phase (phase 3 in Figure 1.1) is lengthened in ischaemic cells so that they repolarise later than unaffected cells (Schamroth, 1975). The T wave field is increased in amplitude (Schamroth, 1975) because the cancellation of opposing impressed electric fields within the myocardium is lessened

(cf. §1.3.5). Depending on the site and size of the ischaemic region, the T wave may change substantially in its spatial form on the body surface.

The E.C.G. changes associated with the ischaemia of cells surrounding an infarcted region (S-T and T wave changes) disappear as recovery occurs from a non-fatal infarction. However the Q waves and other changes associated with the presence of dead cells remain. The diagnosis of the presence and location of a myocardial infarction may be complicated by the presence of an abnormal excitation sequence caused by ischaemia or infarction in the V.S.C.S. Schamroth (1975) has published a substantial review and bibliography on electrocardiography in ischaemia and infarction.

§1.4.2 Electrolyte disturbances

The current understanding of the mechanism of myocardial cellular activation is summarised in Section 1.1. It is clear that the nature of the membrane depolarisation and repolarisation depends on the intracellular and extracellular concentrations of the ions concerned. A change in the extracellular ionic concentration from normal is known as an electrolyte disturbance. The common electrolyte disturbances primarily affect the repolarisation phase of the action potential and therefore the T wave of the E.C.G. (Castellanos and Myerburg, 1978). Only the amplitude and timing of the T wave is altered, not the spatial surface function.

An excess of extracellular potassium (hyperkalemia) causes the T wave to become large with a sharp peak as a function of time. With even more potassium the QRS duration increases and may become continuous with the T wave. A shortage of potassium (hypokalemia) reduces or even inverts the T wave amplitude and the U wave becomes prominent. An excess of calcium (hypercalcemia) reduces the Q-T interval while less calcium than normal (hypocalcemia) lengthens the Q-T interval.

§1.4.3 Hypertrophy

Hypertrophy (an increase in muscle bulk) occurs in the walls of one or more heart chambers, in response to an increased mechanical workload. The increased load may be caused by a leaking heart valve, a narrowed valve opening, another type of obstruction to flow, an increased resistance in the pulmonary circulation or a high systemic blood pressure. In some cases a distension of the walls may accompany the hypertrophy.

The increase in the number of myocardial cells which occurs in hypertrophy causes a corresponding increase in the impressed electric

field which generates the E.C.G. If only the left ventricle is hypertrophied, the increase in the number of cells there usually shifts the position of the QRS potential maximum leftward and upward. Conversely, right ventricular hypertrophy usually shifts the potential maximum towards the right. In both cases the QRS amplitude is increased. Atrial hypertrophy causes a similar increase in the amplitude of the P wave. However, the electrocardiographic diagnosis of hypertrophy, in the absence of a pre-hypertrophy E.C.G. for comparison, is made difficult by the large variation in the E.C.G. among normal healthy subjects (cf. Simonson, 1961). For example, while any E.C.G. which shows a QRS amplitude greater than the upper limit of normal will almost certainly belong to a patient with ventricular hypertrophy, the majority of such cases will be missed by this criteria alone (Castellanos and Myerburg, 1978).

§1.4.4 Arrhythmias - impulse production

In normal sinus rhythm the S-A node acts as the only heart pacemaker. In patients with the sick sinus syndrome, which may be caused by several diseases, a number of intermittent pacemaker abnormalities may be observed, ranging from sinus arrest (no S-A nodal activity) to bursts of sinus tachycardia (fast heart rate paced by the S-A node) (cf. Marriot and Myerburg, 1978). Refractoriness of the tissue surrounding the node may cause some of the S-A nodal impulses to be prevented from propagating further (cf. Schamroth, 1971). As no direct recording of S-A nodal activity is possible (with current electrocardiographic techniques), its activity must be inferred on the basis of the timing and appearance of the P waves. An atrial contraction which is initiated by an impulse from the S-A node should produce the normal P wave described in §1.3.3. During an intracardiac E.C.G. investigation (cf. §1.3.7) it is possible to carry out tests of sinus node function using external pacing. Curry (1975) has reviewed the methods used.

If the S-A node impulses are absent or blocked from reaching the ventricular myocardium, spontaneous depolarisation usually occurs within the A-V system to provide auxilliary pacemaking. A beat produced in this manner is called a junctional beat. Junctional rhythm has a slow rate with normally formed QRS waves. If retrograde (i.e. in the opposite direction to normal) conduction occurs through the A-V node, an abnormal P wave (abnormal since atrial activation is initiated at the A-V node) may appear after the QRS wave in junctional rhythm.

Ordinary myocardial cells may spontaneously depolarise to produce ectopic beats (beats of abnormal origin). Ectopic beats arising in the atrial myocardium are known to occur in some normal persons and commonly occur in patients suffering from digitalis poisoning, atrial overload or ischaemia (Marriot and Myerburg, 1978). They are characterised by an abnormal P wave (again since atrial activation is not in the normal sequence) occurring prematurely. Normal impulse conduction to the ventricles (and therefore a normal QRS wave) occurs in the majority of atrial ectopic beats. Ventricular ectopic beats, as the name suggests, arise from cells within the ventricular myocardium. Again they are not uncommon in normal persons and frequently occur as a result of myocardial infarction, heart failure (inadequate heart pumping) and many other conditions (Marriot and Myerburg, 1978). Because ventricular activation radiates from a single site in a ventricular ectopic beat the QRS wave produced is always of abnormally long duration and grossly altered shape. It appears prematurely and often is followed by a pause before the next sinus beat.

Other, more serious, arrhythmias of impulse production may be initiated by ectopic beats. These include atrial tachycardia, atrial fibrillation, ventricular tachycardia and ventricular fibrillation, in order of increasing severity. A tachycardia (in this context) is caused by a continuous series of premature ectopics from a single group of cells. Fibrillation may be described as a random and continuous sequence of ectopics generated from many sites which produces no coordinated contraction. The electrocardiographic manifestations of these and less common arrhythmias are reviewed in Schamroth (1971) and Marriot and Myerburg (1978).

§1.4.5 Arrhythmias - impulse conduction

Abnormalities of impulse conduction may be divided into those primarily due to a disease causing slowed conduction and those primarily due to the existence of an extra pathway (or pathways) for impulse conduction from the atria to the ventricles. The A-V conduction system is the most frequent site of the first type of abnormality. The term used for slowed conduction is block(!) and it is described as occurring in three degrees (Schamroth, 1971). In 1st degree block all impulses are conducted to their destination, albeit slowly; in 2nd degree block some impulses are not conducted because they encounter refractory tissue; and in 3rd degree block (or complete block) no impulses are conducted through

the site of the block. Block in the A-V conducting system (cf. §1.2.2) may be diagnosed from the time interval between the P and QRS waves in normal sinus rhythm. For example, a P-Q interval of 210 msec or greater is considered to be 1st degree block in the A-V node or V.S.C.S. (Marriot and Myerburg, 1978). If a normal P-Q interval is associated with certain characteristic QRS abnormalities a bundle branch block may be diagnosed. The QRS abnormality is caused by an abnormal sequence of activation due to the late arrival of the excitory impulse from one or more of the bundle branches (Kulbertus and Demoulin, 1975). Experience has shown that A-V block tends to get progressively worse so it is common to investigate such patients with invasive intracardiac electrocardiography (cf. §1.3.7). The development of a reliable non-invasive method for detecting activity in the V.S.C.S. may eliminate the need for such dangerous and costly procedures (see Chapter 7).

The abnormalities caused by the existence of an extra pathway for impulse conduction between the atria and the ventricles are now classified under the heading of the pre-excitation syndrome. Several anatomical routes for these pathways have been described (Sano, 1976; James, 1978), all bypassing the A-V node in some way. Since the A-V node conducts relatively slowly, the impulses from the sinus node are conducted preferentially by the extra pathway in patients with the pre-excitation syndrome. Therefore their electrocardiograms show a short P-Q interval and an abnormally early ventricular activation ("pre-excitation"). The pre-excitation syndrome is not directly harmful but it may lead to fast and unpleasant tachycardias (by allowing an impulse to circulate continuously through atrial and ventricular tissue) and may leave the ventricular myocardium unprotected from very rapid atrial rates (Marriot and Myerburg, 1978). A considerable research effort is currently directed at the investigation of the syndrome and its related arrhythmias using intracardiac and conventional electrocardiography (Curry, 1975) and by computer modelling (Millane *et al.*, 1980). A similar effort is directed at establishing effective treatments which now include drug therapy (Lucchesi, 1978), the surgical division of pathways (Baird and Uther, 1978) and the use of patient-operated pacemakers (Iwa *et al.*, 1978).

CHAPTER 2

THE APPLICATION OF POTENTIAL THEORY TO ELECTROCARDIOGRAPHY

The interpretation of the electrocardiogram is an inverse problem - that is a problem in which the source of a radiated field is to be found from measurements of the field. The unknown source in electrocardiography is the (normal or abnormal) electrophysiological activity in the myocardium. The "radiated" field is the time-varying body surface electrical potential field. A formulation for the electrocardiogram in terms of potential theory is presented in this chapter, along with a review of the possible methods of finding an inverse solution. The first section develops the formulation, after making an appraisal of the assumptions implicit in the formulation. Section 2.2 explores the solutions for the electrocardiographic source. It is shown that, even neglecting the effects of the surface shape and the internal conductivity inhomogeneities, lack of uniqueness in the solution forces the use of *a priori* information about the source. Inverse solution formulations which include both the body surface shape and the conductivity inhomogeneities are considered.

2.1 FORMULATION

An electromagnetic field may be defined in terms of a number of field vector quantities. The relationships between these vector quantities are given by the Maxwell equations (Stratton, 1941)

$$\nabla \times \underline{E} + \partial \underline{B} / \partial t = 0 \quad (1)$$

$$\nabla \times \underline{H} - \partial \underline{D} / \partial t = \underline{J} \quad (2)$$

where \underline{E} is the electric field intensity,
 \underline{H} is the magnetic field intensity,
 \underline{D} is the electric displacement,
 \underline{B} is the magnetic induction, and
 \underline{J} is the current density.

The field quantities in these equations are assumed to be finite throughout the entire field and to be continuous functions of time t and position \underline{x} , at all points excluding those on surfaces which mark an abrupt change in the physical properties of the medium. In order to apply (1) and (2) to the conducting medium which forms the domain of the E.C.G. problem, a number of assumptions are made. These are carefully appraised before proceeding further.

§2.1.1 Assumptions

The first assumption made in establishing a formulation for the E.C.G. is that the system of body tissues is linear. Body tissues are largely composed of weakly ionised solutions. While the properties of the plasma membranes surrounding the cells are definitely non-linear at the microscopic level (cf. Coraboeuf, 1978; Noble, 1979), it seems unlikely that these non-linearities significantly affect the macroscopic conducting properties of an aggregation of cells (Rush and Nelson, 1976). If the passive electrical properties of a region of body tissue can therefore be thought of as equivalent to an ionised solution, the assumption of linearity is justified in the range of fields encountered in electrocardiography (Stratton, 1941). Even in the lungs, where the tissue volume comprises a large fraction of gas, the individual alveoli (the gas compartments through the walls of which gases diffuse to and from the blood) are so small and diffusely distributed that linear macroscopic properties may be assumed (Rush and Nelson, 1976). The magnitude of any Hall effect (Stratton, 1941) is also so small as to be negligible.

The source of the electromagnetic fields is taken to be an impressed current density $\underline{J}_i = \underline{J}_i(\underline{x}, t)$ which macroscopically represents the active and passive ionic currents across the cell membranes within the myocardium. \underline{J}_i is therefore the inverse solution sought for the E.C.G. problem. Any free charge in the body tissues will be distributed with a relaxation time of the order of 10^{-10} sec (Stratton, 1941), a negligibly short time when one considers that the maximum frequency components in the E.C.G. are less than 10^3 Hz (von der Groeben et al., 1968). Therefore the free charge density may be taken to be zero everywhere in the domain of the problem. The representation of the source as an impressed current density does not imply that the cells act as time-varying constant current generators. As pointed out by Lepeschkin (1976c), the conductance of surrounding tissue does have some influence on the membrane ionic currents. The approach adopted here incorporates such

variation into $\underline{J}_i(\underline{x}, t)$. \underline{J}_i may also be specified in several other ways. Frank (1953) and Rudy and Plonsey (1979), for example, choose to represent the source as a dipole layer distributed over a surface approximating the wavefront of depolarisation. The choice is simply one of convenience.

The fields generated by electrophysiological activity are assumed to be conservative. For this assumption to be valid, the contribution of inductive and capacitive effects to the E.C.G. must be negligible. Consider first the effects of self induction. Equation (1) may be expressed in integral form as (Stratton, 1941)

$$\int_C \underline{E} \cdot \hat{\tau} dC = - \partial/\partial t \int_S \underline{B} \cdot \hat{n} dS \quad (3)$$

where C is a contour enclosing the surface S, \hat{n} is the unit normal to S and $\hat{\tau}$ is the unit tangent to C. A realistic estimate of the mean magnetic field within the torso generated by the heart is 5×10^{-10} Wb/m² (Baule and McFee, 1963). Taking a circular contour of 1 m radius and a frequency of 500 Hz (both representing extreme values for the human), the maximum value for $|\underline{E}|$ obtained from (3) is of the order of 1 μ V/m (Plonsey, 1976). Thus the electric field generated on the body surface by self inductive coupling represents only about a tenth of a percent of the total field amplitude.

The effects of capacitance within the body tissues can be assessed on the basis of the second Maxwell equation (2) and some experimental data (Schwan and Kay, 1957). Consider a homogeneous region with conductivity σ and permittivity ϵ , which does not contain impressed sources, so that $\underline{D} = \epsilon \underline{E}$ and $\underline{J} = \sigma \underline{E}$ (Stratton, 1941). Assume for simplicity that all field quantities are complex phasors with angular velocity ω , for example $\underline{E}(\underline{x}, t) = \underline{E}(\underline{x})e^{j\omega t}$. Equation (2) then may be written

$$\nabla \times \underline{H} = \sigma(1 + j\omega\epsilon/\sigma)\underline{E} \quad (4)$$

The studies of Schwan and Kay (1957) on body tissues show that $|\omega\epsilon/\sigma| < 0.15$ throughout the physiological range of frequencies and is much smaller for the major part of the E.C.G. spectrum, therefore this term may reasonably be neglected in comparison with unity (Plonsey, 1976). The presence of inhomogeneities and impressed sources does not effect the conclusion that capacitive effects may be ignored in the E.C.G. The fields may therefore be considered to be conservative and the derivatives with respect to time neglected in (1) and (2). This

property of quasi-stationarity (Plonsey, 1976) justifies the interpretation of the E.C.G. at any instant as representing the nett effect of the myocardial activity at that instant only.

The final assumption made in the formulation is that the properties of the body tissues are isotropic, in particular that the conductivity $\sigma = \sigma(\underline{x})$ is a scalar function of position. Conductivity measurements carried out on living tissues (Rush *et al.*, 1963; Burger and van Dongen, 1961) indicate that the tissues which make up the bulk of the thoracic volume, i.e. lung, blood and fat, exhibit isotropic properties. However, the muscle tissues exhibit significant anisotropy. In heart muscle, Rush *et al.* (1963) report that the conductivity tangential to the heart wall (and therefore parallel to the muscle fibres) is twice the conductivity measured in the direction perpendicular to the wall. In skeletal muscle the ratio of the conductivity in the direction of the muscle fibres to the conductivity in the perpendicular direction can be as high as 15:1. A summary of the data of Rush *et al.* (1963) is presented in Table 2.2. A study of the effects of muscle tissue anisotropy underlying the body surface on the E.C.G. is reported by McFee and Rush (1968). They conclude that the effect of a uniform layer of muscle is approximately the same as the effect of a uniform layer of isotropic medium of different thickness. Thus the main effect of the layer of anisotropic muscle underlying the body surface is to reduce the amplitude of the electrocardiographic surface field, as if that layer is 3 to 5 times thicker, isotropic and of intermediate conductivity (McFee and Rush, 1968). The assumption of uniformity for this surface muscle layer is supported by the results of Burger and van Dongen (1961), who passed current from head to foot and observed little effect on the potential variation as a result of muscle layer variation. Therefore, the presence of this muscle layer has little effect on the interpretation of the electrocardiogram, so that the assumption of isotropy is valid within the thoracic volume. The anisotropy of heart muscle is more difficult to accommodate, since this tissue lies within the source region and it is not of uniform thickness. It is assumed in the following, therefore, that any effects of heart muscle anisotropy are incorporated into the impressed source function. Thus $\underline{J}_1(\underline{x}, t)$ represents not only the electrophysiological activity within the myocardium but also some of the conducting properties of the region.

§2.1.2 Poisson's equation

The assumption of linearity and the choice of an impressed current source density distribution allow the total current density to be expressed for any point within the domain of the E.C.G. problem as

$$\underline{J} = \sigma \underline{E} + \underline{J}_i \quad (5)$$

Taking the divergence of (2), neglecting the contributions of derivatives with respect to time and substituting for \underline{J} from (5) gives

$$\begin{aligned} 0 &= \nabla \cdot \underline{J} \\ &= \sigma \nabla \cdot \underline{E} + \nabla \sigma \cdot \underline{E} + \nabla \cdot \underline{J}_i \end{aligned} \quad (6)$$

Requiring the electric field to be conservative is the same as stating that $\nabla \times \underline{E} = 0$. So, \underline{E} may be expressed directly in terms of the potential V as $\underline{E} = -\nabla V$. Therefore (6) becomes

$$\sigma \nabla^2 V = -\nabla \sigma \cdot \nabla V + \nabla \cdot \underline{J}_i \quad (7)$$

This expression forms the basis of the E.C.G. formulation. It is clearly a form of Poisson's equation for an electrostatic potential field (Stratton, 1941), $\nabla^2 V = -W$, where $W = W(\underline{x})$ embodies the source(s) of that field. In (7) the "source" includes not only the impressed current density of the heart's electrophysiological activity but also the effects of any conductivity variation throughout the thoracic region. At any point \underline{x} where $\underline{J}_i(\underline{x}) = 0$ and σ is constant, (7) reduces to $\nabla^2 V = 0$, which is the Laplace equation (Stratton, 1941).

§2.1.3 Integral equation for potential

Consider for the moment that the impressed current density \underline{J}_i exists in a region κ of constant conductivity σ . The form of Poisson's equation in this case is

$$\nabla^2 V = \nabla \cdot \underline{J}_i / \sigma \quad (8)$$

To find an explicit expression for V in terms of the source term on the right-hand side of (8), both sides must be integrated over κ and the regular closed surface S which bounds κ . Let Φ and Ψ be two scalar functions of position which satisfy certain requirements of continuity (Stratton, 1941) and obey Poisson's equation throughout κ . Green's theorem (Stratton, 1941), then states

$$\iiint_{\kappa} (\Psi \nabla^2 \Phi - \Phi \nabla^2 \Psi) dv = \iint_S (\Psi \partial \Phi / \partial \nu - \Phi \partial \Psi / \partial \nu) dS \quad (9)$$

In (9), dv and dS are the volume and surface elements of integration respectively and $\hat{\nu}$ is the unit normal to S directed out of κ .

Φ is put equal to the potential V , which obeys Poisson's equation (8). Ψ is put equal to $1/4\pi R$, where $R = |\underline{x} - \underline{x}'|$ is the distance from a fixed point P , with position vector \underline{x} , to any point Q , with position vector \underline{x}' . The function chosen for Ψ is the Green's Function for potential in three dimensions (cf. Morse and Feshbach, 1953).

Ψ satisfies Laplace's equation, i.e. $\nabla^2 \Psi = 0$, everywhere except at P , where it is singular because $R \rightarrow 0$.

Consider an interior point $P \in \kappa$. To exclude the singularity, a small surface S_1 of radius α is circumscribed about P . The region κ_1 , bounded by S_1 , is excluded from the volume integral on the left-hand side of (9) (see Figure 2.1). Substituting for Φ and Ψ in (9) gives

$$\iiint_{\kappa - \kappa_1} \nabla \cdot \underline{J}_i(\underline{x}) dv / 4\pi \alpha R = \iint_{S + S_1} (R^{-1} (\partial V / \partial \nu) - V (\partial (R^{-1}) / \partial \nu)) dS / 4\pi \quad (10)$$

where the unit normal $\hat{\nu}$ is outward to S and inward to S_1 .

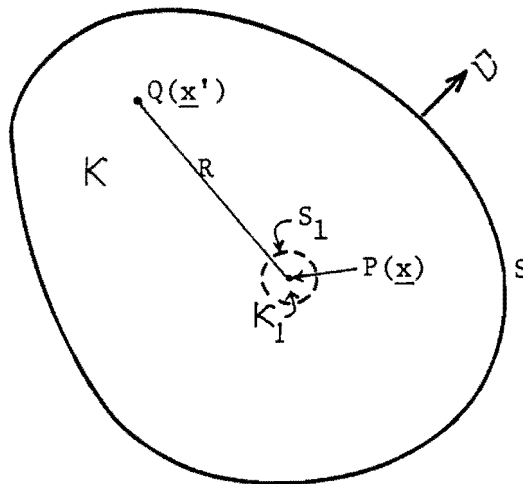


Figure 2.1 Application of Green's theorem to a region $\kappa - \kappa_1$, bounded externally by S and internally by S_1 .

Consider the behaviour of the integral over S_1 as $\alpha \rightarrow 0$. On S_1 , $\partial V/\partial v = -\partial V/\partial R$ and $\partial(R^{-1})/\partial v = 1/\alpha^2$ and therefore

$$\begin{aligned} \lim_{\alpha \rightarrow 0} \iint_{S_1} (R^{-1} \partial V/\partial v - V(\partial(R^{-1})/\partial v)) dS &= \lim_{\alpha \rightarrow 0} (-4\pi\alpha \overline{\partial V/\partial R} - 4\pi\overline{V}) \\ &= -4\pi V(P) \end{aligned} \quad (11)$$

where the $\overline{\quad}$ denotes the mean value over S_1 . The integral equation for the potential at an interior point is therefore

$$V(P) = -\iiint_{\kappa} (\nabla \cdot \underline{J}_1(\underline{x}') dv) / 4\pi\sigma R + \iint_S (R^{-1}(\partial V/\partial v) - V(\partial(R^{-1})/\partial v)) dS / 4\pi, \quad P \in \kappa. \quad (12)$$

Consider now the derivation of the field for a point $P \in S$.

To exclude the singularities in both the volume and surface integrals of (9) as $Q \rightarrow P$, a hemispherical region $\kappa_1 \in \kappa$ is constructed around P . κ_1 is bounded by a hemispherical surface S_1 , radius α , and $S_2 \in S$, where S_2 lies within a radius α from P . As α tends to zero, the integral over S_1 approaches a limit of $-2\pi V(P)$ in exactly the same manner as (11). Also as α tends to zero, the surface S_2 shrinks about P . As a result the potential at P is given by

$$V(P) = -\iiint_{\kappa} (\nabla \cdot \underline{J}_1(\underline{x}') dv) / 2\pi\sigma R + \iint_S (R^{-1}(\partial V/\partial v) - V(\partial(R^{-1})/\partial v)) dS / 2\pi, \quad P \in S. \quad (13)$$

It remains to show that the surface integral in (13), which now contains a singularity, is well behaved. Consider P to lie on a region of S which has non-zero radius a , as shown in Figure 2.2.

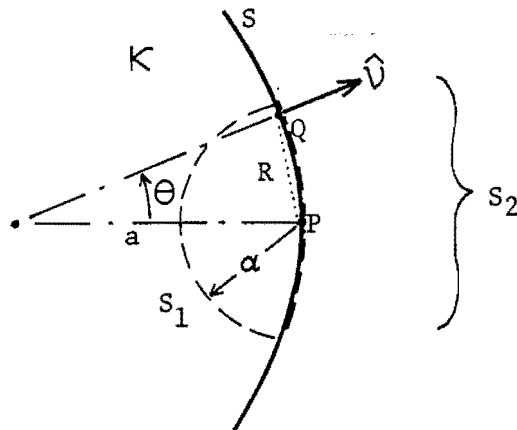


Figure 2.2 Geometry for analysing the behaviour of the surface integral in equation (13).

Consider the contribution to (13) from the portion of the surface integral over S_2 for some finite but small α . Noting from Figure 2.2 that $R \approx a\theta$, $\partial(R^{-1})/\partial v \approx -\sin\theta/a^2\theta^2$ and $dS = 2\pi a^2\theta d\theta$, the integral over S_2 becomes

$$\iint_{S_2} (R^{-1}(\partial V/\partial v) - V(\partial(R^{-1})/\partial v)) dS/2\pi = (\overline{\partial V/\partial v}) \int_0^{\alpha/a} a d\theta + \overline{V} \int_0^{\alpha/a} \sin\theta d\theta/\theta \quad (14)$$

where mean values are used for $\partial V/\partial v$ and V since α is small. Both integrals on the right-hand side of (14) are bounded, therefore the singular surface integral of (13) is well behaved. A similar argument may be used to show that the volume integral in (12) is well behaved at a point in κ where $\nabla \cdot \underline{J}_1$ is non-zero (Stratton, 1941).

Before studying the inclusion of conductivity inhomogeneities into the integral equation, it is instructive to derive an expression for the field generated by the source distribution $\nabla \cdot \underline{J}_1/\sigma$ in an infinite homogeneous conducting region. Clearly the impressed current density \underline{J}_1 is non-zero only within a surface S_0 which completely encloses the heart region. As P is removed a large distance from the region containing the source, V tends to decrease as $1/R$ and $\partial V/\partial R$ as $1/R^2$ (cf. Stratton, 1941). Therefore, as the regular boundary S is removed towards infinity, the quantities $R^{-1}(\partial V/\partial v)$ and $V(\partial(R^{-1})/\partial v)$ tend to decrease as $1/R^3$ in (12). The surface integral in (12) then vanishes for an infinite homogeneous region giving

$$V'(P) = - \iiint_{\kappa} \nabla \cdot \underline{J}_1(\underline{x}') dv/4\pi\sigma R \quad (15)$$

where V' denotes the "infinite homogeneous field" generated by the source.

Plonsey (1976) derives an alternative expression for the potential, using the vector identity $\nabla \cdot (\underline{J}_1/R) = \nabla R^{-1} \cdot \underline{J}_1 + R^{-1} \nabla \cdot \underline{J}_1$. Integrating both sides of the identity over κ and applying the divergence theorem to the left-hand side gives

$$\iint \underline{J}_1 \cdot \hat{v} dS/R = \iiint_{\kappa} \nabla(R^{-1}) \cdot \underline{J}_1 dv + \iiint_{\kappa} R^{-1} \nabla \cdot \underline{J}_1 dv .$$

S may be chosen to lie outside all sources so that \underline{J}_1 is zero everywhere on S and the left-hand side disappears. An alternative form of (15) may then be written:

$$V'(P) = \iiint_{\kappa} \nabla(R^{-1}) \cdot \underline{J}_1 dv/4\pi\sigma \quad (16)$$

This expression has somewhat more appeal than (15), because \underline{J}_1 is expressed as the dipole moment per unit volume and the element of the impressed source $\underline{J}_1 dv$ is a current dipole (Stratton, 1941; Plonsey, 1976).

Equations (8), (15) and (16) are valid only for the case of the source distribution embedded within an infinite homogeneous conducting medium. A physical approximation to this has been experimentally engineered in studies on isolated animal hearts in electrolytic tanks (cf. Taccardi, 1976; Mirvis et al., 1978). However a precise formulation for the electrocardiogram must include the effects of the body surface and the internal conductivity inhomogeneities, which are embodied in the first term on the right-hand side of (7). Green's Theorem is again employed to derive a more general integral equation for potential.

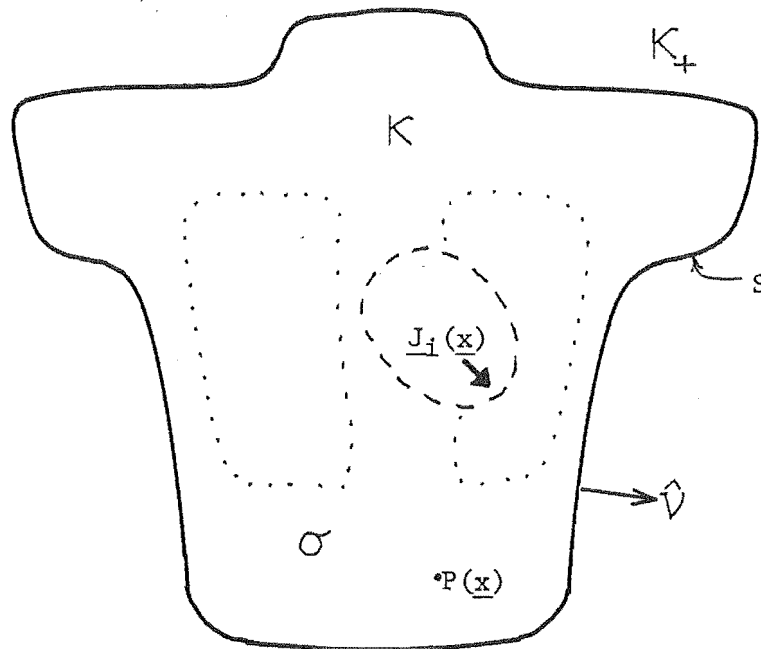


Figure 2.3 An inhomogeneous conducting volume κ bounded by the "body surface" S .

Consider the finite inhomogeneous region κ bounded by the surface S as depicted by Figure 2.3. The impressed source density $\underline{J}_1(\underline{x})$ exists only in the region of the heart. The conductivity $\sigma(\underline{x})$ may vary throughout κ . Green's Theorem (9) is applied for a point P , within κ , and the same substitutions as above are made for Φ and Ψ , giving

$$\begin{aligned}
 V(P) = & - \iiint_{\kappa} \nabla \cdot \underline{J}_i \, dv / 4\pi\sigma R + \iiint_{\kappa} \nabla\sigma \cdot \nabla V \, dv / 4\pi\sigma R \\
 & + \iint_S (R^{-1} \partial V / \partial \nu - V \partial (R^{-1}) / \partial \nu) \, dS / 4\pi \quad , \quad P \in \kappa
 \end{aligned} \tag{17}$$

Equation (17) is a general expression for the potential everywhere within κ . It is evident that the field is simply the sum of the "infinite homogeneous field" of the source (15), and contributions from the outer surface and any regions in which the gradient of conductivity is non-zero. If the surface S represents the body surface (an insulating boundary), the current normal to the surface is zero. Therefore, since $\underline{J} = -\sigma \nabla V$, the first term in the surface integral of (17) disappears. In Chapter 5, a "surface admittance" is applied over a spherical surface S in order to stimulate the effects of different boundary shapes. Since the "admittance" is defined as the ratio of normal potential gradient to potential on S , both terms in the surface integral must then be taken into account.

§2.1.4 The null field concept

The integral formulation derived above can be extended by the application of Green's Theorem (9) for points in different regions. Consider the point P to be in the region κ_+ , outside the surface S (see Figure 2.3). The volume of integration is again κ , which now excludes P and the singularity in R^{-1} . The result is

$$\begin{aligned}
 0 = & - \iiint_{\kappa} \nabla \cdot \underline{J}_i \, dv / 4\pi\sigma R + \iiint_{\kappa} \nabla\sigma \cdot \nabla V \, dv / 4\pi\sigma R \\
 & + \iint_S (R^{-1} \partial V / \partial \nu - V \partial (R^{-1}) / \partial \nu) \, dS / 4\pi \quad , \quad P \in \kappa_+
 \end{aligned} \tag{18}$$

The expression on the right-hand side of (18) is therefore identically equal to zero for any "point of observation" P outside S . This has variously been called the null field (Bates and Wall, 1977) and the extended boundary condition (Waterman, 1979). The usefulness of this integral equation becomes apparent when considering an analytical solution to a potential field problem in terms of a series of functions of position which are orthogonal on a regular surface circumscribing S (cf. Waterman, 1979; Bates, 1975; Bates, 1980). The extended model of Chapter 6 makes use of the null field formulation.

2.2 THE INVERSE SOLUTION

Any interpretation scheme for the electrocardiographic signals measured on the body surface is an inverse solution for the E.C.G. The success of the standard 12-lead interpretation scheme (see Chapter 3) demonstrates that such a solution can be enormously useful in the diagnosis of cardiac and related diseases. However, it has been recognised that more information is available on the body surface than is used with standard lead systems (Boineau, 1974), that the best solutions obtained to date are approximate (Barr and Spach, 1976; Barnard *et al.*, 1976) and that all solutions show a large variation among the normal population (von der Groeben, 1968). The shortcomings of the standard schemes of electrocardiographic interpretation have encouraged a continuing push to find an exact inverse solution - a solution which enables the exact determination of the electrophysiological activity in the heart. It is reasonable to assume that such a solution would allow a better diagnosis to be made than is possible at present. Clearly, to be useful, such a solution must be unique. A scheme which provides the physician with a number of possible and independent interpretations to choose from would severely test his objectivity! It turns out that it is the uniqueness, or rather the lack of it, which hampers the development of an exact inverse solution.

§2.2.1 Lack of uniqueness

To begin with consider how one might attempt to determine the impressed current sources, existing within an infinite homogeneous region of constant conductivity σ , from measurements. The measurements (denoted V_s) are made on a surface S which completely encloses the sources. The voltage at an arbitrary point P is given by (15) and $V(\underline{x}) \rightarrow V_s(\underline{\xi})$ as $P \rightarrow T$, where T is an arbitrary point on S , with position vector $\underline{\xi}$. For brevity of notation the source term is represented by $\rho(\underline{x}') = -\nabla \cdot \underline{J}_1(\underline{x}')/\sigma$ giving

$$V_s(\underline{\xi}) = \iiint_K \rho(\underline{x}') dv / 4\pi R \quad (19)$$

For simplicity take S to be a sphere of radius a . Both V_s and ρ are continuous scalar functions of position and may therefore be each expanded in an infinite series of normalised spherical harmonic functions $Y_{nm}(\theta, \phi)$ (cf. Hobson, 1930; James, 1973; and see Appendix 1). θ and ϕ are the polar and azimuthal angles referred to a coordinate system with its origin at the centre of S . Thus

$$V_s(\underline{\xi}) = \sum_{n=0}^{\infty} \sum_{m=-n}^{+n} \chi_{nm} Y_{nm}(\theta, \phi) \quad (20)$$

and

$$\rho(\underline{x}') = \sum_{n=0}^{\infty} \sum_{m=-n}^{+n} \rho_{nm}(r') Y_{nm}(\theta', \phi')$$

where the unknown coefficients $\rho_{nm}(r')$ are functions of the radial coordinate r' . The constant coefficients χ_{nm} may be straightforwardly found from V_s as

$$\chi_{nm} = \iint_S V_s Y_{nm} dS/4\pi \quad (21)$$

since the Y_{nm} are orthogonal over a closed surface (cf. Appendix 1). R^{-1} is now expanded as a double series of spherical harmonic functions,

$$R^{-1} = \sum_{n=0}^{\infty} \sum_{m=-n}^{+n} (2n+1)^{-1} r^n Y_{nm}(\theta, \phi) r'^{-n-1} Y_{nm}(\theta', \phi') \quad (22)$$

which converges for all points with $r < r'$ (cf. Morse and Feshbach, 1953). Substitute the expressions (20) and (22) in (19), multiply both sides by a "testing function" $Y_{k\ell}(\theta, \phi)$ and integrate over S to get

$$\chi_{nm} = a^{-n-1} \int_0^a \rho_{nm}(r') r'^{n+2} dr' / (2n+1) \quad (23)$$

If V_s is observed all over S then in principle the χ_{nm} can be deduced by (21). However, there are clearly an infinite number of distributions $\rho_{nm}(r')$ which could correspond to any set of χ_{nm} . Thus the measured data cannot be "inverted" uniquely.

The disappointing conclusion reached above emphasises what might be termed a "dimensionality difficulty" in this inverse problem. Since the data measured, i.e. V_s , is essentially two-dimensional (because it is measured on a surface), it is impossible to reconstruct the three-dimensional source distribution solely from a knowledge of V_s . It is no help either (assuming it could be achieved) to make independent measurements on other surfaces also surrounding the sources. For example (again considering an infinite homogeneous region), if measurements are made on another (concentric) spherical surface S' , radius a' , which completely encloses the sources, (23) leads to

$$\chi'_{nm} = a^{n+1} \chi_{nm} / a'^{n+1} \quad (24)$$

Clearly the new χ'_{nm} give no new information about the sources. Extending this argument, knowledge of the potential (or current) field throughout the entire homogeneous region surrounding the sources does not enable a unique inverse solution to be found for those sources. This result is predicted by Helmholtz' theorem (cf. Baker and Copson, 1953; Rush, 1978) which states, for the electrostatic case, that any three-dimensional distribution of sources, confined within a closed boundary, may be replaced by a source distribution over that boundary, so far as the fields external to the boundary are concerned. Conversely, knowledge of the fields external to the boundary can enable no better than a reconstruction of an "equivalent" source distribution on that boundary, i.e. a two-dimensional quantity.

An expression for the equivalent surface source distribution of Helmholtz' theorem is obtained directly from Green's theorem (9). Consider the impressed heart source \underline{J}_1 to be embedded in an infinite homogeneous region. \underline{J}_1 is non-zero only within a region bounded by a closed surface S_0 , the "epicardial" surface. Green's theorem is applied to the infinite region outside S_0 , where there are no sources, with the result

$$V'(P) = - \iint_{S_0} (R^{-1}(\partial V'/\partial v_0) - V'(\partial(R^{-1})/\partial v_0)) dS/4\pi, \quad P \text{ outside } S_0 \quad (25)$$

where \hat{v}_0 is the unit outward normal to S_0 . The equivalent surface sources consist therefore (in the terminology of electrostatics) of a single layer, with amplitude $\partial V'(\underline{\xi})/\partial v_0$, and a double layer, with amplitude $V'(\underline{\xi})$, $\underline{\xi} \in S_0$ (Stratton, 1941). In explanation of these terms, the potential field generated by a single layer source is continuous across the layer but has a discontinuous normal derivative at the layer. The potential field of a double layer source has a continuous normal derivative, but is itself discontinuous at the layer. This potential discontinuity is equal in amplitude to the double layer. The double layer part of (25) is often written as

$$\iint_{S_0} V'(\partial(R^{-1})/\partial \hat{v}_0) dS/4\pi = \iint_{S_0} V' d\Omega/4\pi \quad (26)$$

where $d\Omega$ is the element of "solid angle" (Stratton, 1941; Metz and Pilkington, 1969). Note that a constant potential may be added to the field at all points without affecting (25). This is not surprising in the electrocardiographic context since a constant potential clearly cannot be generated by a flow of current such as the impressed sources

in the myocardium. The definition of a zero potential point is therefore entirely arbitrary (see Chapter 3).

§2.2.2 The use of a priori information

It is clear that there is no exact solution for electrocardiography, even for the straightforward case of an infinite homogeneous region surrounding the sources. However, the use of a *a priori* information about the source does allow a unique solution, albeit simplified, to be found. A simple example is the knowledge that the sources lie on a surface S_0 . Consider S_0 to be a sphere, radius b , concentric within a sphere S , radius a , over which the measurements V_s are made, and that both lie within an infinite homogeneous region. The source distribution is then $\rho(\underline{x}) = \rho(\theta, \phi) \delta(r - b)$, where $\delta(\cdot)$ represents the Dirac delta function. Equation (23) now reduces to

$$\chi_{nm} = a^{-n-1} b^n \rho_{nm} / (2n+1) \quad (27)$$

where the χ_{nm} once again are the expansion coefficients of V_s and the ρ_{nm} are now the constant expansion coefficients of $\rho(\theta, \phi)$. Note that even here, unique inversion is only possible if the value of b is known *a priori*.

Instead of assuming knowledge of the nature of the sources themselves, an alternative approach is to seek the equivalent Helmholtz source distribution on S_0 , with S_0 chosen to completely enclose the heart. For an infinite homogeneous region, (25) allows the determination of the equivalent single and double layer sources on S_0 from measurements made on S (completely outside S_0) for the case when S_0 is spherical at least (Martin and Pilkington, 1972). With S_0 defined as close as possible to the myocardium, though still enclosing all the sources, it is reasonable to expect that the equivalent source distribution on S_0 contains more diagnostic information than the body surface potential field (Forbes, 1974; Barr and Spach, 1976; Boineau, 1974).

Before discussing how (25) may be solved for the unknown equivalent source distribution on S_0 , consider the inclusion of the effects of the body surface. The region external to the sources is assumed to be homogeneous but is bounded by the body surface S , outside which the conductivity is zero (see Figure 2.3). The derivative of the potential normal to S is zero at all points on S since no current may flow across S . Incorporating this boundary condition into the integral equation (13) for the potential on S gives

$$V_s(P) = \iint_{S_0} (V(\partial(R^{-1})/\partial v_0) - R^{-1}(\partial V/\partial v_0)) dS/2\pi - \iint_S V_s(\partial(R^{-1})/\partial v) dS/2\pi, \quad P \in S \quad (28)$$

where the source is specified as an equivalent epicardial surface distribution on S_0 . Assume for the moment that V_s is known over the entire body surface. Then, in principle at least, the integration over S can be performed to find

$$4\pi V'_s(P) = 2\pi V_s(P) + \iint_S V_s(\partial(R^{-1})/\partial v) dS, \quad P \in S \quad (29)$$

V'_s is clearly that potential which would be generated at S by the same source distribution in an infinite homogeneous region (compare (25) and (28)). An assumption implicit in this statement is that V and $\partial V/\partial v_0$ on S_0 are unaltered by the removal of S to infinity. Thus the measured field may be transformed by (29) to estimate the infinite region field. Therefore, the problem of solving (28) reduces to the problem of solving (25) for the sources of an infinite region field (Geselowitz, 1960).

Several approaches to solving the integral equation (25) are possible. One approach is to divide S and S_0 into a large number of small elements (cf. Barr et al., 1977). Consider that the surface S_0 is divided into $N/2$ elements ΔS_{0j} , $j=1,2,\dots,N/2$, where N is even. The surface S is divided into M elements ΔS_i , $i=1,2,\dots,M$. A point P_j is chosen within the j th element of each surface and the whole element is then considered to have the potential $V(P_j)$. The integral in (25) may then be approximated as a summation and M linear equations written as

$$V'_s(P_i) = \sum_{j=1}^{N/2} \beta_{ij} \rho_j, \quad i=1,2,\dots,M \quad (30)$$

In (30),

$$\begin{aligned} \rho_j &= V_{s0}(P_j), \quad j=1,2,\dots,N/2 \\ &= \partial V_{s0}/\partial v_0 \Big|_{P_{j-N/2}}, \quad j=N/2+1,\dots,N \end{aligned} \quad (31)$$

and

$$\begin{aligned} \beta_{ij} &= -(\partial(R_{ij}^{-1})/\partial v_0) \Delta S_{0j}/4\pi, \quad j=1,2,\dots,N/2 \\ &= R_{i,j-N/2}^{-1} \Delta S_{0,j-N/2}/4\pi, \quad j=N/2+1,\dots,N \end{aligned}$$

and R_{ij} is the distance from P_i on S to P_j on S_0 . Assume that the right-hand side of (30) tends to the right-hand side of (25) for N sufficiently large. In matrix notation, (30) may be written

$$[V'_s] = [\beta] [\rho] \quad (32)$$

where $[V'_s]$ and $[\rho]$ are column vectors of dimension M and N respectively and $[\beta]$ is a matrix of dimension M×N. Clearly (32) can only be solved for the N unknowns ρ_j if $M \geq N$. This condition, though necessary, is not sufficient to ensure that (32) is soluble. The system of equations (32) must be well-conditioned (cf. Hildebrand, 1974; Barnard *et al.*, 1967; Rogers and Pilkington, 1968a) if a unique and meaningful solution is to be found by inverting $[\beta]$. Consider the conditioning of $[\beta]$ for N small, say 4, and M=N. The surface S_0 has two segments and the surface S has four measuring points. It is possible with such a simple system to select the four measuring points so that the largest element in each of the rows of $[\beta]$ occurs in a different row. $[\beta]$ is then almost certainly well-conditioned and may be inverted by a standard technique (cf. Hildebrand, 1974) to allow the solution to be found as

$$[\rho] = [\beta]^{-1} [V'_s] \quad (33)$$

However, with N so small, the discrete set of equations (30) are no longer a good representation of the continuous integral equation relating to the physical problem. Therefore the solution (33) is for the wrong problem. An inverse solution for the electrocardiogram obtained in this way would certainly have little relation to the electrophysiology of the heart.

Clearly N must be significantly larger than used in the simple illustration above if the discrete equations (30) are to accurately represent the physical problem. However, $[\beta]$ is certain to be ill-conditioned for a large N. To illustrate this point, consider the three adjacent coefficients in the *i*th row, $\beta_{i,j-1}$, $\beta_{i,j}$ and $\beta_{i,j+1}$, where the *i*th surface element on S lies approximately over the *j*th surface element on S_0 . For N (and thus M) large the three coefficients are certain to be of similar magnitude, as are the coefficients $\beta_{i,j+N/2-1}$, $\beta_{i,j+N/2}$, $\beta_{i,j+N/2+1}$. Furthermore, and most importantly, the β_{ij} are estimated from geometrical measurements with associated measurement errors (cf. Choi and Pilkington, 1981). Additional error is added by the presence of inhomogeneities, which are not taken into account in the formulation of (25), (30) and (31). With even small errors in the coefficients of an ill-conditioned set of equations, its solution may only be determined within large error bounds. The inverse solution for electrocardiography, determined by matrix inversion from an ill-conditioned set of equations with M=N, is probably of little value (Barnard *et al.*, 1967; Rogers and

Pilkington, 1968a). Consider, however, making more measurements than are required by the dimension of $[\rho]$, i.e. $M > N$. Without the presence of error in the β_{ij} (and in the $V'_s(P_i)$, due to errors in potential measurement and the computations in (29)), the additional $M-N$ equations are redundant and may be discarded. With the errors present, (30) becomes an over-determined set of equations which are inconsistent. In other words, choosing any N of the M equations to solve for $[\rho]$ will produce a different result than choosing a different set of N equations and solving for $[\rho]$. The solution sought for the over-determined set of equations is therefore one which is "optimum". The classical method of finding such a solution is the use of the least-squares criterion. Briefly, a solution for the M equations (30) in N unknowns ($M > N$) is to be found such that

$$f(V'_s) = [V'_s - \beta\rho]^T [V'_s - \beta\rho] \quad (34)$$

where the superscript T denotes the matrix transpose, is a minimum with respect to all of the ρ_j . The partial differential of (34) with respect to each ρ_j is equated to zero to produce the normal equations

$$[\beta_j]^T [V'_s] = [\beta_j]^T [\beta\rho] \quad , \quad j = 1, 2, \dots, N, \quad (35)$$

where $[\beta_j]$ is the j th column vector of $[\beta]$. Note that (35) may equivalently be written as

$$[\beta]^T [V'_s] = [\beta]^T [\beta\rho]$$

where a square symmetric matrix $[\beta^T\beta]$ now appears on the right-hand side. Although the symmetry of this matrix simplifies the computation of its inverse, it may still be ill-conditioned (Rogers and Pilkington, 1968a). Provided an accurate inverse can be found for $[\beta^T\beta]$ the optimum solution for (30) according to the least-squares criterion is then

$$[\rho] = [\beta^T\beta]^{-1} [\beta]^T [V'_s] \quad (36)$$

Other methods of solving (30) for $M > N$ have been suggested and may have advantages over the straightforward least-squares approach. One is Gram-Schmidt orthogonalisation (cf. Harrington, 1968; Rogers and Pilkington, 1968a) in which N orthogonal vectors are computed from the matrix $[\beta]$ and the solution computed directly from these. Another method is the use of multiple deflations (cf. Barnard *et al.*, 1967; Lynn and Timlake, 1968) which reduce the $M \times N$ matrix of coefficients

[β] to a square matrix and improve its conditioning in the process. The reader is directed to the references cited above for details of these methods.

So far, a solution for the equation

$$V'(P) = - \iint_{S_0} \left[R^{-1}(\partial V'/\partial v_0) - V'(\partial(R^{-1})/\partial v_0) \right] dS/4\pi, \quad P \text{ outside } S_0 \quad (25, \text{ repeated})$$

has been attempted by a numerical approximation method. An alternative approach is to seek an analytical solution (cf. Harrington, 1968; Bates, 1975, 1980) to (25). Consider the homogeneous "torso" depicted in Figure 2.4.

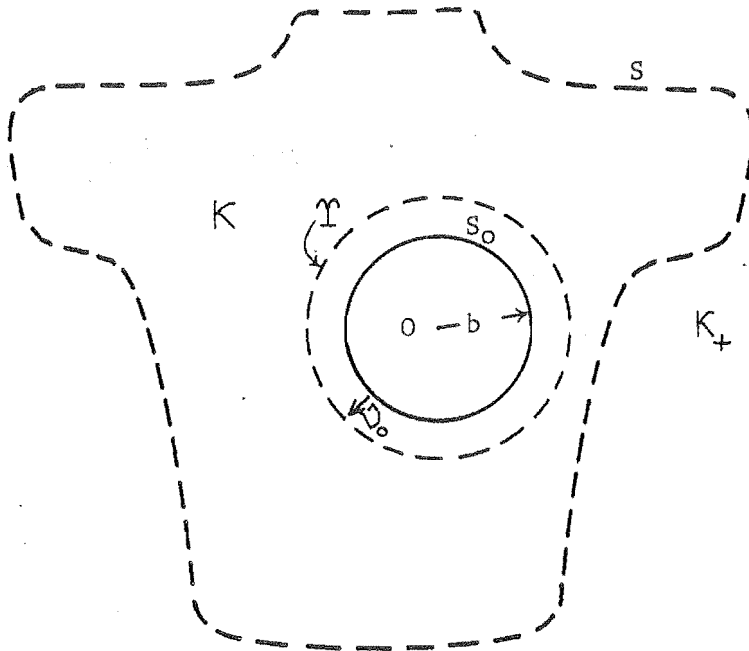


Figure 2.4 A homogeneous "torso" in which the equivalent source on S_0 is to be found from measurements on S .

The potential is measured at all points on S and it is transformed into the infinite region potential by (29) as before. This transformed potential is thus the left-hand side of (25) for $P \in S$. For simplicity, take the "epicardial" surface S_0 to be spherical with radius b . The centre of S_0 is the origin of the coordinates O , which is chosen so that S_0 tightly encloses all of the heart sources. It is assumed that a concentric surface T may be drawn which lies entirely outside S_0 but entirely inside S (see Figure 2.4). The solution for the equivalent

source on S_0 is found by expanding the potential field in a series of suitable functions and equating it to $V'(P)$ for $P \in S$. The region $\kappa U \kappa_+$, outside S_0 , is homogeneous for the field $V'(P)$, therefore Laplace's equation, $\nabla^2 V' = 0$, is satisfied in $\kappa U \kappa_+$. A suitable expansion for $V'(P)$ is therefore (Hobson, 1930)

$$V'(P) = \sum_{n=0}^{\infty} \sum_{m=-n}^n [C_{nm} r^n + B_{nm} r^{-n-1}] Y_{nm}(\theta, \phi), \quad P \in \kappa U \kappa_+ \quad (37)$$

where the B_{nm} and C_{nm} are constant coefficients. There are no sources in the region $\kappa U \kappa_+$ so the potential must be bounded at infinity.

Therefore $C_{nm} = 0$, $n = 1, 2, \dots, \infty$. C_{00} is an arbitrary constant potential which may be assigned to zero. Thus (37) simplifies to

$$V'(P) = \sum_{n,m} B_{nm} r^{-n-1} Y_{nm}(\theta, \phi), \quad P \in \kappa U \kappa_+ \quad (38)$$

where the simplified notation $\sum_{n,m}$ has been adopted for the double summation in (37). On S_0 , therefore,

$$\partial V' / \partial \nu \big|_{S_0} = - \sum_{n,m} (n+1) B_{nm} b^{-n-2} Y_{nm}(\theta, \phi) \quad (39)$$

and

$$V'_{S_0} = \sum_{n,m} B_{nm} b^{-n-1} Y_{nm}(\theta, \phi)$$

Thus the equivalent surface sources on S_0 are determined by the single set of expansion coefficients B_{nm} for the infinite region field $V'(P)$. The methods of obtaining the B_{nm} from the measurements V_S on the body surface are discussed in Section 3.3.

A simple check of the formulae (39) is made by substituting (38) and (39) into (25) along with the double series expansion (22) for R^{-1} . The result for P is

$$\sum_{n,m} B_{nm} r^{-n-1} Y_{nm} = \sum_{k,\ell} r^{-k-1} Y_{k\ell} \sum_{i,j} B_{ij} b^{k-i} ((i+1)A_{ki}^{\ell j} + kA_{ki}^{\ell j}) / (2k+1) \quad (40)$$

where

$$\begin{aligned} A_{ki}^{\ell j} &= \int_0^{2\pi} \int_0^{\pi} Y_{k\ell}(\theta, \phi) Y_{ij}(\theta, \phi) \sin\theta d\theta d\phi / 4\pi \\ &= \delta_{ki}^{\ell j} \quad (\text{see Appendix 1}). \end{aligned}$$

Simplifying the right-hand side of (40), multiplying both sides by the testing function $Y_{k\ell}(\theta, \phi)$ and integrating over the closed surface T gives

$$B_{k\ell} = B_{k\ell}$$

The "epicardial" surface is chosen *a priori* above to be spherical. A non-spherical surface may be chosen instead, though the simple formulae (39) no longer apply.

Several features of this analytic approach to the E.C.G. inverse solution are particularly attractive:

- (1) Both the potential and the gradient of potential are found on the "epicardial" surface S_0 .
- (2) Solution stability is assured, if certain conditions on the shape of S and S_0 are met and if the integrals over S are calculated with sufficient accuracy.
- (3) The integrals over S in (29) need only be calculated once for a given shape and stored in a look-up table, while solving for different sets of measurement data (see Section 3.3).

Similar techniques to that outlined in the paragraph above have been extensively used in electrostatics (Beasley *et al.*, 1979), antennas (Mittra, 1973) and waveguides (Bates and Ng, 1972; Ng and Bates, 1972). The literature contains relatively few references (Arthur *et al.*, 1972; Geselowitz, 1976; Pilkington and Morrow, 1980) to their use in solving the E.C.G. problem in terms of an equivalent source distribution on an "epicardial" surface. A similar approach, however, has frequently been used to find an "equivalent heart generator" as outlined in the next section.

§2.2.3 The equivalent heart generator

The formulation of the inverse E.C.G. solution in terms of an "equivalent heart generator" (which will be referred to as a "generator" from now on) is clearly just a different use of a *a priori* information as compared to the methods outlined in the last section. The equivalent generator approach is allocated a separate section here, because it has been the basis of clinical electrocardiographic interpretation since the first developments by Einthoven (1913). The simplest form for the generator is the fixed position dipole assumed in standard 12-lead electrocardiography and vectorcardiography; more complex are the multiple dipole and the multipole generators. Table 2.1 contains a summary of the various forms of generator which are assumed by various groups in attempting the E.C.G. inverse solution. One principal reference is given for each generator type and the "epicardial" surface potential form is included for completeness. In this section only the single dipole and multiple dipole generators are reviewed. Note, however, that the analytic

TABLE 2.1 The types of equivalent heart generator assumed for inverse electrocardiographic solutions.

Generator	References
Fixed position dipole	Gabor and Nelson, 1954 Einthoven, 1913
Moving dipole	Arthur <i>et al.</i> , 1971 Horan and Flowers, 1971 Mirvis <i>et al.</i> , 1978 Kneppo and Titomir, 1979
Multipole, N = 2 (dipole + quadrapole)	Mashima, 1969 Arthur <i>et al.</i> , 1972 Mirvis <i>et al.</i> , 1978
Multipole, N > 2	Geselowitz, 1960 Geselowitz, 1976 Horan <i>et al.</i> , 1976
"Epicardial" spherical source	Martin and Pilkington, 1972 Barr and Spach, 1976
Double layer spherical cap	Frank, 1953
Multiple dipole, unconstrained	Rogers and Pilkington, 1968b Brody <i>et al.</i> , 1972
Multiple dipole, fixed direction	Barr <i>et al.</i> , 1970
Multiple dipole, specified time dependence and direction	Barnard <i>et al.</i> , 1976 Martin <i>et al.</i> , 1975

technique for finding the "epicardial" potential outlined in the last section is exactly equivalent to solving for a multipole generator (Zablow, 1966; Geselowitz, 1976). See Table 2.1 for references to other generator types.

Consider first that the nett activity in the myocardium is represented by a current dipole within a homogeneous region κ bounded by the body surface S . A dipole at a point with position vector \underline{x}_0 has magnitude and direction specified by the dipole moment \underline{p} (Stratton, 1941). The impressed current source is given by

$$\underline{J}_1(\underline{x}) = \underline{p} \delta(\underline{x} - \underline{x}_0) \quad (41)$$

Using (16) to substitute for the source term in (12) gives an expression for the potential at a point within the homogeneous torso κ ,

$$V(P) = \underline{p} \cdot \nabla(R^{-1}) \delta(\underline{x}' - \underline{x}_0)/4\pi\sigma - \iint_S v_s(\partial(R^{-1})/\partial v) ds/4\pi, \quad P \in K \quad (42)$$

The origin of coordinates is chosen to be \underline{x}_0 and the dipole is oriented in the direction $\theta = 0$. The infinite region potential of the dipole (the first term on the right-hand side of (42)) is then straightforwardly derived as

$$V'(P) = |\underline{p}| \cos\theta/4\pi r^2\sigma \quad (43)$$

(Stratton, 1941). Equation (43) indicates that in (38), the general multipole expansion for the infinite region potential, only the terms B_{10} , B_{11} and B_{1-1} of the set B_{nm} may be non-zero for a dipole situated at the origin of coordinates (corresponding to the three independent components of a vector quantity in three dimensions). If the dipole is moved away from the origin, other coefficients in the set B_{nm} become non-zero, but B_{10} , B_{11} and B_{1-1} remain unaltered (Stratton, 1941; Geselowitz, 1960). Therefore, if these three coefficients can be found, they define an equivalent dipole source, independent of position. Vectorcardiography seeks to directly obtain these three components from a limited number of measurements, as outlined in Section 3.2. Note that finding this set of three coefficients is straightforward for measurements made on a spherical surface (cf. Geselowitz, 1976) and, in principle, (42) allows their exact determination from measurements on the body surface (neglecting the effects of inhomogeneities) using the transformation of (29).

Several groups consider that a solution which includes the equivalent dipole's position as well as moment is more useful than a solution for the moment alone. The method most frequently used to find the dipole position is to equate to zero the terms of the multipole expansion (38) which are of order greater than one, by moving the coordinate origin. If the coefficients B_{20} , B_{21} , etc. are zero, then the field remaining must be that of a dipole at the origin selected. Gabor and Nelson (1954) derived a set of equations for the multipole coefficients and these have been used extensively by others (Arthur *et al.*, 1971; Horan and Flowers, 1971) to find the equivalent dipole position. Arthur *et al.* (1971) computed a locus for the dipole during the QRS complex which is consistent with the known sequence of myocardial activation in normals (cf. Section 1.3). Kneppo and Titomir (1979), however, show a considerable variation in their computed dipole locus in a study of six normals. The results to date do not indicate that the extra information

obtained from the dipole locus is of direct clinical relevance. Arthur *et al.* (1972) warn also that the calculations of the higher order terms in the multipole expansion are liable to be very sensitive to errors in the measurements and to the effects of inhomogeneities.

In the multiple dipole generator, each dipole is chosen *a priori* to represent the activation of a portion of the myocardium. A large research effort has been directed towards obtaining inverse solutions for multiple dipole generators and at least one group (Barnard *et al.*, 1976) report the clinical use of their technique. In principle, the methods used are similar to those employed in the finite element solution for an "epicardial" surface source, outlined in §2.2.2. Equation (30) is formed for the *i*th surface element with the transfer coefficients β_{ij} now relating the *j*th dipole characteristic p_j to the *i*th surface position. The dipole "characteristic" may be one of the three components of \underline{p} , if the dipole is allowed to have any orientation at a fixed location (cf. Rogers and Pilkington, 1968b), or simply the amplitude, if the dipole direction is fixed (cf. Barnard *et al.*, 1976). Often a constraint is applied on the time variation of each dipole (Barr *et al.*, 1970; Baker and Pilkington, 1974) in an attempt to force the solution to have physiological relevance. Attempts to find a solution for unconstrained dipoles (i.e. with no direction or time dependence specified) are disappointing (cf. Rogers and Pilkington, 1968b; Brody *et al.*, 1972). Solutions are generally found to be unstable in the presence of small perturbations (which may correspond to geometrical error, measurement noise or the effects of inhomogeneities). Rogers and Pilkington (1968b) report that their solutions, from data measured *in vivo*, are unrelated to cardiac physiology.

The addition of further *a priori* constraints on the multiple dipole generator leads to more encouraging results. Barnard *et al.* (1967, 1976) solve for a 12-dipole generator, with each dipole having a fixed position and orientation and the further constraint applied that the dipole moment must be non-negative. A significant correlation is reported between the time integral of the selected dipole moments and the bulk of left ventricular muscle in a large series of patients (Barnard *et al.*, 1976). However, the method does not lead to an increase in the accuracy of diagnosis. Barr *et al.* (1970) add constraints on the time variation to a similar multiple dipole generator. The time sequence of the dipole activation reported for their solution shows encouraging similarity to the actual sequence of myocardial activation.

§2.2.4 Inclusion of volume conductor inhomogeneities

The earliest investigators in the field of electrocardiography, including Einthoven (1913), were aware that the tissues of the thorax possess different electrical characteristics and that this might influence the form of the E.C.G. However, the triangle interpretation scheme of Einthoven (1913; cf. Section 3.1) and most other schemes developed since, ignore the effects of conductivity inhomogeneities. There are two principal reasons for this. Firstly, the ready success of the Einthoven and the later interpretation schemes led most investigators to consider the inhomogeneities to be of little significance. Secondly, until recently most investigators lacked the facilities to carry out a detailed study of the inhomogeneity effects or to correct for them.

The electrical resistivities of the tissues making up the majority of the thoracic volume are listed in Table 2.2, from the data of Rush *et al.* (1963). It can be seen from Table 2.2 that the ratio of the most conductive tissue (blood) to the least conductive tissue (fat) is approximately 15 to 1. Bone is not considered because of its relatively small volume and sparse distribution within the thorax. It is now clear that inhomogeneities do contribute, along with the surface shape, to the variation observed among subjects without heart disease (Simonson, 1961; Lepeschkin, 1976c; Rush and Nelson, 1976). Such variation limits the ability of the standard E.C.G. interpretation schemes to distinguish between normals and abnormals (Simonson, 1961). Therefore the formulation of an ideal inverse solution must include the inhomogeneities. To apply such a formulation would clearly require *a priori* knowledge of the location of the regions of different conductivity. Such information can be gained with great accuracy by two-dimensional reflected ultrasound imaging (cf. Feigenbaum, 1976) or by one of the cross-sectional tomographical techniques (cf. Kak, 1979). An alternative method (involving less expense) is to use approximate measurements of the internal organs from standard chest radiographs taken in the antero-posterior (front) and saggittal (side) positions. Such X-ray images are available on virtually every patient who has seen a consultant physician in the past and are readily obtainable on others. This suggestion is discussed further in Chapter 8.

An integral equation (17) for the inhomogeneous body is derived in §2.1.3 and it is repeated below with the boundary condition $\partial V/\partial n = 0$ on S incorporated. Thus

TABLE 2.2 Thoracic tissue resistivities (from Rush et al., 1963)

Tissue	Resistivity (Ω cm)
Blood	162
Liver	700
* Heart (high)	563
(low)	252
Lung	2 100
Fat	2 500
* Skeletal muscle (high)	2 300
(low)	150
Human trunk (average)	463

* 'High' and 'low' refer to the high and low resistivities of anisotropic tissues.

$$V(P) = - \iiint_{\kappa} \nabla \cdot \underline{J}_1 dv / 4\pi\sigma R + \iiint_{\kappa} \nabla V \cdot \nabla \sigma dv / 4\pi\sigma R - \iint_S V(\partial(R^{-1})/\partial v) dS / 4\pi, \quad \text{PEK} \quad (44)$$

The second volume integral in (44) is the contribution to the potential at P of all of the variation in conductivity throughout κ . Note that, even if $\sigma(\underline{x})$ is given *a priori* throughout κ (and is not constant everywhere), the integrand contains $\nabla V(\underline{x}')$, an initially unknown three-dimensional quantity. Thus the "dimensionality difficulty", encountered in §2.2.1, again plagues the formulation of an inverse solution. A reduction in the dimension of the inhomogeneity integral, from volume to surface, is the approach to the problem favoured by all investigators to date (cf. Metz and Pilkington, 1969; Plonsey, 1976; Geselowitz, 1967; and see Chapters 4, 5 and 6). This is achieved by assuming the thorax to be piecewise homogeneous. In view of the quite large disparity in conduction between tissues and the relatively homogeneous nature of each tissue (Rush and Nelson, 1976), dividing the thoracic volume into several homogeneous regions seems entirely reasonable.

Consider the simple piecewise homogeneous "thorax" shown in Figure 2.5. The inner region κ' , which for simplicity is chosen to

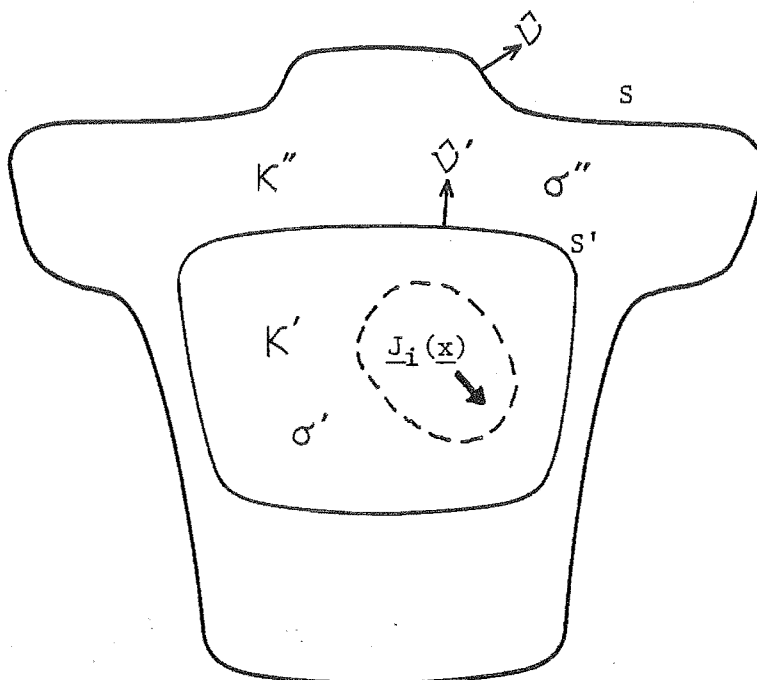


Figure 2.5 A piecewise homogeneous "thorax" with the source $\underline{J}_i(\underline{x})$ entirely within region κ' .

contain all sources, has constant conductivity σ' and is bounded by S' . The region κ'' lies entirely between the non-intersecting surfaces S' and S and has constant conductivity σ'' . The null field equation (18) for the region κ' and a point $P \in \kappa''$, gives

$$0 = - \iiint_{\kappa'} \nabla \cdot \underline{J}_i dV / 4\pi\sigma'R + \iint_{S'} (R^{-1}\partial V / \partial v' - V\partial(R^{-1}) / \partial v') dS / 4\pi, \quad P \in \kappa'' \quad (45)$$

where v' is the outward normal to S' . For the same point P , (12) is applied to the region κ'' giving

$$V(P) = - \iint_{S'} (R^{-1}\partial V / \partial v' - V\partial(R^{-1}) / \partial v') dS / 4\pi - \iint_S V(\partial(R^{-1}) / \partial v) dS / 4\pi, \quad P \in \kappa'' \quad (46)$$

where the sign of the integral over S' has been changed, since v' represents an inward normal to κ'' . Equations (45) and (46) can be added and like terms collected, since they are formulated for the same point P .

Adopting the notation V' for the potential just on the κ' side of S' and V'' for the potential just on the κ'' side of S' , this gives

$$V(P) = - \iiint_{\kappa'} \nabla \cdot \underline{J}_i dv / 4\pi\sigma'R + \iint_{S'} (\partial V' / \partial v' - \partial V'' / \partial v') dS / 4\pi R \quad (47)$$

$$+ \iint_{S'} (V'' - V') (\partial(R^{-1}) / \partial v') dS / 4\pi - \iint_S V (\partial(R^{-1}) / \partial v) dS / 4\pi, \quad P \in \kappa''$$

On S' , the continuity of potential and the normal component of current $\sigma \partial V / \partial v'$ implies that

$$V'' - V' = 0 \quad (48)$$

and

$$\partial V' / \partial v' - \partial V'' / \partial v' = ((\sigma'' - \sigma') / \sigma') \partial V'' / \partial v' \quad (49)$$

so that (47) becomes

$$V(P) = - \iiint_{\kappa'} \nabla \cdot \underline{J}_i dv / 4\pi\sigma'R + (\sigma'' - \sigma') \iint_{S'} (\partial V'' / \partial v') dS / 4\pi\sigma'R$$

$$- \iint_S V (\partial(R^{-1}) / \partial v) dS / 4\pi, \quad P \in \kappa'' \quad (50)$$

In (50), it is evident that the boundary S' , between the two homogeneous regions, acts like a single layer source of magnitude $(\sigma'' - \sigma')(\partial V'' / \partial v') / \sigma'$ (cf. Stratton, 1941). An equivalent integral formulation, with the boundary effect expressed as a double layer source, is also reported (Geselowitz, 1967; Metz and Pilkington, 1969; Plonsey, 1976). Both formulations can easily be extended to any number of non-intersecting surfaces (Metz and Pilkington, 1969).

Despite the reduction of the volume integral over the inhomogeneities in (44) to surface integrals as in (50), an inverse solution which takes the inhomogeneities into account is still difficult to achieve. To my knowledge, there have not been any successful attempts at solving (50) directly. Instead, investigators have concentrated on obtaining a forward solution, i.e. modelling with given sources and inhomogeneities to find the surface field (cf. Section 4.2.2). They hope, by studying the forward solutions obtained by modelling, to learn which inhomogeneities are important and to test the sensitivity of inverse solutions to those inhomogeneities (Forbes, 1974; Swihart, 1976; Cuffin and Geselowitz, 1977). It is also conceivable that such modelling

will enable an inverse solution, initially obtained by assuming homogeneity, to be corrected by an iterative technique (cf. Guardo *et al.*, 1976). Chapter 4 and later chapters discuss the use of modelling to assess the effects on the E.C.G. of the body shape and the conductivity inhomogeneities.

CHAPTER 3

ELECTROCARDIOGRAPHIC MEASUREMENT SCHEMES

The preceding two chapters tacitly assume that the electrocardiographic potential field can be measured simultaneously over the entire body surface or at least over the entire upper torso. It is possible to make such measurements with a large array of electrodes, amplifiers and ancilliary equipment (see for example, Taccardi *et al.*, 1976). However the complexity and cost of the instrumentation involved is too great for routine electrocardiographic practice. The large electrocardiographic array is certain to remain only a research tool. The vast majority of routine electrocardiography is carried out by measuring the body surface potential at only a few selected sites. The sites are generally chosen so that a trained electrocardiographer is able to accurately repeat a set of measurements on the same subject without marking the sites. In the standard 12-lead scheme, for example, the limbs are used as four electrode sites and six chest electrode positions are defined in terms of the underlying body structure. The accurate positioning of the electrodes is clearly vital for accurate E.C.G. interpretation, since abnormalities are often manifested as changes in the orientation of the potential field relative to body landmarks (cf. Section 1.4). Note that in the context of electrocardiography, a lead is a voltage $\Phi(t)$ which is measured from a combination of electrodes on the body.

In this chapter the various E.C.G. measurement schemes in actual use are reviewed. Only the interpretation of the signals measured with these schemes is considered here. It is assumed that the associated instrumentation is suitably well-designed so that any disturbing influences external to the body tissues are negligible. The reader is referred elsewhere for information on the design and influence of the electrodes (Geddes, 1972) and the design of the instrumentation (Kossmann *et al.*, 1967; Dewhurst, 1976). The first section below briefly traces the historical development of the standard 12-lead E.C.G. measurement scheme and introduces the concepts of lead fields and image surfaces. Section 3.2 reviews the schemes put forward for orthogonal

leads which relate directly to the rectangular components of an equivalent dipole source (vectorcardiography). Practical schemes for estimating the total body surface field are discussed in Section 3.3.

3.1 THE STANDARD 12-LEAD E.C.G.

§3.1.1 Description and use

There is little doubt that the most significant individual contribution to the science of electrocardiography has been that of Willem Einthoven (1860-1927). He not only perfected the means of recording high quality electrocardiograms (even at a patient-to-recorder distance of one mile!), but he developed the basis of the interpretation scheme which is still in use today. Einthoven's work in electrocardiography began in 1894 with the capillary electrometer with which body surface E.C.G. signals had been previously observed. He perfected the instrument to a standard that enabled him to introduce the system of feature labelling (P, Q, R, etc.) which has not been altered since. In spite of his success with the electrometer, Einthoven felt a more sensitive instrument was required, so he developed the string galvanometer, which he first reported in 1901. With the new instrument he rapidly extended E.C.G. theory and he documented evidence that the technique could be useful in diagnosing heart disease. He then proposed a method of E.C.G. signal interpretation based on an equivalent dipole source (Einthoven *et al.*, 1913). His method, with some refinements, is still taught to every medical worker in the world as a means of interpreting the standard 12-lead E.C.G. signals. In 1924, Einthoven was awarded the Nobel Prize for his contribution to Medicine.

Einthoven's lead scheme consists of three limb measurement points, the two arms and the left leg. The interpretation of the voltages between these measuring sites is based on the assumption that the body acts as a homogeneous conducting sphere. An equivalent dipole generator is considered to act in the centre of the sphere. The measurement points are considered to lie on the spherical surface, positioned at the apices of an equilateral triangle (see Figure 3.1). For a standing subject the plane of the triangle is vertical and incorporates the centre of the sphere. Let the electrode sites be R (right arm), L (left arm) and F (left leg).

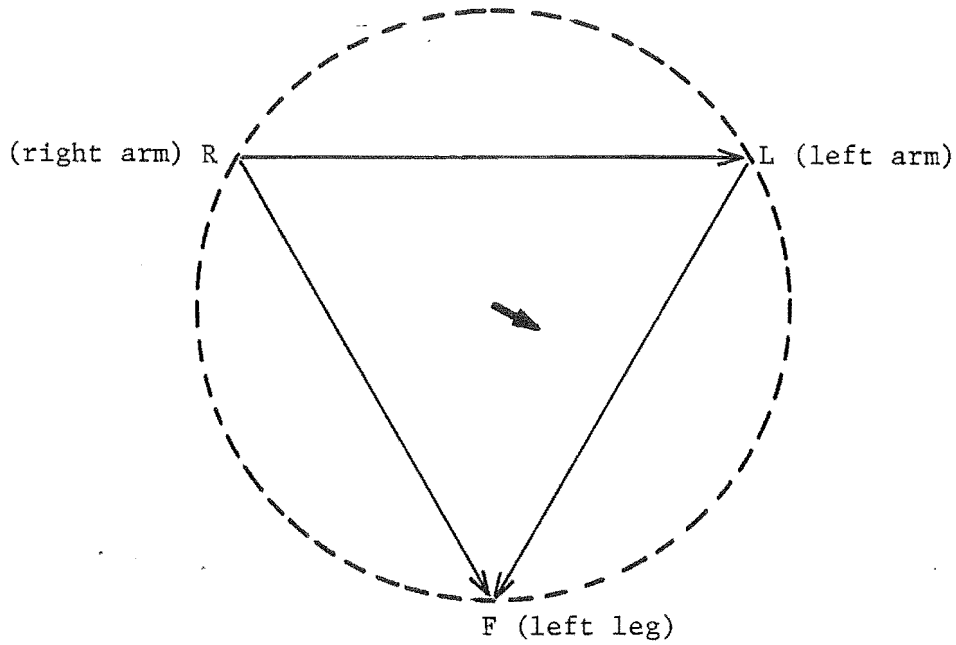


Figure 3.1 The Einthoven triangle, which is used to interpret the limb leads of the standard 12-lead scheme.

Consider now the theoretical basis of the Einthoven interpretation. The field of a dipole with moment \underline{p} embedded in an infinite homogeneous region is derived in equations (41) and (42) as

$$V'(\underline{x}) = \underline{p} \cdot \nabla(R^{-1})/4\pi\sigma$$

For a dipole at the origin and measurements made on a concentric spherical surface S of radius a , this simplifies to

$$V'_S(\underline{\xi}) = \underline{p} \cdot \underline{\xi}/4\pi a^3\sigma \quad (51)$$

As discussed in §2.2.3, the multipole expansion (cf. Equation (38)) for the infinite region field of a dipole at the origin of coordinates has only three non-zero coefficients, $B_{1,-1}$, B_{10} and B_{11} . Therefore, the multipole expansion of V'_S also has only three non-zero coefficients, given by

$$\chi'_{1m} = a^{-2} B_{1m} \quad , \quad m = -1, 0, 1 \quad (52)$$

If an insulating boundary is imposed at S , the multipole expansion for the internal field must include terms (with the coefficients C_{nm}) which are regular at the origin (cf. equation (37)). The field must obey the boundary condition $\partial V/\partial r = 0$ at $r = a$, thus (cf. §2.2.1)

$$-(n+1) B_{nm} a^{-n-2} + n C_{nm} a^{n-1} = 0 \quad (53)$$

It is clear, therefore, that the multipole expansion of the field inside and on the homogeneous sphere contains only terms of the order $n=1$. The multipole coefficients χ_{1m} of the field V_s on the insulated homogeneous sphere are obtained by equating V to V_s at $r = a$ and incorporating (53).

Thus

$$\chi_{1m} = 3 a^{-2} B_{1m}$$

and by analogy with (52) and (51)

$$V_s(\underline{\xi}) = \underline{p} \cdot \underline{\xi} (3/4\pi a^3 \sigma) \quad (54)$$

Thus the spherical insulating boundary acts only as a scaling factor on the dipole field. Equation (54) may be written for a general point on S

$$V_s(\underline{\xi}) = \underline{p} \cdot \underline{\eta}(\underline{\xi}) \quad (55)$$

and in particular, for the apices of the Einthoven triangle,

$$\begin{aligned} V_L &= \underline{p} \cdot \underline{\eta}_L \\ V_R &= \underline{p} \cdot \underline{\eta}_R \\ V_F &= \underline{p} \cdot \underline{\eta}_F \end{aligned} \quad (56)$$

where $\underline{\eta}_L$, $\underline{\eta}_R$ and $\underline{\eta}_F$ are vectors with an equal amplitude ($3/4\pi a^2 \sigma$) and with directions equal to their respective position vectors.

The actual measurements made with the Einthoven system are the voltages between the limb sites. For example, the voltage in Lead I Φ_I is defined as

$$\Phi_I = V_L - V_R \quad (57)$$

and, according to the Einthoven interpretation, may be expressed as

$$\Phi_I = \underline{p} \cdot (\underline{\eta}_L - \underline{\eta}_R) \quad (58)$$

This equation indicates that Φ_I may be interpreted as the component of the dipole moment in the direction of the side of the Einthoven triangle which "joins" the right arm to the left arm. Similarly, Lead II ($V_F - V_R$) and Lead III ($V_F - V_L$) are interpreted as components of the dipole moment in the respective directions (a complete summary of the standard 12-lead scheme is given in Table 3.1, later in this section).

When Einthoven proposed the triangle interpretation scheme (Einthoven *et al.*, 1913) he introduced the "mean QRS axis", a concept used extensively in E.C.G. interpretation. A description of the measurement of this approximate vector quantity and an example of its use in diagnosis will serve here to illustrate how the Einthoven triangle is employed by physicians. Consider first the nature of the body surface E.C.G. field during ventricular activation in a normal person (cf. Figure 1.9). At each of the three instants illustrated in Figure 1.9, the field is estimated at each of the three limb electrodes of the Einthoven scheme (i.e. V_L , V_R and V_F). The corresponding voltages in each of the Leads I, II and III are calculated from (57) and similar equations, and the approximate QRS waves constructed as shown in Figure 3.2a.

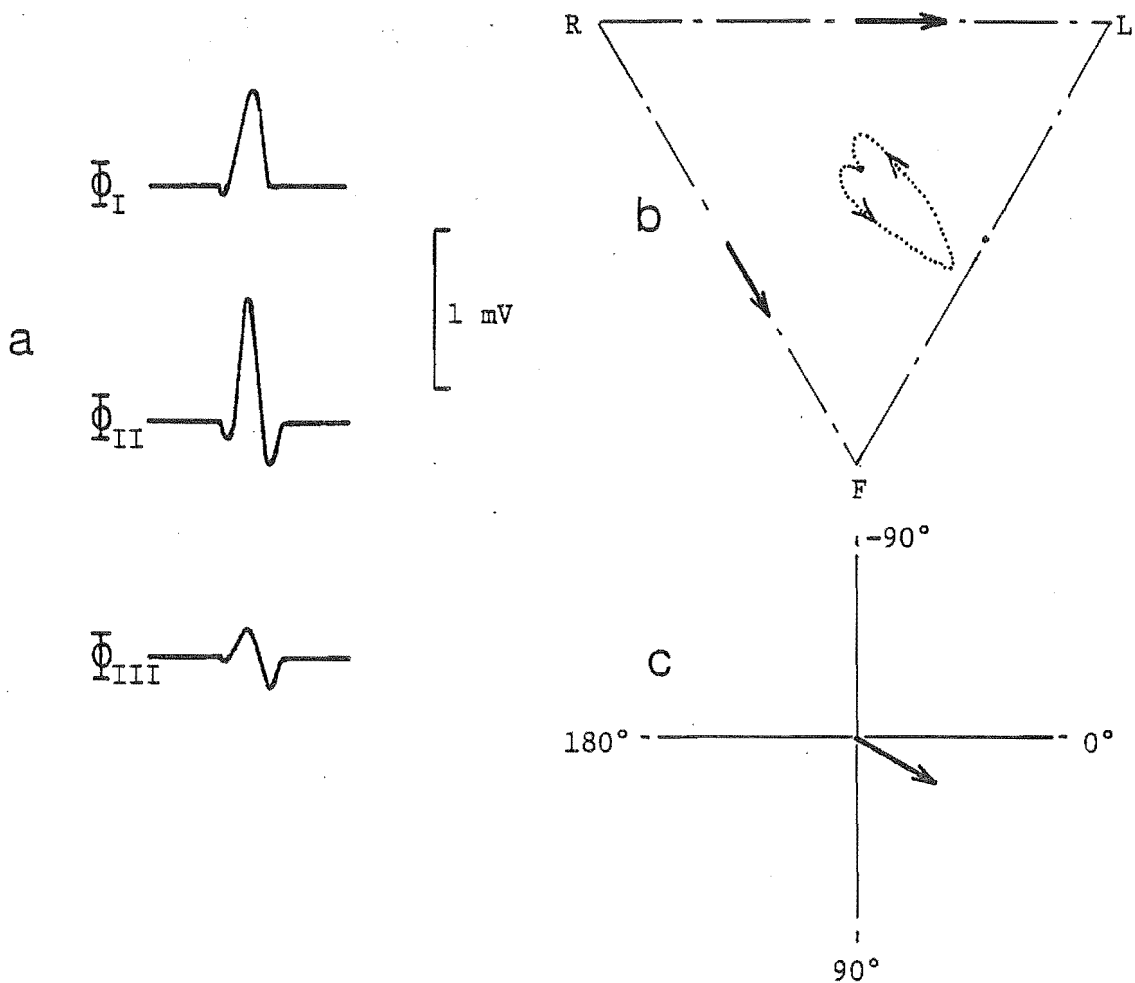


Figure 3.2 The derivation of the "mean QRS axis" from the limb leads. a) Limb leads for the QRS wave depicted in Figure 1.9; b) the Einthoven triangle and the locus of the dipole moment; c) the mean QRS axis.

These then are the E.C.G. signals which would be recorded from the individual depicted in Figure 1.9 during ventricular activation. The Einthoven interpretation of the lead signals is that they each represent a component of the moment of the equivalent dipole in the direction of the respective side of the triangle. Any two of the three leads are sufficient to reconstruct the projection of the dipole moment in the plane of the triangle. By considering many instants, therefore, the locus of the dipole moment projection in that plane is determined. The locus constructed from the lead signals of Figure 3.2a is shown as a dotted line in Figure 3.2b. The component of the "mean QRS axis" in any lead is assumed to be equal to the nett deflection in that lead. For example, the nett deflection in a lead which has a maximum positive QRS voltage of 1.5 mV and a maximum negative voltage of -0.5 mV is 1.0 mV. The leads of Figure 3.2a have their nett deflections indicated on the sides of the triangle in Figure 3.2b and the resulting axis is shown in Figure 3.2c. The angular coordinate depicted in Figure 3.2c is commonly used to describe the axis direction. Defined in this manner, the axis in normal subjects is variously reported to lie in the ranges -30° to 90° (Schamroth, 1975), -30° to 110° (Goldman, 1976) and 15° to 75° (Simonson, 1961).

The use of the "mean QRS axis" in making a diagnosis is illustrated by considering a common pathological condition. In left anterior hemiblock (cf. Castellanos and Myerburg, 1978) the excitatory impulse is blocked in the left anterior branch of the ventricular specialised conduction system (cf. §1.2.2 and §1.4.4) while the other branches conduct the impulse normally. The portion of the ventricular myocardium which the left anterior branch normally excites is therefore activated later than normal by the spread of the depolarisation from other regions of the myocardium. This frequently causes Lead II to have a negative nett deflection while Lead I remains positive. The axis is therefore in the range -30° to -90° (cf. Figure 3.2c), which is described as "left axis deviation". The physicians' interpretation of this E.C.G. abnormality is that the depolarisation spread is more from the right side towards the left side than normal causing a corresponding rotation of the moment of the equivalent cardiac dipole.

Although the Einthoven triangle forms the basis of the standard 12-lead E.C.G. measurement scheme and in essence is unchanged since it was first proposed (Einthoven *et al.*, 1913), a considerable time elapsed before the rest of the scheme was finalised. A summary of the developments up to

1961 is found in Simonson (1961), but it was not until 1967 that the whole world is reported to have accepted the standard (Kossmann et al., 1967). Two major developments stand out above the rest. In 1934, Wilson proposed the first of these - a means of deriving a reference potential from the limb leads. The "Wilson central terminal", V_W , is the average of the three limb potentials V_L , V_R and V_F derived by joining the electrodes to a single terminal with matched resistors, i.e. $V_W = (V_L + V_R + V_F)/3$ (Wilson et al., 1934). Wilson's suggestion that his terminal represents "zero" potential is generally accepted by physicians as a means of interpreting the chest leads, which are the voltages $\phi_i = V_i - V_W$, for $i = 1$ to 6 , where V_i is the potential measured at an anatomically defined site on the chest (see Table 3.1). They are known as unipolar leads since only a single electrode is positioned and the voltage is measured relative to V_W .

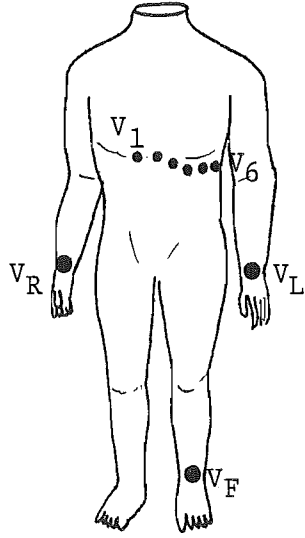
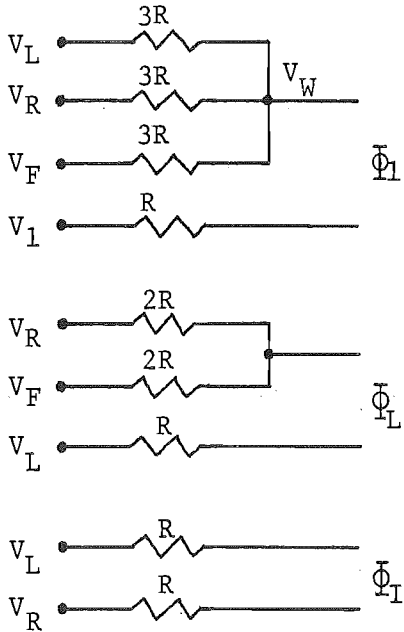
The chest leads are again interpreted on the basis of an equivalent dipole generator at the centre of a homogeneous spherical region. If Wilson's assertion that his terminal represents "zero" potential (i.e. the potential at the point at which the dipole acts) is assumed to be correct, then (55) becomes

$$\phi_i = \underline{p} \cdot \underline{\eta}(\underline{\xi}_i) \quad (59)$$

for each of the chest leads ϕ_i , for $i = 1$ to 6 , with the respective electrode position vectors $\underline{\xi}_i$. Because the chest electrode positions lie approximately on a horizontal plane relative to a standing object (cf. Table 3.1), each ϕ_i is interpreted as the horizontal component of the dipole moment in the direction (approximately) of a line drawn through the heart and the respective chest electrode. Thus, whereas the limb leads of Einthoven are interpreted as the "frontal" plane components, the chest leads are interpreted as the "transverse" plane components (see Figure 3.3 for a definition of these planes).

So far, nine of the leads of the standard 12-lead scheme have been introduced. The remaining three leads were finalised by Goldberger (1942) and are known as the "augmented unipolar limb leads" or more concisely as the "aV" leads. Their development stems from the desire of the physicians of the day to have more components of the heart's activation in the frontal plane. As discussed in §3.1.2, the extra three leads of Goldberger appear to add no new independent information.

TABLE 3.1 The standard 12-lead E.C.G. measurement scheme.

Lead type	Symbol	Voltage measured	
Limb leads	I II III	$\Phi_I = V_L - V_R$ $\Phi_{II} = V_F - V_R$ $\Phi_{III} = V_F - V_L$	
Augmented unipolar limb leads	aV_L aV_R aV_F	$\Phi_L = V_L - (V_R + V_F)/2$ $\Phi_R = V_R - (V_F + V_L)/2$ $\Phi_F = V_F - (V_L + V_R)/2$	
Chest leads	v_1 v_2 v_3 v_4 v_5 v_6	$\Phi_1 = v_1 - v_W$ $\Phi_2 = v_2 - v_W$ $\Phi_3 = v_3 - v_W$ $\Phi_4 = v_4 - v_W$ $\Phi_5 = v_5 - v_W$ $\Phi_6 = v_6 - v_W$	

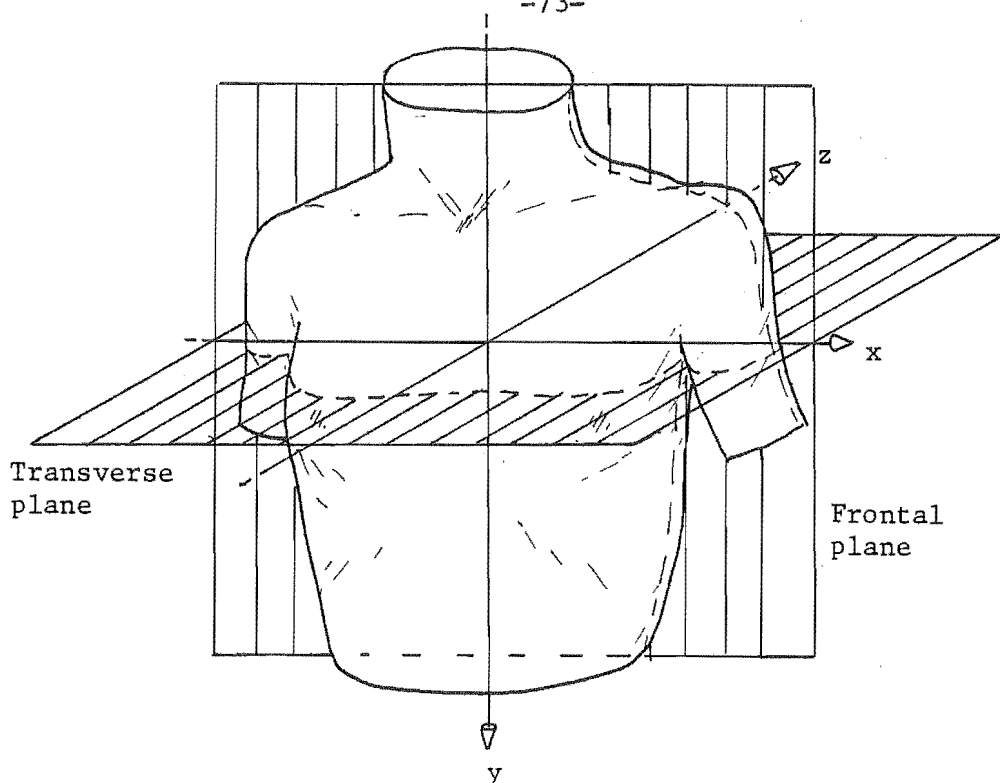


Figure 3.3 . The rectangular coordinates and planes defined relative to the torso (cf. Kossmann et al., 1967).

Their incorporation into the standard E.C.G. interpretation scheme illustrates the "pattern recognition" approach to electrocardiography which is used by the majority of physicians. The aV leads use no extra electrodes, they are derived directly from the three limb electrode potentials as

$$\begin{aligned}\Phi_i &= V_i - (V_j + V_k)/2 \\ &= \underline{p} \cdot \{ \underline{\eta}_i - (\underline{\eta}_j + \underline{\eta}_k)/2 \}\end{aligned}\tag{60}$$

where i, j and k cyclically take the meanings L, R and F, and Φ_F denotes the voltage in Lead aV_F, etc. (cf. Table 3.1). Employing the frontal plane angular coordinate shown in Figure 3.2c, Φ_L is the -30° component of the dipole moment, Φ_R is the 210° component, etc. Combining the three limb leads and the three aV leads therefore gives six components of the dipole moment in the frontal plane uniformly spaced at 30° intervals.

Table 3.1 summarizes the standard 12-lead measurement scheme. Next to the standard symbol for each lead is the lead equation in terms of the electrode potentials. Note that the lead symbol V_1 should not be confused with the potential V_1 measured at the corresponding electrode. The reader is referred to Wilson et al. (1954) or Goldman (1976) for a precise description of the chest electrode sites depicted on the diagram.

The lower diagram on the right-hand side of Table 3.1 shows the resistance network which is employed by most E.C.G. equipment manufacturers so that the first amplifier stage of the electrocardiograph sees an equal series impedance with each lead connection. This is important to ensure adequate rejection of interfering common-mode signals (Kossmann *et al.*, 1967; Dewhurst, 1976). The resistance R is best chosen to be large relative to the resistance of the electrode/body/electrode combination ($1\text{ k}\Omega$ to $10\text{ k}\Omega$ with silver/silver chloride electrodes) and small relative to the input impedance of the first amplifier stage. Most equipment commercially available also includes an electrode on the right leg. This additional electrode reduces the sensitivity of the measuring system to common-mode signals, particularly interference from the mains supply (cf. Dewhurst, 1976).

§3.1.2 Critique

Much has been written both in praise and in condemnation of the standard 12-lead E.C.G. measurement scheme (cf. Simonson, 1961; Frank, 1954a; Kossmann *et al.*, 1967). Whatever the inadequacies of the scheme, it is easily applied and taught to trainees and it is supported by a vast accumulation of empirical data. This critique makes no attempt to assess the scheme in terms of its successes and failures in clinical diagnosis, it is confined rather to assessing the performance of the 12-lead scheme as an inverse solution of the E.C.G. The reader is referred elsewhere for an appraisal of the scheme's clinical performance in separating normal from abnormal subjects (cf. Simonson, 1961; Castellanos and Myerberg, 1978).

On first learning about the 12-lead scheme, a person with scientific background is immediately struck with the apparent redundancy in the lead signals. The moment of a fixed position dipole is entirely characterised by three independent components, yet here is a scheme measuring twelve components. True, but a more careful appraisal of the scheme is necessary before discarding nine of the leads. First consider the frontal plane. Only three electrode sites are used in measuring the six frontal plane leads (Leads I, II, III, aV_L , aV_R , aV_F). Once any two of the six leads have been measured, the projection of the dipole moment in the frontal plane can be estimated on the basis of the Einthoven assumption. For example, if Leads I and aV_F are measured and the rectangular coordinate system of Figure 3.3 is adopted, (55) and (57) give

$$\begin{aligned} p_x &= \sqrt{3} \Phi_I / |\underline{n}_L| \\ p_y &= 3 \Phi_F / 2 |\underline{n}_L| \end{aligned} \tag{61}$$

where p_x and p_y denote the x and y components of \underline{p} . Since these components in the frontal plane can be estimated from any two of the six leads, it follows that an estimate of any missing lead may be made from p_x and p_y (Frank, 1954a). Thus it would appear that some of the leads are redundant. However (61) assumes that the dipole, body and electrode combination act according to the homogeneous spherical model proposed by Einthoven. If this model is significantly in error then all six leads cannot uniquely be determined from measurements of only two. For example, it is not possible to express Φ_L and Φ_R directly in terms of Φ_I and Φ_F . It is possible therefore that more than two frontal leads are necessary for interpreting the E.C.G. signals of the limb electrodes.

In the transverse plane, six chest electrode sites are used for six measurements. Again, on the basis of the Einthoven assumption, most of these appear redundant. However it has been found that the chest leads, by virtue of their proximity to the heart, do show variation which cannot be accounted for by a single fixed-position dipole source (cf. Horan *et al.*, 1976; Arthur *et al.*, 1972). It is generally accepted therefore that the large number of chest leads may enable localised changes in the E.C.G. potential field to be detected where they may otherwise go unnoticed.

There is another and more important reason for the retention of a number of apparently redundant leads in the 12-lead scheme. The standard method of recording E.C.G. lead signals is by means of a pen recorder (frequently of the heated-stylus type) which has a paper speed of 25 mm/sec and a sensitivity of 10 mm/mV (cf. Kossmann *et al.*, 1967). The QRS wave at this paper speed is inscribed less than 2 mm wide. The leads are rarely recorded simultaneously in more than groups of three. Frequently they are recorded singly and then representative beats from each lead are pasted onto a form for presentation to the physician. Only a crude estimation of the locus of the dipole moment can be made with this standard 12-lead E.C.G. presentation. The "mean QRS axis" is an example of such an estimation (cf. §3.1.1). Consider Figure 3.4, where two distinctly different loci (a and b) are proposed for the projection of the dipole moment in the frontal plane during the QRS.

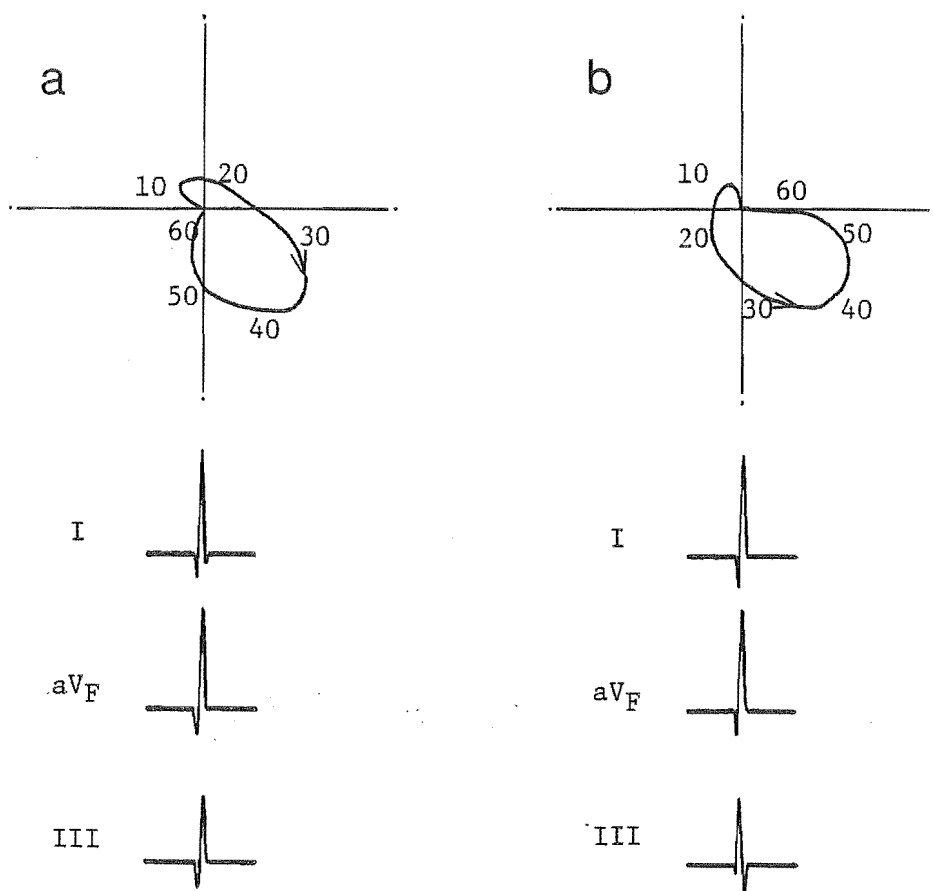


Figure 3.4 Illustration of the importance of redundant leads in the standard 12-lead E.C.G. measurement scheme. Distinguishing locus b from locus a is difficult with Leads I and aV_F alone.

Assume for the moment that distinguishing the dipole locus in Figure 3.4b from that in Figure 3.4a is useful in making a diagnosis. The arrows indicate the direction of increasing time. Below the loci the corresponding Leads I, aV_F and III are approximately constructed. Note that Leads I and aV_F are almost identical in the two cases. Therefore an interpretation based on Leads I and aV_F (one of the possible "minimum" sets of frontal leads) may lack vital information. However Lead III is distinctly different in Figure 3.4b from Figure 3.4a. This result may seem paradoxical until one considers the method of recording. When the QRS wave is drawn only 2 mm wide in each lead, it is almost impossible to accurately assess the deflection in one lead relative to another lead at the same instant. There is therefore a phase uncertainty in comparing leads. This uncertainty may be increased if the frequency

response of the pen recorder is not adequate to precisely record the QRS wave (cf. Kossmann et al., 1967). Furthermore, when each lead is assessed from different heart beats, the beat-to-beat variation (cf. Kini et al., 1974; Simonson, 1961; Ruttkay-Nedecky, 1976) also adds to the phase uncertainty between leads. It is clear therefore that the inclusion of "redundant" leads in the standard 12-lead E.C.G. measurement scheme can assist in interpretation.

So far in this section the assumption made by Einthoven that the body acts as a homogeneous sphere and that the heart activation is represented by a central dipole has not come under scrutiny. Clearly the validity of the assumption must be established, at least approximately, if one is to have confidence in the use of the interpretation scheme. Two methods which are closely related have been used by many researchers in assessing the accuracy of the Einthoven interpretation scheme. The first of these is the generation of an image surface for the torso on which lead signals are assessed. The second is the generation of lead fields inside the body. The use of these methods is briefly reviewed below in relation to the three limb leads (Leads I, II and III).

The image surface method of assessing E.C.G. leads was first proposed by Burger and van Milaan (1948) and was used extensively by Frank (1954b). Consider the expression (53) for the surface field of a dipole, $V_s(\underline{\xi}) = \underline{p} \cdot \underline{\eta}(\underline{\xi})$. For a homogeneous spherical region with the dipole at the centre, it follows that $\underline{\eta}(\underline{\xi}) = k\underline{\xi}$, where k is a constant. If the conducting region surrounding the source is bounded by an irregular surface and/or inhomogeneous medium, no such simple relationship exists between $\underline{\eta}$ and $\underline{\xi}$. However, $\underline{\eta}(\underline{\xi})$ can be measured for any given dipole position and conducting region. The measurement may be carried out with a suitable experimental apparatus (cf. Burger and van Milaan, 1948; Frank, 1954b; Toyoshima, 1979) or by modelling the forward E.C.G. solution (Okada, 1956; cf. Chapters 5 and 6). Burger and van Milaan (1948) suggested that the function $\underline{\eta}(\underline{\xi})$ be considered in the form of an image surface $S'(\underline{\eta})$ so that for each point $\underline{\xi}$ on S there is a unique point $\underline{\eta}$ on S' . For a homogeneous spherical region and a dipole at the sphere's centre, S and S' are identical. In general however they are not identical and S' depends on the position chosen for the dipole as well as the characteristics of the medium. The use of the image surface in electrocardiography is illustrated by considering Lead I. Equation (58) expresses the voltage in Lead I as $\phi_I = p \cdot (\underline{\eta}_L - \underline{\eta}_R)$.

The vector $\underline{F}_I = \underline{\eta}_L - \underline{\eta}_R$, drawn between the corresponding points of the image surface, therefore graphically represents the component of the dipole moment by that lead. Not only can the validity of an equivalent dipole interpretation scheme be tested by this method but the sensitivity of any lead to the assumed dipole position can also be assessed.

The assessment by Frank (1954b) of the limb leads by means of the image surface concept stands out as one of the most useful contributions to the science of electrocardiography. He constructed a three-dimensional homogeneous conducting model of the human torso and placed within it a dipole source at a point representative of the position of the ventricular myocardium. He then energised the dipole separately in the x, y and z directions (cf. Figure 3.3) and made a large series of measurements for each dipole direction. Finally he combined the components of $\underline{\eta}(\underline{\xi})$ so obtained to construct the image surface. The resulting lead vectors \underline{F}_I , \underline{F}_{II} and \underline{F}_{III} are reproduced in Figure 3.5 from Frank (1954b).

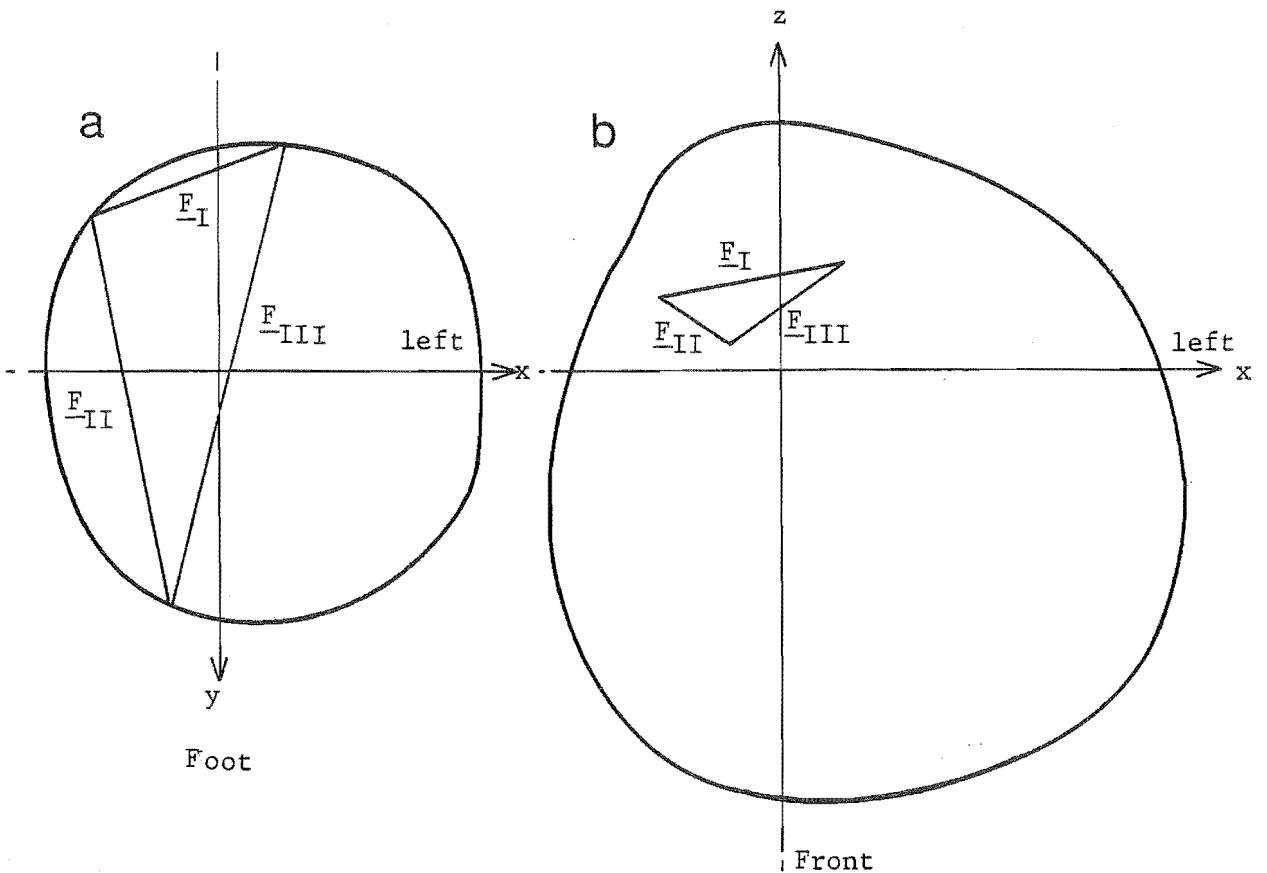


Figure 3.5 The measured image surface and lead vectors of a typical adult male projected on the a) frontal and b) transverse planes (from Frank, 1954b).

In Figure 3.5a the frontal projection is shown with the origin representing the point chosen for the dipole. In Figure 3.5b the transverse projection is shown viewed from above. Several interesting conclusions may be reached from these results.

- (1) None of the limb leads represents the components of the dipole moment assumed in the Einthoven interpretation, yet the error in the lead vector angle is not gross.
- (2) The sensitivity of Lead I is approximately half that of Leads II and III.
- (3) The error in treating the lower regions of the torso and legs as a single point is negligible (cf. Figure 2 in Frank, 1954b).
- (4) The image surface predicted is remarkably close to a sphere, although the limb measuring points do not lie on the apices of an equilateral triangle (cf. Figure 2 in Frank, 1954b).

Caution must be exercised in the interpretation of these results since a homogeneous torso model was used and a single dipole position assumed. Frank's results for a homogeneous torso agree very well with some earlier experiments by Burger and van Milaan (1948) carried out on an experimental model which included some inhomogeneities (cf. Frank, 1954a). Some evidence exists therefore that the conclusions above are still valid in the presence of inhomogeneities. Another study reported by Frank (1956a) and using the same homogeneous model shows that the image surface is very sensitive to the position assumed for the dipole. Lead I in particular is shown to be very sensitive to the dipole position. Although the image surface generation technique has seldom been employed (cf. Toyoshima et al., 1979) since Frank's work of the early 1950's, it remains in my opinion one of the most useful techniques proposed for electrocardiographic research.

The lead field is a concept allied to the image surface. Described first by Brody and Romans (1953), it is a vector function of position \underline{x} which defines the sensitivity of a given lead to a dipole at \underline{x} . Schmitt (1957, 1976) describes the same field as a vector impedance since it relates a voltage measurement to a current dipole. In the terminology already introduced, the field of Lead I is given by

$$\underline{F}_I(\underline{x}) = \underline{n}_L(\underline{x}) - \underline{n}_R(\underline{x}) \quad (62)$$

and similarly for other leads, where \underline{n}_L , \underline{n}_R , etc. are now expressed in terms of a dipole at \underline{x} rather than at the origin. The lead field may be estimated by the same experimental method described above for Frank's

(1954b) image surface determinations with the measurements repeated for many dipole positions. An alternative method suggested by Brody and Romans (1953) is based on the Helmholtz principle of reciprocity. According to this principle, if a current dipole consisting of a current source of magnitude G at point \underline{x}_1 and an equal sink of current at \underline{x}_2 produce a voltage Φ in a lead, then a voltage Φ would be measured between \underline{x}_1 and \underline{x}_2 if a current of magnitude G were passed through the medium by the lead electrodes. Thus a lead field $\underline{F}(\underline{x})$ may be measured by energising the lead and measuring the potential gradient at \underline{x} . Arzbaecher and Brody (1976) extend the lead field to a tensor quality which relates the voltage in a lead to a multipole source at \underline{x} , though no practical application of a tensor lead field has yet been reported.

In summary, the 12-lead E.C.G. measurement scheme employs a highly redundant set of measurements to solve for an equivalent dipole generator. The redundant leads, while not theoretically necessary to the solution, do help the physician to interpret an electrocardiogram presented in the usual 25 mm/sec pen recorder format. Experimental studies carried out on realistic torso models indicate that significant inaccuracies are present in the Einthoven triangle interpretation of the limb leads, but that the inaccuracies are not sufficiently large to invalidate the technique. Lead I is approximately half as sensitive as the other limb leads. The use of either the image surface or the lead field concept is clearly valuable in the assessment of an E.C.G. measurement scheme.

3.2 ORTHOGONAL LEAD SCHEMES

The moment of a current dipole is characterised by three orthogonal components. If the heart current source is assumed to act as a dipole then clearly these three components constitute a complete description of the generator at each instant of time. An orthogonal lead scheme (commonly called a vectorcardiogram) is designed to produce three lead signals, Φ_x , Φ_y and Φ_z , each proportional to one of the dipole moment rectangular components. Such schemes are attractive (especially to a person with scientific training) since they have no redundant leads. However the information from orthogonal leads must be presented in a different format than the 25 mm/sec pen recordings of the standard 12-lead scheme to avoid the phase uncertainty mentioned in §3.1.2. The usual form of presentation of the vectorcardiogram is by means of two or

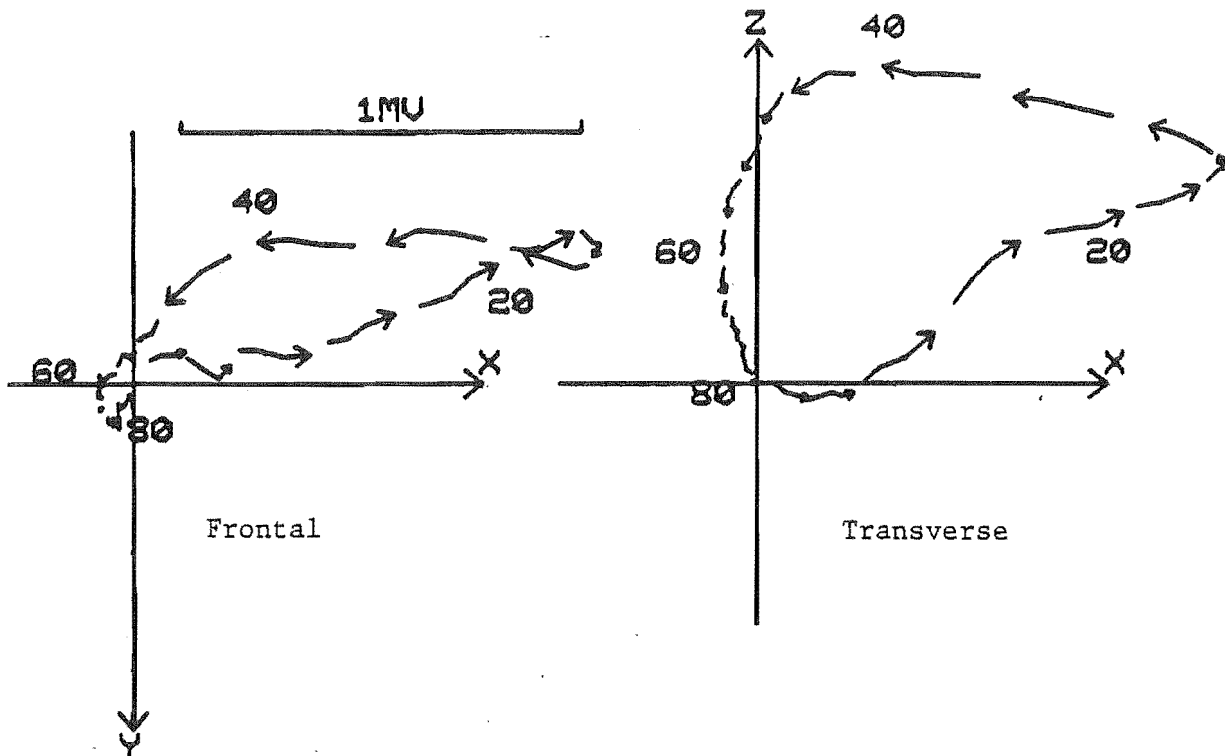


Figure 3.6 A typical format for the presentation of a vectorcardiogram (from Bones, 1976).

three plots of one lead versus another (commonly called "loops") with time indicated in milliseconds from the onset of activation. Figure 3.6 illustrates a typical orthogonal lead presentation for the QRS wave produced by a laboratory computer (Bones, 1976). A plot of Φ_x versus Φ_y gives the frontal plane projection of the locus of the dipole moment; a plot of Φ_z versus Φ_x gives the transverse plane projection viewed from above (cf. Figure 3.3). Each arrow represents 3 msec with a 1 msec gap to the next arrow.

A number of orthogonal lead schemes have been proposed but the scheme proposed by Frank (1956b) is the most popular. The Frank technique is therefore singled out for a detailed description below. Then follows a brief summary of other orthogonal lead schemes and some comments are appended on the general acceptance of the vectorcardiogram.

§3.2.1 The Frank lead scheme

The work of Ernest Frank has been introduced above in §3.1.2. Over a period of approximately five years in the early 1950's, Frank carried out a number of well-designed experiments which culminated in

the proposal of "an accurately, clinically practical system for spatial vectorcardiography" (Frank, 1956b) which is now known as the Frank lead scheme.

Frank experimentally determined the image surfaces for lifesize homogeneous torso models as described in §3.1.2 (Frank, 1954b). He repeated the image surface determination for dipoles in a number of positions within a cube with side 5 cm, centred on a typical ventricle location (Frank, 1956a). He then selected a number of electrode sites which are simple to locate and which experience suggested may be suitable for an orthogonal lead system. For the i th electrode site he derived the x , y and z components of the electrode vector \underline{n}_i and developed equations of the form

$$V_i = p_x n_{xi} + p_y n_{yi} + p_z n_{zi}, \quad i = 1, 2, 3, \dots \quad (63)$$

From this over-determined set of equations, he obtained (by an undisclosed method, possibly by trial and error) an acceptable set of lead vectors which are "insensitive to individual variability of ventricle location" (Frank, 1956b). He based this last conclusion on the finding that the three lead vectors remained accurate to within $\pm 5\%$ in angle and $\pm 20\%$ in length for the range of dipole locations that he tested.

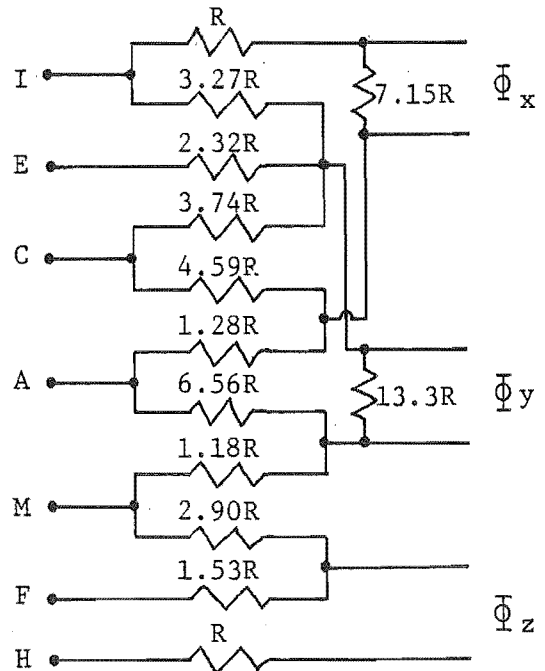
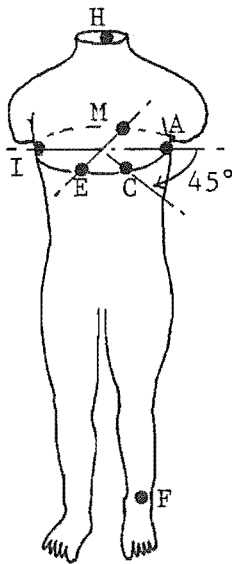
The lead system that Frank proposed is summarized in Table 3.2. There are seven electrodes positioned on the subject, connected by a resistor network to derive the three orthogonal leads. An additional electrode on the right leg is used by the manufacturers of E.C.G. equipment to improve the rejection of interfering common-mode signals. The five electrodes identified by the symbols I, E, C, A and M are located at precisely the level of a transverse section through the subject. Frank (1956b) states that these electrodes should be at the level of the ventricles and describes a novel method of finding this level by E.C.G. measurements. However, for routine clinical practice he concedes that the level of the fifth interspace may be used for these five electrodes without the addition of significant error. This conclusion is supported by a recent study (Berson *et al.*, 1978).

§3.2.2 Other orthogonal lead schemes and critique

The first orthogonal lead scheme was proposed by Wilson *et al.* (1947), who suggested a fourth electrode, positioned at the back midline at the level of the ventricles, in addition to the three limb electrodes

TABLE 3.2 The Frank orthogonal lead scheme (Frank, 1956b).

Symbol	Electrode position	Lead equations
I	right midaxillary line	$\Phi_x = 0.610 V_A + 0.171 V_C - 0.781 V_I$ $\Phi_y = 0.655 V_F + 0.345 V_M - 1.000 V_H$ $\Phi_z = 0.133 V_A + 0.736 V_M - 0.264 V_I - 0.374 V_E - 0.231 V_C$
E	front midline	
C	45° between E and A	
A	left midaxillary line	
M	back midline	
F	left leg	
H	back of the neck	



(i.e. right arm, left arm and left leg). Four electrodes are the minimum number required to derive the three orthogonal components of the dipole moment. This is easily shown by considering Poisson's equation (8). Since $\nabla^2 k = 0$ for any constant k , a constant potential may be added to any solution to Poisson's equation. Therefore to the equations (55), (56), etc., expressing an electrode potential as $V = \underline{\eta} \cdot \underline{p}$, there should be added a constant potential V_0 representing the potential at the position of the dipole. The complete expression for the potential at the i th electrode is therefore

$$V_i = \underline{\eta}_i \cdot \underline{p} + V_0 \quad (64)$$

Note that all the lead signals discussed so far in this chapter are defined as potential differences so that the neglect of V_0 is justified. In considering the minimum number of electrodes necessary to estimate the orthogonal components of the dipole moment, however, equation (62) includes four unknowns (p_x , p_y , p_z and V_0). Therefore at least four independent electrode sites are necessary to generate four independent equations of the form of (64) and thus uniquely determine the dipole moment.

The four-electrode scheme of Wilson *et al.* (1947) is commonly called the "Wilson tetrahedron". Several methods were proposed for deriving three orthogonal leads from the four electrodes (cf. Wilson *et al.*, 1947; Frank, 1956a). An example is (Wilson *et al.*, 1947)

$$\begin{aligned} \Phi_x &= V_L - V_R \\ \Phi_y &= 3(V_F - V_W)/4 \\ \Phi_z &= V_B - V_W \end{aligned} \quad (65)$$

where V_B is the potential measured at the back electrode and V_W is the Wilson central terminal as defined in §3.1.1 (Wilson *et al.*, 1934). Frank (1956a) applied his homogeneous torso model data to a study of the Wilson tetrahedron lead scheme. He found that the leads Φ_x and Φ_z of (65) are strongly affected by alterations in the dipole position and that (as pointed out in §3.1.2) the leads derived from the limb electrodes do not accurately represent the orthogonal dipole components in the frontal plane. In view of these failings the Wilson tetrahedron and several other simple vectorcardiographic measurement schemes (for example the "Cube" of Grishman and Scherlis, 1952) are known as "uncorrected" schemes.

The Frank lead scheme described in §3.2.1 is one of a number of "corrected" orthogonal lead schemes which use more than the minimum number of electrodes. The information from the extra electrodes in the corrected schemes is used to reduce the dependence of the orthogonal leads on the dipole position and on the other factors which vary from patient to patient. A number of the corrected orthogonal lead schemes are summarized in Table 3.3. All of the schemes listed in Table 3.3 have seen some service outside the laboratories in which they were developed. The number of electrodes used in deriving the orthogonal leads is also listed. It is interesting to note that in a detailed report (Kossmann *et al.*, 1967), prepared for the American Heart Association in 1967, a recommendation is made that the corrected lead schemes should be used in preference to the uncorrected schemes. The report does not recommend any one particular corrected scheme. However, the popularity of the Frank lead scheme is likely to ultimately lead to its general acceptance for vectorcardiography.

TABLE 3.3 Corrected orthogonal E.C.G. measurement schemes.

Name of scheme	Number of measuring electrodes	Reference
Frank	7	Frank (1956b)
Helm	2 large sponge electrodes, 5 conventional electrodes	Helm (1957)
SVEC III	14	Schmitt and Simonson (1955)
McFee-Parungao axial	9	McFee and Parungao (1961)
Rijlant	72	Rijlant (1958)

Vectorcardiography has not achieved the popularity and widespread use that its proponents in the 1950's and early 1960's expected. It remains largely a tool of the research worker in cardiology and is little applied in everyday clinical practice. One explanation for the lack of interest is that the methods of vectorcardiography were proposed to a medical profession well satisfied with the standard 12-lead scheme.

When Einthoven first showed the world the possibilities of electrocardiography, his method was an entirely new one and it was taken up readily by most physicians of the day. When vectorcardiography schemes were proposed they seemed to offer very little new information, just minor refinements of an already accepted diagnostic tool. Little has changed since to convince most physicians that they need more than the standard 12-lead E.C.G. Indeed vectorcardiography is seldom taught to cardiological trainees on a formal basis. Even the sophisticated computer-based E.C.G. analysis systems now on the market use the standard 12-lead E.C.G. signals as their input data (cf. Meijler *et al.*, 1980).

The lack of acceptance of vectorcardiography must to some degree be due to the way vectorcardiograms are presented for interpretation. Most physicians seem to find it easier to interpret the 12 pen-recorder traces of the standard scheme than the "loops" of the vectorcardiogram (cf. Figure 3.6). This is probably because they have become used to treating E.C.G. interpretation as a form of pattern recognition. In assessing the vectorcardiogram loops, pattern recognition still plays an important role, but notice must also be taken of the timing of various features in relation to the total interval of the QRS wave (cf. Witham, 1975). Vectorcardiographic equipment of early design uses an oscilloscope and camera to record the loops with the intensity controlled by a saw-tooth oscillator. The resulting photograph has a number of "comet" shaped marks, which are regularly spaced in time and whose tails indicate the direction of the loop inscription. The precise determination of the timing of loop features with this technique is tedious, which has probably also contributed to the lack of acceptance. Modern developments in digital electronics (in particular the microprocessor) allow the design of equipment which displays the vectorcardiographic loops with explicit timing information (cf. Bones, 1976). However, the cost of the equipment is unlikely to be comparable to that of a conventional E.C.G. recorder, because of the necessity of including a suitable device for making permanent recordings (cf. Kossmann *et al.*, 1967).

In summary, the orthogonal lead schemes, particularly the Frank scheme, undoubtedly offer advantages in E.C.G. interpretation over the standard 12-lead scheme (Kossmann *et al.*, 1967), yet they have not gained general acceptance. This is in part due to their being seen as only a modification of an established method, rather than a new method of cardiac diagnosis. Their lack of use in everyday clinical practice must be attributed to the relatively expensive and sophisticated equipment

required and to a reticence by physicians to learn a different type of electrocardiographic data presentation.

3.3 MEASUREMENT OF THE TOTAL BODY SURFACE FIELD

The standard 12-lead scheme and the orthogonal lead schemes discussed in Section 3.2 use a relatively small number of electrodes. These lead schemes sample the body surface potential field at insufficient points to extract the greater part of the information contained in the field (Barr *et al.*, 1971). Moreover, when using a small number of electrodes, the variations among subjects in body build, internal inhomogeneities, etc. (cf. Section 1.3), may make the positioning of the electrodes very critical (Berson *et al.*, 1979; Barr *et al.*, 1971). To be fair, the standard 12-lead and orthogonal lead schemes are designed to find the characteristics of an equivalent dipole generator. Any extra information in the potential field is deliberately ignored. However, the proposals for a more exact inverse solution reviewed in Chapter 2 (for example, attempts to detect localised activity in regions of the myocardium), require the extraction of more information from the body surface field. There are also several groups studying the entire body surface field in pathological conditions (cf. Flowers *et al.*, 1973, 1976; Boineau, 1974): they feel that a suitable display (cf. Henderson *et al.*, 1978; Wynne *et al.*, 1979; Monro *et al.*, 1974) of the two-dimensional potential field enables a direct interpretation to be made.

The studies of Taccardi and others (cf. Taccardi *et al.*, 1976) have proved the technical feasibility of simultaneously measuring the body surface field at hundreds of electrode sites for electrocardiographic research. Nobody, however, would suggest such an approach for clinical practice. The natural question to ask is, therefore: how many electrodes are necessary to measure the body surface field to a sufficient accuracy for finding an inverse solution and where should they be positioned? This section reviews the progress made to date in answering that question.

Establishing the accuracy required in the body surface field measurement is clearly fundamental in determining the number of electrodes required and their positions. To achieve this one might specify the accuracy required for characterising the coefficients of

a multipole expansion of the equivalent heart source, where the coefficients are to be found from the body surface measurements. The equivalent source field (i.e. the field which would be produced by the same source in an infinite homogeneous medium) may be expanded (38) as

$$V'(\underline{x}) = \sum_{n,m} B_{nm} r^{-n-1} Y_{nm}(\theta, \phi)$$

for any point outside the source region, where the B_{nm} are the unknown source multipole coefficients. The coordinate origin is chosen in the heart region so that the expansion converges at all points $\underline{\xi}$ on the body surface S (cf. Geselowitz, 1976). A relationship between the measured surface field V_s and the equivalent source field (without taking inhomogeneities into account) may be found from the null field integral equation (18). Thus for a point P outside S ,

$$0 = \sum_{n,m} B_{nm} r^{-n-1} Y_{nm}(\theta, \phi) - \sum_{p,q} r^{-p-1} Y_{pq}(\theta, \phi) \quad (66)$$

$$\iint_S V_s(\theta', \phi') \left[\partial / \partial v (r'^p Y_{pq}(\theta', \phi')) \right] dS / 4\pi(2p+1)$$

where r', θ', ϕ' are the coordinates of a point on S . Take P to lie on a spherical surface centred on the coordinate origin and completely outside S . Multiplying both sides of (66) by a testing function $Y_{k\ell}(\theta, \phi)$ and employing the orthogonality of spherical harmonic functions gives

$$B_{k\ell} = \iint_S V_s(\theta', \phi') \left[\partial (r'^k Y_{k\ell}(\theta', \phi')) / \partial v \right] dS / 4\pi (2k+1) \quad (67)$$

Assume that a large number N of electrodes are used to measure V_s at positions (θ_j, ϕ_j) , where $j = 1, 2, \dots, N$. A number of multipole coefficients $B_{k\ell}$, $k = 1, 2, \dots, K, \ell = -k, \dots, k$ are to be estimated to within a specified tolerance τ from the least number of electrodes possible. One approach to finding a suitable set of electrode positions is to divide S into N regions each centred on an electrode position j . The computation

$$\beta_{k\ell}^{(N)} = \sum_{j=1}^N V_s(\theta_j, \phi_j) \left[\partial (r^k Y_{k\ell}(\theta_j, \phi_j)) / \partial v_j \right] \Delta S_j / 4\pi(2k+1) \quad (68)$$

is carried out for $k = 1, 2, \dots, K$, etc. In (68) ΔS_j is the area of the segment surrounding electrode position j and \hat{v}_j is the unit outward normal to S at that point. It is assumed that, in the limit as N becomes large, $\beta_{k\ell}^{(N)} \rightarrow B_{k\ell}$. Now the computations are repeated for subsets of M electrodes with $M < N$. Then for each subset $|\beta_{k\ell}^{(M)} - \beta_{k\ell}^{(N)}|$ is compared to τ for $k = 1, 2, \dots, K$, etc. A subset of electrodes is chosen for which

$|\beta_{kl}^{(M)} - \beta_{kl}^{(N)}| \leq \tau$ and M is a minimum. This set of electrode positions is "optimal" for the particular measured surface field on which it is based. To be of practical use in electrocardiography, however, such an electrode position set must be optimal for the set, denoted here by $\{V_s^1\}$, of all measured surface fields. The procedure outlined above is likely to produce a large number of different "optimal" electrode sets when applied to $\{V_s^1\}$. As a consequence, the investigators who have employed this approach to studying the electrocardiogram have made the final choice of an electrode position set by other methods.

Geselowitz and colleagues (cf. Geselowitz, 1976) use the above procedure and conclude that 16 electrodes are sufficient to achieve a good estimate of the dipole and quadrupole source coefficients (i.e. $K = 2$). They do not, however, report how their final selection of the optimal electrode sites is carried out. Barr et al. (1971) also employ a similar technique (although they specify the source as a linear combination of dipoles rather than as a multipole expansion) in a study which is frequently quoted. They confirm that the optimal electrode set selected by the above procedure does vary from subject-to-subject and from time-to-time in the same subject. Their final selection of 24 electrode sites is carried out by trial and error (cf. Barr et al., 1971).

An alternative approach to dividing S into a large number of sub areas is to express V_s as a series expansion. For example, a group at Imperial College use a Fourier expansion for the surface field (cf. Monro et al., 1975) and study the dipole and quadrupole coefficients (i.e. $K = 2$) of an equivalent multipole source (cf. Guardo et al., 1976). They employ a computational model with a given source and a realistic (though homogeneous) torso to generate a surface field, then compute the components of a two-dimensional Fourier expansion from regularly spaced samples of the surface field (Monro et al., 1974). Finally they estimate the dipole and quadrupole coefficients of the source and assess the errors in the process. They conclude (Guardo et al., 1976) that a system of 26 electrodes is adequate to accurately determine the dipole and quadrupole coefficients. This number is chosen to give them eight "equally spaced" samples along any body circumference which lies in a transverse plane or in a vertical plane which includes the y axis (cf. Figure 3.3). The estimation of the surface potential field between the sampled points is achieved by band-limited interpolation.

So far, the problem of determining the number of electrodes required has been approached by considering the inverse solution. Another, more direct, approach is to assess the number of electrodes necessary to measure the field to an accuracy which is not significantly improved by the addition of more electrodes. For example: measure the potential at a large number N of electrode positions to establish the entire body surface field. Then on the basis of a selected subset of M electrodes, use an interpolation method to estimate the potential at the other $N - M$ positions. Finally, estimate some parameter of "goodness of fit". By this method, Lux *et al.* (1978) conclude that about 30 electrodes (chosen from a set of $N = 192$) are necessary to represent the surface field with a maximum error of $32 \mu\text{V}$. Other workers use the R.M.S. error over the $N - M$ positions where the potential is estimated to assess possible electrode sets. Barr *et al.* (1971), for example, find that with an R.M.S. error of 4% in the presence of 1% noise, their 24 electrode scheme (mentioned above) allows the potential field to be reconstructed without significant alteration in important features. Their assessment is based on the visual appearance of potential plots of the surface potential field with rectangular coordinates (cf. Barr *et al.*, 1971).

Much work remains to be carried out before any set of electrode positions becomes accepted as standard for the determination of the entire body surface field. It may be that no single electrode set is appropriate for all applications. To date the studies of the groups at the Duke University, Durham (cf. Barr *et al.*, 1971) and at the Imperial College, London (cf. Guardo *et al.*, 1976) have resulted in the proposal of lead schemes with similar numbers of electrodes despite the fact that the methods used are significantly different. The electrode arrays proposed by these two groups are reproduced in Figure 3.7. It is interesting to note that, unlike the regular 26 electrode array of the latter group (cf. Figure 3.7b), the positions proposed by Barr *et al.* (1971) appear to be randomly spread over the chest and back, with a higher concentration near the heart (cf. Figure 3.7a).

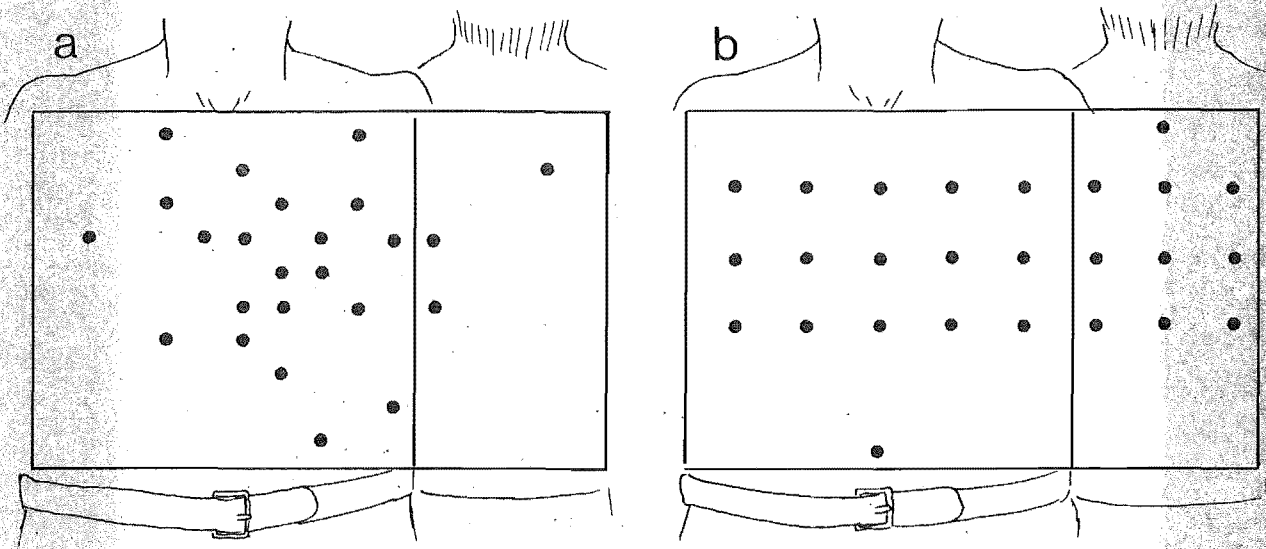


Figure 3.7 The electrode positions proposed by two research groups for measuring the body surface E.C.G. field.
a) Barr et al. (1971); b) Guardo et al. (1976).

CHAPTER 4

MODELLING

In the context of electrocardiography, modelling involves both the simulation of an electrical source (which acts in some way like the excitable tissues of the heart) and the definition of a surface over which a potential field is estimated or measured. The medium postulated to lie between the source and the surface must approximate some properties of the tissues within the human body. Modelling is performed for a variety of reasons but it is directed ultimately at helping in the perfection of an inverse solution for electrocardiography. As a consequence, if a practicable, exact inverse solution is ever found there will be no further need for modelling. Among the reasons most frequently proffered for indulging in modelling are: testing an hypothesis of the origin of the E.C.G. features observed in a particular group of patients; testing a proposed inverse solution method; studying the effects of the human body tissues on the E.C.G.; predicting the type of small signals which may be received from the specialised conduction tissues of the heart. Both of the latter two applications of modelling receive attention in the following chapters.

Models for the electrocardiogram fall into two major categories: analogue or experimental (i.e. involving actual measurements) and mathematical (usually involving digital computation). Only the latter category of model is considered here. The reader is referred to Frank (1954b), Rush (1971) and Toyoshima *et al.* (1979) for examples of experimental electrolytic tank models. Scher *et al.* (1971) and Salu *et al.* (1978) report significant animal experimental studies of the effects of the body on the E.C.G. Taccardi (1976) and Mirvis *et al.* (1978) report on isolated heart experimental models. Mathematical models offer various advantages over experimental models. They are relatively inexpensive to develop and use, in contrast to the elaborate apparatus often needed in experimental modelling. Once a mathematical model is developed, a large number of results may be obtained by, for example, simply changing parameters in a computer program; whereas the amount of data which can be obtained from analogue models is often limited by the

time and expense involved. However, some useful results (mentioned in what follows) have been obtained with analogue models.

Mathematical modelling in electrocardiography can be conveniently separated into two main divisions. This chapter is therefore partitioned in this manner. Section 4.1 deals with models of the electrophysiological sources, ignoring the effects of the surrounding conductive tissues. In Section 4.2 the modelling of the effects of body inhomogeneities and surface shape are reviewed. This review of mathematical modelling provides the background to the work presented in Chapters 5 and 6.

4.1 MODELLING THE CARDIAC GENERATOR

An inverse solution for electrocardiography can at best determine an equivalent cardiac generator from measurements made on the body surface, rather than a unique representation of the electrophysiological activity (cf. Section 2.2). The form of the generator must be specified *a priori*. Assuming that the methods reviewed in Chapter 3 allow such a generator to be accurately determined, it remains to relate the properties of the generator to electrophysiological activity. This is an important application for modelling.

In this section two models for the activation of cardiac tissue are reviewed. The first model is for the field produced by a single fibre of cardiac muscle cells (e.g. a Purkinje fibre). The second model is for the activation of the ventricular myocardium as a whole.

§4.1.1 Model for a single fibre

The development of a model for the potential field generated by a single fibre of cardiac cells is important in electrocardiography, for two reasons. Firstly, the myocardium is made up of a very large number of such fibres arranged in interleaving bundles (cf. Section 1.2). Therefore a model for a single fibre may provide the basis of a more general model for the myocardium as a whole. The second reason is that such a model may possibly predict the very small fields generated at the body surface by the specialised conduction system of the heart (cf. Section 1.2). Work of the latter type is presented in Chapter 6 and the modelling results are compared with measurements in Chapter 7.

Consider a single fibre of cardiac muscle embedded in an infinite homogeneous conducting medium. The fibre consists of a number of cells each enclosed by a membrane (cf. Section 1.1). The outer membrane surface of the fibre is assumed to be of uniform cross-sectional shape throughout the length of the fibre (see Figure 4.1).

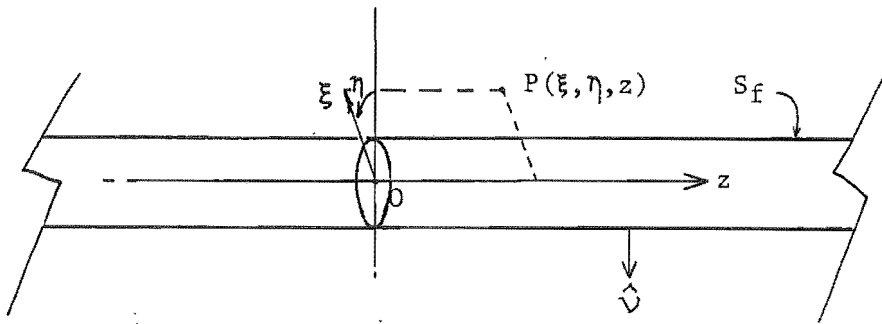


Figure 4.1 A cylindrical (long) cardiac fibre embedded in an infinite homogeneous conducting medium.

A cylindrical polar coordinate system (ξ, η, z) is defined with z along the axis of the fibre. Activation proceeds along the fibre in the positive z direction. Each small element dS of the membrane experiences a change in transmembrane voltage given by the cardiac action potential (cf. Figure 1.1) of the cells in the fibre. The activation is assumed to be uniform so that every point lying on any perpendicular section of the fibre simultaneously experiences the same phase of the action potential.

To derive the field of the single fibre, consider the scalar function $\Psi = \sigma V$ (Plonsey, 1974). Inside the fibre, σ is approximately constant within each cell (Langer and Brady, 1974) and within the spaces between cells. Therefore Ψ obeys the Laplace equation (cf. §2.1.2) within each cell, the spaces between cells and in the external medium. At each membrane, however, Ψ is discontinuous by an amount $(\sigma_+ V_+ - \sigma_- V_-)$, where σ_+ and σ_- are the conductivities external and internal to the membrane. V_+ and V_- are the potentials just outside and just inside the membrane. The derivative of Ψ normal to the membrane is given by

$$\partial\Psi/\partial\nu = \sigma \partial V/\partial\nu + V \partial\sigma/\partial\nu \quad (69)$$

where $\hat{\nu}$ is the unit outward normal to the membrane. The condition of current continuity across the membrane ensures that $\sigma_+ \partial V_+/\partial\nu = \sigma_- \partial V_-/\partial\nu$ and the last term in (69) is zero except within the membrane.

Therefore the term $\partial\Psi/\partial\nu$ has identical value on either side of the (very thin) membrane and can be considered to be continuous across the membrane. Thus Ψ is a potential function which has a discontinuity at each membrane surface, but has a continuous normal derivative at that surface. Such a potential function necessarily arises from a double layer source on the surface with strength equal to the magnitude of the discontinuity and with direction given by the normal to that surface (Stratton, 1941). Therefore Ψ may be written

$$\Psi(P) = \sum_i \iint_{S_i} (\sigma_+ V_+ - \sigma_- V_-) (\partial(R^{-1})/\partial\nu) dS/4\pi \quad (70)$$

for some point P not lying on a membrane surface. The summation in (70) is over all of the closed membrane surfaces S_i .

Within the fibre, each membrane surface is adjacent and parallel to another membrane surface, separated only by a very thin intracellular space (cf. Section 1.1). Since the activation proceeds uniformly along the fibre in the z direction, it may be assumed that the function $(\sigma_+ V_+ - \sigma_- V_-)$ has an equal and opposite amplitude on each pair of adjacent membrane surfaces. The distance between a point on one membrane and the nearest point on the adjacent membrane is very small (of the order of 10^{-6} mm). The contribution of internal membrane surfaces to the integral in (70) is therefore negligible for P external to the fibre. As a result, the potential at an external point is given by

$$V(P) = \iint_{S_f} (\sigma_o V_+ - \sigma_i V_-) (\partial(R^{-1})/\partial\nu) dS/4\pi\sigma_o \quad (71)$$

where σ_o is the conductivity external to the fibre, σ_i is the intracellular conductivity and S_f is the outer fibre surface. To simplify (71), define

$$\sigma_o V_f = \sigma_o V_+ - \sigma_i V_- \quad (72)$$

for the region inside the fibre and on S, where $V_f = V_f(z)$ at any instant. Equation (71) therefore becomes

$$V(P) = \iint_{S_f} V_f (\partial(R^{-1})/\partial\nu) dS/4\pi \quad (73)$$

Applying the divergence theorem (Stratton, 1941) to the vector function ($V_f \nabla(R^{-1})$) within the fibre transforms (73) to

$$V(P) = \iiint_{\kappa_f} \nabla \cdot [V_f \nabla(R^{-1})] dv/4\pi \quad (74)$$

where κ_f is the region inside the fibre. For P external to the fibre, $\nabla^2(R^{-1}) = 0$ everywhere in κ_f . Equation (74) then simplifies to

$$V(P) = \iiint_{\kappa_f} (\partial V_f / \partial z) (\partial(R^{-1}) / \partial z) dv/4\pi \quad (75)$$

remembering that V_f is a function of the z coordinate only. Now, V_f is linearly related to the transmembrane voltage ($V_+ - V_-$), which changes with time and z according to the propagation of the cardiac action potential. Therefore $\partial V_f / \partial z$ is non-zero only in those regions of the fibre which are actively depolarising or repolarising at any given instant. The field external to the fibre is equivalent to the field of a double layer source spread throughout those regions of non-zero $\partial V_f / \partial z$. The double layer is directed in the z direction and has an amplitude equal to $\partial V_f / \partial z$.

Consider a Purkinje fibre (more correctly a bundle of fibres) with a diameter of 2 mm, a conduction velocity of 2 m/sec and an action potential similar to that shown in Figure 1.1. The actively depolarising region of the fibre is confined to an interval of z equal to the velocity multiplied by the depolarisation rise time (say 4 msec), i.e. approximately 2 mm. The distance along the fibre between the depolarisation wavefront and the following repolarisation wavefront is 10 cm. This is approximately equal to the length of the fibres within the specialised ventricular conduction tissues (cf. Section 1.2). It is reasonable to assume, therefore, that depolarisation and repolarisation are not occurring simultaneously within the fibre being modelled. Because of the small volume of the fibre actively depolarising at any instant, the source may be approximated by an equivalent dipole. The validity of this approximation is shown below. The equivalent dipole is positioned on the axis of the fibre in the centre of the active region and acts in the z direction (i.e. in the direction of propagation of the activation). If the equivalent dipole amplitude is denoted by p_e the field may be determined by

$$V_e(P) = p_e \partial(R^{-1}) / \partial z \quad (76)$$

The origin of the coordinates may be conveniently chosen to be the dipole position, so that $R = |\underline{x}|$. A suitable choice for the dipole amplitude is

$$p_e = \iiint \partial V_f / \partial z \, dv / 4\pi \quad (77)$$

where the integration is performed over the volume actively depolarising. Note that in equation (77) p_e is proportional to the area of the depolarisation wavefront.

Two numerical examples illustrate the negligible error introduced to the single-fibre model by the assumption of a dipole source. The parameters used in the first example are illustrated in Figure 4.2 and the results are presented in Table 4.1. A smooth function is chosen for $\partial V_f / \partial z$ in the depolarising region:

$$\begin{aligned} \partial V_f / \partial z &= (1 + \cos(\pi z / b)) / 2b, \quad -b \leq z \leq b \\ &= 0, \quad z < -b \quad \text{and} \quad z > b \end{aligned} \quad (78)$$

The equivalent dipole amplitude is then, by (77),

$$p_e = a^2 / 4 \quad (79)$$

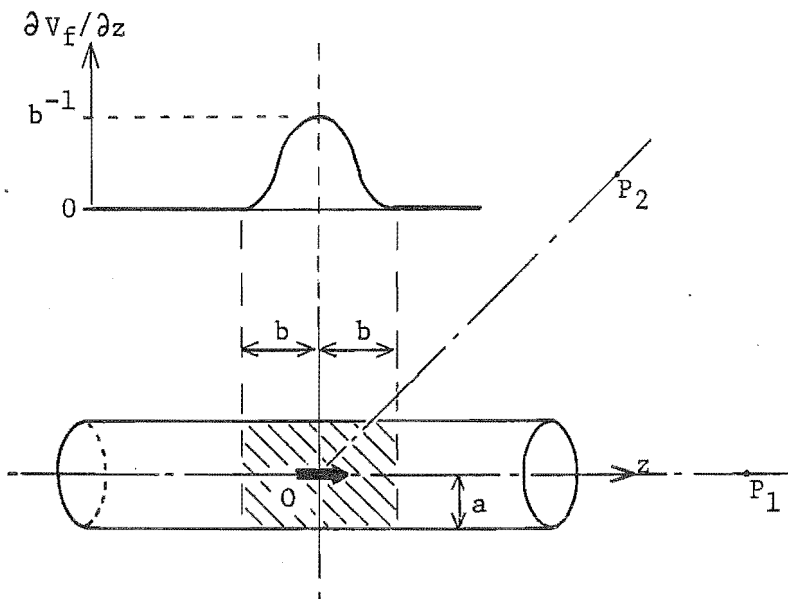


Figure 4.2 The single active fibre modelled in the first numerical example.

TABLE 4.1 Numerical results for the fibre illustrated in Figure 4.2 with $a = 1$ mm and $b = 1$ mm.

z coordinate	P_1		P_2	
	Numerical integration	Equivalent dipole	Numerical integration	Equivalent dipole
2b	0.0588	0.0625	0.0264	0.0221
3b	0.0278	0.0277	0.0136	0.00982
4b	0.0160	0.0156	0.00630	0.00552
5b	0.0103	0.0100	0.00400	0.00356
10b	0.00261	0.00250	0.000986	0.000884
20b	0.00065	0.00063	0.000245	0.000221
100b	0.000026	0.000025	0.0000097	0.0000088

In Table 4.1, $V(P_1)$ and $V(P_2)$ are presented for both the numerical integration of (75) and the equivalent dipole given by (78) and (79). The points P_1 lie on the z axis while the points P_2 lie on a line at an angle of $\pi/4$ from the z axis (see Figure 4.2). The analytical expressions for the potentials are

$$V(P_1) = \int_0^a r dr \int_{-b}^b (z - z') \{(z - z')^2 + r^2\}^{-3/2} \{1 + \cos(\pi z'/b)\} dz'/4\pi$$

$$V_e(P_1) = a^2/4z^2$$

$$V(P_2) = \int_0^\pi d\theta \int_0^a r dr \int_{-b}^b \{2z(z - z' + r\cos\theta) + z'^2 + r^2\}^{-3/2} (z - z') \{1 + \cos(\pi z'/b)\} dz'/b\pi$$

$$V_e(P_2) = a^2/8\sqrt{2} z^2 .$$

The results for V_e presented in Table 4.1 are calculated by Simpson's rule, dividing the range of z' and r into intervals of 0.05 mm and (for $V_e(P_2)$) dividing the range of θ into intervals of $\pi/8$.

The results in Table 4.1 show that the dipole approximation for the cylindrical fibre introduces less than 12% error at distances greater than $4b$. This result should be no surprise: the potential field of a multipole source positioned at the origin of the spherical coordinate system (r, θ, ϕ) in an infinite homogeneous conducting region is (38)

$$V'(P) = \sum_{n,m} B_{nm} r^{-n-1} Y_{nm}(\theta, \phi)$$

For a source that can exist physically, $B_{00} = 0$ (i.e. no free charge can exist in the region) and all the other B_{nm} are finite. For r large, therefore, the dipole terms ($n=1$) predominate over the higher order terms. Extending the argument further, the potential field caused by the depolarisation of a small bundle of fibres which is not cylindrical will still be predominately dipolar in the far field. This is illustrated below with another numerical example.

Consider a "sheet" of fibres with a uniform rectangular cross-section as shown in Figure 4.3.

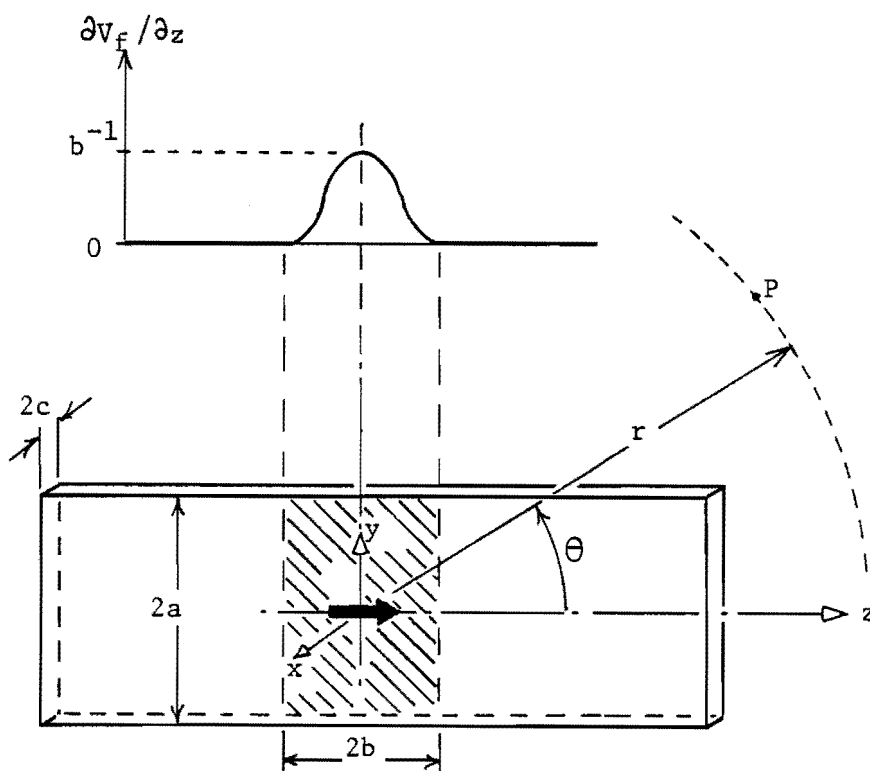


Figure 4.3 The "sheet" of fibres with rectangular cross-section modelled in the second numerical example.

The smooth function (78) is again chosen for $\partial V_f / \partial z$ in the depolarising region of the bundle of fibres. For a point in the plane of the y and z axes at a distance r from the origin and an angle θ from the z axis (see Figure 4.3),

$$V(P) = \int_{-b}^b \{1 + \cos(\pi z/b)\} \int_{-a}^a \int_{-c}^c (r \cos \theta - z) \{ (r \cos \theta - z)^2 + (r \sin \theta - y)^2 + x^2 \}^{-3/2} dx dy dz / 8\pi b$$

and

$$V_e(P) = ac \cos \theta / \pi r^2$$

Similar expressions apply for the field in the plane of the x and z axes. In Figure 4.4, the potential is plotted as a function of θ at a constant radius in the plane of the y and z axes and in the plane of the x and z axes. The parameters of the example ($c=1$, $a=10$) are chosen to model the activation of the left bundle branch (cf. §1.2.2) which has been described as a sheet of fibres (cf. Spach and Barr, 1976; James, 1978). At a radius of 50 mm (representing the minimum distance from the left bundle branch to the body surface) the potential field of the equivalent dipole deviates by less than 4% from the potential calculated by numerical integration (performed by Simpson's rule with equal division of the x, y and z axes into intervals of 0.25 mm).

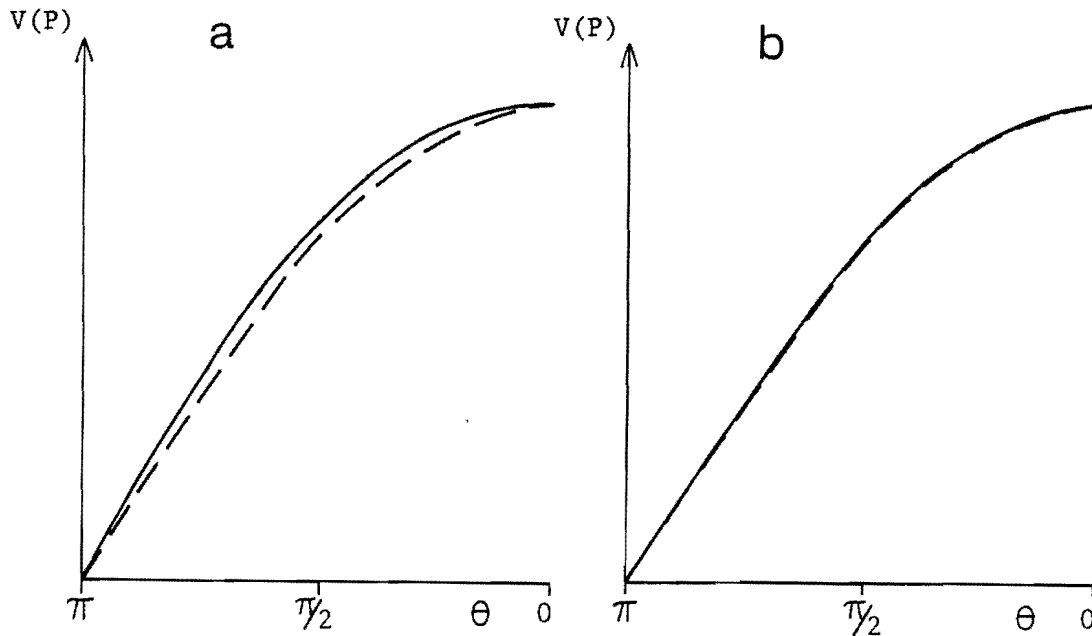


Figure 4.4 The potential field produced by the "sheet" of fibres illustrated in Figure 4.3 (solid lines) and by an equivalent dipole (dashed lines) with $a=10$, $b=1$, $c=1$ and $r=50$. a) y-z plane, b) x-z plane.

The term "far field" is used herein to describe all of space which lies at a greater radial distance than r_f from the centre of the region which is depolarising. The above two numerical examples indicate that r_f is approximately equal to three times the maximum dimension of the region actively depolarising at any instant and that an equivalent dipole is a suitable model for the potential generated by a fibre or bundle of fibres in the far field. The degree to which this conclusion may be affected by the presence of the body surface is investigated in §6.3.1.

§4.1.2 Model for the ventricular myocardium

While a single equivalent dipole models the field generated by the uniform activation of a bundle of fibres, such a simple model is limited in its application to the whole ventricular myocardium, although it must be remembered that the great majority of E.C.G. interpretation schemes are based on an equivalent dipole (cf. Sections 3.1 and 3.2). During ventricular activation a wavefront of depolarisation spreads through the ventricular myocardium (cf. §1.2.3 and §1.3.4). At least two approaches to modelling the cardiac generator during ventricular activation are possible. The most popular approach is to divide the myocardium into a number of segments (cf. Solomon and Selvester, 1973; Swihart, 1976; Salu and Marus, 1976). The activation of each segment is modelled by a dipole. The second approach is to model the wavefront of depolarisation as a double-layer source (cf. Frank, 1953; Rudy and Plonsey, 1979). Details of these approaches are discussed below.

In the multiple dipole model, the ventricular myocardium is divided into M segments κ_j , $j = 1, 2, \dots, M$ (see Figure 4.5a). The activation of the j th segment is represented by a dipole at the position $\underline{x}_j(t)$. The moment of the dipole $\underline{p}_j(t)$ is defined as

$$\underline{p}_j(t) = \iiint_{\kappa_j} (\nabla \cdot \underline{J}_1) \underline{x} \, dx \quad (80)$$

in rectangular coordinates, the x component of $\underline{p}_j(t)$ is defined by

$$p_{jx}(t) = \iiint_{\kappa_j} (\nabla \cdot \underline{J}_1) x \, dx$$

and the y and z components are defined in a similar manner. Ideally, the position of the dipole is chosen to minimise the higher order moments of the electrophysiological sources in the j th segment. Thus, with

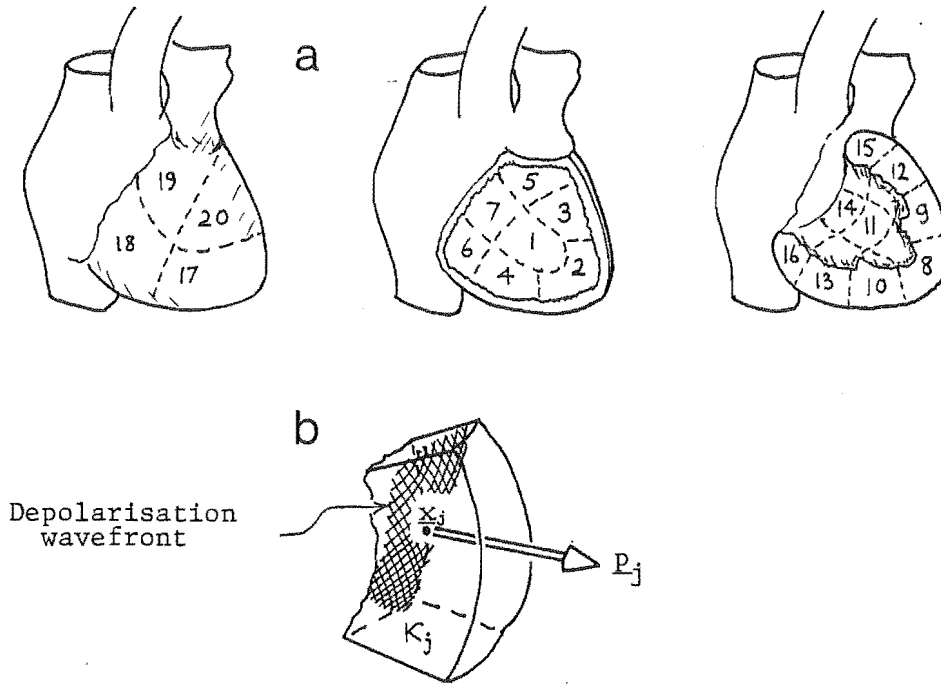


Figure 4.5: The multiple dipole model for the ventricular myocardial activation: a) the partitioning of the myocardium suggested by Selvester *et al.* (1967); (b) the segment κ_j .

$\underline{x}_j = (x_j, y_j, z_j)$, x_j is chosen such that

$$\sum_{n=2}^{\infty} \iiint_{\kappa_j} (\nabla \cdot \underline{J}_1) (\underline{x} - \underline{x}_j)^n dx$$

is a minimum and y_j and z_j are chosen in the same manner. The multiple dipole model of the ventricular myocardial activation assumes (quite reasonably) that the fields of all the dipoles may be summed to find the total field and that, as M becomes large, the field tends to that which is produced by the corresponding continuous source distribution. The infinite homogeneous region field of the myocardial model is then

$$V'(P, t) = \sum_{j=1}^M \underline{p}_j(t) \cdot \nabla(R^{-1}) \delta(\underline{x} - \underline{x}_j(t)) \quad (81)$$

In practice the investigators who have used the multiple dipole model have assumed that the position and the direction (i.e. $\underline{p}_j/|\underline{p}_j|$) of each dipole is constant. Selvester *et al.* (1967) use the myocardial activation data of Durrer *et al.* (1970) to specify 20 dipole positions and directions. Each of the dipole moments vary in amplitude according to the area of the depolarisation wavefront (assumed to be very thin) lying within the corresponding myocardial segment at each instant.

Using a similar model, Kulbertus *et al.* (1975) report simulations of electrocardiograms for normal myocardial excitation and several abnormalities of impulse conduction (cf. §1.4.5). Salu and Marcus (1976) also use the data of Durrer *et al.* (1970) for their model of the myocardial excitation, which includes 1500 dipoles. Each dipole represents the activation of a small trapezoidal region of myocardium and is turned on or off with time according to the activation sequence being simulated. Simulations of myocardial hypertrophy (cf. §1.4.3) produce electrocardiograms resembling those of hypertrophic patients (Salu and Marcus, 1976).

The second approach to modelling the excitation of the ventricular myocardium is to represent the wavefront of depolarisation as a double layer source. This was first suggested by Frank (1953) and the following is largely a summary of his method and results. The double layer representation of myocardial excitation is an extension of the model for a single fibre or bundle of fibres presented in §4.1.1. As the wave of depolarisation moves through the tissue it is possible to define a surface (albeit a convoluted one) which cuts all the cells undergoing depolarisation at any one instant. Suppose a smooth approximation to this surface is $S_d(t)$ with unit normal \hat{v}_d , defined in the direction of the advancing wavefront. Then (75) may be written as

$$V(P) = \iiint_{\kappa} (\partial V_f / \partial v_d) (\partial(R^{-1}) / \partial v_d) dv / 4\pi \quad (82)$$

where κ is now the region occupied by the myocardium. Thus the source of the external potential field is confined to the (thin) region about and including $S_d(t)$ where $\partial V_f / \partial v_d$ is non-zero. The conduction velocity of the excitation within the ventricular myocardium is approximately 0.4 m/sec (Scher, 1976) and the rise time of the action potential is approximately 1 msec (Kootsey and Johnson, 1976). Therefore the width of the region undergoing depolarisation is only 0.4 mm. The similarity between the fields of a depolarising region of finite, though small, dimensions and of a dipole is demonstrated in §4.1.1. In an analogous manner the three dimensional source quantity embodied in (82) may be replaced by a double layer source spread over S_d . The double layer strength $\tau(\underline{\xi})$, where $\underline{\xi}$ lies on S_d , may be interpreted as the dipole moment density on S_d . The infinite region field is then given by

$$V'(P) = \iint_{S_d} \tau(\underline{\xi}) (\partial(R^{-1}) / \partial v_d) \cdot dS / 4\pi \quad (83)$$

The computation of $V'(P)$ is simplified significantly if τ is chosen to be a function of time only. Little experimental data has been amassed to support or dispute this choice. Kootsey and Johnson (1976) feel that the uniformity in the changes of transmembrane voltage throughout the ventricular myocardium supports the assumption of a uniform surface source layer. Solomon and Selvester (1971) estimate τ from animal experiments to be 1.8×10^{-13} coulomb metre/square metre.

An interesting and useful property of double layer surface sources may be employed if τ is constant over S_d . Consider that S_d is in the form of an irregular "cup" (see Figure 4.6).

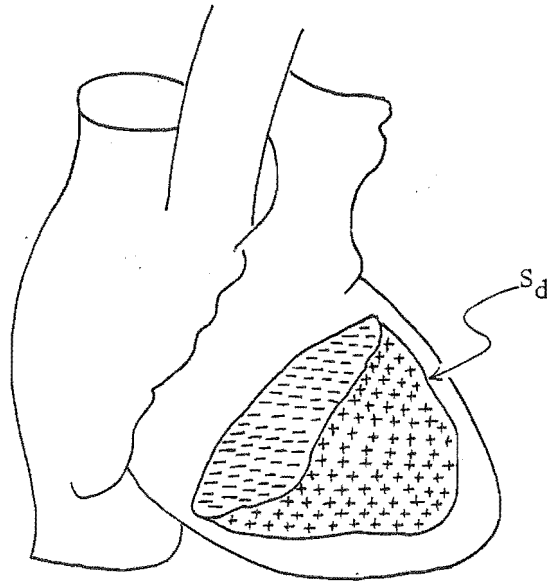


Figure 4.6 The depolarisation wavefront in the ventricular myocardium represented as a "cup shaped" double layer S_d .

The addition of a closed uniform double layer has no effect on the field at an external point (Stratton, 1941). Therefore, adding a layer of density $-\tau$ over the closed surface $S_d \cup S_c$, where S_c closes the top of the "cup", will not effect $V'(P)$. Over S_d the surface source layers exactly cancel and thus $V'(P)$ may be written as

$$V'(P) = \iint_{S_c} \tau \partial(R^{-1})/\partial v_d \, dS/4\pi \quad (84)$$

The surface S_c may be chosen for computational convenience. This property is exploited usefully by Frank (1953) in assessing a double layer model for myocardial activation. Frank assumes that S_d has a circular rim and he chooses S_c to be a spherical cap with its centre of curvature at the origin of the coordinates (see Figure 4.7a).

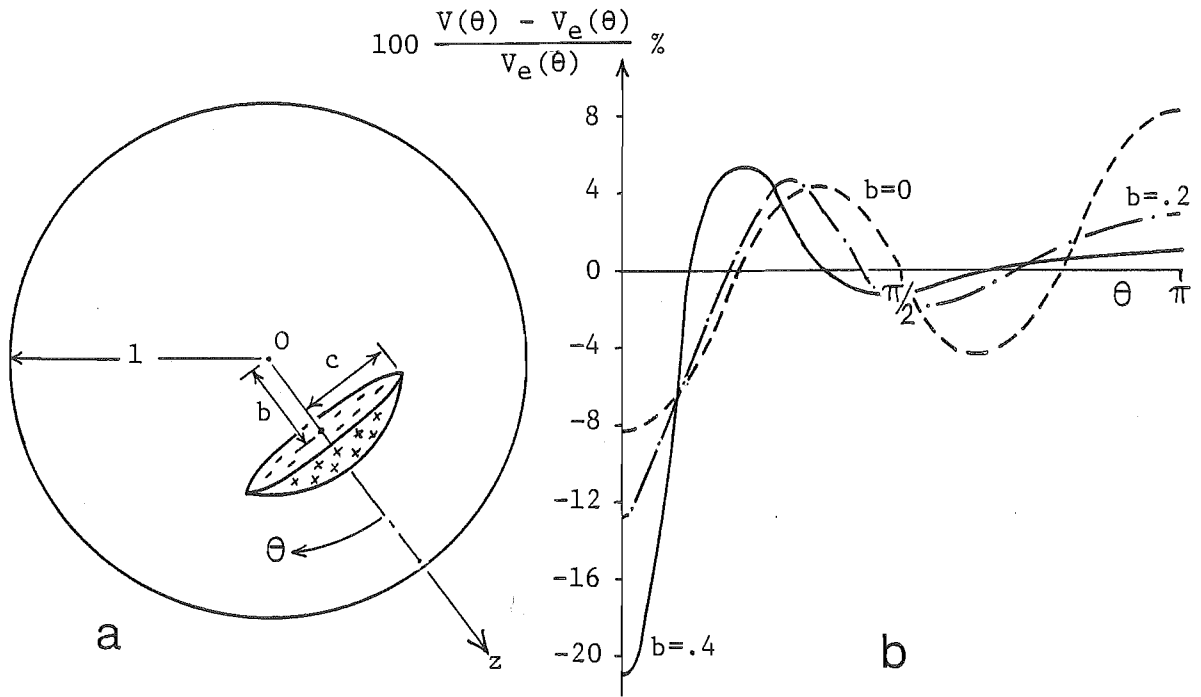


Figure 4.7 The spherical cap double layer model of the ventricular myocardium.

He calculates the potential field which would be generated by the layer on a spherical homogeneous body centred on the same origin. The field V_e of a dipole of the same total moment positioned in the centre of the rim is calculated for comparison.

Some of Frank's results (1953) are reproduced in Figure 4.7b, the vertical axis of which is the difference between the double layer and "equivalent" dipole potentials expressed as percentages of the maximum of the dipole field (the latter occurs on the z axis - see Figure 4.7a). The horizontal axis is the polar angle θ measured from the z axis. Both the source and the field generated are symmetrical about the z axis. Note that appreciable differences (i.e. greater than 10 per cent) occur only in the small region $\theta \leq 18^\circ$, and that $V_e > V$ there. Recall that the standard E.C.G. measurement schemes (cf. Sections 3.1 and 3.2) assume an equivalent dipole source. If the double layer of Frank accurately models the cardiac generator, his results indicate that significant error in the interpretation occurs if an electrode is positioned such that $\theta < 18^\circ$. However, for electrodes outside that region of the field, little error is introduced by the assumption of a dipole source (Frank, 1953).

With the ideas reviewed here, Frank makes another useful contribution to the science of electrocardiography to stand alongside his work on lead systems (cf. Sections 3.1 and 3.2). However its significance is limited by the assumption of a homogeneous and spherical body. In Chapters 5 and 6 the double layer source formulation of Frank is used in models for investigating the effects of conductivity inhomogeneities and surface shape on the E.C.G.

Some experimental work with isolated animal hearts in electrolytic tanks (cf. Taccardi, 1976; Mirvis, 1978) has suggested that the field generated by the ventricular myocardial activation is more complex than that produced by either a dipole or a spherical cap double layer at some instants in the cardiac cycle. In the presence of an abnormality, such as myocardial infarction (cf. §1.4.1), the complexity is likely to be more pronounced. In Section 8.1 an extension to Frank's spherical cap model is suggested, which may provide the basis of a more widely applicable model for the ventricular activation.

4.2 MODELLING THE SURROUNDING TISSUES

The models and results reviewed in Section 4.1 relate to the electrophysiological sources of the heart embedded in a (hypothetical) infinite homogeneous conducting region. The infinite region field of the sources, $V'(P)$, forms one term of the integral equation (17) for electrocardiography. Other terms in equation (17) account for the effect of the surrounding tissues. In this section a review is made of the attempts to model the effects of the surrounding tissues which have appeared in the literature. The review is divided into the modelling of the body surface and the modelling of the internal conductivity inhomogeneities (although some workers have attempted to incorporate both in the same model).

§4.2.1 Body surface

It was realised by the earliest workers in electrocardiography that the potential field measured on the body surface was influenced to some degree by the presence of the body/air boundary. The interpretation scheme of Einthoven (1913) assumes a spherical boundary for the body, centred on a dipole source which represents the activation of the heart.

Such a concentric spherical boundary affects only the amplitude of the surface potential field as detailed in Section 3.1. The experimental work of Frank (1954b) reviewed in Section 3.1 shows the limitations of the assumption of a concentric spherical body surface. This limitation is unfortunate since the sphere offers many computational advantages over irregular boundaries. Frank's image surfaces (cf. Figure 3.5) do, however, indicate that the body can often be usefully represented by a sphere. Of particular interest is the potential field on the chest, which is the part of the body surface closest to the myocardium and therefore where much of the E.C.G. information is concentrated (cf. Section 1.3). The chest is also a convenient place for applying electrodes of the popular stick-on variety. The studies of the non-invasive detection of signals from the specialised conduction tissues, reported in Chapter 7, utilise chest electrodes because this allows the maximum voltage to be measured. Before turning to more realistic body surfaces, therefore, the spherical boundary is investigated as a model for the chest surface.

Consider an impressed current source embedded within a homogeneous conducting region bounded by a spherical insulating surface S with radius a . The origin of coordinates is the centre of the sphere. The potential field may be expanded in multipoles as (37)

$$V(P) = \sum_{n,m} [B_{nm} r^{-n-1} + C_{nm} r^n] Y_{nm}(\theta, \phi)$$

for r greater than the minimum radius from the origin which circumscribes all the sources, and less than or equal to a . The imposition of the spherical insulating boundary requires that the expansion coefficients satisfy equation (53) (cf. §3.1.1). Thus the surface potential is given by

$$V_s = \sum_{n,m} (2n+1) B_{nm} a^{-n-1} Y_{nm}(\theta, \phi)/n \quad (85)$$

Comparing (85) with the infinite region expansion (38) indicates that the presence of the insulating boundary at $r=a$ has an amplifying effect on the field and that the lower order terms are accentuated over the higher order terms. As discussed in §3.1.1, the field of a dipole positioned at the origin is amplified by a factor of 3 by the presence of the insulating boundary. Next, consider a dipole positioned on the axis $\theta=0$ at a distance b from the origin and directed along the axis. The infinite region field is found by the coordinate transformation given in Appendix I. The imposition of the spherical boundary at $r=a$ again weights the expansion terms of order $n=1$ by a factor of 3 while higher order terms

are weighted by lesser factors (cf. equation (85)). As a result V_s becomes less "peaked" in front of the dipole when the insulating boundary is present than when it is absent.

It is instructive to see how realistically the field of a model source on a spherical "chest" matches a typical measured electrocardiographic field. Figure 4.8 provides such a comparison. In Figure 4.8a a measured E.C.G. field is shown, in the form of contours of equal potential, over the chest of a male subject (Taccardi, 1976). This example is relatively complex with two negative minima of potential observed. In Figure 4.8b, the field of a dipole on a spherical insulating boundary is shown. The dipole direction and position relative to the surface is chosen so that the major features of the field match those of Figure 4.8a. Similarly the field of a uniform double layer source of the sort described by Frank (1953, cf. §4.1.2) is shown in Figure 4.8c. It is clear from these examples that the use of a spherical boundary to model the field on the chest region does not introduce large errors. The results presented in Chapter 5 for models of non-spherical boundaries confirm that spherical boundaries are adequate for many modelling purposes.

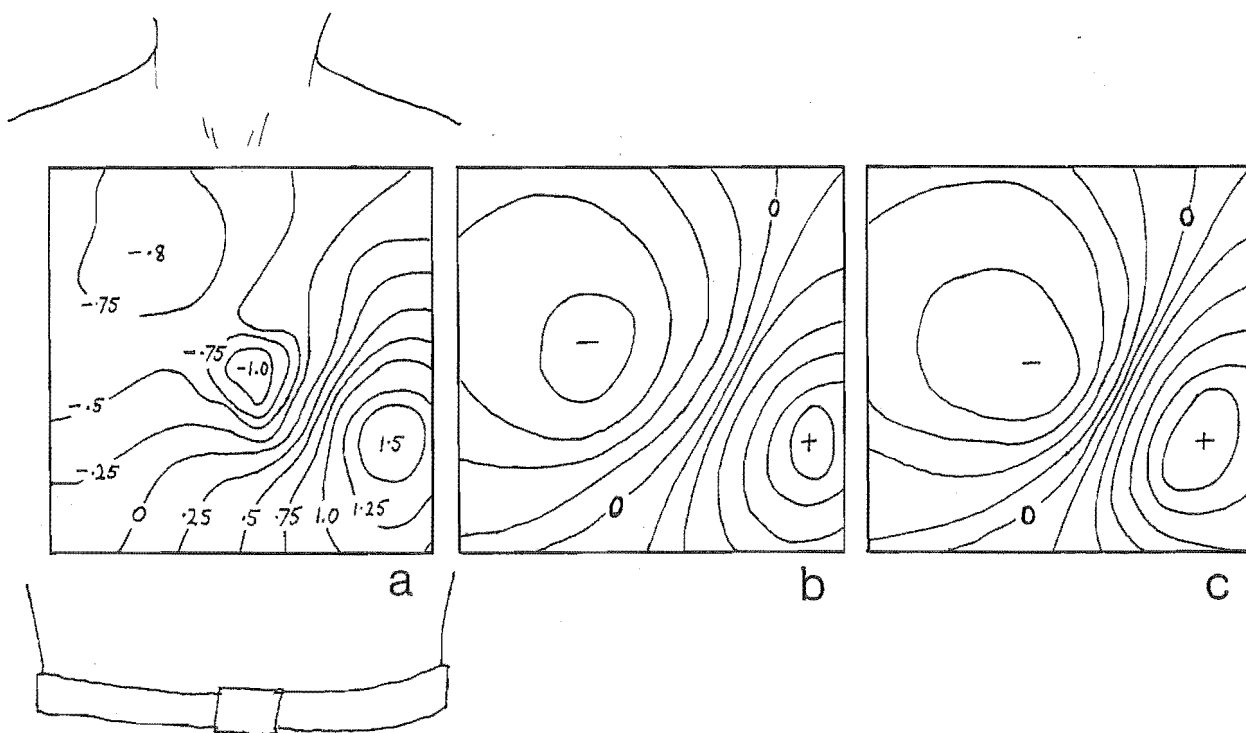


Figure 4.8 Comparison of a) a measured E.C.G. field over the chest of a male subject (Taccardi, 1976) with that produced by b) a dipole and c) a uniform double layer source on a spherical boundary.

Most investigators of the inverse electrocardiography problem consider that the shape of the body is important in the interpretation of the E.C.G. Several of these investigators have carried out modelling of realistic body shapes in order to test their particular method of inverse solution (cf. Guardo et al., 1976; Cuffin and Geselowitz, 1977; Lynn et al., 1967). Two methods are reported to date for modelling a realistic body surface. Gelernter and Swihart (1964; cf. Swihart, 1976) use an iterative procedure to solve for the potential on a surface which is divided into a large number M of small surface elements. The Gelernter-Swihart method is described below.

Let $\underline{\xi}_i$ be a position on S_i , the i th surface element of S , and \hat{v}_i be the unit outward normal to S at $\underline{\xi}_i$. The first step of the Gelernter-Swihart method is to calculate the infinite homogeneous region field V' of the given source distribution by equation (19). A single layer of charge with density ω_i is then distributed on S_i . The magnitude of the electric field due to the layer of charge on S_i is given by (Stratton, 1941)

$$E_i(P) = \iint_{\Delta S_i} \omega_i |\nabla(R^{-1})| dS / 4\pi\sigma \quad (86)$$

In the limit as P tends close to $\underline{\xi}_i$, the integral in (86) tends to $\omega_i/2\sigma$. For the first iteration, then, the surface density is chosen to be

$$\omega_i^{(1)} = 2\sigma \partial V'(\underline{\xi}_i) / \partial v_i \quad (87)$$

so that the boundary condition $\partial V / \partial v = 0$ is satisfied with respect to ΔS_i only.

The charge that has been placed on each ΔS_i also affects the field at every other element $j \neq i$. In the following iteration, therefore, the perturbing fields at ΔS_i produced by the charges on all of the other $M-1$ elements are summed. A new charge density $\omega_i^{(2)}$ is then calculated to satisfy the boundary condition with respect to ΔS_i only. The process continues until (hopefully) convergence to a meaningful solution is achieved. The potential over S is then computed by adding the potential due to the charge layer on S to V' due to the original source distribution.

The second method reported for modelling a realistic body surface is direct numerical solution of (29), the integral equation for potential on S in terms of V' , again by dividing S into M small elements. This method is chosen by most investigators (cf. Barnard et al., 1976; Cuffin and Geselowitz, 1977; d'Alche et al., 1974). Using the notation

introduced above, the surface integral in (29) is replaced by a summation to give

$$V_s(\underline{\xi}_i) = 2 V_s'(\underline{\xi}_i) - \sum_{j=1}^M V_s(\underline{\xi}_j) (\partial R(\underline{\xi}_i, \underline{\xi}_j)^{-1} / \partial v_j) \Delta S_j / 2\pi \quad (88)$$

where the boundary condition $\partial V / \partial v = 0$ has been incorporated. In matrix notation (88) becomes

$$[V_s] = 2 [V_s'] + [\beta] [V_s] \quad (89)$$

where $[\beta]$ is of dimension $M \times M$. The most direct method of solving (89) would seem to be finding the inverse of $[I - \beta]$, where I is the square identity matrix. However no such inverse exists because $[I - \beta]$ is singular (Barnard et al., 1967). Yet the integral equation (29) clearly has a solution, since it describes a physical system. It is reasonable to assume then that a solution may also be found for (89). The reader is referred to Lynn and Timlake (1968) for a comprehensive treatment of this problem and for details of their solution by the method of multiple deflations.

The methods of modelling realistic body shapes outlined above have been used by several investigators. However, none, to my knowledge, has carried out studies of the effect of changing the body surface. Rather they set up a body shape and study the effects of changing the source and/or removing the surface altogether. This is probably because the finite element techniques require the coordinates of each small element of the surface to be specified (i.e. entered into a computer) and their solution by iteration requires a considerable time on a large computer. Furthermore, Swihart (1976) admits that the convergence of the solution, with the charge perturbation method, only occurs if the surface is very finely divided in those regions where the curvature is large and where the potential gradient is steep. The same considerations are certain to apply for the method based on the integral equation. Cuffin and Geselowitz (1977), for example, use 1426 triangular elements to represent the torso. It would be extremely time consuming to model a number of different torso shapes with so many elements having to be individually specified. Two alternative methods of studying the effects of boundary shape are presented in Chapters 5 and 6. Both of these methods may be implemented on a small computer and both enable the effects of changes in boundary shape to be tested with relative ease.

§4.2.2 Internal conductivity variation

An integral equation for the inhomogeneous body is derived in §2.2.4. It is repeated here for convenience:

$$V(P) = - \iiint_K \nabla \cdot \underline{J}_i \, dv / 4\pi\sigma R + \iiint_K \nabla V \cdot \nabla \sigma \, dv / 4\pi\sigma R - \iint_S V \, \partial(R^{-1}) / \partial v \, dS / 4\pi \quad (90)$$

If σ is given throughout the body, then, in principle at least, this general integral equation may be used to find the surface potential arising from any given source distribution. If σ varies continuously throughout K , however, the practical difficulties of solving (90) are formidable if not insurmountable. Instead the approach taken by all investigators to date is to model the torso as a piecewise homogeneous region, so that the variation of σ is reduced to discontinuities on the boundaries separating adjacent subregions. Equation (90) then simplifies to the form (cf. §2.2.4)

$$V(P) = - \iiint_K \nabla \cdot \underline{J}_i \, dv / 4\pi\sigma R + (\sigma'' - \sigma') \iint_{S'} (\partial V'' / \partial v') \, dS / 4\pi\sigma' R - \iint_S V (\partial(R^{-1}) / \partial v) \, dS / 4\pi \quad (91)$$

The second integral in (91) is repeated for each internal boundary surface separating homogeneous regions (σ' inside, σ'' outside). Three methods (at least) have been reported for finding a forward solution for the piecewise homogeneous "torso". These are briefly reviewed below.

The first method is that of Gelernter and Swihart (1964; cf. Swihart, 1976). In an exactly analogous manner to their modelling of the body surface, outlined in §4.2.1, Gelernter and Swihart distribute a layer of charge over the internal boundary surfaces. At the ℓ th iteration, a surface charge of density $\omega_i^{(\ell)}$ is distributed on S_i' , the i th surface element of the internal boundary surface S' . The charge density is related to the normal derivative of potential calculated in the previous iteration by

$$\omega_i^{(\ell)} = 2(\sigma' - \sigma'') (\partial V(\underline{\xi}_i) / \partial v_i)^{(\ell-1)} / (\sigma' + \sigma'') \quad (92)$$

The derivative of V in (92) is evaluated just on the inside of $\Delta S_i'$. This value of ω_i' obeys the boundary condition (49) at $\underline{\xi}_i$ with respect to $\Delta S_i'$. The iteration continues in the same manner as for the application of this method to the modelling of the outer surface only (cf. §4.2.1).

The second method of modelling the internal conductivity variation is to numerically solve the governing integral equation (91). The outer surface is divided into M elements and all the internal boundary surfaces are similarly divided, to form a total of N surface elements. Assuming, for brevity, that there is only one internal surface S' and replacing each integral in (50) by a summation gives either

$$V_S(\underline{\xi}_i) = 2 V_S'(\underline{\xi}_i) + k \sum_{j=1}^{N-M} (\partial V''(\underline{\xi}_j)/\partial v_j') \Delta S_j' / 4\pi R(\underline{\xi}_i, \underline{\xi}_j) - \sum_{j=1}^M V_S(\underline{\xi}_j) (\partial R(\underline{\xi}_i, \underline{\xi}_j)^{-1} / \partial v_j) \Delta S_j / 2\pi, \quad \underline{\xi}_i \in S \quad (93)$$

or

$$\partial V''(\underline{\xi}_i)/\partial v_i' = 2\partial V'(\underline{\xi}_i)/\partial v_i' + k \sum_{j=1}^{N-M} (\partial V''(\underline{\xi}_j)/\partial v_j') (\partial R(\underline{\xi}_i, \underline{\xi}_j)^{-1} / \partial v_i') \Delta S_j' / 2\pi - \sum_{j=1}^M V_S(\underline{\xi}_j) (\partial R(\underline{\xi}_i, \underline{\xi}_j)^{-1} / \partial v_j) \Delta S_j / 4\pi, \quad \underline{\xi}_i \in S' \quad (94)$$

where $k = (\sigma'' - \sigma')/\sigma'$. Note that in (94) both sides are written for a point $\underline{\xi}_i$ on S' and then differentiated with respect to \hat{v}_i' , the outward normal at the "point of observation". There are M equations of the form of (93) and N-M equations of the form of (94). There are N unknowns comprising V_S at M points and $\partial V''/\partial v'$ at N-M points. There are thus N equations for N unknowns and the system of equations is in principle solvable. In matrix notation the system can be written as

$$[\Phi] = 2[\Phi'] + [\beta] [\Phi] \quad (95)$$

where $[\beta]$ is now of dimension $N \times N$. As in §4.2.1, $[I - \beta]$ is singular (Barnard et al., 1967). The reader is again referred to Lynn and Timlake (1968) for a comprehensive treatment of the method of solution. Some pertinent comments are also made by Swihart (1976).

The third method which has been applied to modelling the internal conductivity variations of the body is analytical, in contrast to the previous two. It is based on a system of spherical boundaries known as the "eccentric spheres model" (Bayley et al., 1969; Rudy and Plonsey, 1979). Each boundary is non-intersecting and separates two homogeneous regions. Within each region which does not contain sources, the potential obeys Laplace's equation and therefore may be exactly represented by a convergent series of spherical harmonic functions (37) with constant coefficients (provided the origin of coordinates is chosen appropriately).

Bayley *et al.* (1969) and after them, Rudy and Plonsey (1979), specify a spherical cap double layer source of the type suggested by Frank (1953; cf. §4.1.2). The potential expansion in each region is equated to the expansion in the adjoining region, by applying the boundary conditions of continuity of current and voltage at each boundary surface. This method is discussed in detail in §5.1.1.

Few results have been published from model studies of the conductivity inhomogeneities in the torso. Brody (1956) presents a simple theoretical study which indicates that the effect of the intracardiac blood pool (of relatively high conductivity) is to relatively enhance the outer surface potential field of a radially directed dipole source "in the myocardium" over a tangentially directed dipole. This has become known as the "Brody effect". Later, more elaborate, studies have confirmed the existence of the Brody effect (cf. Rudy and Plonsey, 1979; McFee and Rush, 1967) although some of my results in Section 5.2 indicate that its significance may have been over-emphasized. Other published studies have done little more than confirm that conductivity inhomogeneities are likely to have an effect. In my opinion nobody has comprehensively studied how these effects relate to the degree of inhomogeneity, the shape of internal boundaries or their relationship to the source distribution. The "eccentric spheres model" offers advantages over the approximate numerical methods (described earlier in this section), in that the geometry of the model may be straightforwardly changed and the surface field recomputed, but few results of this type have been so far presented (cf. Bayley *et al.*, 1969; Rudy and Plonsey, 1979). Furthermore, the symmetry of this model restricts the validity of some of the conclusions made in these studies (cf. Rush and Nelson, 1976). Experimental tank experiments and *in vivo* experiments have also confirmed the importance of the inhomogeneities in the E.C.G. potential field (cf. Rush and Nelson, 1976; Rush, 1971; Salu *et al.*, 1978; Scher *et al.*, 1971), but they again fall short of providing comprehensive results on inhomogeneity effects. A review of the state-of-art in studies of the effects of both inhomogeneity and anisotropy on the E.C.G. has been given by Rush and Nelson (1976).

In view of the apparent shortcomings in the published studies of the effects of the torso (both in surface shape and internal inhomogeneities) on the electrocardiogram, there is clearly a need for more work in this area. In Chapter 5 a model is presented which generalizes the analytic methods embodied in the "eccentric spheres model" to incorporate a non-spherical outer boundary. Then in Chapter 6 an alternative model

is presented which incorporates non-spherical internal and outer surfaces. It is shown that the generalized models provide the basis for a more comprehensive understanding of the effects of the torso on the E.C.G.

PART II

COMPUTATIONAL AND EXPERIMENTAL RESULTS

CHAPTER 5

SIMPLE MODEL (SURFACE ADMITTANCE)

In this chapter I present the first of two computational models which further the study of the effects of the internal conductivity inhomogeneities and body surface shape on the electrocardiogram. The second model is presented in Chapter 6.

The models presented in Chapters 5 and 6 represent the interior of the body as a three-dimensional piecewise homogeneous region. Within each region the potential field is represented by a series of regular functions. Analytic techniques are employed to solve for the surface potential V_s with given sources, inhomogeneities and surface shape. The analytic approach is favoured for this study over the alternative finite element techniques (cf. Sections 2.2 and 4.2) for several reasons. Firstly, the latter techniques require the use of extensive computing facilities not normally available in cardiac departments. Secondly, numerical convergence is virtually assumed in many cases using analytic methods and it is easy to check in others. Thirdly, altering the source specification for a given model does not require a rerun of the complete computation as it would with a finite element technique. These points are discussed further in Chapter 8.

The simple model presented in this chapter is similar to that developed by Rudy and Plonsey (1979), but it allows the effects of changes in the body surface shape to be evaluated by the incorporation of the theoretical device known as "surface admittance". The theory of the model is presented in Section 5.1. Results of the application of the model are given in Section 5.2. To illustrate that the surface admittance method can successfully model even sharp changes in the surface boundary, a model for a two-dimensional "limb" is presented in Section 5.3. The "limb" simulation is carried out in two dimensions so that approximate numerical results may be compared with accurate calculations based on conformal mapping. The results are discussed in Section 5.4.

5.1 DETAILS OF THE MODEL

§5.1.1 Internal boundaries

A spherical surface S has its centre at the point O as shown in Figure 5.1. The interior of S is subdivided into regions of constant conductivity bounded by an arbitrary number of non-intersecting spherical surfaces S' , S'' , etc. The surface S' has its centre at the point O' and similarly for S'' , etc. The piecewise constant conductivity is denoted by σ . The position vector of an arbitrary point is denoted by \underline{x} . Impressed sources $\underline{\rho}(\underline{x})$ can be arbitrarily distributed throughout the interior of S . The surface potential V_S is to be found for a source distribution, a particular distribution of internal inhomogeneities and a specific boundary condition on S , all of which are given.

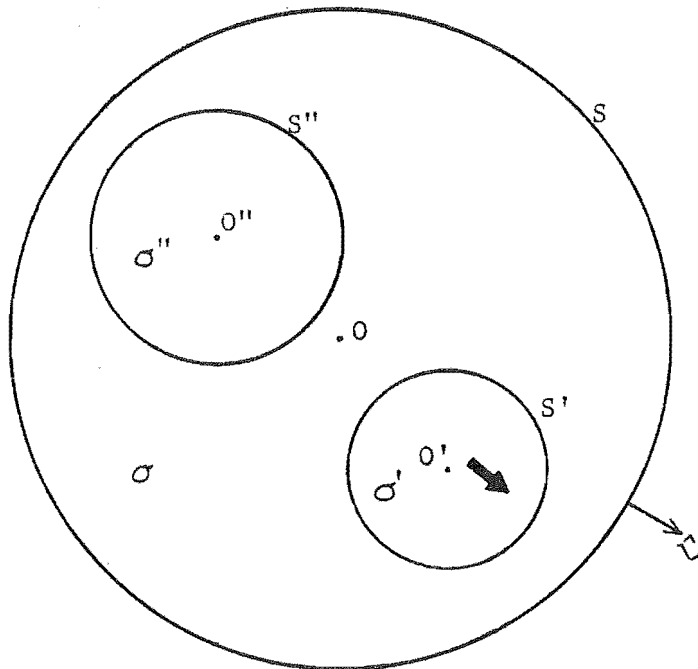


Figure 5.1 Piecewise homogeneous model with spherical boundaries.

Consider first the field throughout the interior of S . Within each homogeneous region $\nabla^2 V = 0$ at points where there are no sources. Therefore V may be expanded in a double series of spherical harmonic functions (37) at any point within each region. Let the field within S' (cf. Figure 5.1) be denoted V' . If $\underline{\rho}(\underline{x})$ is zero everywhere within S'

and there are no other boundaries within S' (i.e. the interior of S' is homogeneous) the expansion for V' must be regular everywhere within S' . Therefore, with the origin of coordinates lying within S' ,

$$V'(x) = \sum_{n,m} C_{nm}' r^n Y_{nm}(\theta, \phi) \quad (96)$$

is a complete and convergent expansion for the potential at any point within S' . If, on the other hand, $p(x)$ is non-zero somewhere within S' or the interior is only piecewise homogeneous, V' is no longer required to be regular everywhere. However, if it is possible to specify that the sources and internal boundaries lie sufficiently far inside S' , then the expansion (37) for V' is complete and converges just inside S' . Thus, with the origin of coordinates conveniently chosen to be O' ,

$$V'(x) = \sum_{n,m} (B_{nm}' r'^{-n-1} + C_{nm}' r'^n) Y_{nm}(\theta', \phi') \quad (97)$$

for $r' > T$, where T is the radius circumscribing all internal sources and boundaries within S' . In (97) the terms with the coefficients B_{nm}' are regular at infinity and represent the contribution to the field of sources and internal boundaries at radii $< T$. The terms with the coefficients C_{nm}' are regular at the origin and represent the contribution to the field of the boundary S' and everything that lies outside it.

By arguments similar to those in the last paragraph, it may be shown that the field just outside S' , denoted V'' , may also be expressed in the form of (97) in terms of the coefficients \tilde{B}_{nm}'' and \tilde{C}_{nm}'' . Again, for convenience, the origin of coordinates may be chosen to be O' . The potential and current are required to be continuous across the boundary S' (Stratton, 1941). Using (97), the continuity of the potential requires that

$$\sum_{n,m} (B_{nm}' r'^{-n-1} + C_{nm}' r'^n) Y_{nm}(\theta', \phi') = \sum_{n,m} (\tilde{B}_{nm}'' r'^{-n-1} + \tilde{C}_{nm}'' r'^n) Y_{nm}(\theta', \phi') \quad (98)$$

with r' equal to the radius of S' . If both sides of (98) are multiplied by a testing function $Y_{uv}(\theta', \phi')$ and integrated over the closed sphere S' , the orthogonality of the spherical harmonic functions (cf. Appendix 1) allows (98) to be simplified to

$$B_{uv}' r'^{-u-1} + C_{uv}' r'^u = \tilde{B}_{uv}'' r'^{-u-1} + \tilde{C}_{uv}'' r'^u \quad (99)$$

for all values of the expansion indices u and v and for r' equal to the radius of S' . Similarly, the continuity of the current across S' and the orthogonality of the $Y_{nm}(\theta', \phi')$ require that

$$\sigma'(u C'_{uv} r'^{u-1} - (u+1)B'_{uv} r'^{-u-2}) = \sigma''(u \tilde{C}''_{uv} r'^{u-1} - (u+1)\tilde{B}''_{uv} r'^{-u-2}) \quad (100)$$

where σ' and σ'' are the conductivities inside and outside S' , respectively. Thus the boundary S' generates the two sets of simultaneous linear equations (99) and (100) in the four sets of expansion coefficients.

If the interior of S' is homogeneous and without sources, the coefficients B'_{uv} are equal to zero as explained above. If the interior of S' contains sources, but no internal boundaries, the B'_{uv} are found by expanding the sources as a multipole series. For $r > T$ the field due to the sources inside S' only is found from (19) and equated to the terms of the expansion (97) which are regular at infinity. Thus

$$\sum_{n,m} B'_{nm} r'^{-n-1} Y_{nm}(\theta', \phi') = \iiint_{\kappa_0} \frac{\rho(\underline{x}')}{\kappa_0} dv / 4\pi R \quad (101)$$

where κ_0 is the region which encloses all sources. The term R^{-1} is now expanded by (22), both sides of (101) are multiplied by a testing function $Y_{uv}(\theta', \phi')$ and the orthogonality of the spherical harmonic functions is used to give

$$B'_{uv} = \iiint_{\kappa_0} \frac{\rho(\underline{x}')}{\kappa_0} r'^u Y_{uv}(\theta', \phi') dv / 16\pi^2(2u+1) \quad (102)$$

So far in this section a single internal boundary has been discussed with or without sources in the interior. Now consider two or more internal spherical boundaries arranged so that each homogeneous region is bounded by one or two spheres (see Figure 5.2). For simplicity, consider that the sources in the model depicted in Figure 5.2 are totally enclosed within S' . Adopting the notation of Figure 5.2, the expansion coefficients B''_{uv} and C''_{uv} for V'' just outside S' are equated to the coefficients of V' by (99) and (100) with r' put equal to the radius of S' . Note that the expansion of V'' at this stage is in coordinates with their origin at O' . To equate V'' to V across the next boundary S'' the expansion for V'' must be expressed in terms of O'' . This is achieved by the coordinate transformations given in Appendix 1 (cf. Hobson, 1930). V'' is then written

$$V'' = \sum_{u,v} (B''_{uv} r''^{-u-1} + C''_{uv} r''^u) Y_{uv}(\theta'', \phi'')$$

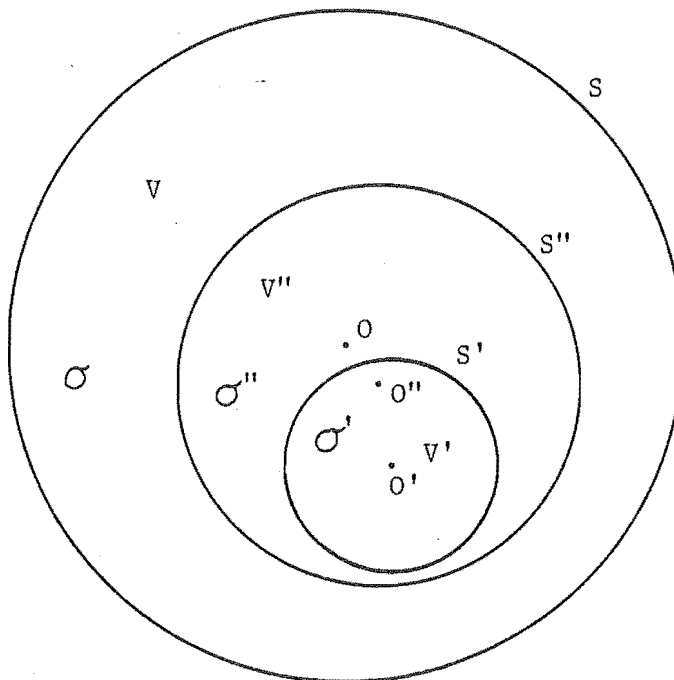


Figure 5.2 Model with two internal spherical boundaries. S' is totally enclosed within S''.

where the B''_{uv} and C''_{uv} are each expressed as combinations of the \tilde{B}''_{uv} and \tilde{C}''_{uv} . The process of matching the field expansions with (99) and (100) (incorporating appropriate notation changes) and transforming the coordinates, is repeated for S''. Finally V is written

$$V = \sum_{u,v} (B_{uv} r^{-u-1} + C_{uv} r^u) Y_{uv}(\theta, \phi) \tag{103}$$

where O is the origin of the coordinates (r, θ, ϕ) .

Each internal boundary introduces two sets of independent linear equations relating the coefficients of the field inside and outside. The coefficients after a coordinate transformation are also linearly related to their predecessors. Therefore the final coefficients of the field expansion inside S may be written

$$\begin{aligned} B_{uv} &= B_{uv} (C_{uv}, B'_{nm}) \\ \text{and} \quad C_{uv} &= C_{uv} (B_{uv}, B'_{nm}) \end{aligned} \tag{104}$$

where the B'_{nm} are the coefficients of the source expansion given by (102). The final set of independent linear equations required to find a solution for (104) is supplied by the boundary condition imposed on S. In the simple case of S having zero conductivity outside, $\partial V / \partial r = 0$ everywhere on S so that

$$u C_{uv} r^{u-1} - (u + 1) B_{uv} r^{-u-2} = 0 \quad (105)$$

where r is equal to the radius of S . Other boundary conditions on S are dealt with in §5.1.2.

It remains for me to deal with a more complicated arrangement of spherical boundaries than that depicted in Figure 5.2 and described above. An example is the model depicted in Figure 5.1. The procedure adopted in such cases is based on the integral equation (12) introduced in §2.1.3. The same procedure is used in the extended model presented in Chapter 6 (cf. §6.1.2) and is therefore not repeated here. The reader should note that some simplification of the extended model formulation is possible if the internal boundaries separating homogeneous regions are spherical.

§5.1.2 Surface admittance

Although the outer surface S of the model is spherical, the effects of realistic torso shapes can be assessed by postulating an admittance boundary condition on S . The admittance boundary condition is an approximate concept, which has proved very useful in radio science, microwave engineering and geophysics (cf. Wait, 1964, 1979). A simple example will suffice to introduce the use of the admittance condition. Consider how a bulge in the torso may be modelled. The current in the region of the bulge is (say) flowing in the direction of η , a coordinate defined tangential to S , and the bulge is centred at $\eta = \eta_0$. If the bulge were physically present, current would flow outwards over some range of $\eta < \eta_0$ and an equal amount would flow inwards over some range of $\eta > \eta_0$. The model therefore must permit a corresponding current flow through S , that is S must have non-zero "admittance". The boundary condition is chosen so that the resulting current streamlines follow the profile of the bulge being modelled.

The surface admittance on S is denoted by $\Lambda(\theta, \phi)$ and the boundary condition on S is specified as

$$\Lambda(\theta, \phi) = (\partial V(\underline{\xi}) / \partial r) / V(\underline{\xi}) \quad , \quad \underline{\xi} \in S \quad (106)$$

By forcing $\Lambda(\theta, \phi)$ to vary appropriately over S , arbitrary torso shapes can be approximated. To incorporate the boundary condition into the model computations, Λ is expanded as a multipole series with coefficients γ_{pq} . V and $\partial V / \partial r$ are expanded by (103) and the expansions are substituted in (106) after multiplying both sides by V . Thus

$$\begin{aligned} \sum_{u,v} (B_{uv} r^{-u-1} + C_{uv} r^u) Y_{uv}(\theta, \phi) \cdot \sum_{p,q} \gamma_{pq} Y_{pq}(\theta, \phi) \\ = \sum_{u,v} \left[u C_{uv} r^{u-1} - (u+1) B_{uv} r^{-u-2} \right] Y_{uv}(\theta, \phi) \end{aligned} \quad (107)$$

where r is put equal to the radius of S . Next, both sides of (107) are multiplied by a testing function $Y_{nm}(\theta, \phi)$ and integrated over S to give

$$\sum_{u,v} h_{uv} \sum_{p,q} \gamma_{pq} A_{nup}^{mvq} = d_{nm} \quad (108)$$

where
$$h_{uv} = B_{uv} r^{-u-1} + C_{uv} r^u$$

and
$$d_{nm} = n C_{nm} r^{n-1} - (n+1) B_{nm} r^{-n-2} .$$

The A_{nup}^{mvq} are the Adams dynamo integrals (cf. James, 1973) defined by

$$A_{nup}^{mvq} = \int_0^{2\pi} \int_0^{\pi} Y_{nm}(\theta, \phi) Y_{uv}(\theta, \phi) Y_{pq}(\theta, \phi) \sin\theta \, d\theta \, d\phi / 4\pi \quad (109)$$

Exact formulae for the efficient computation of the A_{nup}^{mvq} are found in James (1973).

Equation (108) represents an independent set of simultaneous linear equations relating the B_{nm} and C_{nm} . These, coupled with the sets of equations relating the expansion coefficients of the field in adjacent internal regions (as outlined in §5.1.1), are sufficient to solve for the B_{nm} and C_{nm} in terms of the B_{uv}' . The effective torso surface shape must then be found by plotting the current flow near S . It is not possible to analytically drive the effective surface shape using a non-zero admittance boundary condition. Therefore a torso shape cannot be specified exactly by this method, since the effective shape is also dependent on the details of the impressed sources and the internal variation in σ . However, for a wide range of surface admittance functions the effective shape is remarkably insensitive to variations in the source and body construction. This is illustrated in §5.2.2 by numerical examples.

The method of solution outlined above for the simple model is based on the expansion of the potential as a series of spherical harmonic functions as in (103). This series expansion is not an ideal description of the field in certain cases, because its convergence is either slow or questionable. Such a case is the discontinuity in the surface admittance

function apparently necessary to model a sharp effective boundary change. The two-dimensional study presented in Section 5.3 shows, however, that a sharp boundary change can be usefully approximated with the surface admittance technique.

5.2 APPLICATIONS OF THE SIMPLE MODEL

In this section the application of the simple model to the study of electrocardiographic sensitivity is illustrated. Only simple applications are presented, but they make clear the power and usefulness of the model. Two forms are used for the source representing the heart generator. The first form is a single current dipole located at a point. The second form used for the source is the spherical cap double layer of Frank (1953) (cf. §4.1.2). In the applications presented, the internal boundaries and surface admittance functions are chosen to be symmetrical about a particular axis and this reduces significantly the size of the matrix which must be inverted to solve for the surface field.

§5.2.1 Conductivity inhomogeneities

The first application of the simple model is shown in Figure 5.3. The interior of an insulating sphere S , of unit radius, is partitioned into two regions of different conductivity by a single spherical boundary with a radius of 0.5. The centre of the inner sphere is offset by 0.3 and the dipole source is offset by 0.55 from the centre of the outer sphere, and both lie on the axis $\theta = 0$ (θ is the polar angle). In Figure 5.3a the surface potential $V_S(\theta)$ is plotted for the dipole oriented along the axis $\theta = 0$. In Figure 5.3b the dipole is oriented perpendicular to the axis in the plane $\phi = 0$ and $V_S(\theta)$ is plotted for the same plane. In each case the conductivity of the inner region σ' takes a range of values (cf. Figure 5.3), while the region between the two boundaries has unit conductivity (i.e. $\sigma = 1$). In each case, the amplitude of the dipole source is scaled by $1/\sigma'$ to keep the amount of impressed current constant (cf. equation (8)).

Figure 5.3 shows that the surface potential field (compared to the homogeneous model, $\sigma' = \sigma$) is attenuated for $\sigma' > \sigma$ and amplified for $\sigma' < \sigma$, regardless of the orientation of the source. The shape of $V_S(\theta)$ is virtually unaffected by the presence of the inhomogeneity in this first example. The cases where $\sigma' > \sigma$ are clearly of most relevance to

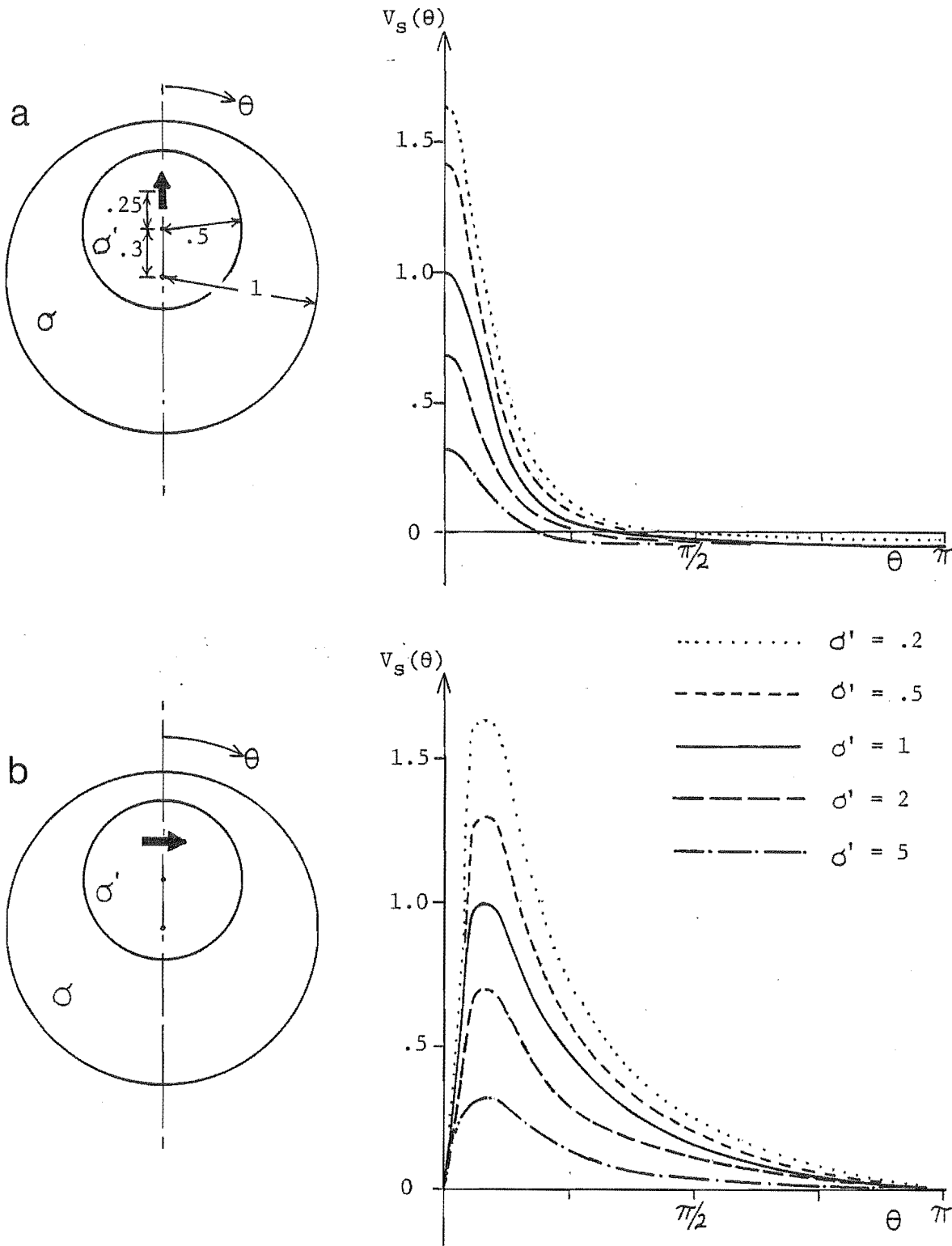


Figure 5.3 Model for the effect of a single region of different conductivity on the field of a dipole a) radially oriented, b) tangentially oriented.

the E.C.G., as the blood within the heart and the great vessels has a higher conductivity than the surrounding tissues (cf. Table 2.2). For $\sigma' = 2\sigma$, the field of the radial dipole (cf. Figure 5.3a) is attenuated by 31% in peak-to-peak amplitude, while the field of the tangential dipole (cf. Figure 5.3b) is attenuated by 34%.

In Figure 5.4 the effect of a thin, uniform shell of different conductivity, just inside S, is illustrated. The shell is 0.1 thick and its conductivity σ takes a range of values. The conductivity σ' of the inner region is fixed at unity. The dipole source is positioned on the axis $\theta = 0$ and is offset by 0.7 from the centre of the spherical boundaries in all cases. In Figure 5.4a the dipole is oriented along the axis, while in Figure 5.4b it is oriented perpendicular to the axis in the plane $\phi = 0$.

The surface fields of both the radially and tangentially oriented dipoles are attenuated for $\sigma > \sigma'$ (i.e. a shell of relatively high conductivity) and amplified for $\sigma < \sigma'$ (i.e. a shell of relatively low conductivity). The former effect can be interpreted as the field being "shorted" by the shell: in the limit as σ tends to infinity, no variation in potential will occur on S. Conversely as σ becomes small, the outer boundary is effectively moved inwards, because little current then flows in the shell. The "move inwards" of the outer boundary brings it nearer the source, so V_S increases in peak-to-peak amplitude. A secondary effect of the shell is a slight change in the shape of $V_S(\theta)$, which makes the source dipole appear to be in a different position. For $\sigma > \sigma'$, the source dipole appears to be closer to the centre, while for $\sigma < \sigma'$, the source dipole appears to be more offset from the centre.

In Figure 5.5, a Frank double layer source (cf. §4.1.2) is specified in a model which is otherwise the same as Figure 5.3a. The double layer is in the form of a uniform spherical cap with a rim which is 0.35 in radius and which is offset by 0.3 from the centre of the inner boundary. The conductivity of the inner region again takes various values greater and less than the conductivity of the outer region.

The plots on the right-hand side of Figure 5.5 show that the peak-to-peak amplitude of $V_S(\theta)$ is changed by the presence of the inhomogeneity, but the shape of $V_S(\theta)$ is not changed significantly. For $\sigma' > \sigma$, V_S is attenuated, while for $\sigma' < \sigma$, V_S is amplified. Note that the field of the spherical cap double layer source is less peaked at the positive maximum than the field of a dipole in a similar position (cf. Figures 5.3a and 5.5).

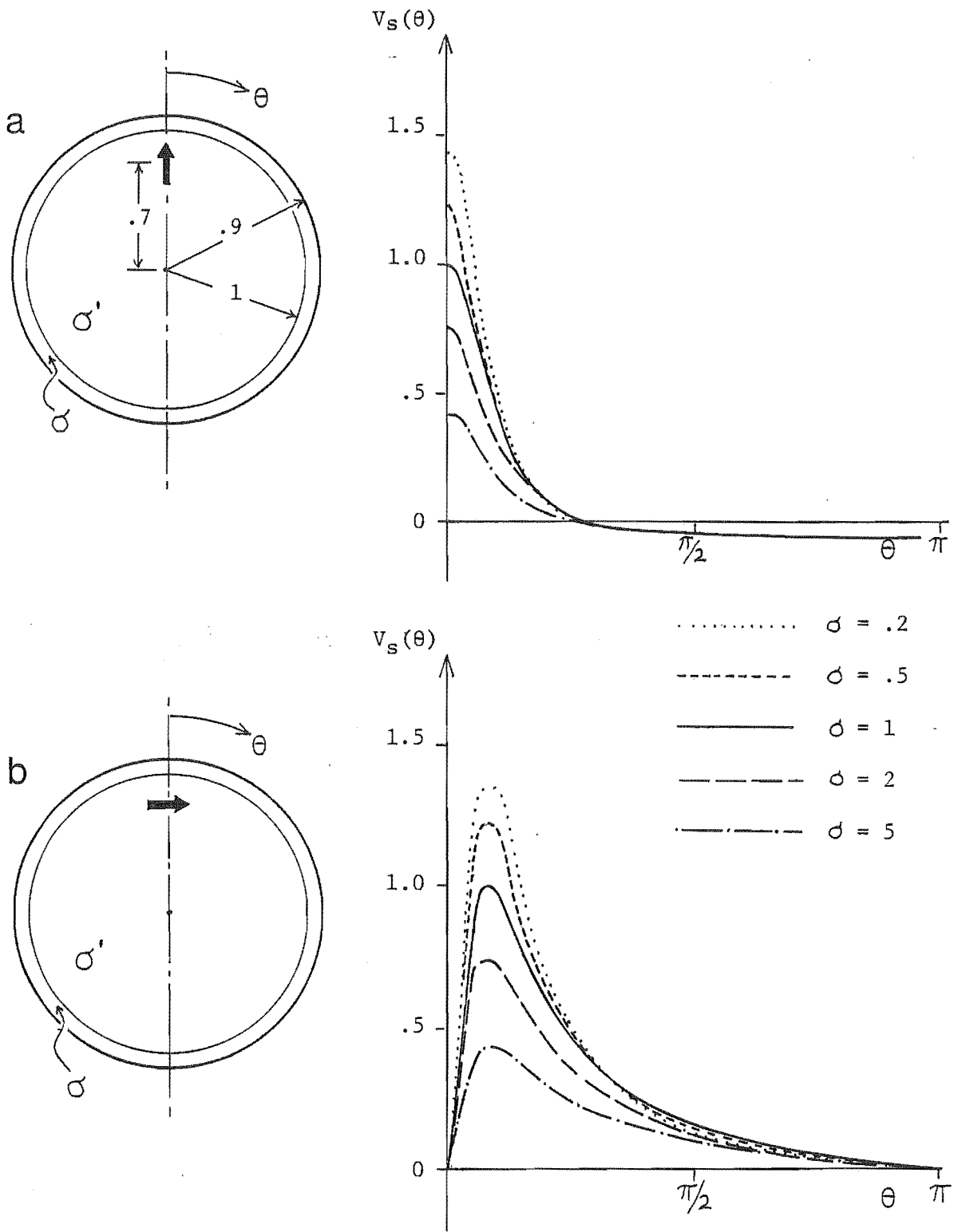


Figure 5.4 Model of the effect of a thin, uniform shell of different conductivity. a) Dipole source oriented radially, b) dipole source oriented tangentially.

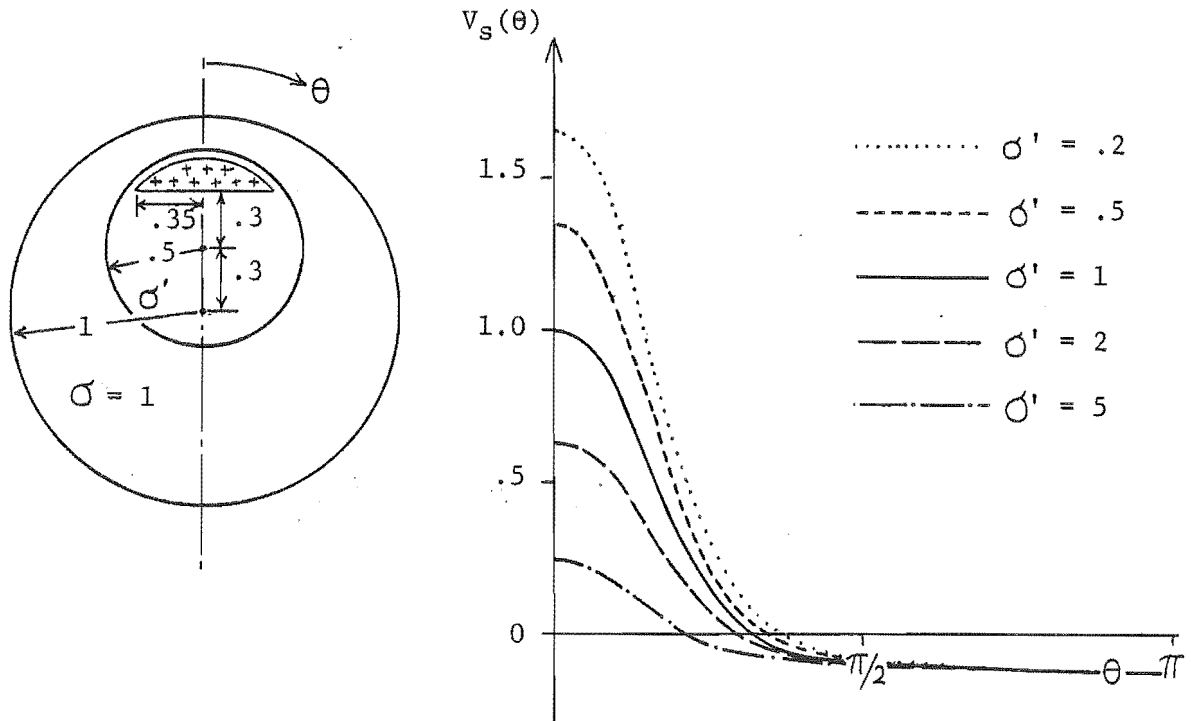


Figure 5.5 The effect on the field of a spherical cap dipole layer source on the spherical conductivity inhomogeneity shown (cf. Figure 5.3a).

The next applications of the simple model are presented in Figures 5.6 and 5.7. Two possible mechanisms for the effect of respiration on the E.C.G. are tested, by postulating a "torso" with three homogeneous regions. The innermost region (with $\sigma' = 2.5$) represents the heart and major vessels and contains the source. The next region represents the lung tissue and has conductivity σ'' . In the first case (i.e. Figure 5.6), σ'' is given various values, while all the other parameters of the model are kept constant. In the second case (i.e. Figure 5.7), the size of the lung region is altered, while all the other parameters are kept constant ($\sigma'' = 0.2$). In both cases, the outermost region has unit conductivity.

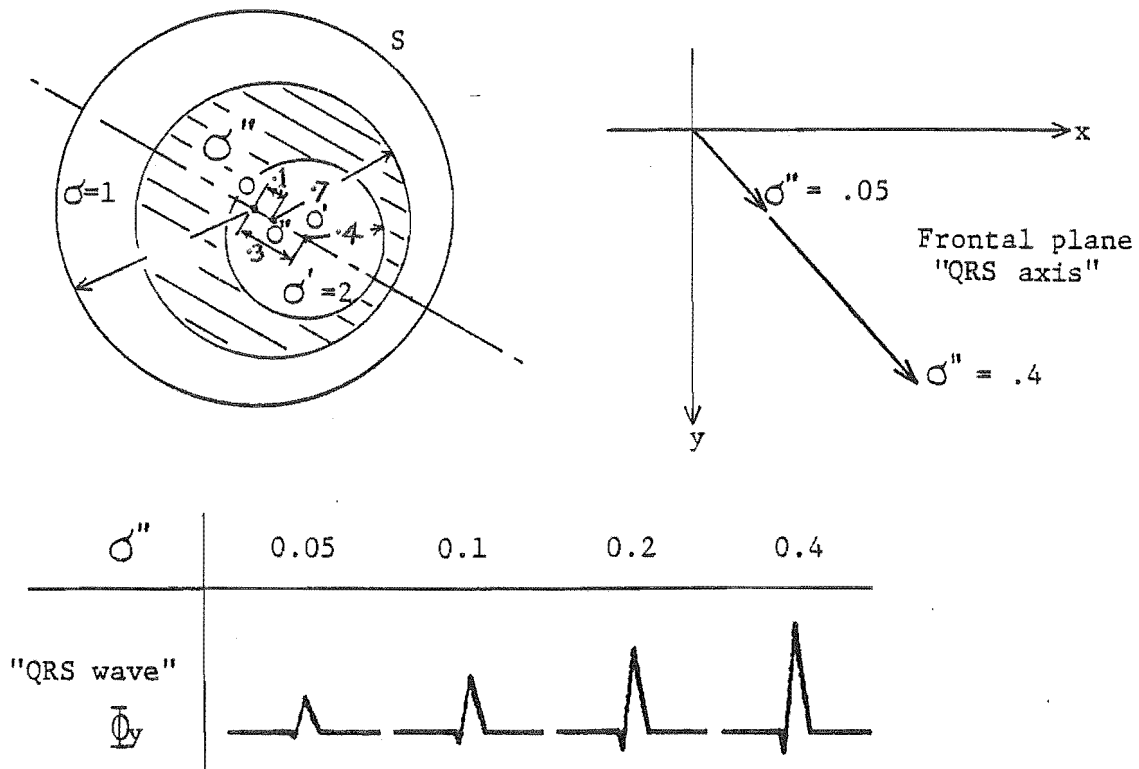


Figure 5.6 Model of the effect of respiration on the basis of the conductivity of lung tissue changing (cf. Figure 5.7).

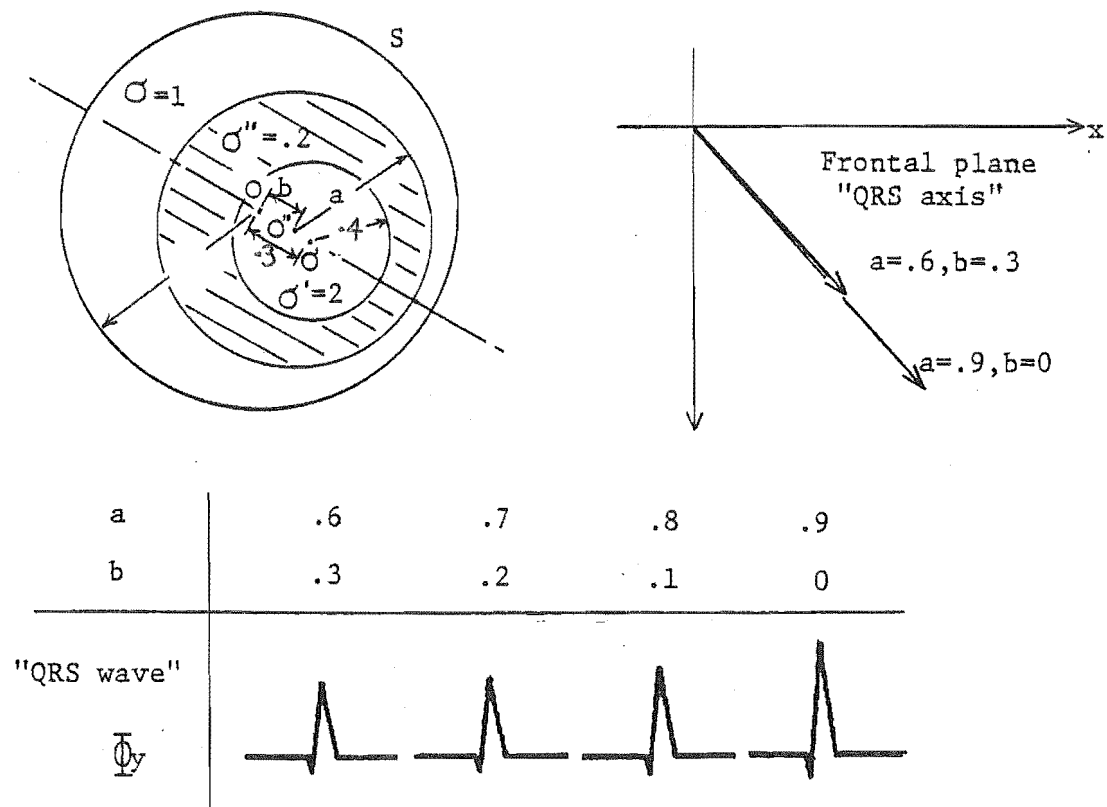


Figure 5.7 Model of the effect of respiration on the basis of the size of the lung region changing (cf. Figure 5.6).

The boundaries are symmetric about the axis $\theta = 0$. Seven positions were chosen on S to correspond approximately to the positions of the electrodes of the Frank E.C.G. lead system (cf. §3.2.1), relative to the axis $\theta = 0$. The lead voltages Φ_x , Φ_y and Φ_z were then computed from the model for each of three source dipoles, which represent early, mid and late ventricular activation respectively (cf. §1.3.2). In Figure 5.6b, the frontal plane "vector" (cf. Section 3.2) is plotted for $\sigma'' = 0.05$ and for $\sigma'' = 0.4$. Similarly, in Figure 5.7b the frontal plane vector is plotted for the largest and smallest "lung" regions considered. In Figures 5.6c and 5.7c the "QRS wave" of lead Φ_y is plotted for each arrangement of the lung region.

As the conductivity of the "lung" increases, the amplitude of the E.C.G. field is increased (cf. Figure 5.6c) according to the simple model. The same changes have little effect on the direction of the frontal plane vector (cf. Figure 5.6b). The effect on the E.C.G. field of changing the size of the lung region is to increase its amplitude as the size is increased. The effect is most marked when the outer lung boundary is closest to S (cf. Figure 5.7c). Again, these changes have an insignificant effect on the frontal plane vector of the field, as can be seen in Figure 5.7b.

§5.2.2 Surface shape

The application of the simple model to the study of the effects of changes in the body surface shape is now illustrated. In Figure 5.8, the outer insulating boundary of a homogeneous sphere is deformed in the vicinity of $\theta = 0$. Four examples are given, as shown on the left of Figure 5.8. The source dipole in each example is either oriented along the axis $\theta = 0$ or perpendicular to the axis in the plane of $\phi = 0$. The boundary deformation is either a "dent" or a "bulge". On the right of Figure 5.8, the resulting surface potential functions $V_s(\theta)$ are plotted, both for each effective surface shape (solid line) and for the corresponding homogeneous sphere (dotted line). The admittance boundary conditions $\Lambda(\theta)$, used to produce the effective shapes, are also plotted. The approximate analytic expressions for $\Lambda(\theta)$ and for the effective torso surfaces (specified by the radius of the surface $r_s(\theta)$) are listed in Table 5.1.

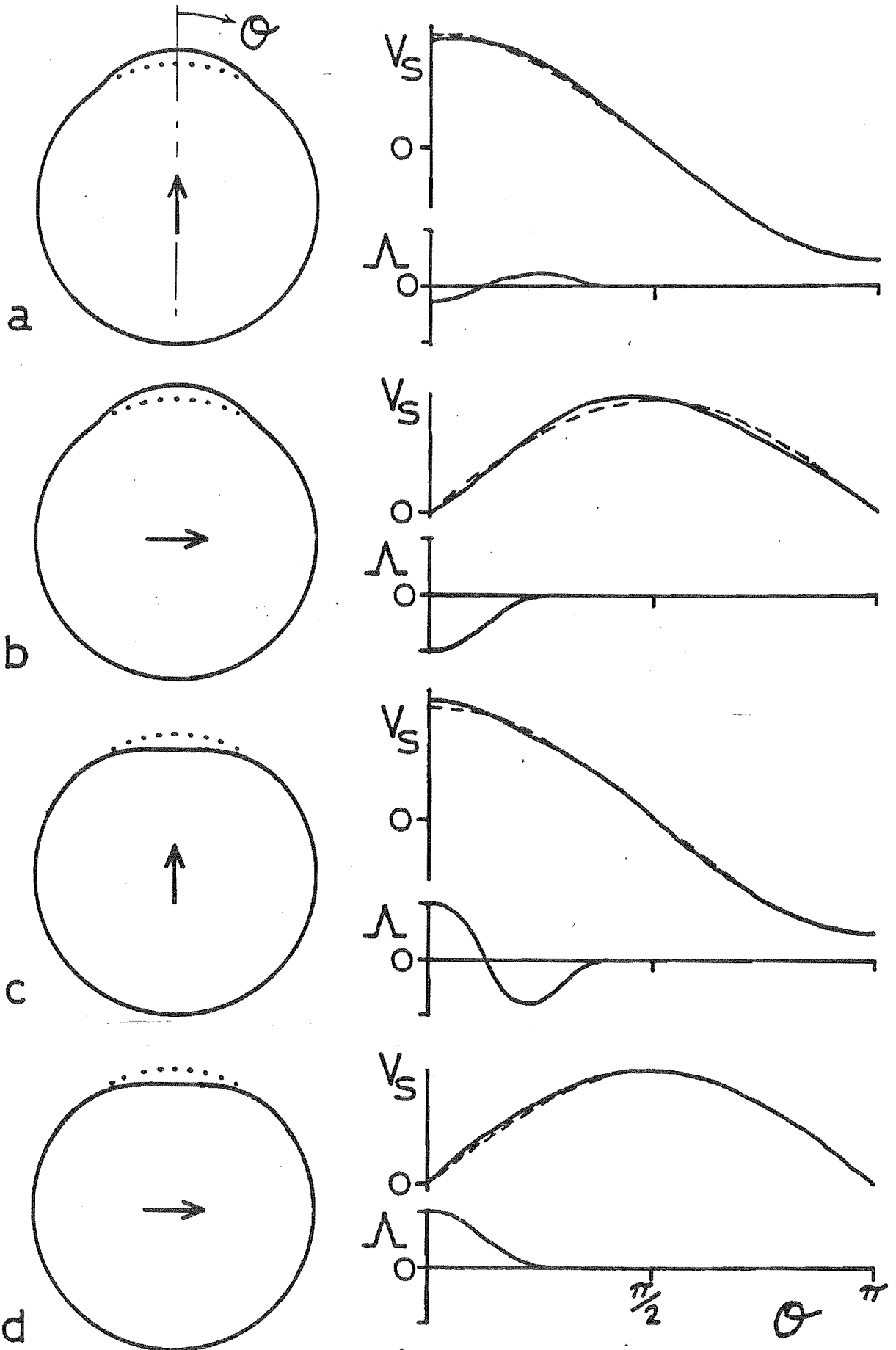


Figure 5.8 The application of the simple model to homogeneous conducting spheres deformed near $\theta = 0$. $V_S(\theta)$ is plotted with (solid lines) and without (dashed lines) the boundary alteration. Approximate analytic expressions for $\Lambda(\theta)$ and the effective surface radius $r_S(\theta)$ are listed in Table 5.1.

TABLE 5.1 Analytic expressions for the surface admittance $\Lambda(\theta)$ and the (approximate) effective surface radius $r_s(\theta)$ over the range of θ specified. Over the range of θ not specified, $\Lambda = 0$ and $r_s = 1$. θ is expressed in radians.

Figure	$\Lambda(\theta)$	$r_s(\theta)$
5.8a	$-(\cos 4\theta)/4$, $\theta < 1.18$	$1.044 + 0.022 \cos(3.92\theta)$, $\theta < 0.8$
5.8b	$-(\cos 4\theta + 1)$, $\theta < 0.79$	$1.028 + 0.028 \cos(5.24\theta)$, $\theta < 0.6$
5.8c	$\cos 4\theta$, $\theta < 1.18$	$0.949 - 0.051 \cos(5.24\theta)$, $\theta < 0.6$
5.8d	$(\cos 4\theta + 1)/2$, $\theta < 0.79$	$0.975 - 0.025 \cos(3.92\theta)$, $\theta < 0.8$
5.9a	$-(\cos 4\theta + 1)$, $0.79 < \theta < 2.36$	$1.062 + 0.062 \cos 4\theta$, $0.79 < \theta < 2.36$
5.9b	$-(\cos 4\theta)/8$, $0.39 < \theta < 2.75$	$1.044 + 0.044 \cos 4\theta$, $0.79 < \theta < 2.36$
5.9c	$(\cos 4\theta + 1)$, $0.79 < \theta < 2.36$	$0.940 - 0.060 \cos 4\theta$, $0.79 < \theta < 2.36$
5.9d	$-(\cos 6\theta)$, $0.79 < \theta < 2.36$	$0.922 - 0.078 \cos 4\theta$, $0.79 < \theta < 2.36$

Figure 5.9 illustrates the application of the simple model to an homogeneous conducting sphere with the outer surface modified in the region of $\theta = \pi/2$ (i.e. the equator). In each of the four cases shown, the boundary is symmetric about the axis $\theta = 0$ and a single dipole source is positioned as indicated by the arrows. $V_S(\theta)$ is again plotted with (solid lines) and without (dashed lines) the alteration in the surface shape. The approximate analytic expressions for $\Lambda(\theta)$ and $r_s(\theta)$ are listed in Table 5.1.

It is clear from Figures 5.8 and 5.9 that $V_S(\theta)$ is affected noticeably by the changes in surface shape modelled. Although the maximum change in potential at any point is never large (less than 10% of the maximum excursion of V_S over S), the gradient of V_S can be altered appreciably, as is illustrated particularly by the cases a and b in Figure 5.9. In general, a movement of the surface away from the source causes a decrease in the surface potential in the neighbourhood of the change (and vice versa), which might be expected from the nature of the dipole field (cf. equation (43)).

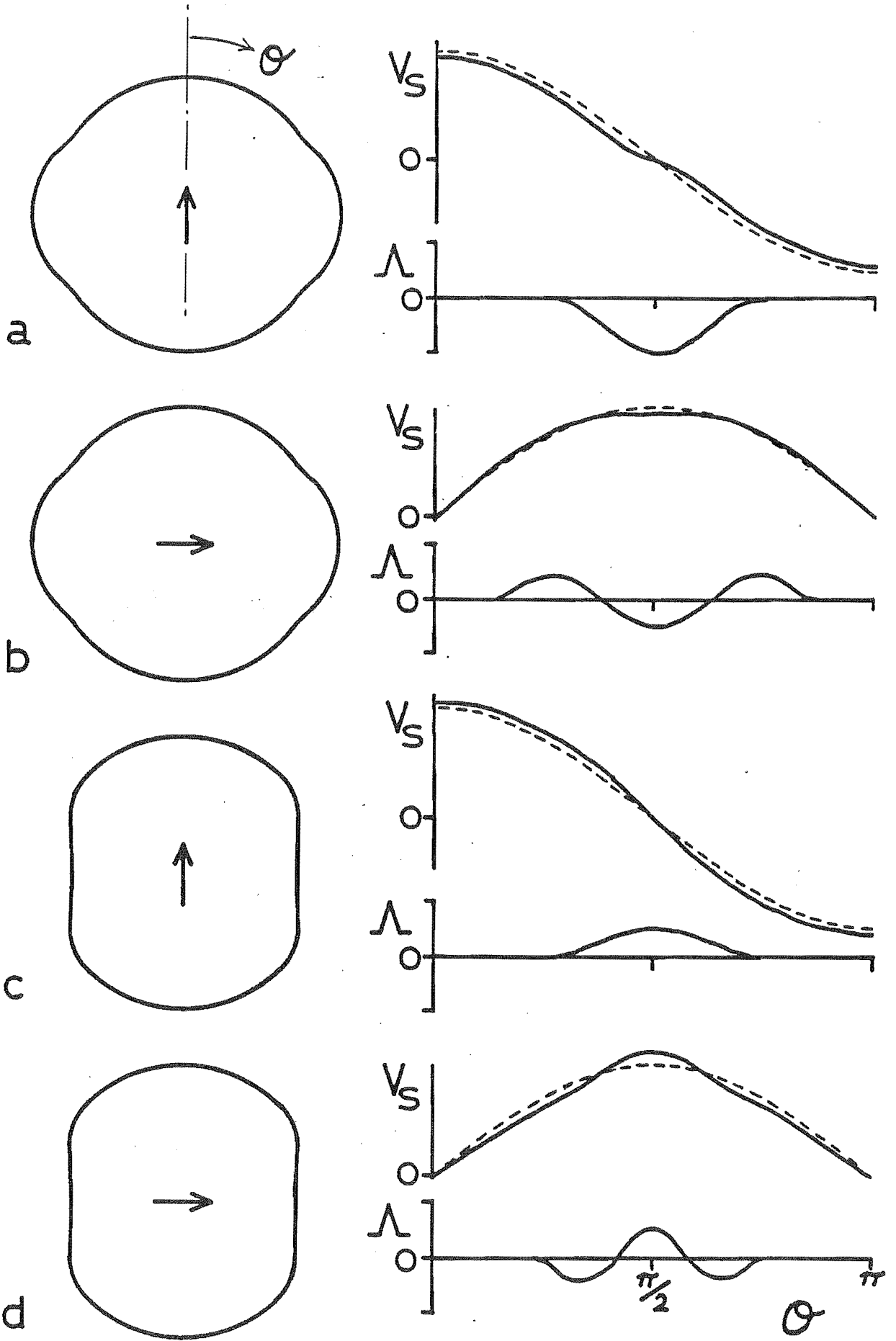


Figure 5.9 Application of the simple model to homogeneous conducting spheres deformed near $\theta = \pi/2$. $V_S(\theta)$ is plotted with (solid lines) and without (dashed lines) the boundary alteration (cf. Figure 5.8 and Table 5.1).

The above examples (i.e. Figures 5.8 and 5.9) show that the effective boundary surface depends to some degree on the source distribution. Figure 5.10 illustrates, however, that the effective shape is remarkably insensitive to changes in the source.

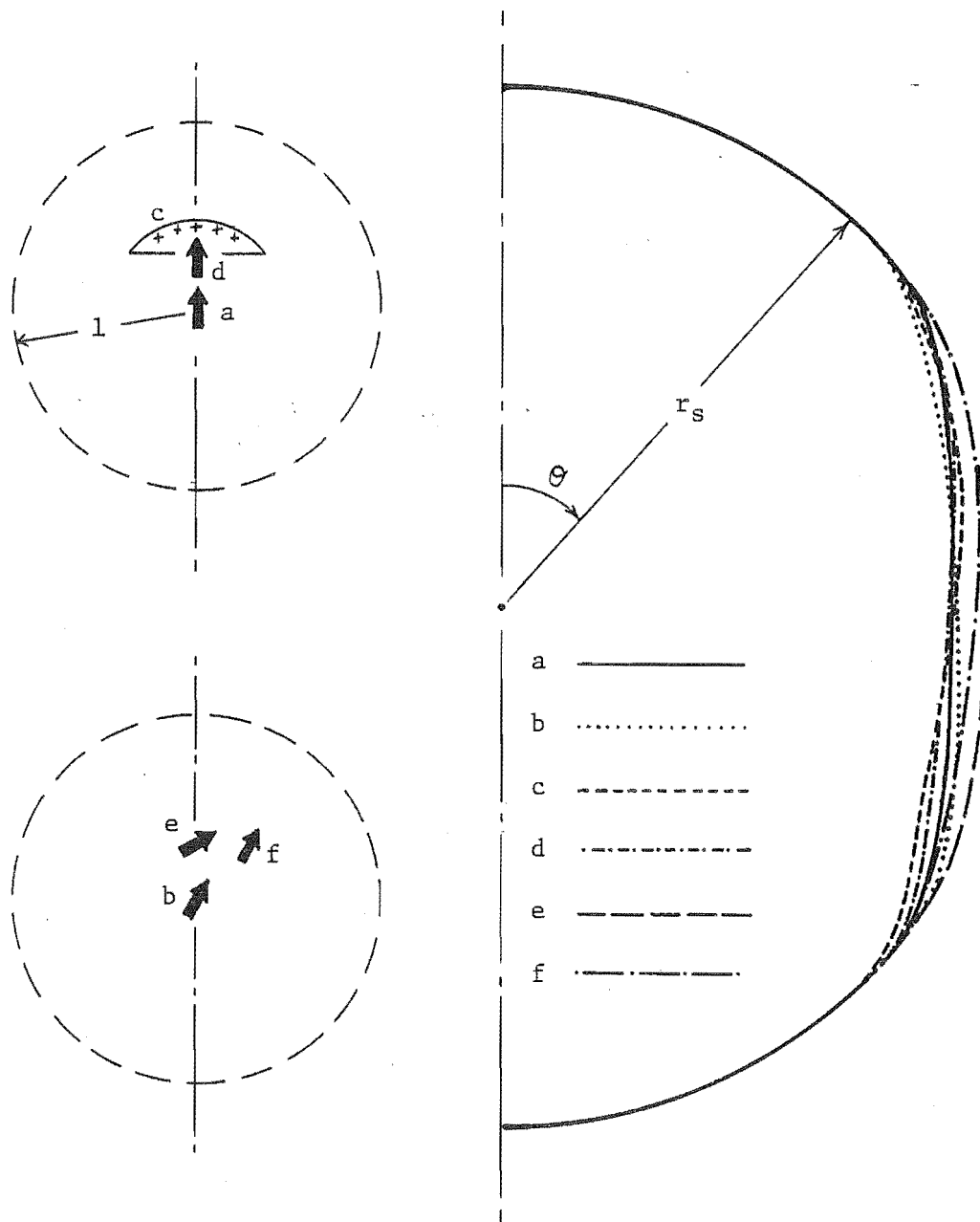


Figure 5.10 The effective surface shape generated by the surface admittance function $\Lambda(\theta) = (\cos 4\theta + 1)$ with six different source specifications.

Figure 5.10 relates to a single admittance condition and six different source distributions. The admittance condition is

$$\Lambda(\theta) = \cos 4\theta + 1, \quad \pi/4 \leq \theta \leq 3\pi/4 \quad (110)$$

with $\Lambda(\theta) = 0$ outside the range specified in (110). The six source distributions are: a) a dipole at $(0,0,0)$ directed along the axis $\theta = 0$; b) a dipole at $(0,0,0)$ directed at an angle $\pi/6$ from the axis; c) a Frank spherical cap (cf. §4.1.2), offset by 0.3 and with a rim diameter of 0.35; d) a dipole at $(0.25,0,0)$ directed along the axis; e) a dipole at $(0.3,0,0)$ directed at an angle $\pi/3$ from the axis; and f) a dipole at $(0.4,\pi/4,0)$ directed at $\pi/6$ from the axis. On the right-hand side of Figure 5.10, the effective surface shape for each combination of the source and the admittance boundary condition is plotted in the plane $\phi = 0$. The effective surfaces for the sources a, c and d are axially symmetric, while those for the sources b and e are anti-symmetric about the plane $\phi = \pm\pi/2$. The effective surface for the source f is asymmetric.

§5.2.3 Computational details

All of the model computations presented in this section were performed on a PDP 11/10 minicomputer with 24K 16-bit words of memory and two 2.4M byte cartridge disks. The multipole series used to represent the potential and the surface admittance function had a maximum order N of 15 (i.e. the coefficients of the higher order terms were assumed to be zero). In the multipole expansions of the dipole and the spherical cap sources, only those coefficients of degree $m = 0$ and $m = 1$ are non-zero (cf. equation (38)). Because the boundary surfaces and the admittance boundary conditions specified in §5.2.1 and §5.2.2 are symmetric about the axis $\theta = 0$, no coupling occurs between coefficients of different degree (cf. equations (99), (100) and (108)). Therefore only those coefficients with $m = 0$ and $m = 1$ had to be computed in the solutions presented above.

The sets of simultaneous equations (104) and (105) or (108) were solved for the expansion coefficients B_{nm} and C_{nm} by matrix inversion. The Gauss-Jordan inversion method (cf. Hildebrand, 1974) was used (the computer program was based on the I.B.M. MINV subroutine). The maximum size of the matrix which had to be inverted (to solve to the 15th order) was 16×16 . I found it necessary to compute the matrix elements with

double precision (2x4-byte) arithmetic.

The convergence of the solutions was checked by repeating the computations with $N < 15$. If the change in V_s was negligible when N was reduced from 15 to (say) 14, the solution was assumed to have converged. Two examples of the convergence behaviour observed with the simple model are shown in Figures 5.11 and 5.12. A mean square error function is defined by

$$\text{MSE}(N) = \frac{\iint_S \left[V_s^{(15)} - V_s^{(N)} \right]^2 dS}{\iint_S \left[V_s^{(15)} \right]^2 dS} \quad (111)$$

where $V_s^{(N)}$ is the solution found to the Nth order. Consider the model shown in Figure 5.11a. $\text{MSE}(N)$ is plotted as a percentage in Figure 5.11b for the parameters shown. It is clear that convergence has been achieved and that there is little point in computing any higher order terms for this model.

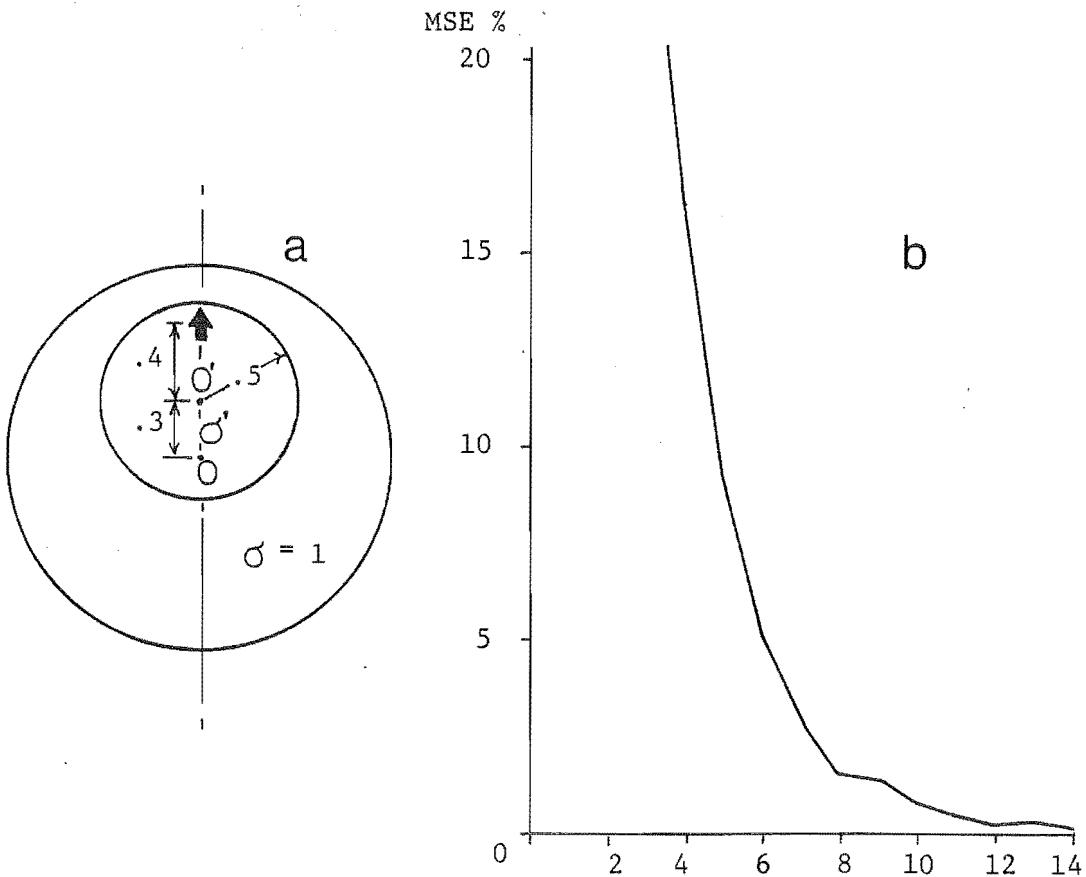


Figure 5.11 Convergence of the solution V_s of the model depicted in a). $\text{MSE}(N)$, defined by (111), is shown plotted against N in b).

The number of terms which must be included in the potential expansions to achieve satisfactory convergence of the solution is clearly dependent on the geometry of the model. When the source dipole and/or the internal spherical boundaries are eccentrically positioned, a larger number of expansion terms are necessary to achieve convergence than if they are symmetrically positioned. For example, for the model depicted in Figure 5.12, the number of expansion terms necessary to achieve convergence (defined as $MSE(N) \leq 1\%$) is plotted against the eccentricity of the single internal boundary. The source dipole is offset by 0.4 from O' and it is directed along $\theta = 0$. The radius of the internal boundary S' is fixed at 0.5 and the offset of O' from O is denoted c . The conductivities σ' and σ are 5.0 and 1.0 respectively. Figure 5.12b shows that as the eccentricity of the source/inhomogeneity combination is increased, so must the number of expansion terms. When the source and inhomogeneity are brought close to S ($c > 0.3$), the number of terms required for convergence increases rapidly.

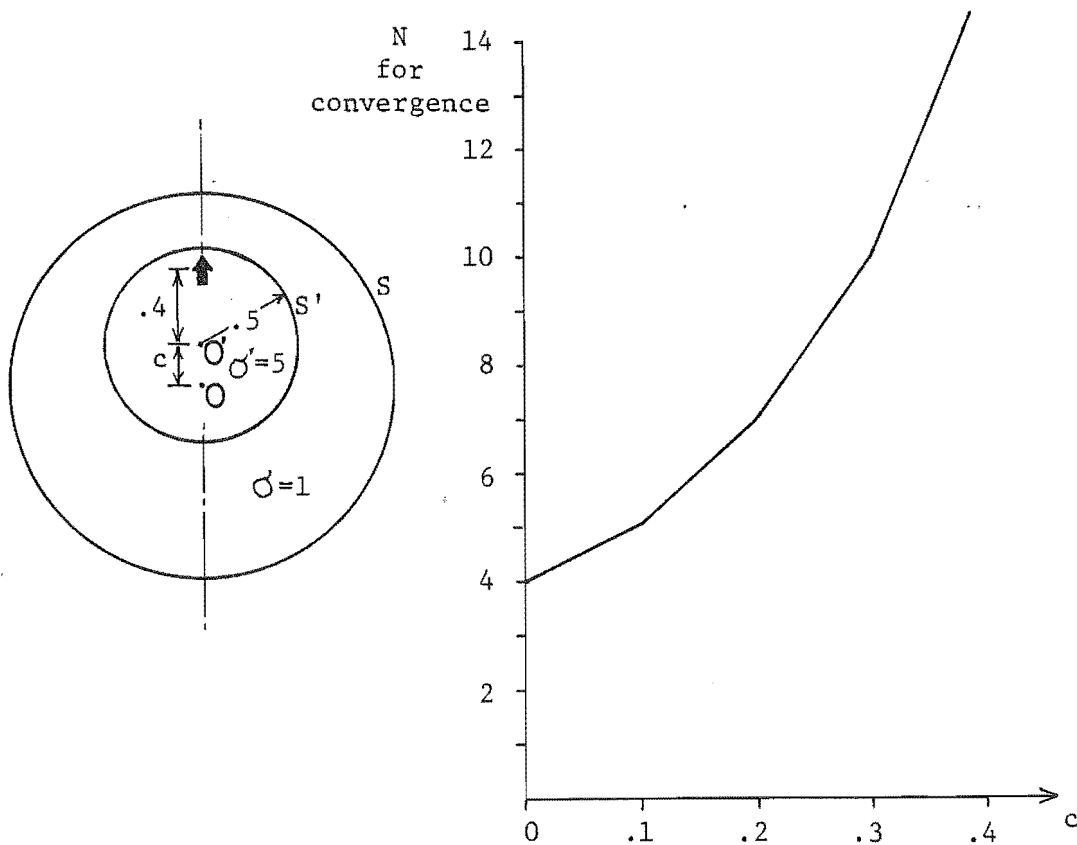


Figure 5.12 The effect of boundary and source eccentricity on the convergence of the solution for the simple model.

5.3 TWO-DIMENSIONAL STUDY OF A SHARP BOUNDARY CHANGE

The results presented in §5.2.2 illustrate the usefulness of the surface admittance boundary condition in modelling gradual changes in torso shape. The real torso of course includes surface features which change sharply. Of particular importance are the limbs and head. Previous investigators who have modelled "realistic" torsos (e.g. Cuffin and Geselowitz, 1977; Rush, 1971; Frank, 1954b) have "cut off" the limbs and head, assuming these to have negligible effect on the E.C.G. The experimental observation that moving the limbs or head has negligible effect on the measured electrocardiographic field tends to support this view. However, a model of a "limb" is presented in this section to provide a more objective assessment of these effects. At the same time, the limb model illustrates how well the surface admittance method can account for sharp changes in the body surface.

The limb modelling is carried out in two dimensions because an exact field mapping technique is then available - conformal mapping. The results of the approximate surface admittance method can thus be checked against the exact solution.

The limb model is shown in Figure 5.13. A straight homogeneous conducting channel, of width a and extending to infinity in the $+x$ and $-x$ directions, represents the torso. A source of current and an equal sink of current are situated at $x = +\infty$ and $x = -\infty$ respectively. The current is uniformly distributed across the channel at infinity so that, if the channel was uniform along its total length, the potential would be given by $V = x$ at any point inside the channel. At $x = 0$ a second channel, with the same conductivity and of width $2b$, adjoins the first and extends to $y = -\infty$. This second channel represents the limb. The channels are surrounded by an insulating medium.

I have chosen this particular model for two reasons. Firstly, the symmetrical arrangement of straight rectangular boundaries is conveniently handled by both the conformal mapping and surface admittance methods. Secondly, the current arising from the activation of the heart flows approximately parallel to the skin surface in the regions underlying most of the real torso surface. Only under those regions of the torso surface where a maximum or minimum of potential occurs is there a significant component of current normal to the surface. Therefore it is quite realistic to study the effects of the model "limb" on a flow of

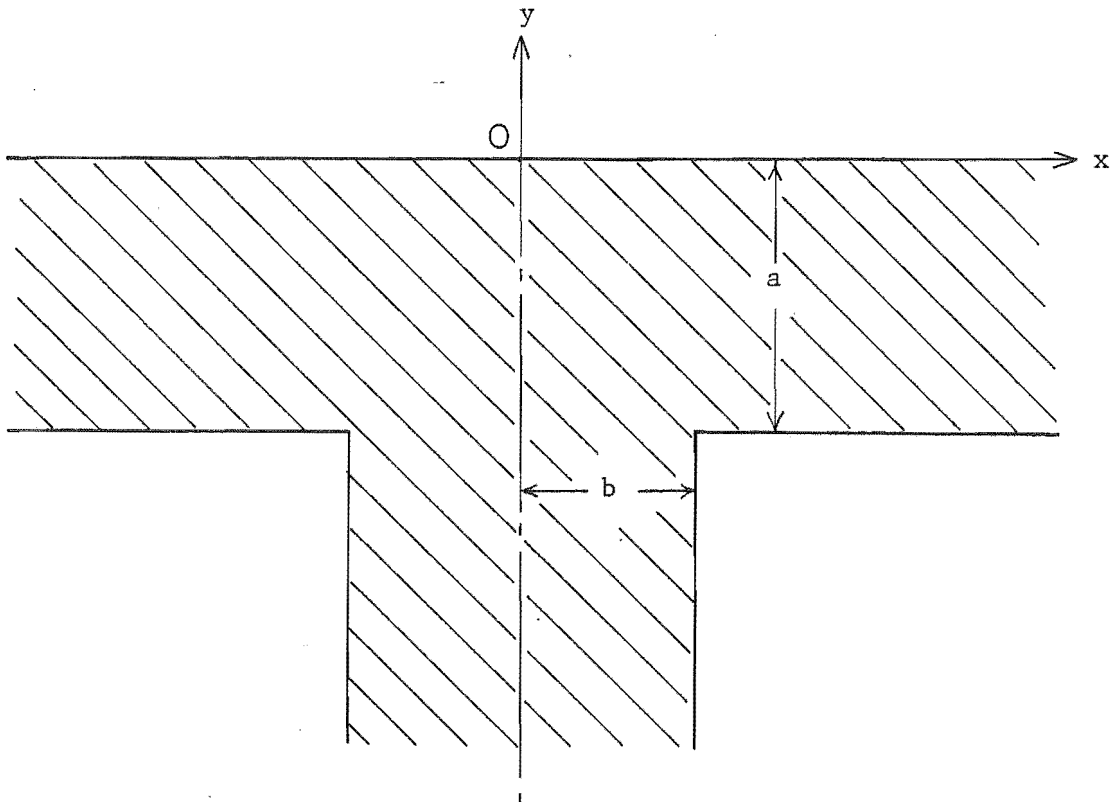


Figure 5.13 The two-dimensional limb model. The model is symmetric about the y-axis. The "limb" extends to $y = -\infty$, the "torso" extends to $x = \pm\infty$.

of current which is forced to flow parallel to the surface of the model "torso".

In §5.3.1 and §5.3.2 the application of the conformal mapping and surface admittance methods to the limb model are discussed. The results of both methods are presented in §5.3.3.

§5.3.1 Conformal mapping

A method of mapping the interior of a polygonal region upon the upper half of the complex plane was developed independently by Schwarz and Christoffel (cf. Weber, 1950). Their method is now known as the Schwarz-Christoffel (S-C) transformation. The potential field of the limb model depicted in Figure 5.13 is found by two S-C transformations. The first is depicted in Figure 5.14a and the second in Figure 5.14b.

Initially, a uniform complex potential field is set up in a channel of width a , extending from $x' = 0$ to $x' = +\infty$ in the z' complex plane (cf. Figure 5.14a). Since the model is symmetric about the y' -axis, only the right half of the z' plane is treated.

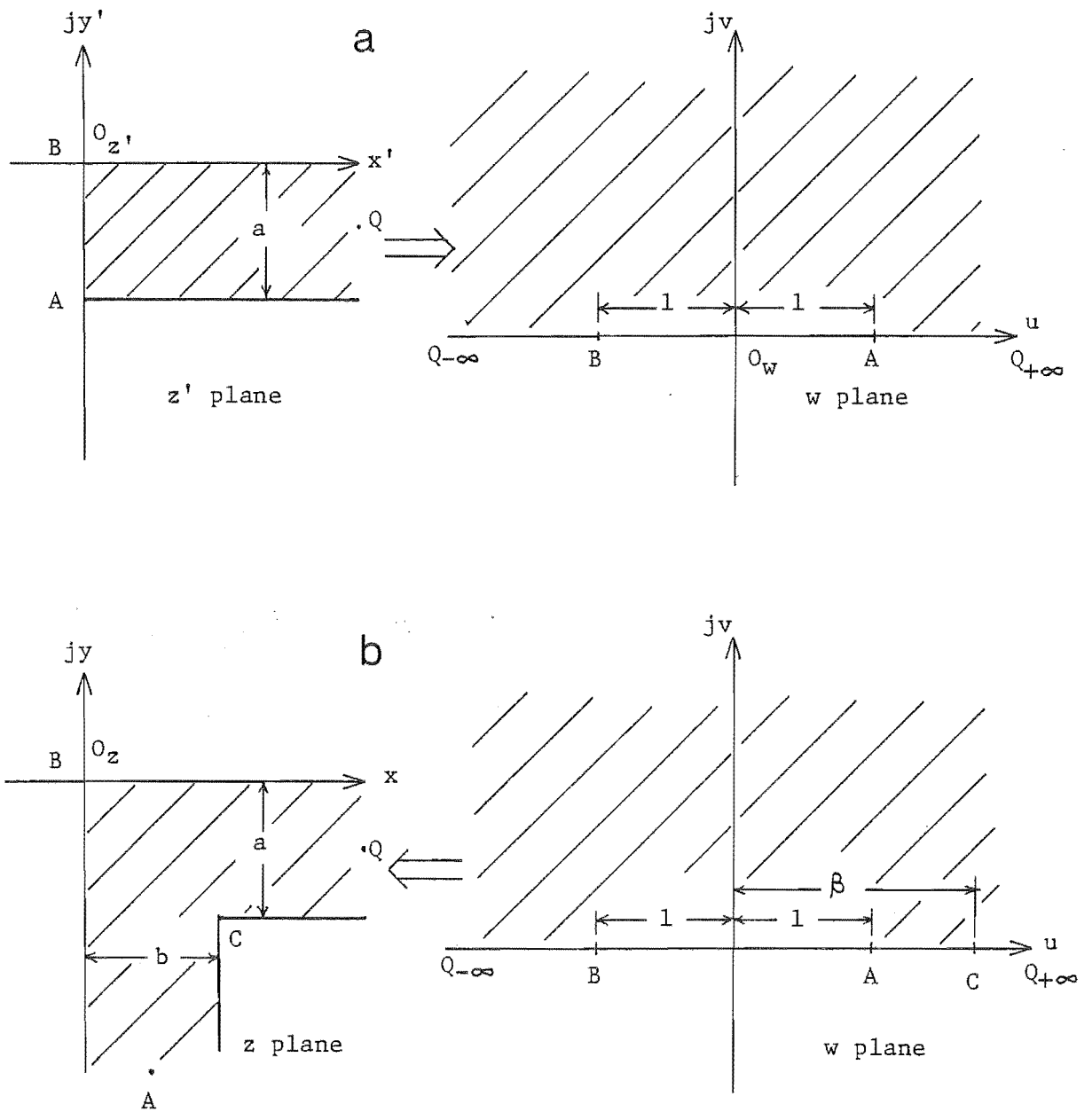


Figure 5.14 The two Schwarz-Christoffel transformations necessary to solve the limb model.

The potential within the channel is given by

$$V(z') = x' \quad , \quad -a \leq y' \leq 0 \quad (112)$$

The S-C transformation maps the interior of the right half channel in the z' plane onto the entire upper half of the w complex plane (cf. Figure 5.14a). The point 1 in the w plane represents the corner at the point

$-ja$ in the z' plane. The point -1 in the w plane represents the corner at the point 0 in the z' plane. The appropriate mapping function (Weber, 1950) is found by integrating

$$dz'/dw = C_1 (w^2 - 1)^{-\frac{1}{2}}$$

where C_1 is a constant to be evaluated. Integration gives

$$z' = C_1 \cosh^{-1}(w) + C_2 \quad (113)$$

where C_2 is another constant. Equating the left and right sides of (113) at the points $w = \pm 1$ gives

$$\begin{aligned} 0 &= C_1 \cosh^{-1}(-1) + C_2 \\ -ja &= C_1 \cosh^{-1}(+1) + C_2 \end{aligned}$$

from whence C_1 and C_2 are found. Substituting for C_1 and C_2 and inverting (113) gives finally

$$w = \cosh((z' + ja)\pi/a) \quad (114)$$

The second transformation maps the entire upper half of the w plane onto the right half of the z complex plane (cf. Figure 5.14b). The point β in the w plane represents the corner at the point $b - ja$ in the z plane (where the "limb" meets the "torso"). Symmetry about the y -axis requires that only the right half of the z plane need be treated. The S-C transformation in this case is given by (Weber, 1950)

$$dz/dw = C_3 (w - \beta)^{\frac{1}{2}} (w - 1)^{-1} (w + 1)^{-\frac{1}{2}}$$

which can be integrated to give

$$\begin{aligned} z &= C_3 \sqrt{2(\beta - 1)} \tan^{-1} \left[\frac{\sqrt{(\beta - 1)(w + 1)}}{(2w - 2\beta)} \right] + C_3 \ln \left[\frac{\sqrt{(w + 1)/(w - \beta)} + 1}{\sqrt{(w + 1)/(w - \beta)} - 1} \right] \\ &\quad - C_3 \ln \left[\frac{\sqrt{(w + 1)/(w - \beta)} - 1}{\sqrt{(w + 1)/(w - \beta)} + 1} \right] + C_4 \end{aligned} \quad (115)$$

where β , C_3 and C_4 are constants which must be evaluated. Equating the left and right sides of (115) at the points $w = \pm 1$ and $w = \beta$ gives

$$\begin{aligned} \beta &= 1 + 2b^2/a^2 \\ C_3 &= -\pi/a \\ C_4 &= -ja \end{aligned} \quad (116)$$

Thus these two S-C transformations map the uniform potential field in a uniform infinite channel onto the non-uniform potential field in the limb model. The lines of constant potential in the limb model are found by mapping the lines $x' = k$, where k is a constant, in the z' plane onto the z plane. Similarly the current streamlines are found by mapping the lines $y' = k$ in the z' plane onto the z plane. Some illustrative results are presented in §5.3.3.

§5.3.2 Surface admittance method

The surface admittance boundary condition method is now used to find an approximate solution for the limb model. Only the field within the torso channel and on the torso surface ($y = -a$) is considered since it is the effect of the "limb" on this field which is of interest. Three steps are carried out:

- (1) An analytic function which is consistent with the physical layout of the model is chosen to represent the potential field within the torso channel.
- (2) The analytic function is forced to satisfy an appropriate admittance boundary condition along the surface of the torso channel onto which the "limb" adjoins.
- (3) An approximate solution is found for the potential within the torso channel (and this is compared to the conformal mapping solution).

The potential field within the homogeneous conducting region depicted in Figure 5.13 obeys the Laplace equation $\nabla^2 V = 0$. The method of separating variables (Weber, 1950; Stratton, 1941) yields solutions to the Laplace equation of the form $V = X(x)Y(y)$, where

$$\begin{aligned} \partial^2 X / \partial x^2 &= -\alpha^2 X \\ \text{and} & \\ \partial^2 Y / \partial y^2 &= \alpha^2 Y \end{aligned} \tag{117}$$

and where α takes any real or imaginary value. The field within the torso channel is governed by several boundary conditions (cf. Figure 5.13):

- (1) The model is symmetric about the y -axis, therefore

$$V(0, y) = 0 \tag{118a}$$

- (2) No current may flow across the boundary at $y = 0$, therefore

$$\partial V/\partial y = 0 \quad , \quad y = 0 \quad (118b)$$

(3) As $|x|$ becomes large, the field across the channel becomes uniform, therefore

$$\partial V/\partial x = 1 \quad , \quad |x| \text{ large} \quad (118c)$$

The functions $X = \sin\alpha x$ and $Y = \cosh\alpha y$, for α real, explicitly satisfy the first two of the boundary conditions (118) and the two second order differential equations (117). The analytic expression

$$V = x + \int_0^{\infty} H(\alpha) \sin\alpha x \cosh\alpha y \, d\alpha \quad (119)$$

is therefore suitable to represent the potential in the torso channel. In equation (119), the integral accounts for the perturbation of the field by the "limb", while the first term on the right-hand side explicitly satisfies (118c). Because both of the functions in x on the right-hand side of (119) are odd, this expression also has the correct property of antisymmetry about the y -axis.

The second step is to apply an admittance boundary condition $\Lambda(x)$ on the surface $y = -a$ (i.e. along the outer "torso" surface and across the base of the "limb"). The form that $\Lambda(x)$ must take to simulate the effect of the "limb" is known *a priori* from the solution found by conformal mapping. In Figure 5.15, V , $\partial V/\partial y$ and $(\partial V/\partial y)/V$ are plotted for the parameter values $a = b = 1$ along the surface $y = -1$ in the vicinity of the "limb". It is clear that, because $V(x, -1)$ does not deviate greatly from the line $V = x$, $(\partial V/\partial y)/V$ has a similar shape to $\partial V/\partial y$. I therefore choose the form

$$\Lambda(x) = \partial V/\partial y \quad , \quad y = -1 \quad (120)$$

for the boundary condition (i.e. a current rather than a true admittance condition) to simplify the remaining steps. Only the case with the parameter values $a = b = 1$ is considered here.

For $a = b = 1$, $\partial V/\partial y$ is approximately equal to $1.6 x^3$ in the range $|x| < 1$ and zero everywhere else (cf. Figure 5.15). Therefore, differentiating (119) with respect to y at $y = -1$ and equating with $\Lambda(x)$ gives

$$\begin{aligned} - \int_0^{\infty} \alpha H(\alpha) \sinh\alpha \sin\alpha x \, d\alpha &= 1.6 x^3 \quad , \quad |x| < 1 \\ &= 0.8 \quad , \quad |x| = 1 \\ &= 0 \quad , \quad |x| > 1 \end{aligned} \quad (121)$$

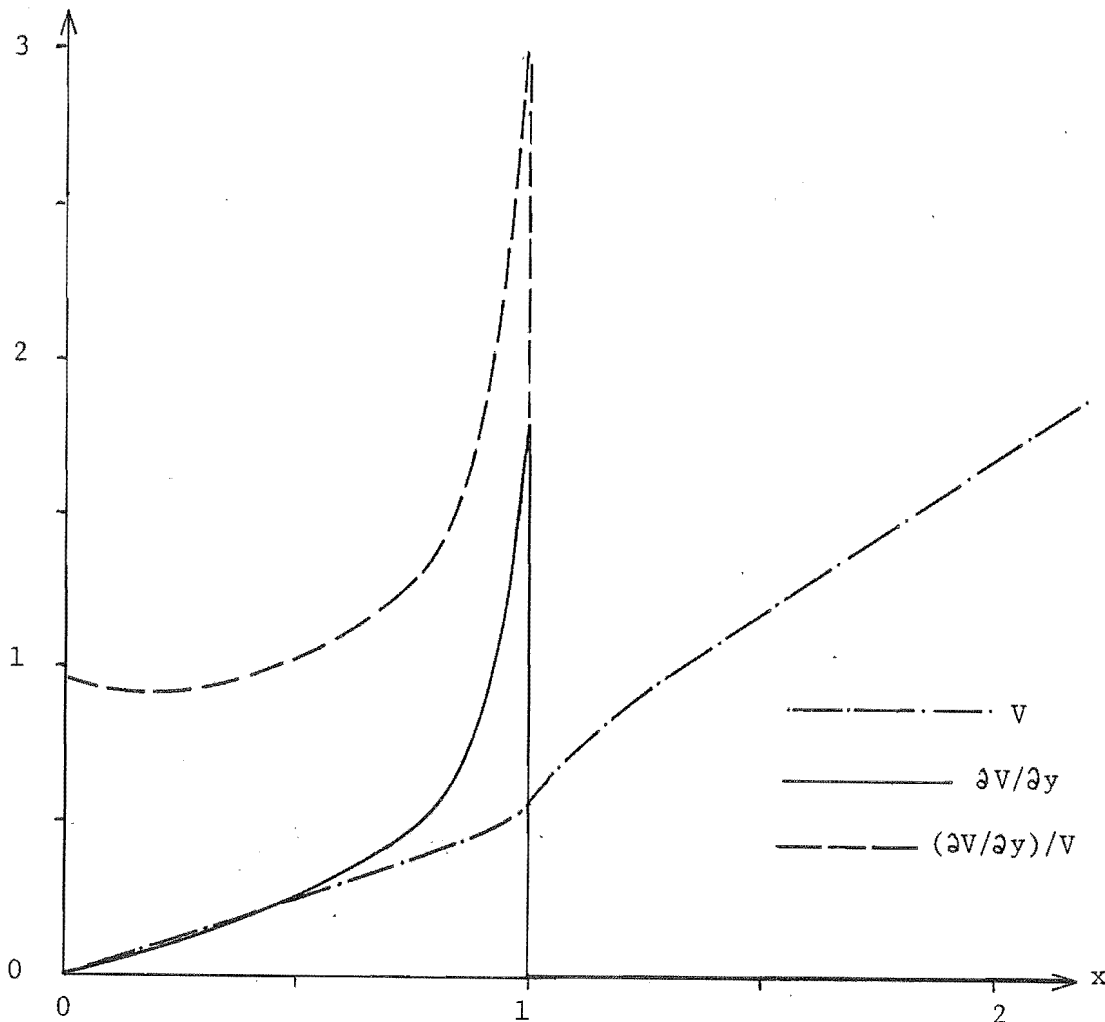


Figure 5.15 Plots of V , $\partial V/\partial y$ and $(\partial V/\partial y)/V$ along $y = -1$ from the conformal mapping solution with $a = b = 1$.

Defining $B(\alpha) = -\alpha H(\alpha) \sinh \alpha$, it is clear from (121) that $B(\alpha)$ and $\Lambda(x)$ form a Fourier sine integral pair (Stratton, 1941; Weber, 1950), and therefore

$$B(\alpha) = (2/\pi) \int_0^1 1.6 x^3 \sin \alpha x \, dx \quad (122)$$

Integrating by parts gives

$$B(\alpha) = (3.2/\pi) \{ (6\alpha^{-3} - \alpha^{-1}) \cos \alpha + (3\alpha^{-2} - 6\alpha^{-4}) \sin \alpha \} \quad (123)$$

While $B(\alpha)$ smoothly approaches zero as α tends to zero (cf. equation (122)), $H(\alpha)$ tends to a large positive value in the vicinity of $\alpha = 0$. Therefore, the accurate numerical computation of V from (119) is difficult to achieve.

Because of the difficulty encountered in the above, I have used an alternative method to calculate the potential field for the surface admittance model. The Fourier sine integrals in (119) and (121) are

approximated by finite Fourier sine series (cf. Weber, 1950), with α taking only the discrete values α_n , $n = 0, 1, 2, \dots, M$. The values for the α_n are chosen by applying the boundary condition (118c) on two additional boundaries at $x = \pm \mu$, where $\mu \gg 1$. The potential field is assumed to be uniform for $|x| > \mu$. Replacing the integral in (119) with its discrete analogue, equation (118c) requires that

$$\sum_{n=0}^M H(\alpha_n) \alpha_n \cos \alpha_n \mu \cosh \alpha_n y = 0$$

for all values of y . Therefore,

$$\alpha_n = (2n + 1) \pi / 2 \mu, \quad n = 0, 1, 2, \dots, M \quad (124)$$

Using the notation $B_n = B(\alpha_n) = -\alpha_n H_n \sinh(\alpha_n)$, equation (119) is now written

$$V(x, y) = x + \sum_{n=0}^M H_n \sin \alpha_n x \cosh \alpha_n y \quad (125)$$

and (122) becomes (Weber, 1950)

$$B_n = (2/\mu) \int_0^1 1.6 x^3 \sin \alpha_n x \, dx, \quad n = 0, 1, 2, \dots, M \quad (126)$$

The integration in (126) is performed by parts as shown in (123).

§5.3.3 Results

The solution to the two-dimensional limb model found by conformal mapping is presented in Figure 5.16 for various widths of the "torso" relative to the width of the "limb" (i.e. various values of the ratio a/b). Because the model boundaries are symmetric (and the field is antisymmetric) about the y -axis, only the right half plane is shown in each case. Contours of equal potential (isopotentials) are plotted. The voltage between the adjacent isopotentials is equal to $b/20$. If the "limb" was not present, these isopotentials would be perpendicular to the "torso" boundaries and physically spaced $b/20$ apart. In each of the cases shown in Figure 5.16, the perturbation to the shape of the isopotentials by the presence of the "limb" is significant only in the approximate range $|x| \leq 2b$. However, note that the potential at any point on the "torso" surface for $|x| > b$ is lowered in magnitude by the presence of the "limb".

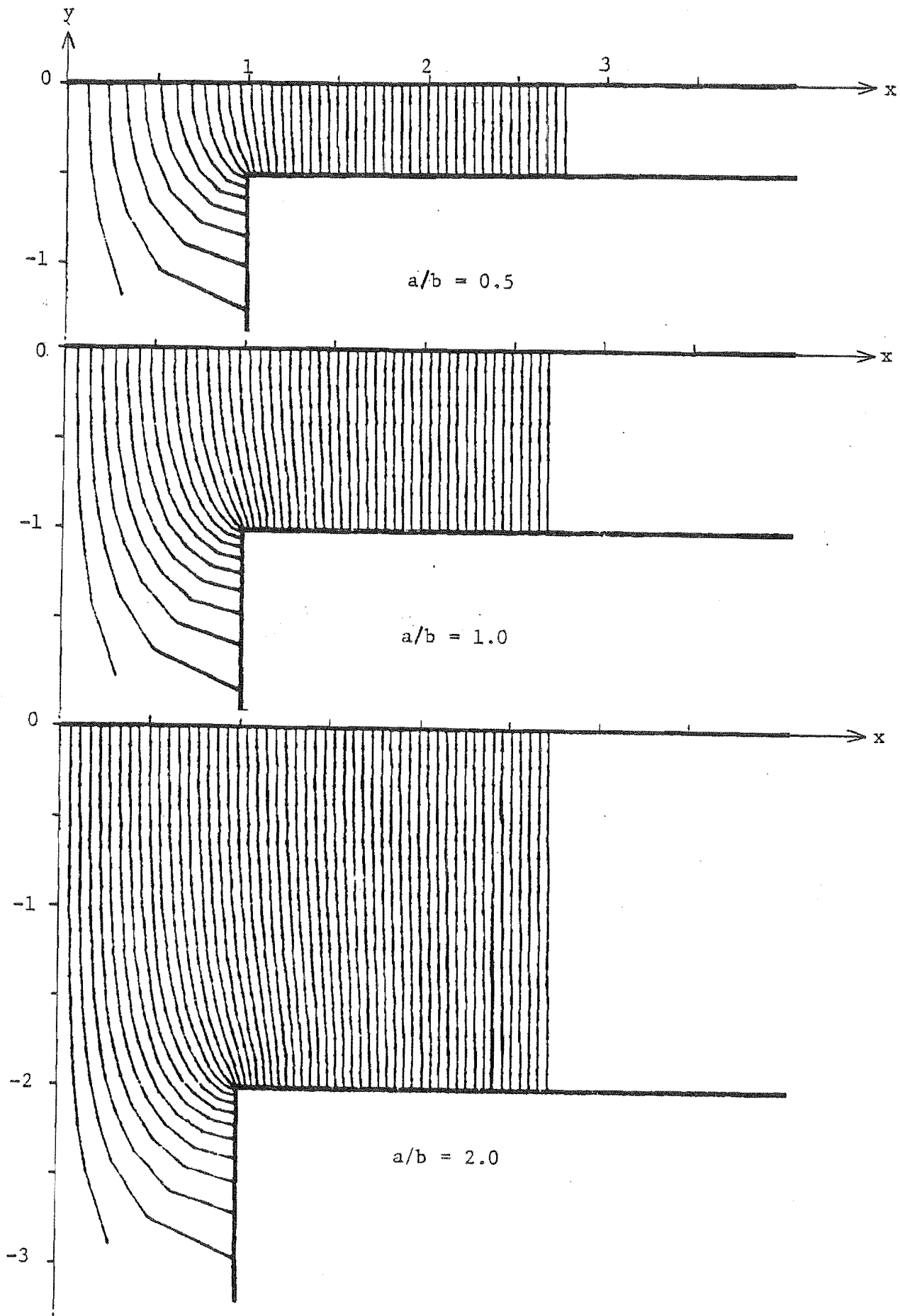


Figure 5.16 Exact limb model solutions by conformal mapping. Isopotentials ($b/20$ volts apart) are plotted for three values of the ratio a/b (cf. Figure 5.13).

The approximate solution for the limb model by the surface admittance method is now presented (for the parameter values $a = b = 1$). In Figure 5.17 the function chosen for $\Lambda(x)$ (cf. equation (121) and Figure 5.15) is plotted as a dashed line for positive values of x ($\Lambda(x)$ is an odd function). On the same plot, the solid line is the approximation to $\Lambda(x)$ found by differentiating equation (125) with respect to y at $y = -1$, with the coefficients B_n given by (126). The case shown has the parameter values $\mu = 5$ and $M = 50$. The discontinuity in $\Lambda(x)$ at $x = 1$, which corresponds to the sharp boundary change in the model where the limb surface meets the torso surface (cf. Figure 5.13), gives rise to the oscillatory behaviour of the series approximation (Gibbs phenomenon).

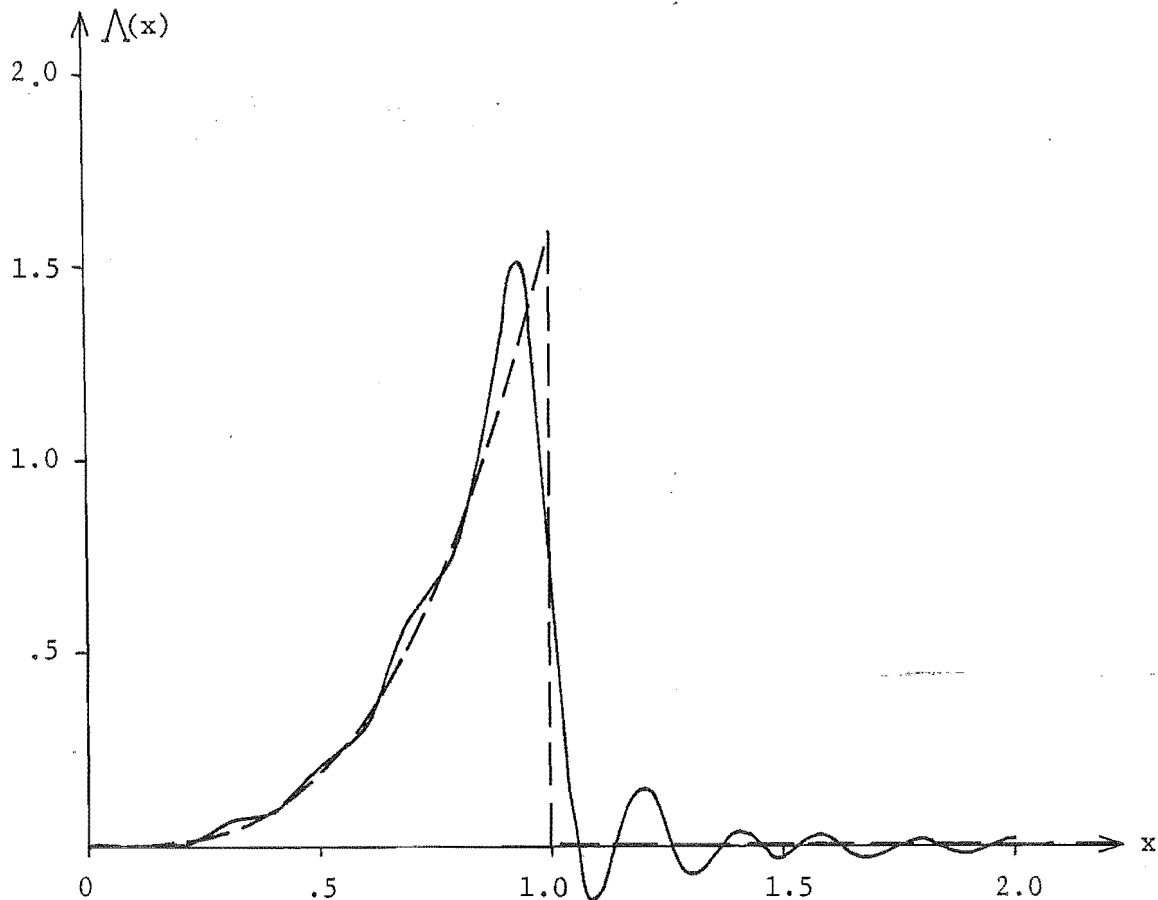


Figure 5.17 The "admittance" boundary condition $\Lambda(x) = \partial V / \partial y|_{y=-1}$ for the two-dimensional limb model. The function chosen *a priori* (dashed line) and the series approximation to it (solid line) are plotted (parameter values $\mu = 5$, $M = 50$).

The results of the approximate solution method are compared to those by conformal mapping in Figures 5.18 and 5.19.

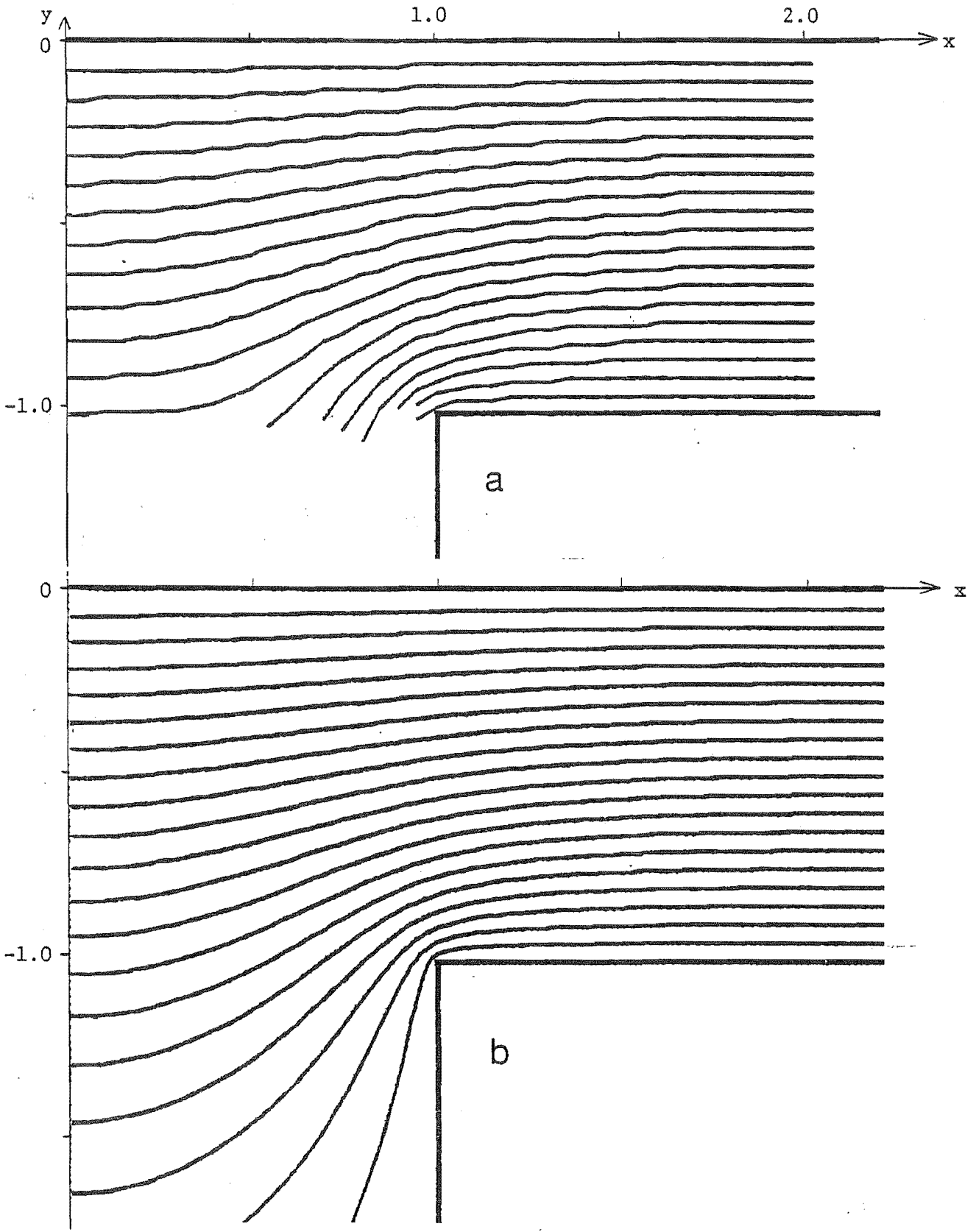


Figure 5.18 Comparison of the solutions a) by the surface admittance method and b) by conformal mapping. Current streamlines are plotted (an equal quantity of current flows between each adjacent pair of lines).

The parameter values for the approximate solution are $\mu = 5$ and $M = 50$ in each case. In Figure 5.18 the current streamlines in the vicinity of the "limb" are plotted for the two methods. Close agreement between the current plots is seen.

In Figure 5.19, the two solutions for the potential along the line $y = -1$ (i.e. the "torso" surface and the base of the "limb") are plotted for positive values of x . The solution by conformal mapping indicates that the total voltage across the "limb" at the "torso" surface (which I denote ΔV) is 1.1. Without the "limb", ΔV would equal 2, therefore the presence of the "limb" causes a 45% drop in ΔV . The approximate solution by the surface admittance method has an error of less than 2% of ΔV at all points on the "torso" surface (see Figure 5.19).

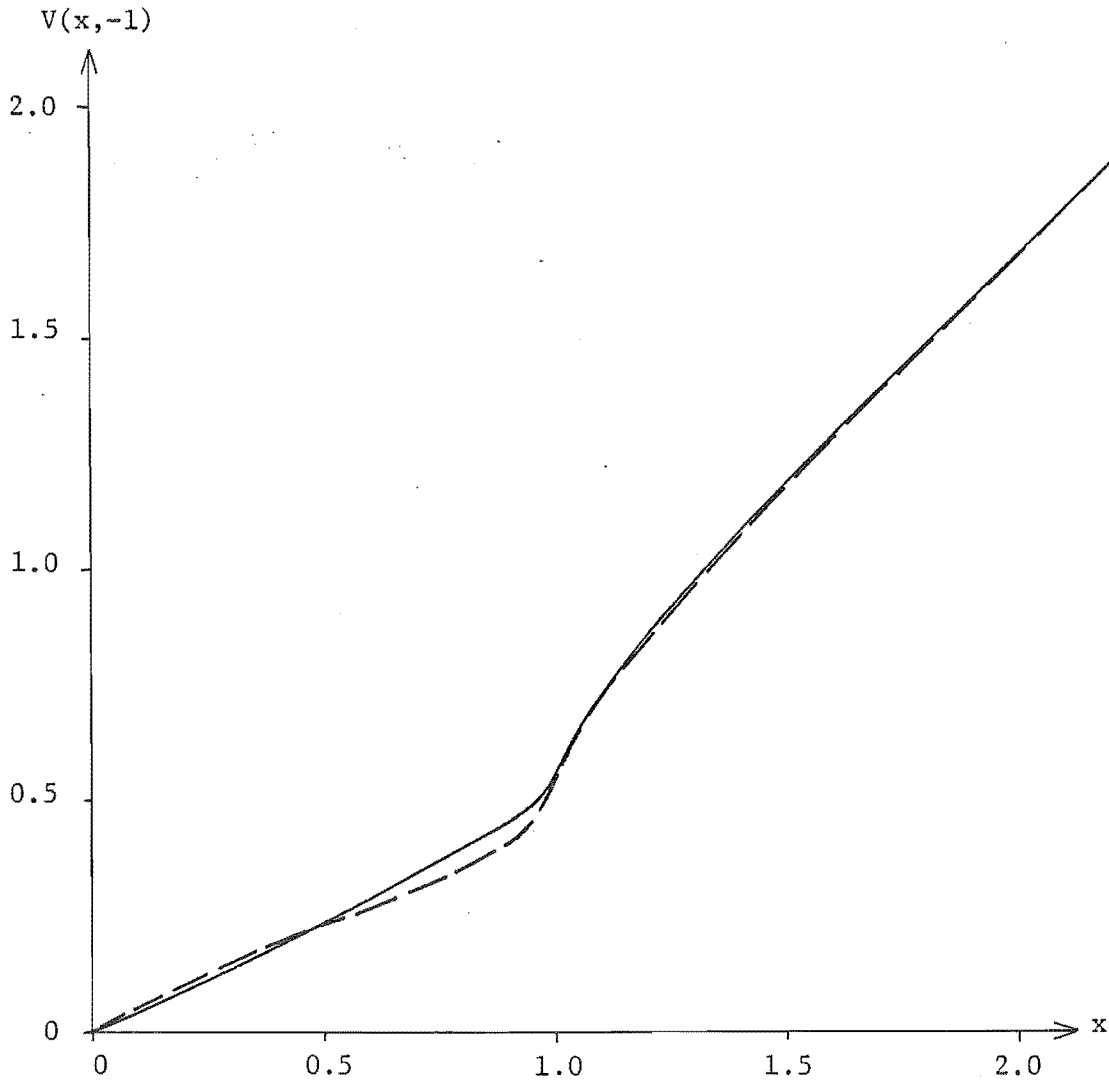


Figure 5.19 Comparison of the "torso" surface potential $V(x, -1)$ by the approximate method (dashed line) and by conformal mapping (solid line).

5.4 DISCUSSION

The simple model presented in this chapter provides a method of studying the sensitivity of the E.C.G., without recourse to complicated and expensive experimentation. The applications of the model which are presented in Section 5.2 are illustrative only, they do not represent the limits of its usefulness. Any number of non-intersecting spherical boundaries may be incorporated to model a piecewise homogeneous variation in the internal conductivity. There is also no theoretical requirement for the model to be axially symmetric, though the use of symmetry clearly simplifies the computation of a solution. Similarly, there is no objection to combining the internal inhomogeneities with the surface changes modelled by the surface admittance method. An example of a "parallel" spherical boundary (rather than the "series" boundaries used in §5.2.1) is presented in §6.2.1 (see Figure 6.7). The introduction of more boundaries, the combining of internal inhomogeneities with surface changes or (in particular) the loss of symmetry, all increase the size of the matrix which must be inverted to solve for the surface potential.

The maximum order N of the potential expansion which is necessary to achieve convergence of the solution is dependent on the geometry chosen for the model (cf. §5.2.3). In my experience, however, it is possible to achieve convergence for the outer surface field with N significantly lower than that necessary for the field to converge throughout the interior of the model. This suggests that the surface field is relatively insensitive to the precise shape of the conductivity inhomogeneities. A similar conclusion has been reached in studies of the imaging of the conductivity of an inhomogeneous body, by means of measurements made on the outside surface (Bates *et al.*, 1980; Dey and Morrison, 1979).

One of the most widely quoted results of the theoretical studies of the E.C.G. is that of Brody (1956), which predicts the effects of the blood in the heart (cf. §4.2.2). The Brody prediction is based on a dipole source near a perfectly conducting sphere. The model presented in Figure 5.3 is, in my opinion, a more realistic representation of the physical relationship of the cardiac generator (again represented by a dipole) and the blood within the heart region. For $\sigma' = 2\sigma$ (cf. §5.2.1), my model predicts that there is only a very slight difference between the effect of the inhomogeneity on the field of a radially directed dipole and on the field of a tangentially directed dipole. In contrast, Brody (1956) predicted a marked difference between the two. I feel therefore

that his result has received undue attention.

Several mechanisms are possible for the effect of respiration on the E.C.G., i.e. changes in: the heart's position, the geometry of the body surface, the amount of blood in the heart, the lung conductivity or the lung volume. Alternatively, the effect may be due to a combination of several of these changes or some other factor not mentioned. My results with the simple model establish the likelihood of some of these mechanisms being dominant. Figure 5.3 shows that an increase in the conductivity of the heart region during inspiration (due to an increase in the negative intrathoracic pressure raising the intracardiac blood volume - Ruttkay-Nedecky, 1976) is likely to decrease the amplitude of the E.C.G. Likewise, the decrease in the mean lung conductivity during inspiration causes a decrease, while the associated increase in lung volume causes an increase in the E.C.G. amplitude, according to the simple model (cf. Figures 5.6 and 5.7). Indeed, the amplitudes of the QRS and T waves do decrease on inspiration (Flaherty et al., 1967; Ruttkay-Nedecky, 1976; and see Table 1.3). Therefore it is possible that these three factors all contribute to the effects of respiration on the E.C.G. amplitude, although it is unlikely that any produce the spatial changes which are also reported (Ruttkay-Nedecky, 1976; cf. Table 1.3). The most likely mechanism for the latter spatial effect is a slight rotation in the axis of the heart, caused by the movement of the diaphragm.

The two-dimensional limb model of Section 5.3 indicates that the presence of a limb, or other similar protrusion from the torso, causes only a minor perturbation to the E.C.G. field in the vicinity of the limb. A smooth bulge is shown in §5.2.2 to cause similar effects on the E.C.G. field (cf. Figure 5.8). The isopotential contours which pass close to a limb are likely to be deflected slightly away from the centre of the limb, compared to the path they would take if the limb was missing. Note that the breasts are likely to cause similar effects on the E.C.G. field. It is unlikely that the magnitude of these effects is sufficient to alter the measurements made by the standard techniques (cf. Chapter 3), especially as the relationship of the electrode positions to the limbs and the head are consistent. The presence of the breasts, however, may explain (in part at least) the lower voltages observed in the chest leads in women as compared to men (cf. Simonson, 1961). I feel that some correction for the presence of the limbs needs to be made to the measured E.C.G. field in order to perform an exact inverse solution (cf. Sections

2.2 and 3.3). It is easier to make such a correction than to incorporate the limbs in the formulation of an inverse solution as discussed in §2.2.2.

CHAPTER 6

EXTENDED MODEL (INTEGRAL EQUATION

In this chapter the simple model presented in Chapter 5 is extended to allow the boundaries separating regions of constant conductivity to be non-spherical. The outer boundary is also permitted to be non-spherical, so that the surface admittance boundary condition need not be invoked in the formulation. The basis of the solution of the extended model is the integral equation introduced in §2.1.4 and §2.2.4. The potential field within the homogeneous regions of the model and on the boundaries separating them is again represented as a series of regular functions. The degree of realism which may be incorporated into the model computation is not limited by any theoretical objections to the analytic techniques employed. However, a limitation is imposed by the size of the computer available for performing the computations and by the length of time it takes to find a solution.

In Section 6.1 the formulation of the extended model is described in detail. In Section 6.2 the application of the extended model is illustrated with a number of numerical computations. Only simple examples are invoked, but they make clear the power and usefulness of the model. The model is used in Section 6.3 to predict the signal generated on the body surface by the activation of the ventricular specialised conduction system (V.S.C.S., see §1.2.2). Various electrode configurations are tested with the model and the effects on the signal of variations in the V.S.C.S. anatomy are studied. The model study of Section 6.3 provides a basis for interpreting the experimental results reported in Chapter 7. The extended model results are discussed in Section 6.4.

6.1 DETAILS OF THE EXTENDED MODEL

§6.1.1 Single coordinate system

Like the simple model, the extended model represents the body as a piecewise homogeneous conducting region. Consider the "torso" depicted in Figure 6.1. For simplicity, assume that the sources are contained

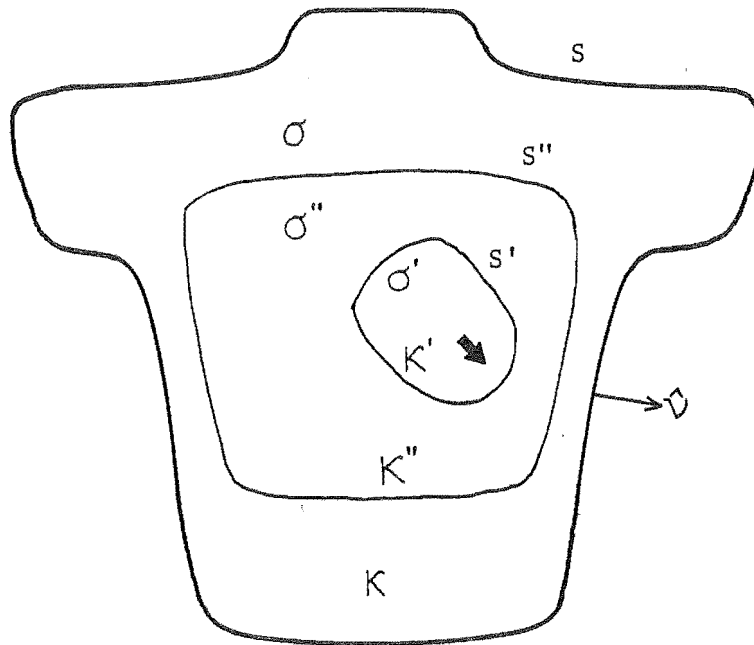


Figure 6.1 A piecewise homogeneous torso with two internal boundaries "in series".

within the boundary S' (i.e. in the region κ'). Recall that in §2.2.4 the integral equation (50) is derived for the somewhat simpler "torso" depicted in Figure 2.5. Incorporating the extra boundary shown in Figure 6.1 and the appropriate notation changes into (50) gives

$$\begin{aligned}
 V(P) = & - \iiint_{\kappa'} \nabla \cdot \mathbf{J}_i \, dv / 4\pi\sigma'R + (\sigma'' - \sigma') \iint_{S'} (\partial V'' / \partial v') \, dS / 4\pi\sigma'R \\
 & + (\sigma - \sigma'') \iint_{S''} (\partial V / \partial v'') \, dS / 4\pi\sigma''R \\
 & - \iint_S V(\partial(R^{-1}) / \partial v) \, dS / 4\pi \quad , \quad P \in \kappa' \cup \kappa'' \cup \kappa
 \end{aligned}
 \tag{127}$$

The inclusion of further internal boundaries in the model may be accommodated by the inclusion of further surface integrals on the right-hand side of (127). Provided each boundary is accounted for in this manner, the formulation may be applied to any piecewise homogeneous "torso".

Within each homogeneous region of the model, the potential is expanded in a convergent series of suitable basis functions. Assume for the moment that a single series of spherical harmonic functions converges throughout each region, provided a suitable origin of coordinates is chosen. Thus in the region κ' , V' is expanded by (97), in κ , V is

expanded by (103), and so on. If the internal boundary surfaces S' , S'' , etc. are non-spherical, it is not possible to directly relate the expansion coefficients of adjacent regions, as it is with the simple model. Instead, the integral equation (127) is used to solve for the unknown potential expansion coefficients. In each of the surface integrals on the right-hand side of (127), the appropriate expansion is substituted for R^{-1} . The exact form of the latter substitution depends on the point P at which the potential on the left-hand side of (127) is evaluated. Consider the surface integral over S' . The point P and the point of integration on S' are given the coordinates (r, θ, ϕ) and (r', θ', ϕ') , respectively, in the same coordinate system with origin O inside S' . The sphere, centred on O , which just circumscribes S' is denoted T_+ and the sphere which just inscribes S' is denoted T_- (see Figure 6.2).

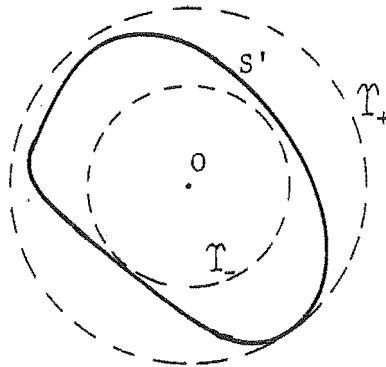


Figure 6.2 Definitions of the surfaces T_- and T_+ which just inscribe and circumscribe (respectively) the surface S' .

Then, for P outside T_+ , the surface integral over S' on the right-hand side of (127) may be written (the constants are neglected for brevity)

$$\iint_{S'} (\partial V'' / \partial v') dS / R = \sum_{n,m} r^{-n-1} Y_{nm}(\theta, \phi) (2n+1)^{-1} \sum_{u,v} \iint_{S'} [\partial((B''_{uv} r'^{u-1} + C''_{uv} r'^u) Y_{uv}(\theta', \phi')) / \partial v'] r'^n Y_{nm}(\theta', \phi') dS, \quad P \text{ outside } T_+ \quad (128)$$

For P inside T_- , the expression is

$$\iint_{S'} (\partial V''/\partial v') dS/R = \sum_{n,m} r^n Y_{nm}(\theta, \phi) (2n+1)^{-1} \sum_{u,v} \iint_{S'} [\partial((B''_{uv} r'^{-u-1} + C''_{uv} r'^u) Y_{uv}(\theta', \phi'))/\partial v'] r'^{-n-1} Y_{nm}(\theta', \phi') dS, \quad P \text{ inside } T_- \quad (129)$$

Thus the surface integral is transformed into an infinite series of functions which are regular everywhere outside T_+ in the first case (128) and functions which are regular everywhere inside T_- in the second case (129).

Each of the integrals on the right-hand side of (127) can be expressed in the form of (128) or (129) depending on the position of P. To solve for the unknown expansion coefficients, P is chosen to lie on concentric spherical surfaces (I shall refer to them as "test surfaces") which do not intersect the boundary surfaces. The spherical harmonic functions are orthogonal over all such test surfaces. Therefore the terms in $r^n Y_{nm}(\theta, \phi)$ and those in $r^{-n-1} Y_{nm}(\theta, \phi)$ may be independently equated on both sides of (127) for all values of n and m. Thus, provided the surface integrals on the right-hand side of (128) and (129) and all similar integrals can be computed, each test surface produces two independent sets of linear equations with constant coefficients. However, because the equations are independent of the test surface radius, only one test surface is needed within each homogeneous region.

The integrals on the right-hand sides of (128) and (129) are of four types:

$$\begin{aligned} I_{nm}^{uv} &= \iint \partial(r^{-u-1} Y_{uv})/\partial v r^{-n-1} Y_{nm} dS \\ J_{nm}^{uv} &= \iint \partial(r^u Y_{uv})/\partial v r^{-n-1} Y_{nm} dS \\ K_{nm}^{uv} &= \iint \partial(r^{-u-1} Y_{uv})/\partial v r^n Y_{nm} dS \\ L_{nm}^{uv} &= \iint \partial(r^u Y_{uv})/\partial v r^n Y_{nm} dS \end{aligned} \quad (130)$$

where $Y_{nm} = Y_{nm}(\theta, \phi)$. These integrals must be computed numerically for each non-spherical surface in the extended model. Note, however, that the integrals need only be computed once for a given boundary surface,

even though the surface is used in several model computations.

For the model depicted in Figure 6.1, if one test surface is defined in each of the regions κ , κ'' and κ' , six independent sets of linear equations are obtained. There are three regions in this model, each requiring two sets of expansion coefficients for the potential field. In the case of the region κ' , the test surface must be chosen to lie outside all sources. One set of equations, therefore, simply relates the coefficients B'_{nm} to the given source distribution as shown in §5.1.1 (see equation (102)). Once the B'_{nm} are found, five sets of linear independent equations must be solved for the five remaining sets of unknown expansion coefficients. In practice, of course, all the expansions must be truncated so that only finite sets of expansion coefficients need be evaluated. The solution is then found by matrix inversion. Provided sufficient terms are retained in the expansions to ensure numerical convergence, the solution is meaningful.

In a model of the human torso, such as the one depicted in Figure 6.1, it may not be possible to fit a spherical test surface in between two boundary surfaces. Or, in the case of the surface S' containing the sources, it may not be possible to specify a test surface which completely contains the sources. In certain of these situations, it is still possible to find a solution for the extended model by having recourse to an additional analytic method. This is the null-field method, already introduced in Chapter 2 (cf. §2.1.4). If a spherical test surface is constructed completely outside S , and P is positioned on this test surface, the left-hand side of (127) is identically zero (cf. equation (18)). Each of the surface integrals on the right-hand side of (127) may then be expressed in terms of a series of functions $r^{-n-1} Y_{nm}(\theta, \phi)$ in the manner of (128). Accordingly, a single set of independent linear equations is formed as above, by equating each multipole on the test surface.

§6.1.2 Several coordinate systems

The model "torso" considered in §6.1.1 has two internal boundaries, the smaller of which is totally enclosed in the larger (see Figure 6.1). I call this a "series" combination of boundary surfaces. Now consider a model with "parallel" interior boundary surfaces as shown in Figure 6.3.

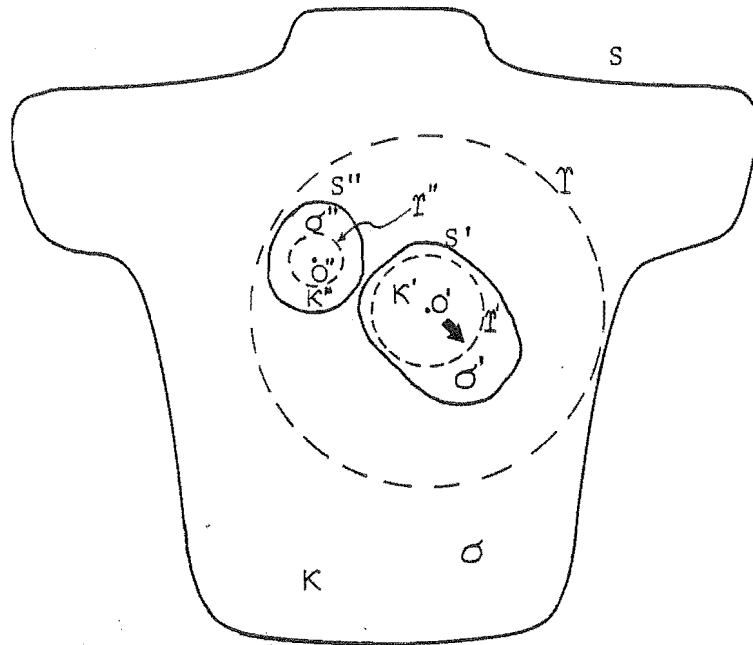


Figure 6.3 A model "torso" with "parallel" inner boundary surfaces.

The sources are contained in κ' . Clearly it is unlikely that the potential in each region of this model is accurately represented by a convergent series of spherical harmonic functions in a single coordinate system. Therefore the field in κ' and just outside S' is represented by a convergent series in one coordinate system, with origin O' suitably positioned within κ' . Another coordinate system, with origin O'' positioned within κ'' , is used to expand the field in κ'' and just outside S'' . The field just inside and on S is represented by a series with the coordinate origin O' or the origin O'' , depending on which is most suitable. Alternatively (if necessary), a third coordinate system and origin is defined for this purpose. Thus several coordinate systems are used to represent the potential field in the vicinity of all the "parallel" internal boundary surfaces and S .

As in §6.1.1, the solution for the model with several coordinate systems (see Figure 6.3) is found by means of an integral equation.

Thus

$$\begin{aligned}
 V(P) = & - \iiint_{\kappa} \nabla \cdot \underline{J}_1 \, dv / 4\pi\sigma'R + (\sigma' - \sigma) \iint_{S'} (\partial V' / \partial v') \, dS / 4\pi\sigma R \\
 & + (\sigma'' - \sigma) \iint_{S''} (\partial V'' / \partial v') \, dS / 4\pi\sigma R \\
 & - \iint_S V(\partial(R^{-1}) / \partial v) \, dS / 4\pi \quad , \quad P \in \kappa U \kappa' U \kappa''
 \end{aligned} \tag{131}$$

This equation is similar to (127) except for appropriate notation changes. Some extra steps are required in its solution, however, over and above the procedure outlined for the example in §6.1.1. Assume that two spherical test surfaces, which do not intersect the boundary surfaces, may be constructed within κ' and κ'' and a third may be constructed within κ , circumscribing S' and S'' . I shall denote these T' , T'' and T , respectively (see Figure 6.3). The test surface T' is constructed to include all of the impressed sources. For a point on T' , equation (131) may be written with each surface integral in the general form of (129). Provided that V_S is expressed in terms of the coordinates with origin O' , only the integral over S'' differs from those dealt with in §6.1.1. Expanded, that integral is (neglecting the constants)

$$\begin{aligned}
 \iint_{S''} (\partial V'' / \partial v') \, dS / R = & \sum_{n,m} r'^n Y_{nm}(\theta', \phi') (2n+1)^{-1} \\
 & \sum_{u,v} \iint_{S''} [\partial \{ (B''_{uv} r''^{-u-1} + C''_{uv} r''^u) Y_{uv}(\theta'', \phi'') \} / \partial v''] \\
 & r'^{-n-1} Y_{nm}(\theta', \phi') \, dS \quad , \quad P \in T'
 \end{aligned} \tag{132}$$

Note that the two spherical harmonic functions in the integrand on the right-hand side of (132) are in different coordinate systems. To compute the right-hand side of (132) in terms of the integrals (130), therefore, each of the harmonics $r'^{-n-1} Y_{nm}(\theta', \phi')$ must be expressed as a series of harmonics in the coordinate system (r'', θ'', ϕ'') by the transformation of origin formulae given in Appendix 1 (Hobson, 1930). Note that, because S'' lies outside T' , the coordinate r'' of any point on S'' is less than the coordinate r' of that point.

Writing the integral equation (131) with each integral expanded as illustrated by (132) and, where necessary, performing coordinate transformations, results in the generation of linear equations in the unknown expansion coefficients. The expansions of the potential field

are only required to converge in limited regions. The expansion of V' is required to converge within the region bounded by T' and S' . Because there are no sources within κ'' , the B''_{nm} are identically equal to zero and the expansion for V'' must converge everywhere within κ'' and on S'' . The expansion of V must converge in the region between T and S . By this reasoning there are four sets of unknown expansion coefficients (C'_{nm} , C''_{nm} , B_{nm} , C_{nm}) to be found in this problem. The test surfaces T' and T'' are used to generate one set of linear equations each (by equating terms of the $r^n Y_{nm}(\theta, \phi)$ type). The test surface T is used to generate two sets of linear equations (by equating both types of harmonic function). Thus the solution of the model in Figure 6.3 reduces to the simultaneous solution of four sets of equations in an equal number of unknowns. The solution is obtained by matrix inversion.

In §5.1.1, the reader is referred to this section for the procedure adopted for the model depicted in Figure 5.1. That model is identical to the above, except that the boundaries are spherical. The boundary condition $\partial V / \partial \nu = 0$ on S provides a direct relationship between the B_{nm} and C_{nm} (i.e. one set of equations). The remaining three sets of equations are generated by using the three test surfaces, as described above. With spherical boundaries, the integrals (130) are straightforward to find analytically, because the spherical harmonic functions are orthogonal over these surfaces.

It is sometimes advantageous to employ the null field concept for a model with "parallel" inner boundaries. If one of the test surfaces T' or T'' cannot be constructed within its respective region (because of the shape of the boundary surfaces or the nature of the source distribution), an additional test surface is constructed, circumscribing S . Over this alternative test surface, the left-hand side of (131) is put identically equal to zero. Then terms in $r^{-n-1} Y_{nm}(\theta, \phi)$ are equated on the right-hand side of (131), to form one additional set of equations. Thus the total number of equations is still sufficient to solve for the potential.

6.2 APPLICATIONS OF THE EXTENDED MODEL

The sensitivity of electrocardiographic signals to variation of conductivity within the torso is studied in this section, using the extended model developed in Section 6.1. The computational examples are as simple as is consistent with demonstrating the points of interest.

In particular, it is considered adequate to take S to be a sphere (normalised to unit radius) because the effects on E.C.G. signals of changes in torso shape have already been investigated in Sections 5.2 and 5.3.

§6.2.1 Conductivity inhomogeneities

The first application of the extended model is shown in Figure 6.4. Two homogeneous regions are separated by a boundary S' which takes three shapes, denoted 1, 2 and 3. Each boundary is symmetric about the axis $\theta = 0$ (analytic expressions for the S' are listed in Table 6.1). The dimensions of the S' are chosen so that the volumes of the two regions are equal in each case. The source in each case is a dipole which is located at the centre of the outer boundary and directed along the axis. In Figure 6.4a, V_S is plotted against θ , for each of the internal boundary shapes, with $\sigma' = 5$ and $\sigma = 1$. In Figure 6.4b, V_S is plotted for $\sigma' = 1$ and $\sigma = 5$.

The shape of the internal boundary in this first example has a significant effect on the peak-to-peak amplitude of the surface potential function but only a slight effect on the shape of the function. When the inner region is more conducting than the outer region (see Figure 6.4a), the amplitude of V_S for the egg-shaped S'_1 is greater than for the spherical S'_2 and $V_S(\theta)$ is flattened in the region of the axis. The amplitude of V_S is least for the doughnut-shaped S'_3 and the field in this case is very slightly peaked in the region of the axis (see Figure 6.4a). In Figure 6.4b (where $\sigma > \sigma'$), V_S is greatest in amplitude for the internal boundary shape S'_3 and least in amplitude for S'_1 . The spherical S'_2 again produces a surface field with an amplitude in between those for the other two cases. In Figure 6.4b, V_S is peaked (near the axis) for the boundary S'_1 and very slightly flattened for S'_3 .

Models with three homogeneous regions are presented in Figures 6.5 and 6.6. The inner spherical boundary S' has a radius 0.5 and it is concentric with S . The third boundary S'' takes two non-spherical shapes (a and b). The analytic expressions for these surface shapes are given in Table 6.1. The conductivity of the region between S' and S'' (σ'') assumes a range of values, while the other two regions have unit conductivity. The source in Figure 6.5 is a dipole offset by 0.3 from the centre of S' and directed along the axis $\theta = 0$. The source in Figure 6.6 is a spherical cap of the Frank type (see §4.1.2), with a circular rim which has radius 0.35 and which is offset by 0.3 from the centre of S' .

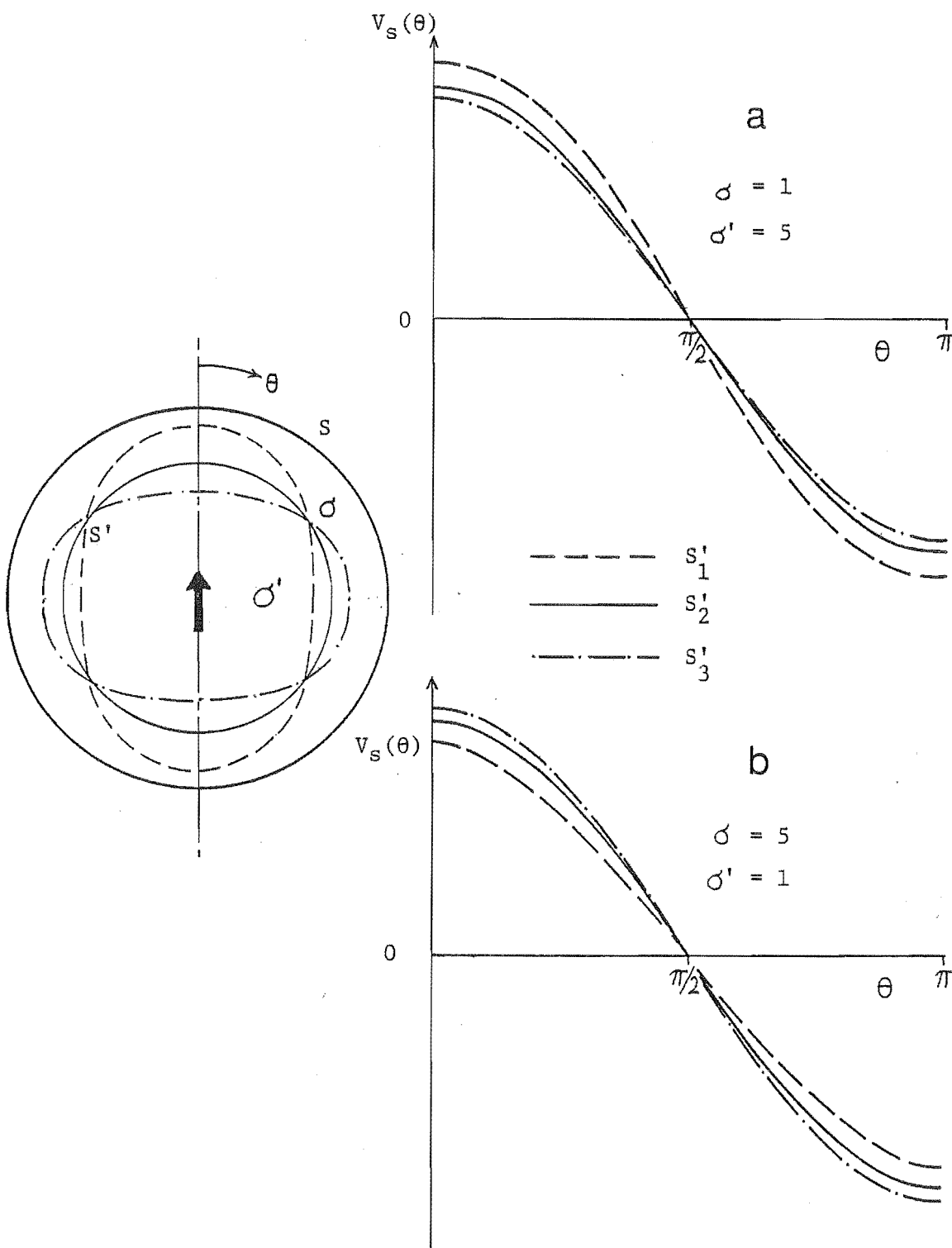


Figure 6.4 The extended model with two homogeneous regions. The boundary S' takes three shapes (1, 2 and 3). The source dipole is directed along the axis $\theta = 0$. The conductivities are a) $\sigma = 1$, $\sigma' = 5$; b) $\sigma = 5$, $\sigma' = 1$.

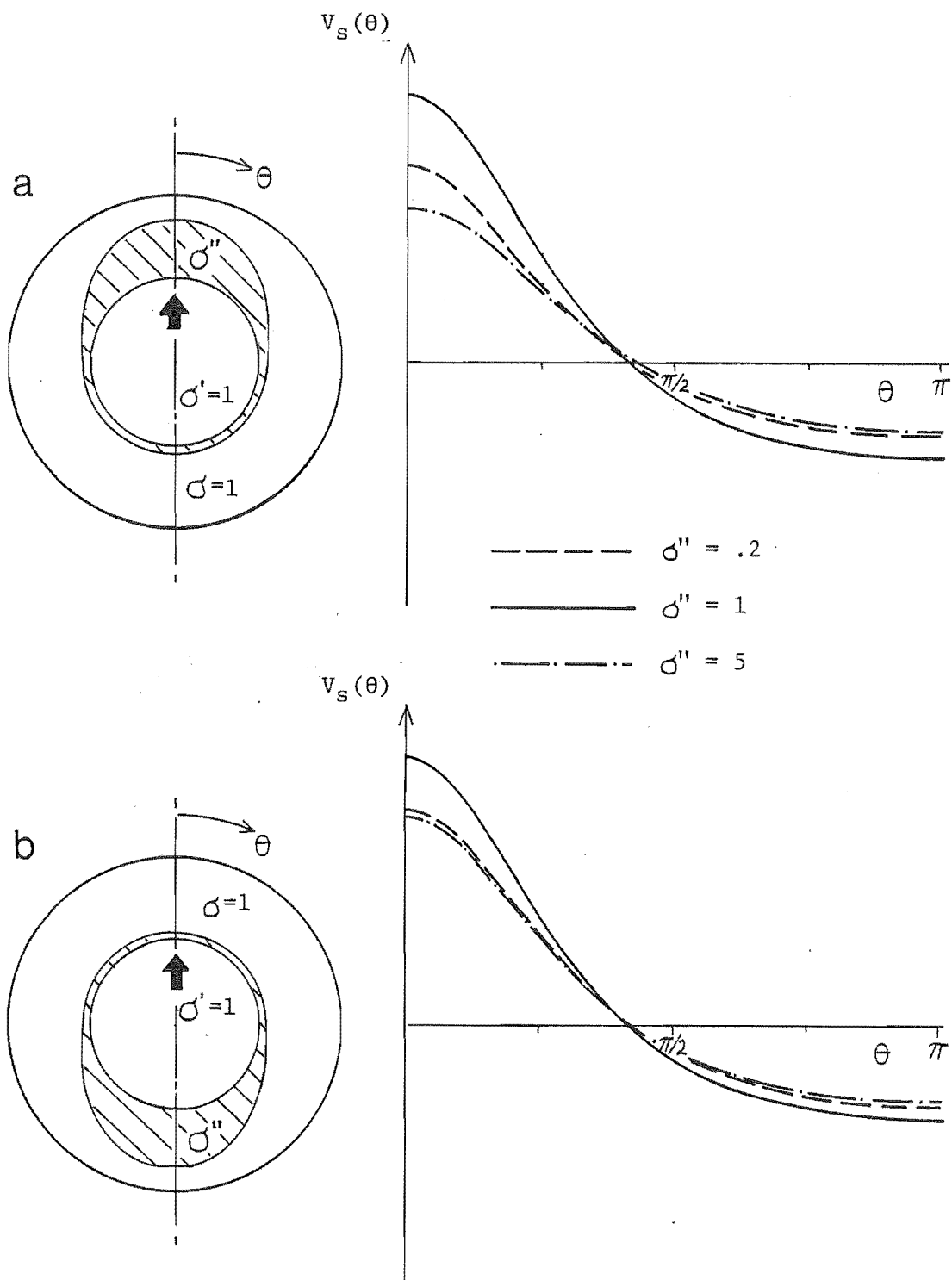


Figure 6.5 Models with three homogeneous regions. The boundary S'' takes two non-spherical shapes (a and b). The source dipole is directed along the axis and offset by 0.3 from the centre of the outer and inner spherical boundaries. The surface potential field is plotted for several values of σ'' .

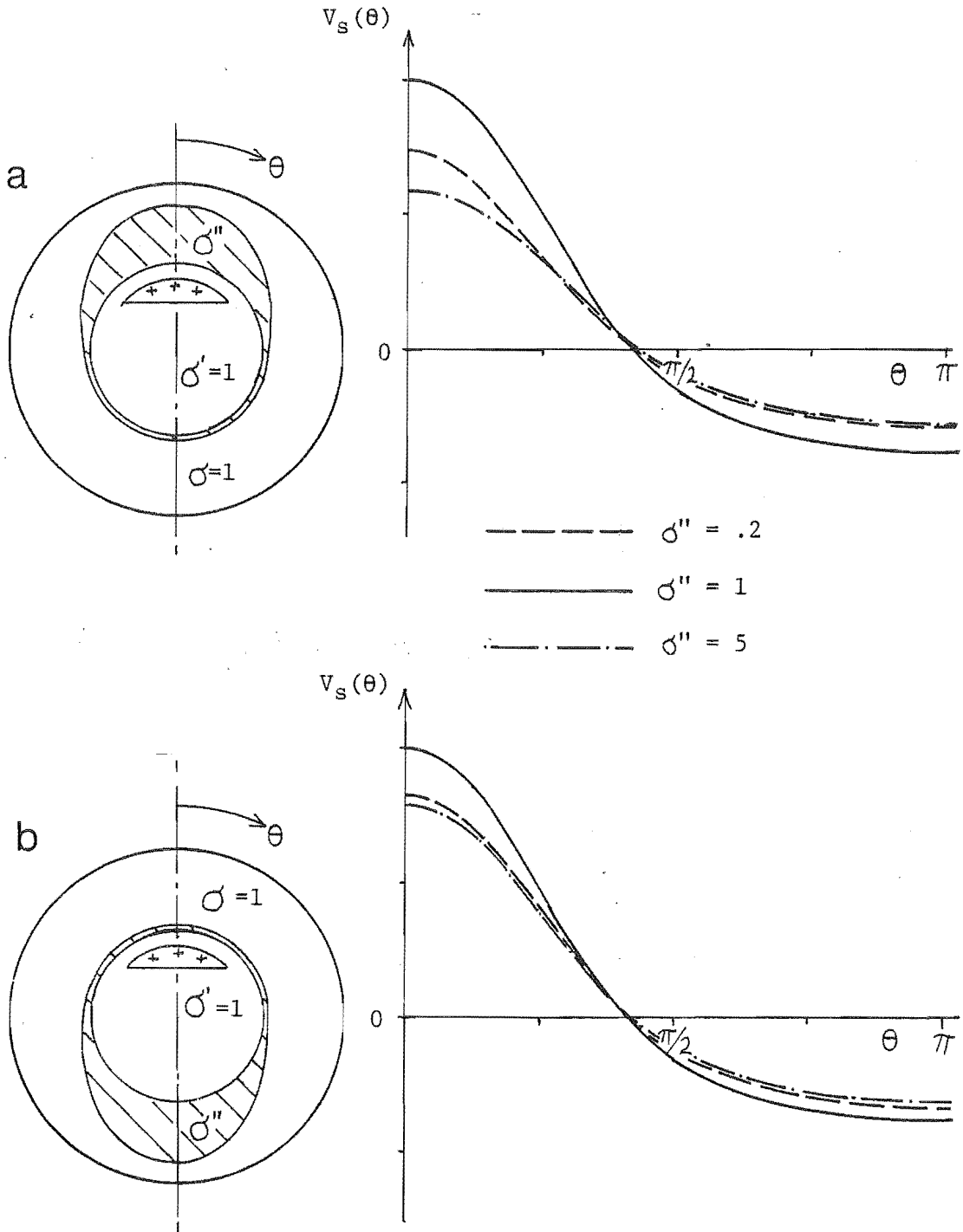


Figure 6.6 Models with three homogeneous regions, as in Figure 6.5, except that the source is a spherical cap (cf. §4.1.2) with a circular rim of radius 0.35, offset by 0.3 from the centre of S .

TABLE 6.1 Analytic expressions for the non-spherical boundaries in Figures 6.4, 6.5 and 6.6. The radial coordinate from the centre of the outer spherical boundary is expressed as a function of the polar angle θ .

Figure	Surface radius, $r_S(\theta)$
6.4	$\begin{cases} r_{S1} = 0.6 + 0.3 \cos^2 \theta \\ r_{S2} = 0.71 \\ r_{S3} = 0.792 - 0.264 \cos^2 \theta \end{cases}$
6.5a, 6.6a	$\begin{cases} 0.7 + 0.15 \cos 2\theta, & \theta < \pi/2 \\ 0.55 & , \theta \geq \pi/2 \end{cases}$
6.5b, 6.6b	$\begin{cases} 0.55 & , \theta < \pi/2 \\ 0.7 + 0.15 \cos 2\theta, & \theta \geq \pi/2 \end{cases}$

The inhomogeneities modelled in Figures 6.5 and 6.6 all attenuate the surface field, whether σ'' is greater than or less than unity. The attenuation is increased when the bulk of the inhomogeneity is close to the source. The changes to the shape of V_S are small in all cases.

In the next application of the extended model, the effects of an insulating region embedded within a homogeneous sphere are investigated, as shown in Figure 6.7. The internal boundary S' (with $\sigma' = 0$) is spherical and "parallel" (cf. §6.1.2) in the sense that the source lies outside S' . In Figures 6.7a and 6.7b the radius of the inhomogeneity r_0 is varied, while in Figures 6.7c and 6.7d the offset of the inhomogeneity from the centre γ is altered (with $r_0 = 0.3$). The source dipole in each case is positioned at the centre of S and it is either directed along the axis $\theta = 0$ or perpendicular to the axis in the plane of $\phi = 0$.

The presence of the insulating region in the models of Figure 6.7 causes a change in the peak-to-peak amplitude of V_S , along with a significant alteration in the shape of the function. The inhomogeneity causes the amplitude of V_S to decrease, when the dipole is directed along the axis, i.e. towards the inhomogeneity (cf. Figures 6.7a and 6.7c).

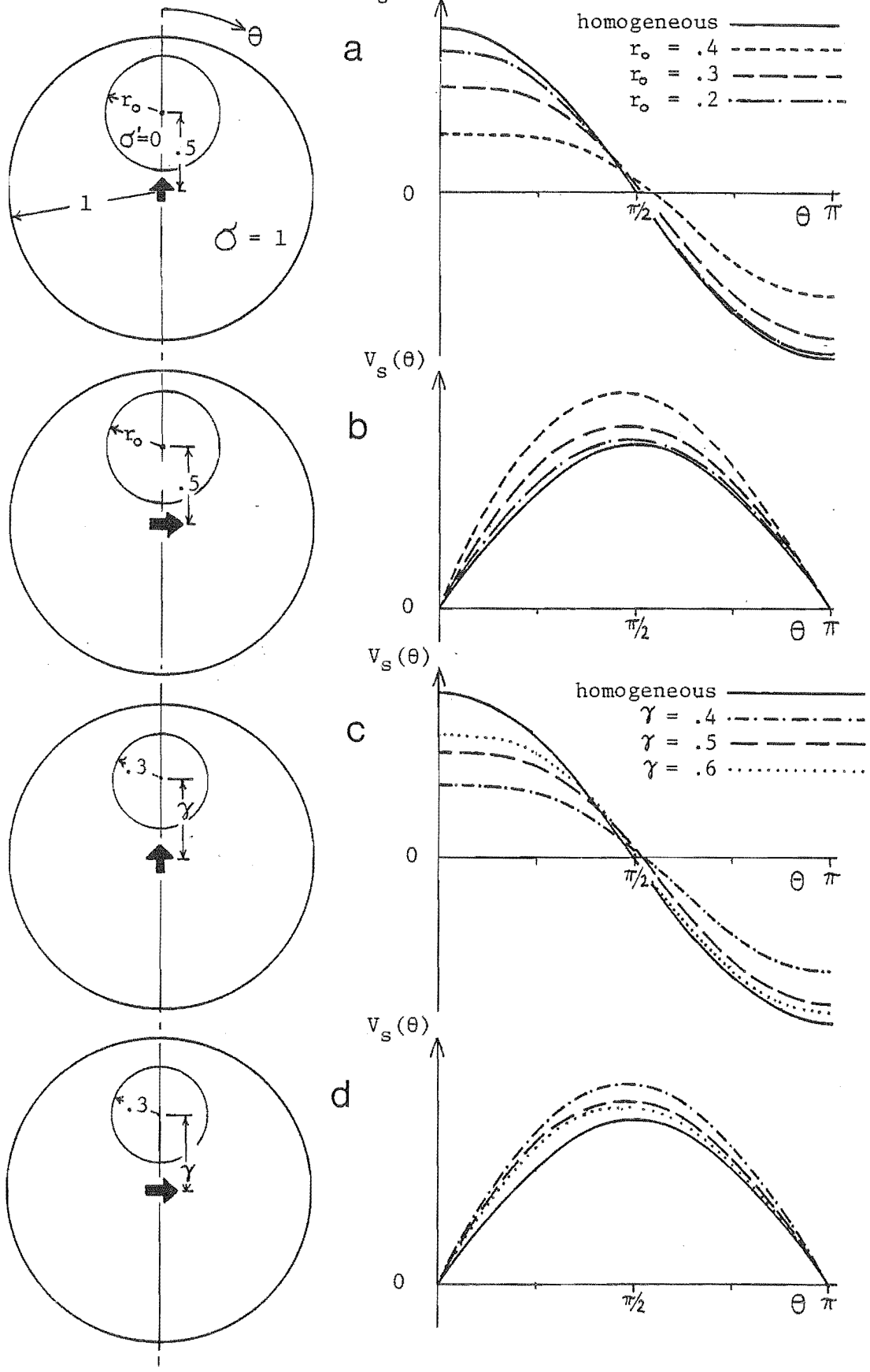


Figure 6.7 Modelling the effect of an insulating spherical region on the field of a dipole in a homogeneous sphere. Either the radius r_0 of the inhomogeneity is altered (a and b), or the offset γ is altered (c and d).

When the dipole is directed perpendicular to the axis (i.e. tangential to the inhomogeneity), V_S is increased in amplitude by the presence of the inhomogeneity (cf. Figures 6.7b and 6.7d). Changing the size and the position of the inhomogeneity has various effects on V_S . As r_0 is increased with the dipole directed along the axis, V_S decreases considerably in peak-to-peak amplitude and becomes flattened near the inhomogeneity (see Figure 6.7a). When the dipole is directed perpendicular to the axis, an increase in r_0 causes V_S to increase in amplitude and become more asymmetric (i.e. the point of maximum potential is moved away from $\theta = \pi/2$ - see Figure 6.7b). Moving the inhomogeneity inwards in the model, while maintaining its size ($r_0 = 0.3$), causes the amplitude of V_S to decrease with the dipole directed along the axis, while it causes the amplitude of V_S to increase with the dipole perpendicular. The shape of $V_S(\theta)$ varies only slightly as γ is changed from 0.6 to 0.4.

§6.2.2 Computational details

The model computations presented in this section were again performed on a PDP 11/10 computer (cf. §5.2.3). All solutions were found to the 15th order (i.e. $N = 15$). All the models have boundaries which are axially symmetric, so only the coefficients of a single polar mode ($m = 0$ or $m = 1$) had to be computed (cf. §5.2.3).

The solution of the integral equation (127) requires the formation of sets of simultaneous linear equations, as discussed in Section 6.1. Each of the integrals over the internal non-spherical boundaries on the right-hand side of (127) contains the normal derivative of the potential on the outside of that boundary. Alternatively, by manipulating equation (49) to

$$\partial V' / \partial v' - \partial V'' / \partial v' = ((\sigma' - \sigma'') / \sigma'') \partial V' / \partial v' \quad (133)$$

these integrals may be written so that their integrands contain the normal derivative of the potential on the inside of the boundary. I have found that the convergence of the solutions of the models presented in Figures 6.4, 6.5 and 6.6 is markedly improved by incorporating the mean of the two alternative expressions (49) and (133) in the integrals over the non-spherical boundaries. The integrals (130) were calculated for all values of the expansion indices by Simpson's rule, with the range of θ (0 to π) divided into 100 equal intervals (the integrands are

independent of ϕ). Each of the applications of the extended model presented in §6.2.1 required the computation of two sets of expansion coefficients to the 15th order. The solutions were found by matrix inversion, as discussed in §5.2.3.

The convergence of the solutions was checked by repeating the computations with $N < 15$. Two examples of my experience with the extended model are shown in Figures 6.8 and 6.9. The convergence of the solution to the model in Figure 6.4a (with the doughnut-shaped internal boundary S'_3) is demonstrated in Figure 6.8 by means of two new mean square error functions. The first, which tests how well the potential continuity boundary condition (cf. §2.2.4) is satisfied at S'_3 , is defined as

$$\text{MSE}'(N) = \frac{\iiint_{S'_3} (V' - V)^2 \, dS}{\iiint_{S'_3} V^2 \, dS} \quad (134)$$

$\text{MSE}'(N)$ is plotted as a solid line in Figure 6.8 with a logarithmic scale.

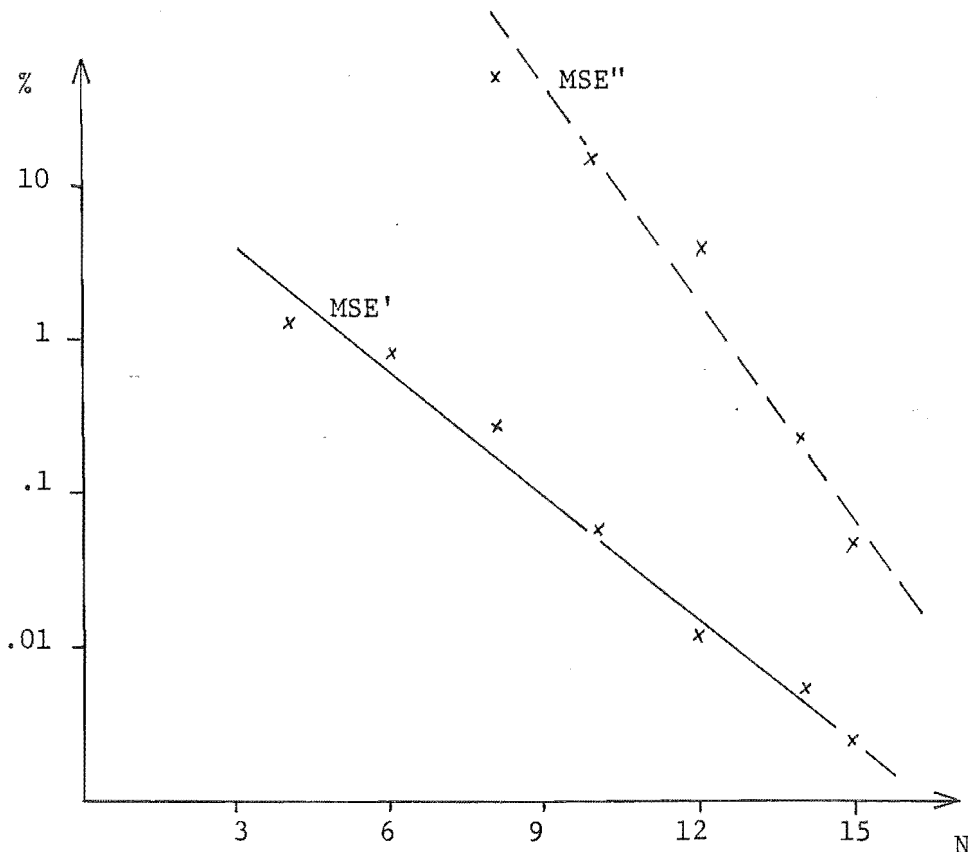


Figure 6.8 The convergence behaviour of the solution to the model of Figure 6.4a (S'_3). $\text{MSE}'(N)$ and $\text{MSE}''(N)$ (see equations (134) and (135)) are plotted on a logarithmic scale.

Note that convergence to $MSE' < 1\%$ is achieved for $N \geq 6$. The second mean square error function, which tests how well the current continuity boundary condition is satisfied at S'_3 , is defined as

$$MSE''(N) = \frac{\iint_{S'_3} (\sigma' \partial V' / \partial \nu - \sigma \partial V / \partial \nu)^2 dS}{\iint_{S'_3} (\sigma \partial V / \partial \nu)^2 dS} \quad (135)$$

$MSE''(N)$ is plotted as a dashed line in Figure 6.8. Convergence to $MSE'' < 1\%$ is only achieved for $N \geq 13$.

In Figure 6.9, the convergence of the solution of the model of Figure 6.7a is shown for $r_0 = 0.3$. The original mean square function $MSE(N)$, defined as in equation (111), is plotted on a logarithmic scale for the surface potential functions V_S and $V_{S'}$. The convergence of the potential is much more rapid on the outer surface than on the internal boundary. Convergence to $MSE < 1\%$ is achieved for V_S with $N \geq 1$ and for $V_{S'}$, with $N \geq 6$. In both of the examples presented here, $\log(MSE)$ is linearly related to N .

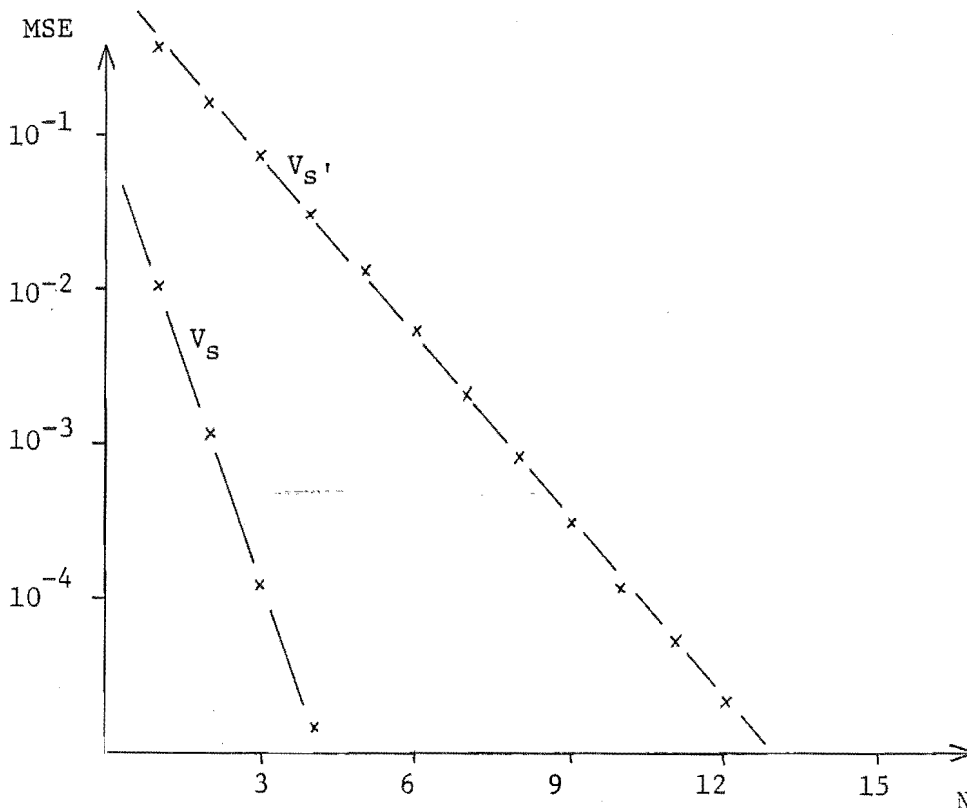


Figure 6.9 The convergence behaviour of the solution for the model of Figure 6.7a ($r_0 = 0.3$). MSE (cf. equation (111)) is plotted for V_S and $V_{S'}$.

6.3 MODELLING THE FIELD PRODUCED BY THE VENTRICULAR SPECIALISED CONDUCTION SYSTEM

The ventricular specialised conduction system (V.S.C.S.) transports the cardiac excitatory impulse from the A-V node to the ventricular myocardium. The system comprises the common bundle of His and the bundle branches (cf. §1.2.2). The V.S.C.S. distributes the impulse to a considerable portion of the ventricular endocardium to initiate a coordinated ventricular contraction. The detection of the activation of the V.S.C.S. tissues is important in the diagnosis of several types of cardiac arrhythmia and in assessing what treatment is appropriate for patients who suffer from arrhythmias (cf. §1.4.5; Curry, 1975; Narula, 1975). For example, the finding that the propagation of the impulse along the length of the V.S.C.S. takes more than 55 msec, in a patient who is being investigated for "heart block" (cf. §1.4.5), would prompt most physicians to consider fitting an implanted pacemaker.

The positioning of electrodes within the right side of the heart by catheterisation (cf. §1.3.7) is undoubtedly the most accurate and reliable technique at present available for detecting the activation of the V.S.C.S. However, catheterisation involves some degree of risk and discomfort for the patient and it is expensive to perform (Ross *et al.* 1980). Recently Barbari *et al.* (1973, 1975, 1979) and other groups (Flowers *et al.*, 1974; Furness *et al.*, 1975; van den Akker *et al.*, 1976) have reported the use of signal averaging for the non-invasive recording of signals arising in the V.S.C.S. However, comments by some clinical electrophysiologists (Fisher, 1978) indicate that the method is not yet accepted as a viable alternative to catheter studies. There are three possible reasons for this scepticism:

- (1) None of the published results of the non-invasive method show the slightest resemblance to the distinct "clean" H spike that is the pride of every physician who performs cardiac catheterisation (Myers *et al.*, 1978; see Figure 1.11).
- (2) The published results vary considerably in the type of waveform produced after averaging (see, for example, Figure 7.1).
- (3) The technique has yet to be utilised clinically as an alternative to catheter studies.

The modelling study presented in this section demonstrates the reasons for the first of the objectives above. In Chapter 7, some results are

presented which mollify the second objection. Some comments pertinent to the clinical utilisation of the non-invasive method are made in Section 8.4.

§6.3.1 The signal detected by an intracardiac catheter

Most catheter studies of V.S.C.S. activation are carried out with a catheter which has two or more platinum electrodes spaced approximately 10 mm apart at the end. The catheter is positioned through the tricuspid valve, so that the end portion is in the proximity of and approximately parallel to the bundle of His, which is embedded in the intraventricular septum (see Damato, 1969). A great deal of experience has been gained with the methods and instrumentation involved in catheter studies. The role of a model in this context is to test the sensitivity of the catheter signal to influences such as the distance from the catheter to the tissue being activated and the speed of the propagation of the activation along the tissue. Some results of this type are presented below.

In §4.1.1, a model is developed for the potential field produced by a thin bundle of fibres. The simplified representation of the impressed sources in the depolarising region of the fibre bundle as a current dipole, is shown to introduce negligible error. In this section, therefore, a current dipole is used to represent the bundle of His (and, in §6.3.2, to represent each of the bundle branches).

The field of a dipole in an infinite homogeneous region is given by (43). The influence of the body surface on this field must be considered before a model for the catheter signals can be established. Consider a dipole (representing the bundle of His) positioned at a radius of 0.6 within a homogeneous sphere of unit radius (crudely representing the body surface), as shown in Figure 6.10. The method presented in Section 5.1 allows the field throughout the sphere to be found analytically. On the relative scale introduced above, a catheter positioned in the vicinity of the bundle of His is within a radius of 0.2 of the source dipole (cf. Figure 6.10). On the right-hand side of Figure 6.10, the field of the dipole at that radius is plotted, with and without the "body surface". It is clear from the plot that the presence of the body surface changes the "near" field of the source dipole by less than 4% of the peak-to-peak amplitude. Because the catheter lies wholly within a region of approximately homogeneous

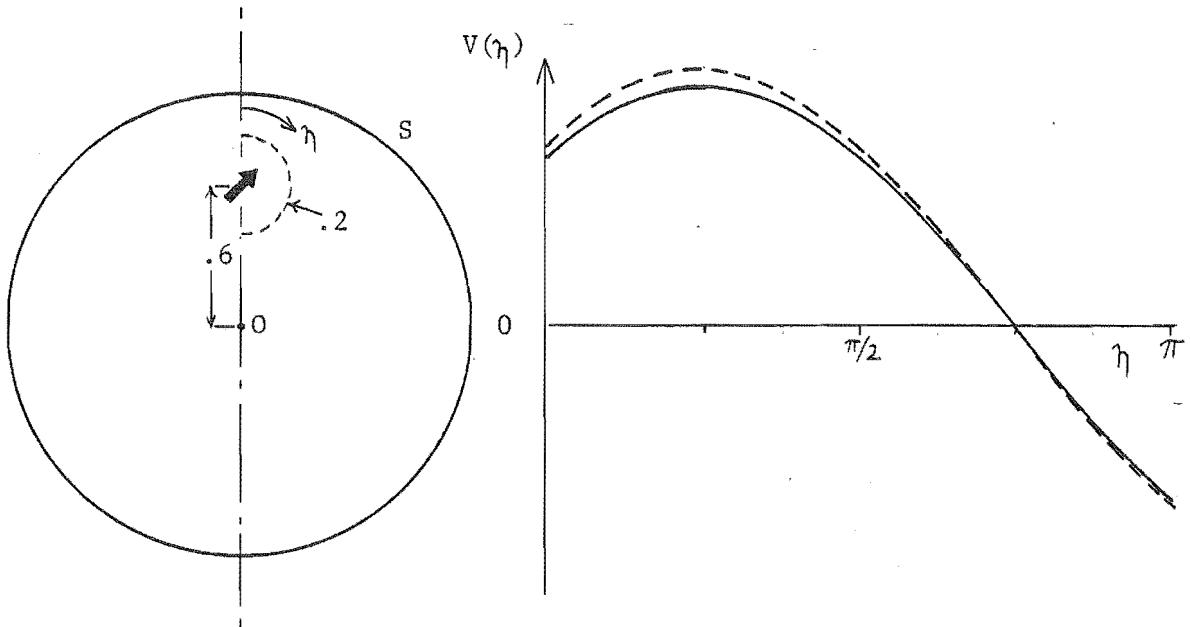


Figure 6.10 Simple model to establish that the body surface has little effect on the near field of the bundle of His. Potential is plotted at a radius of 0.2 from the dipole source, with (dashed line) and without (solid line) the "body" surface.

conductivity (the intracardiac blood), the effects of conductivity inhomogeneities on the "near" field of the bundle of His are also likely to be small.

Having established a basis for a simple model of the His bundle field in the region of an intracardiac catheter, I shall now consider the signal received by that catheter. The model is shown in Figure 6.11. Two electrodes (e and f) are positioned at a distance d from the axis of the "bundle of His" and in the same plane as that axis. The signal of interest is the voltage between those electrodes as a function of time. The origin of coordinates (and the position of the current dipole) is taken to be the point on the axis of the (thin) bundle undergoing depolarisation at time t . The potential at a point $P(r, \theta)$ is then

$$V'(P) = C \cos\theta/r^2$$

where C is an arbitrary amplitude constant and r, θ are the coordinates defined as shown in Figure 6.11 (symmetry about the axis $\theta = 0$ is assumed).

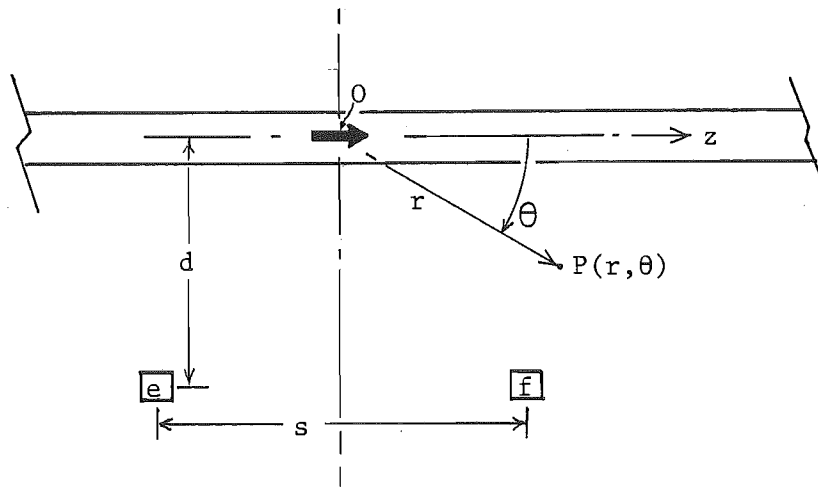


Figure 6.11 Model for the signals received by a bipolar electrode catheter near the bundle of His.

The propagation of activation along the bundle in the direction z (cf. Figure 6.11) is equivalent to moving the electrodes in the direction $-z$ with the source dipole position unchanged. The voltage between the electrodes is thus straightforwardly derived as

$$\begin{aligned} \Phi_{ef}(t) = & C(s/2 - vt) ((s/2 - vt)^2 + d^2)^{-3/2} \\ & + C(s/2 + vt) ((s/2 + vt)^2 + d^2)^{-3/2} \end{aligned} \quad (136)$$

where v is the velocity of propagation along the bundle, s is the separation of the electrodes and t is time, with $t = 0$ at the instant shown in Figure 6.11.

$\Phi_{ef}(t)$ is plotted in Figure 6.12. In Figures 6.12a and 6.12b, respectively, the effects of changing the distance d and the velocity of propagation v are illustrated. The solid line in both plots is the signal predicted for typical parameter values ($s = 10$ mm, $d = 10$ mm and $v = 1.5$ m/sec). The width of the positive-going spike is approximately 10 msec, which indicates that, with these parameter values, the activation within the bundle is only detected in the interval -7.5 mm $< z < 7.5$ mm (cf. Figure 6.11).

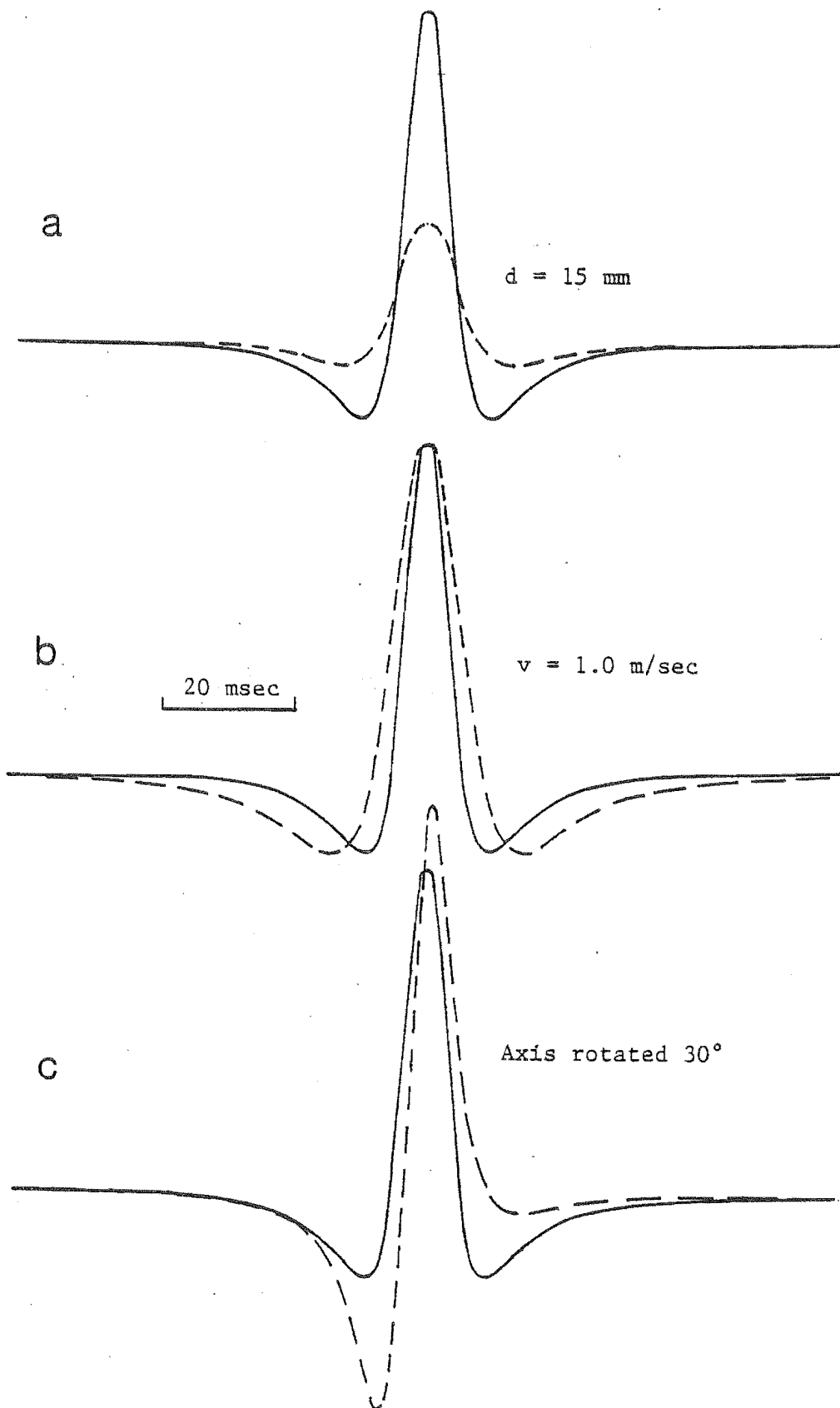


Figure 6.12 The catheter signals predicted by a model for the activation of the bundle of His (cf. Figure 6.11) with typical parameter values (solid lines, $s = 10$ mm, $d = 10$ mm, $v = 1.5$ m/sec), a) with d varied, b) with v varied and c) with the catheter axis rotated by 30° .

In other words, an intracardiac catheter with a pair of closely spaced electrodes is only sensitive to the depolarisation of the portion of the bundle of His in its immediate vicinity. Movement of the catheter away from the bundle attenuates the signal, with a coincident widening of the interval within which the depolarisation is detected (dashed line in Figure 6.12a). A similar alteration of the shape of the signal is predicted for a slower propagation of activation along the bundle (dashed line in Figure 6.12b). A change in signal amplitude may also result from a slower propagation rate, due to the lower number of individual cells depolarising per unit time. However, I know of no data on which to base such changes in the model. Note that the results presented in Figure 6.12 (a and b) appear to quash any notion of measuring the velocity of impulse propagation from the analysis of the shape of the intracardiac catheter signals. Such a velocity measurement would require two separate pairs of electrodes a known distance apart.

The effect of the catheter being inclined to the bundle axis is illustrated in Figure 6.12c. An increase in the amplitude is evident, along with a distortion of the shape of the signal. Rotation of the catheter axis so that the electrodes no longer lie in the plane of the bundle axis results in similar changes. Clearly, no signal is received if the electrodes lie on a line perpendicular to the axis of the bundle of His.

§6.3.2 The body surface field

In the introductory remarks to this section, I commented on the variations in the published results of the non-invasive detection of the signals from the V.S.C.S. This has certainly contributed to the scepticism of some physicians to the new technique (cf. Fisher, 1978). I have the impression that many physicians expect the signal detected at the body surface to look similar to the signal detected by an intracardiac catheter. I show below, by using the models already presented, that the body surface signals must look quite different to the catheter signals.

The model used to predict the body surface field generated by the activation of the V.S.C.S. is shown in Figure 6.13. The body is represented by a homogeneous spherical region of unit radius. The activation of the V.S.C.S. is represented by three current dipoles. The dipole positions $\underline{x}_j(t)$ and moments $\underline{p}_j(t)$, $j = 1$ to 3, are based on the approximate location of the V.S.C.S. tissues within the "body", as determined from an atlas of cross-sectional anatomy (Pernkopf, 1963).

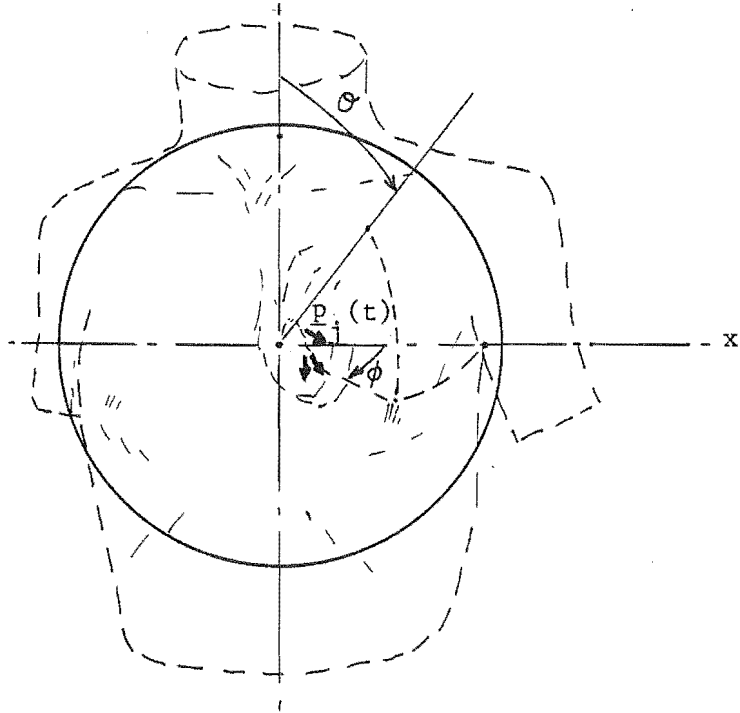


Figure 6.13 The model used to predict the body surface potential field produced by the activation of the V.S.C.S.

Dipole 1 represents the bundle of His and the right bundle branch. Dipoles 2 and 3 represent the left anterior and left posterior bundle branches, respectively. The period of the V.S.C.S. activation is divided into 18 instants t_i , $i = 1$ to 18. In Table 6.2, the $\underline{x}_j(t_i)$ are listed using the coordinates (r, θ, ϕ) (see Figure 6.13). The dipole directions are also listed in Table 6.2 using the angular coordinates (η, γ) , where $\eta = \hat{\theta} \cdot \underline{p} / |\underline{p}|$ and $\gamma = \hat{\phi} \cdot \underline{p} / |\underline{p}|$. The magnitudes of the dipole moments are plotted against time in Figure 6.14.

The surface field of the V.S.C.S. activation model is found by first deriving the infinite homogeneous region field V' of the dipole sources (at each instant) and then imposing the boundary condition $\partial V / \partial r = 0$ at the boundary S . The infinite region field is given by (81), with M taking the value 3. Expand R^{-1} by (22), V' by (38), and substitute both in (81) to give

$$B_{nm} = (2n+1)^{-1} \sum_{j=1}^3 \underline{p}_j \cdot \nabla(r_j^n Y_{nm}(\theta_j, \phi_j)) \quad (137)$$

where the B_{nm} are the expansion coefficients of V' .

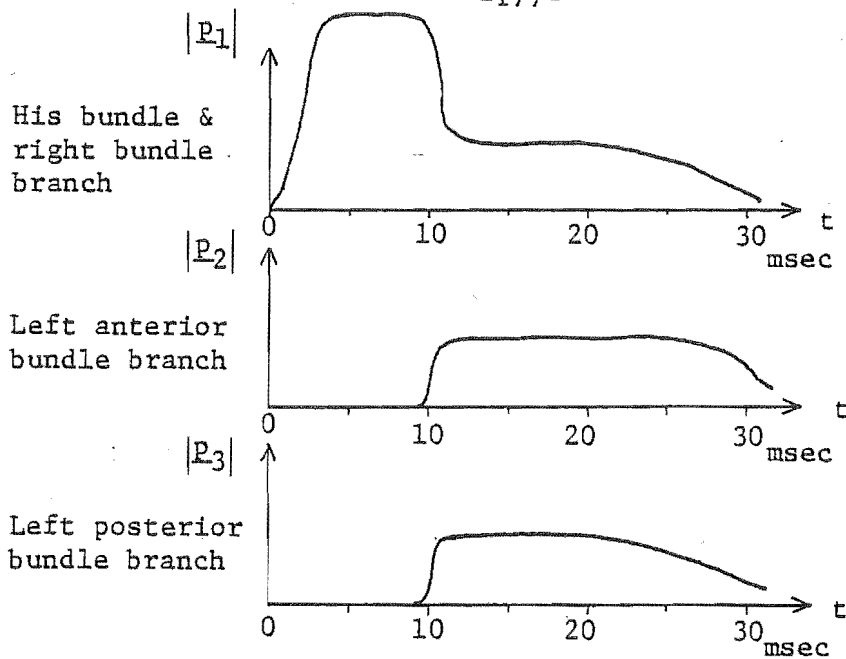


Figure 6.14 The magnitudes of the three source dipoles of the V.S.C.S. activation model.

TABLE 6.2 The dipole positions $x_j(t_i)$, expressed in the coordinates (r, θ, ϕ) , and the dipole directions, expressed in the angular coordinates (η, γ) . Angles are in radians, time is in milliseconds.

i	t_i	Dipole 1					Dipole 2					Dipole 3				
		r	θ	ϕ	η	γ	r	θ	ϕ	η	γ	r	θ	ϕ	η	γ
1	0	.559	1.13	1.43	1.45	0.54										
2	1	"	"	"	"	"										
3	2	"	"	"	"	"										
4	3	"	"	"	"	"										
5	5	.575	1.14	1.38	1.45	0.54										
6	7	.595	1.15	1.36	1.40	0.54										
7	9	.606	1.17	1.33	1.92	0.42										
8	11	.633	1.18	1.31	1.65	0.77	.616	1.20	1.29	2.11	0.65	.595	1.21	1.29	2.27	-.05
9	13	.648	1.19	1.30	1.96	0.82	.623	1.24	1.26	1.96	0.47	.594	1.24	1.25	2.27	-.05
10	15	.656	1.22	1.29	2.10	0.94	.640	1.26	1.22	1.85	0.47	.593	1.27	1.21	2.18	-.03
11	17	.668	1.25	1.26	2.31	1.01	.660	1.28	1.19	1.80	0.49	.608	1.25	1.16	2.18	-.03
12	19	.678	1.29	1.26	2.38	1.08	.681	1.30	1.16	1.78	0.42	.602	1.33	1.13	2.18	-.06
13	21	.689	1.33	1.25	2.48	1.08	.696	1.31	1.14	1.79	0.33	.608	1.35	1.10	2.15	-.07
14	23	.700	1.37	1.24	2.50	1.12	.709	1.33	1.11	1.78	0.23	.614	1.37	1.06	2.06	-.09
15	25	.715	1.41	1.24	2.55	1.13	.726	1.34	1.08	1.77	0.15	.620	1.40	1.02	2.04	-.18
16	27	.725	1.45	1.24	2.55	1.13	.737	1.35	1.06	1.76	0.07	.627	1.42	0.97	1.82	-.17
17	29	.744	1.48	1.24	2.63	1.15	.753	1.36	1.03	1.70	-.02	.635	1.43	0.95	1.96	-.24
18	31	.736	1.52	1.24	2.63	1.15	.761	1.36	1.00	1.60	-.07	.644	1.46	0.90	1.82	-.37

The complete expansion of the field inside S is of the form of (37). Imposing the boundary condition $\partial V/\partial r = 0$ on S requires that (86) is satisfied, as discussed in §4.2.1. Therefore the surface field is

$$V_s = \sum_{n,m} (2n + 1) B_{nm} Y_{nm}(\theta, \phi)/n \quad (138)$$

with the B_{nm} specified by (137).

Figure 6.15 shows the signal $\Phi_{gh}(t)$ computed from (138) for a chest bipolar lead. The approximate position of the lead electrodes g and h are shown on the left-hand side of Figure 6.15. These electrode positions are similar to those used to make the measurements reported in Chapter 7. Note that $\Phi_{gh}(t)$ has an initial positive deflection and a notch at approximately 10 msec. The notch corresponds to the time when the activation in the V.S.C.S. model moves from the bundle of His into the bundle branches. $\Phi_{gh}(t)$ is distinctly different than the catheter signal (cf. Figures 6.12 and 6.15). It clearly is sensitive to activation throughout the V.S.C.S. (though note the effects of different electrode positions modelled in §6.3.3).

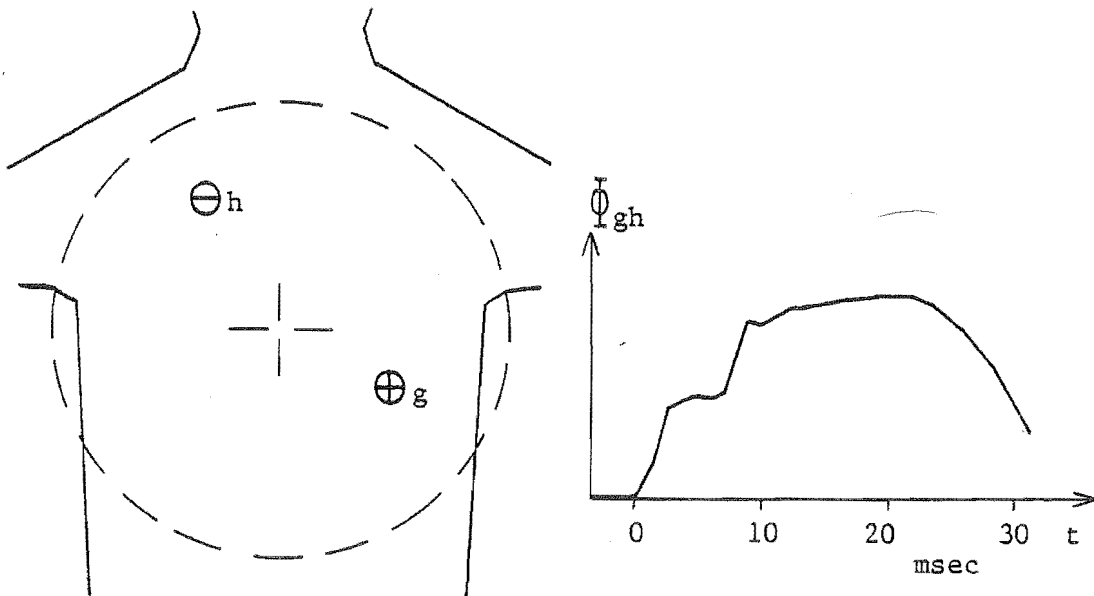


Figure 6.15 The signal $\Phi_{gh}(t)$ predicted by the V.S.C.S. activation model for the bipolar chest lead with the electrode positions shown.

§6.3.3 Sensitivity of the V.S.C.S. surface field

The model discussed in §6.3.2 has been used to test the sensitivity of the body surface field, arising from the activation of the V.S.C.S., to changes in the positions of the electrodes and to changes in the anatomical location of the V.S.C.S. tissues. The results are presented in Figures 6.16 and 6.17.

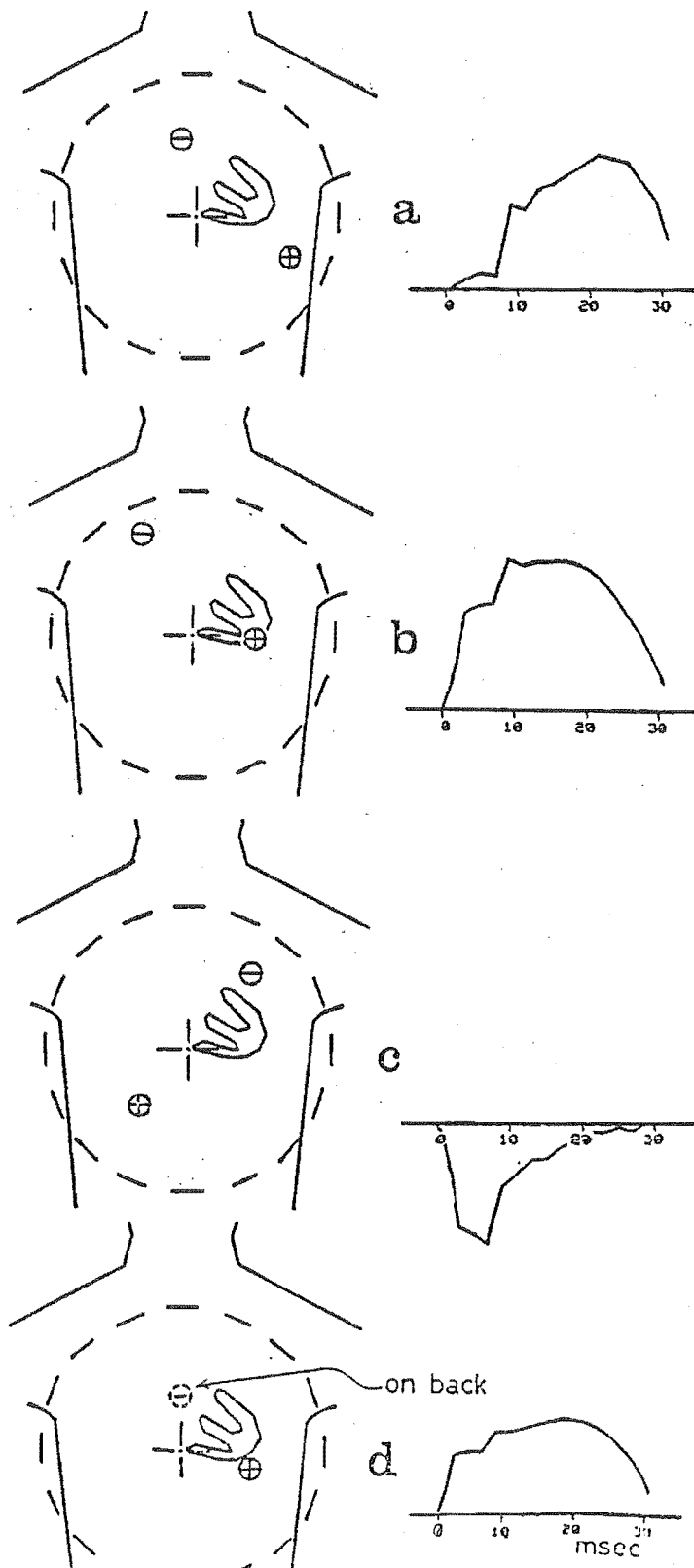


Figure 6.16 The effects of changing the electrode positions on the model V.S.C.S. signals.

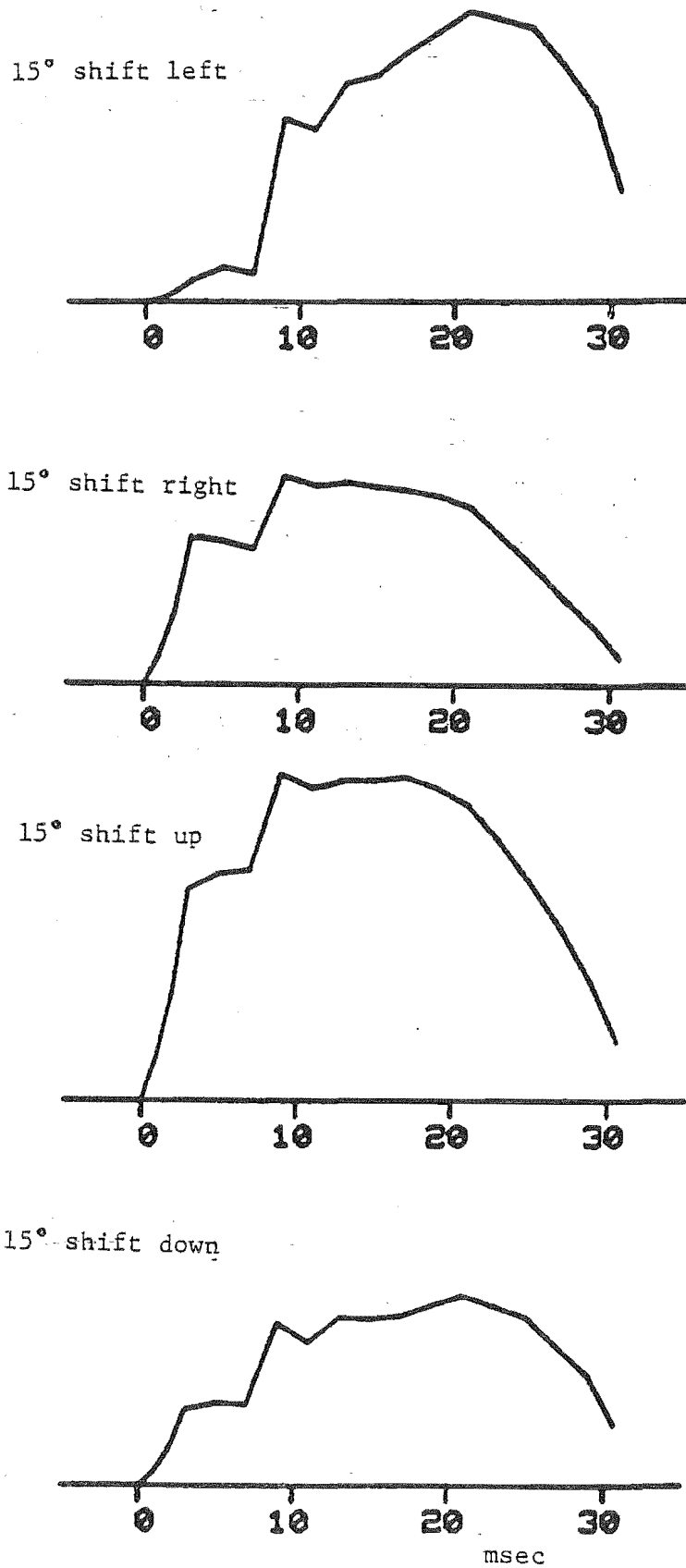


Figure 6.17 Effects of minor changes in the anatomy of the V.S.C.S. tissues on the body surface field, measured by the bipolar chest lead shown on the left of Figure 6.15.

The effects of changing the electrode positions are illustrated in Figure 6.16. The signal appears to be more sensitive to the position of the positive electrode than to the position of the negative electrode. For example, moving the negative electrode from the upper right chest to the back has little effect (cf. Figures 6.16c and 6.15), whereas moving the pair diagonally down to the left affects the early portion of the signal significantly (cf. Figures 6.16a and 6.16b). A slightly higher amplitude signal is received with the electrode positions of Figure 6.16b, than with those of Figure 6.15, though the notch in the signal is less obvious.

In Figure 6.17, the effects of minor changes in the anatomical positions of the V.S.C.S. tissues are illustrated, for the original electrode positions of Figure 6.15. The shift left or right in Figure 6.17, refers to a decrease or an increase respectively in the azimuthal angles ϕ_j and γ_j . The shift up or down in Figure 6.17, refers to a decrease or an increase respectively in the polar angles θ_j and η_j . In each case the model predicts a slight change in the signal.

6.4 DISCUSSION

The extended model presented in Section 6.1 is a useful tool for the assessment of the effects on the E.C.G. of body surface shape and internal conductivity inhomogeneities. The extended model can be applied to more realistic "bodies" than the simple model presented in Chapter 5, but it is still relatively straightforward to implement on a small computer. One disadvantage of the extended model (not encountered with the simple model) is the necessity to calculate the integrals (130) for each non-spherical boundary. These must be recalculated every time a non-spherical boundary is modified.

The results presented in Section 6.2 support the view, expressed in Section 5.4, that the internal conductivity inhomogeneities have only slight effects on the shape (i.e. spatial variation) of the E.C.G. field. They have a significant effect, however, on the peak-to-peak amplitude of the E.C.G. field. Since the current and the potential are related by $\underline{J} = -\sigma \nabla V$, the peak-to-peak amplitude of the field (for any given current source) is directly related to the mean conductivity of the body. However, the relationship of the E.C.G. field to the shape

and the positions of the inhomogeneities is much less obvious. Some insight into this relationship is provided by the applications of the extended model presented in Section 6.2. In the model of Figure 6.4, the mean conductivity of the interior of S is kept constant, while the shape of the inhomogeneity is altered. An explanation for the effects shown in Figure 6.4 is found by considering a current streamline which passes close to the surface. The streamline passes through three regions in series (κ_1 , κ_2 and κ_3), as illustrated in Figure 6.18. The regions κ_1 and κ_3 are internal, while κ_2 is parallel to S. The peak-to-peak amplitude of V_S is the voltage drop across κ_2 . When the inhomogeneity of Figure 6.4a is egg shaped (i.e. bounded with S_1' and with $\sigma' > \sigma$), κ_2 has a lower mean conductivity than when the inhomogeneity is spherical. Consequently, V_S has a higher amplitude in the former case (cf. Figure 6.4a). When the inhomogeneity is doughnut shaped (i.e. bounded by S_3'), κ_2 has a relatively high mean conductivity, and therefore V_S has a low amplitude. Conversely, when $\sigma > \sigma'$, the effects on the surface field amplitude are reversed (cf. Figure 6.4b).

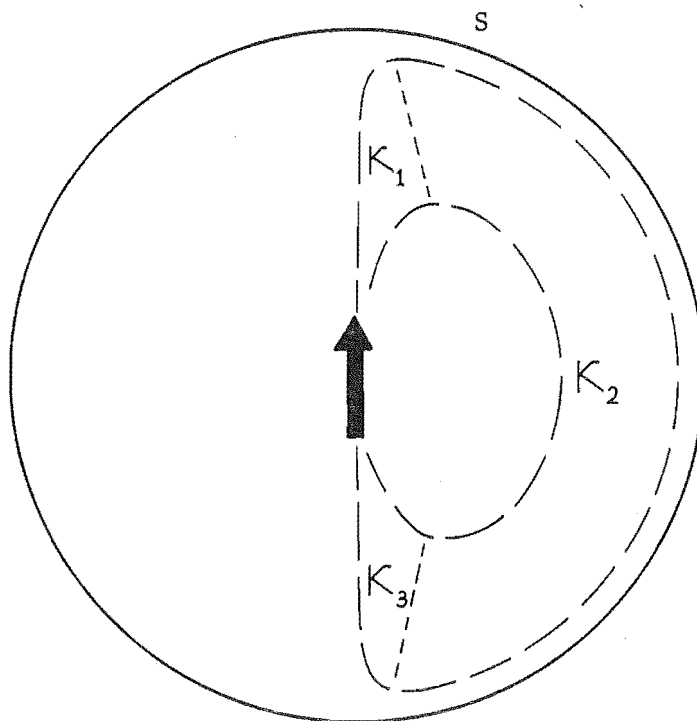


Figure 6.18 A current streamline is divided into three series regions to explain the effect of inhomogeneities on the surface field.

The three-series-region explanation offered above can also be applied to the results of Figure 6.7. The insulating region (I shall refer to it as the "hole") in Figure 6.7 is located on the axis $\theta = 0$. When the dipole is directed along the axis, the hole lowers the mean conductivity of κ_1 , causing a decrease in the peak-to-peak amplitude of V_s , compared to the homogeneous case (cf. Figures 6.7a and 6.7b). When the dipole is directed perpendicular to the axis, the hole lowers the mean conductivity of κ_2 . Consequently, the peak-to-peak amplitude of V_s is increased in this second case and the magnitude of $\partial V_s / \partial \theta$ is greater in the region over the hole than in the corresponding region on the other side of the source (cf. Figures 6.7b and 6.7d). The effect of the hole on V_s is increased as it becomes larger and as it is moved closer to the source dipole. A similar effect is seen in Figure 6.5 for $\sigma'' = 0.2$. The peak-to-peak amplitude of V_s is lower when the bulk of the (low conductivity) inhomogeneity is close to the source dipole (cf. Figure 6.5a), than when it is further from the source (cf. Figure 6.5b).

Figure 6.9 demonstrates that convergence is achieved more readily on S than on the interior surface(s). In Section 5.4, I make a similar observation for the simple model and I suggest that V_s is insensitive to the precise shape of the conductivity inhomogeneities. Two observations, following from the results in Section 6.2, support this view. Firstly, the results of Figure 6.5 (with $\sigma'' = 0.2$) and Figure 6.7c are remarkably similar, as noted in the last paragraph, despite the distinctly different shape of the inhomogeneities. Secondly, in the applications of the extended model that I have studied, the shape of V_s does not change significantly when an inhomogeneity is added.

The two models for the field generated by the activation of the V.S.C.S. (cf. Section 6.3) show clearly that the signal measured on the body surface differs markedly from the signal measured with an intra-cardiac catheter. The electrodes on the catheter are so closely spaced and so close to the V.S.C.S. tissues, that a significant signal is only received from the activation over a small portion of the V.S.C.S. Because the activation proceeds rapidly past the point closest to the pair of electrodes, the signal has a sharp peak (cf. Figure 6.12; Myers *et al.*, 1978). The frequency bandwidth of the amplifiers used in catheter studies (typically 40 to 500 Hz; cf. Narula, 1975) retains enough of the signal spectrum to allow the accurate timing of the H spike

relative to other events (cf. Fisher, 1978). However, the model of §6.3.2 predicts that the signal measured on the body surface is continuous throughout the period of the activation of the V.S.C.S. and changes relatively slowly. Consequently, the surface signal contains a considerable proportion of low frequency information (performing a Fourier transform on the model signal shows that more than 75% of the signal energy lies below 40 Hz). Clearly, therefore, the instrumentation required for the non-invasive detection of the V.S.C.S. signals must have a frequency response which extends well below 40 Hz. This point receives more attention in the discussion on instrumentation in Section 7.1.

The results presented in §6.3.3 predict that the surface V.S.C.S. signal is relatively insensitive to minor changes in the electrode positions and in the anatomical location of the tissues. It seems likely, therefore, that the electrode positions shown in Figure 6.15 (and used in making the measurements reported in Chapter 7) are adequate for most patients. Because the right ventricle lies somewhat closer to the chest surface than the left ventricle, it is likely that this bipolar chest lead is more sensitive to the activation of the right bundle branch, as opposed to the left bundle branches.

CHAPTER 7

NON-INVASIVE MEASUREMENT OF SIGNALS FROM
THE VENTRICULAR SPECIALISED CONDUCTION SYSTEM

The measurement of the activation of the ventricular specialised conduction system (V.S.C.S.) is a recent development in cardiac medicine, although the role of the V.S.C.S. has long been established from pathological studies and electrocardiography. During the last decade, the electrophysiology study by catheterisation (Damato, 1969; Curry, 1975; Narula, 1975; §1.3.7) has gained acceptance as a diagnostic tool. Although a large number of parameters of impulse propagation are typically measured during an electrophysiology study, only the H-V interval (the time of propagation from the His bundle to the ventricular myocardium) has been firmly established in clinical practice (Fisher, 1978). This is not to say that cardiac electrophysiology studies are not useful in other ways (Curry, 1975). If a method of non-invasive detection of the V.S.C.S. signals can be devised which reliably measures the H-V interval, some patients may not have to undergo invasive studies. Moreover, a non-invasive technique can be performed and repeated at much less cost (cf. Ross et al., 1980) and with no risk or discomfort to the patient.

This chapter presents a study of the use of signal processing techniques to detect the V.S.C.S. signals from surface electrocardiograms in a number of subjects. In Section 7.1 a brief review is made of the literature relating to the non-invasive detection of the V.S.C.S. signals. The methods employed in the study reported here are covered in Section 7.2. The results are presented in Section 7.3 and discussed in Section 7.4.

7.1 REVIEW

The standard interpretation of the electrocardiogram (cf. Chapter 3) assumes that the segment of the waveform between the P wave and the QRS wave (commonly called the P-R segment) contains no recognisable signals. However, both the repolarisation of the atrial myocardium (Tranchesti et al., 1960) and the activation of the V.S.C.S. are

occurring during the P-R segment in normal sinus rhythm (cf. Section 1.3). The amplification used for the standard E.C.G. presentation is sufficient to display the P, QRS and T waves with 1 cm of pen deflection per 1 mV, but it is clearly inadequate for displaying signals expected to be in the order of 1 μ V in amplitude. Furthermore, even if additional stages of amplification are added to an electrocardiograph, it is likely that the level of noise present will obscure the V.S.C.S. signals. Traditionally, therefore, the occurrence of the V.S.C.S. activation has been inferred from the temporal relationship of the P and QRS waves (see for example Marriot and Myerburg, 1978; Schamroth, 1971) rather than directly observed.

Moves to extract more information from the E.C.G. were made during the 1960's as a result of the improvements occurring in analogue electronic circuitry and the blossoming of digital electronics (Tranchesti et al., 1960; Cronvich et al., 1968; van der Groeben et al., 1968). After the development of invasive catheter techniques for detecting the activation of the bundle of His (Damato et al., 1969), attention was directed to non-invasively detecting the same information. Berbari et al. (1973) and Flowers et al. (1974) both published successful studies carried out on dogs. These early studies were followed by reports of similar measurements successfully carried out on human subjects. The reader is referred to Berbari et al. (1979) for a bibliography of the major publications up to 1979. I know of only one paper (Takeda et al., 1979) which reports the clinical use of "the non-invasive detection of signals from the V.S.C.S." (to avoid repeating this cumbersome expression, I henceforth use the abbreviation NID).

Signal averaging has been used by almost all investigators of NID to date. It is a method of improving the reception of small repetitive signals in the presence of random noise (Davenport and Root, 1958). Let a signal corrupted by random noise be $f(t)$. Within $f(t)$ a repetitive waveform is present with a period $\geq \tau$. The averaged waveform is given by

$$\bar{f}(t) = (1/N) \sum_{i=1}^N w_i(t) f(t + T_i) \quad (139)$$

for $0 \leq t < \tau$. In (139) T_i is a timing reference for the i th repetition, $w_i(t)$ is a weighting function for the i th repetition which is non-zero only for $0 \leq t < \tau$, and N is the number of repetitions averaged.

The signal-to-noise ratio of $\bar{f}(t)$ is a factor of \sqrt{N} times the signal-to-noise ratio of any one repetition of $f(t)$ (Davenport and Root, 1958). The signals from the V.S.C.S. are known to precede the QRS wave of the E.C.G. in normal sinus rhythm. The time taken for the activation

to traverse the V.S.C.S. is approximately constant (cf. §1.3.4), therefore the V.S.C.S. signals can be expected to be repetitive and synchronised with the start of the QRS wave. All investigators of NID use the QRS wave to derive the timing reference T_1 and put $w_1(t)$ equal to unity over the interval corresponding to the P-R segment of the E.C.G. The investigators have reported that NID can be successful when a large number of heart beats are averaged.

Some of the important details of the methods used to date for NID are listed in Table 7.1. In all cases a pair of electrodes are used to derive a single differential E.C.G. signal from the body surface. In several studies (indicated by an asterisk in Table 7.1), however, several electrode positions are evaluated. In all of the studies the positive electrode is positioned on the chest, either on the sternum or to the left of the sternum. The negative electrode is positioned on the right chest in five studies and on the back in three (see Table 7.1). The investigators have aimed to receive a signal of maximum amplitude and positive polarity, thus the electrode positions used indicate a general belief that the V.S.C.S. surface field has a positive maximum somewhere on the left chest. This view is supported by the model study presented in Section 6.3 (cf. Figure 6.16). Sources of unwanted signals must also be considered in choosing the electrode sites for NID. Such sources include the skeletal muscles and the muscles which control respiration. The posterior position may have been chosen for the negative electrode in some studies to reduce the interference from muscular sources.

All of the instrumentation systems used for NID have a high gain, low internal noise differential amplifier connected to the electrodes. The first stage of amplification is isolated from the electrical mains supply to eliminate the risks of patient electrocution (Dewhurst, 1976). Considerable variation is reported in the frequency bandwidth chosen for the NID instrumentation (cf. Table 7.1). I denote the low and high cut-off frequencies (-3 dB) by f_l and f_h , respectively. Most investigators have chosen f_l in the range of 30 to 70 Hz. They report that the use of a lower f_l produces "gradients" which obscure the V.S.C.S. signals. I believe that they are referring to the low frequency spectral content of the E.C.G. With the very high gains used for NID these low frequency components during the P-R segment are liable to drive the final amplifier stage into saturation. Therefore these investigators have filtered out the low frequencies.

TABLE 7.1 Summary of some important aspects of the experimental design of published studies using signal averaging to detect V.S.C.S. signals.

Electrode site +	Electrode site —	Bandwidth Hz	Number of beats averaged	Authors
cardiac apex	mid right atrial border	70 - 250	256	Furness <i>et al.</i> , 1975
sternum, 4th	posterior midline, 4th	50 - 300	100 - 500	Hishimoto and Sawayama, 1975 and Takeda <i>et al.</i> , 1979*
V ₃	posterior, 6th	10 - 1000	256	van den Akker <i>et al.</i> , 1976
V ₆	V _{6R} *	10 - 300	50 - 200	Berberi <i>et al.</i> , 1976
left parasternum, 4th	right parasternum, 3rd	30 - 300	256	Wajszczuk <i>et al.</i> , 1978
left midclavicular, 4th	right midclavicular, 4th	40 - 500	150 - 500	Vincent <i>et al.</i> , 1978
V ₆	V _{6R}	0.3 - 300	100	Berberi <i>et al.</i> , 1979

* Several electrode placements tested.

However, it seems likely from the model study of Section 6.3 and from the work published by Berbari *et al.* (1979) that much of the V.S.C.S. signal lies in the low frequency spectrum. Therefore a very low f_l is suggested by Berbari *et al.* (1979) and used in my study. The choice of f_h is less contentious; in the published studies it ranges from 250 Hz to 1000 Hz (cf. Table 7.1). Advantages in choosing a relatively low f_h are a corresponding decrease in the digital sampling and conversion rate necessary, and a reduction in the bandwidth of noise received. An advantage of choosing a higher value for f_h , however, is that the onset of the QRS wave can be detected more precisely for determining the T_i (Ribeiro *et al.*, 1980).

Several methods for obtaining an accurate time reference T_i from the i th QRS wave have been reported. Furness *et al.* (1975) and Wajszczuk *et al.* (1978) simply detect when a low pass filtered E.C.G. signal reaches a preset threshold. Hishimoto and Sawayama (1975), Takeda *et al.* (1979) and Vincent *et al.* (1978) use an analogue slope detector similar to that of a conventional test oscilloscope. The other investigators (see Table 7.1) have built custom-made QRS detectors which carry out more sophisticated analogue processing. It is likely that those relying on either the threshold or slope QRS wave detectors are seriously compromising the effectiveness of the signal averaging process. Ishijima (1978) and Ribeiro *et al.* (1980) present analyses of the attenuation in the averaged V.S.C.S. signal caused by error in the T_i . Clearly the attenuation is greatest on the high frequency components of the signal. Ishijima assumes the error in the T_i to be normally distributed. If, for example, the standard deviation of the error in the T_i is 2 msec, the spectral component in the signal at 100 Hz is attenuated by greater than 50% (Ishijima, 1978). Some investigators have established limits for the errors in their QRS wave detection systems. For example, van den Akker *et al.* (1976) report that their T_i are accurate to 0.5 msec. In the study presented in Sections 7.2 and 7.3, a signal correlation method is used to limit the error in the T_i to ± 1 msec.

The most common method of signal processing employed in NID sets $w_i(t)$ equal to 1 over the P-R segment and zero elsewhere (see equation (139)). Certain alternatives are reported, however. Ishijima (1978) reports that the H-V interval is not precisely constant (in dogs at least). He proposes that the averaging be performed by

$$\bar{f}(t) = (1/N) \sum_{i=1}^N w_i(t) f(\alpha_i t + T_i) \quad (140)$$

where the constants α_i are chosen on the basis of a *a priori* knowledge of the variation in the H-V interval. In particular, Ishijima (1978) found a (slight) negative correlation between the R-R interval and the H-V interval. He attempted to correct for the H-V interval variation but achieved no improvement in the averaged results. Marriot *et al.* (1980) suggest making the $w_i(t)$ constant over the *i*th averaging window and inversely proportional to the variance of the noise in that window with

$$\sum_{i=1}^N w_i(t) = 1 .$$

They predict a significant improvement in the signal-to-noise ratio with their technique. Ros (1980) reports that the respiratory variation in the P-R interval can be used to distinguish the V.S.C.S. signals from the end of the P wave. A similar method is detailed in §7.2.3.

At least two authors (Trethewie, 1977; Flowers *et al.*, 1981) report direct observations of the V.S.C.S. signals without recourse to signal averaging. It seems quite likely that these "signals" are related to activity in the V.S.C.S. but it is extremely difficult to reliably detect significant features in the presence of even a small level of noise. This is discussed further in §7.3.1.

I have reviewed above the major contributions to the research on NID and discussed some important aspects of the methods used. It remains for me to summarize the results obtained to date. A sample waveform from each of ten papers quoted in this section is reproduced in Figure 7.1. The electrode sites and instrumentation (and of course the subjects) vary from study to study, so a meaningful comparison is difficult. However, the effect of differing frequency response is clearly apparent. Waveforms a to h inclusive are ordered (from highest to lowest) according to the value of f_ℓ used (cf. Table 7.1). Waveforms a to e inclusive were obtained with $f_\ell \geq 30$ Hz and show a corresponding predominance of high frequency spectral components. In contrast, the waveform of Berbari *et al.* (1979) obtained with $f_\ell = 0.3$ Hz shows a significant low frequency content (waveform h). Similar waveforms are reported by Mohammad-Djafari *et al.* (1981). Waveforms f and g were obtained with $f_\ell = 10$ Hz.

The last two waveforms in Figure 7.1 were measured by Trethewie (1977) and Flowers *et al.* (1981), respectively, without signal averaging.

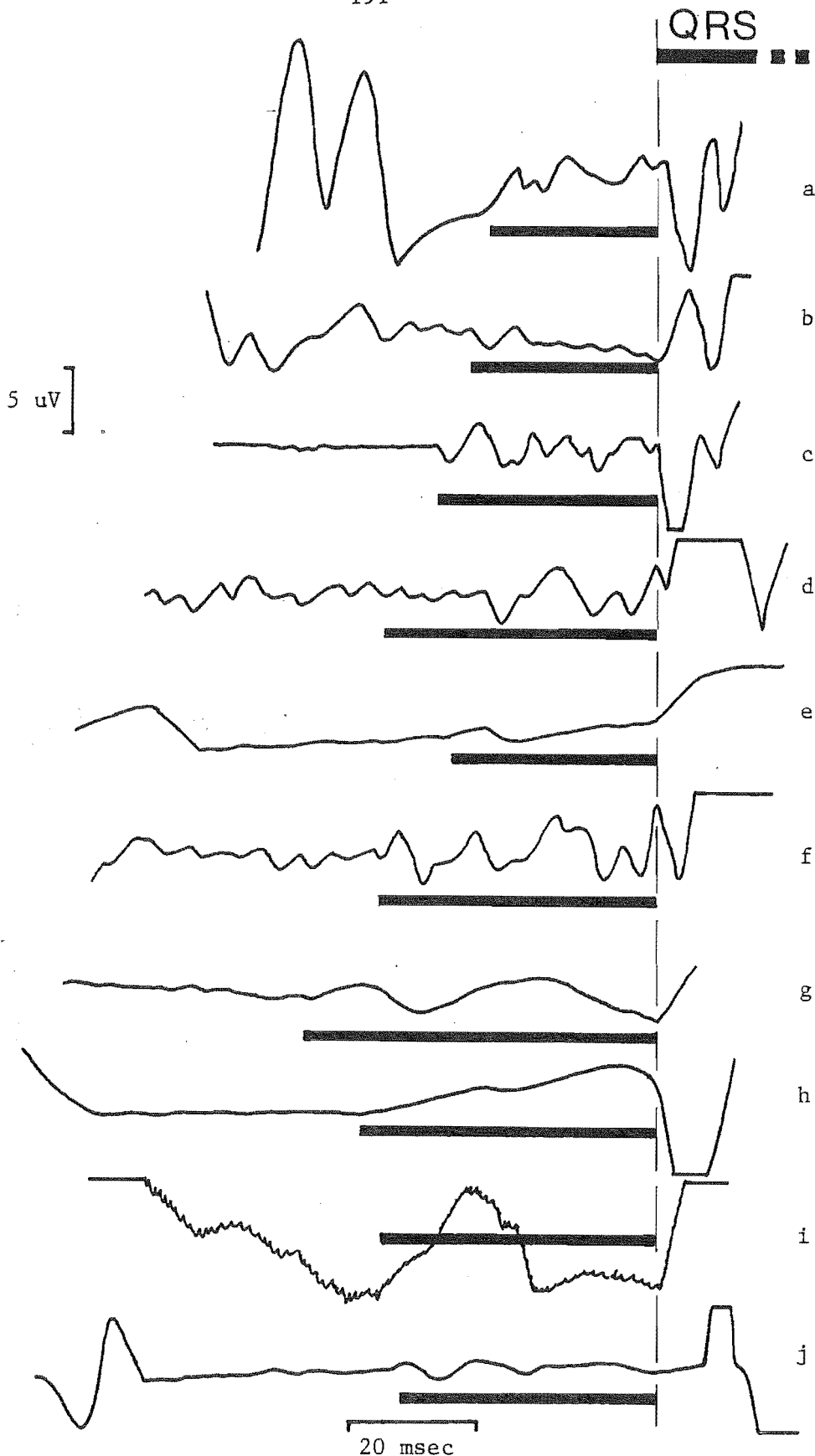


Figure 7.1

A sample waveform from each of ten published studies of NID. Waveforms a to h inclusive were obtained by signal averaging, i and j were measured directly. a) Hishimoto and Sawayama, 1975; b) Furness *et al.*, 1975; c) Takeda *et al.*, 1979; d) Vincent *et al.*, 1978; e) Wajszczuk *et al.*, 1978; f) van den Akker *et al.*, 1976; g) Berbari *et al.*, 1976; h) Berbari *et al.*, 1979; i) Trethewie, 1977; j) Flowers *et al.*, 1981.

Trethewie's waveform was measured with a bipolar lead described elsewhere ("Lead A" in Trethewie, 1953) and an instrumentation system with a bandwidth of 0.05 to 2300 Hz. Flowers *et al.* measured their waveform by means of a number of electrodes and amplifiers connected in parallel and their system had a bandwidth of 35 to 300 Hz (f_l was adjustable in the range 10 to 35 Hz).

7.2 METHODS

In this section the methods I have used to non-invasively detect the V.S.C.S. signals in a number of subjects are described. Every effort has been made in the study to achieve optimal conditions for the reception of the very small signals. A bipolar lead is positioned by a *priori* reasoning to maximize the expected V.S.C.S. signals. The instrumentation and the measurement protocol are designed to reduce interference to a minimum. For the same reason the computer programs for processing the electrocardiographic signals are designed to give the best possible performance rather than to operate at high speed.

It was not practical to carry out the measurements near the PDP 11/10 computer used for signal processing. Therefore a tape recorder was used to record the data permanently in digital form. A single electrocardiographic signal only was recorded and processed to reduce the instrumentation costs, development time and internal noise to the maximum possible. The complete wiring diagram of the instrumentation is contained in Appendix 2. For information on other equipment mentioned, the reader is referred to the technical manuals of the manufacturers concerned (these are listed in Appendix 2).

§7.2.1 Instrumentation

A block diagram of the instrumentation used in this study is shown in Figure 7.2. A commercially designed differential preamplifier (Medelec AA6, Mk I) forms the first stage of amplification. This preamplifier has a gain of 100 over the bandwidth of D.C. to 20 kHz. The input impedance is greater than 10 M Ω and the common-mode rejection is greater than 110 dB at 50 Hz (cf. Dewhurst, 1976). The inputs of the preamplifier are protected from electrostatic discharges by very low leakage current diodes (BAV 45) connected between the inputs and the power supply earth (cf. Appendix 2).

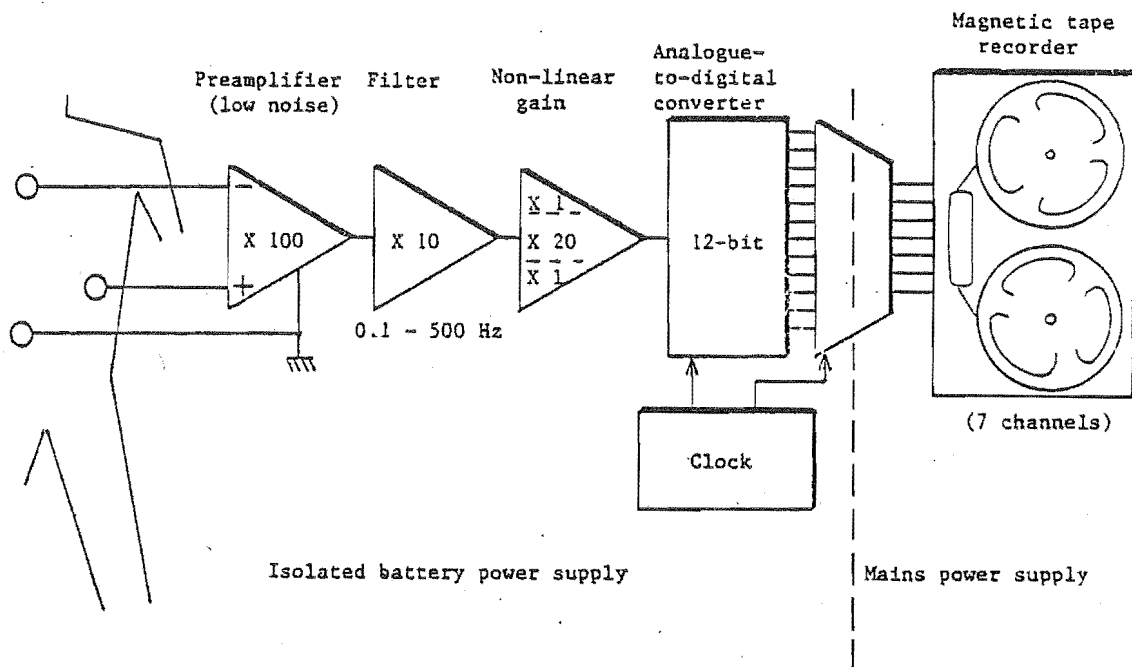


Figure 7.2 Block diagram of the instrumentation used for the NID study.

To reduce the common-mode signal received by the preamplifier, a third electrode is applied to the subject's chest and connected to the power supply earth at the preamplifier (cf. Figure 7.2). The metal box enclosing the preamplifier is earthed at the same point. The electrode-connecting wires are shielded almost to the electrode connectors. The single-ended output of the preamplifier is connected to the next stage of the instrumentation by a shielded cable.

The second stage of the instrumentation is a band-pass filter with a gain of 10 over the band 0.1 to 500 Hz (-3 dB points). The wide band is used to ensure that all information relating to the V.S.C.S. activity is received. The model study of Section 6.3 led me to believe that most of the energy contained in the V.S.C.S. signal would lie in the frequencies below 50 Hz so f_l is chosen as 0.1 Hz. The response of the instrumentation cannot be extended to d.c. since a small mismatch in the polarization voltages across the electrodes (cf. Geddes, 1972) would then drive later stages of amplification into saturation. The f_l chosen corresponds to a time constant of 1.6 sec for a step offset applied to the input.

The third stage of the instrumentation is a non-linear amplifier. Signals of magnitude less than 0.125 volts at the input of this amplifier experience a gain of 20 while signals of larger magnitude experience unity gain. The gain characteristic of the operational amplifier circuit used (cf. Appendix 2) is similar to that shown in Figure 7.3. The purpose of this stage is to allow the QRS wave through without clipping while the V.S.C.S. signals are amplified sufficiently to be detected after analogue-to-digital conversion. All of the E.C.G. waveform is required because the detection of the QRS wave for timing purposes is carried out offline when the data is played back from the recorder (see below). An alternative approach (which was considered at the time of designing the instrumentation) is to record two channels of information, one at a gain sufficient to detect the V.S.C.S. signals (but too great to avoid amplifiers saturating on the larger signal features) and one at a lower gain for triggering the signal averaging. The single channel approach is adopted here to simplify the instrumentation. Note that other investigators have avoided this particular design decision by carrying out the QRS triggering in real time using analogue circuitry. I do not consider that any analogue device yet designed can provide a QRS trigger which is accurate enough (cf. Section 7.1) for NID in the presence of sinus arrhythmia and other rhythm disturbances (cf. §1.4.4 and §1.4.5).

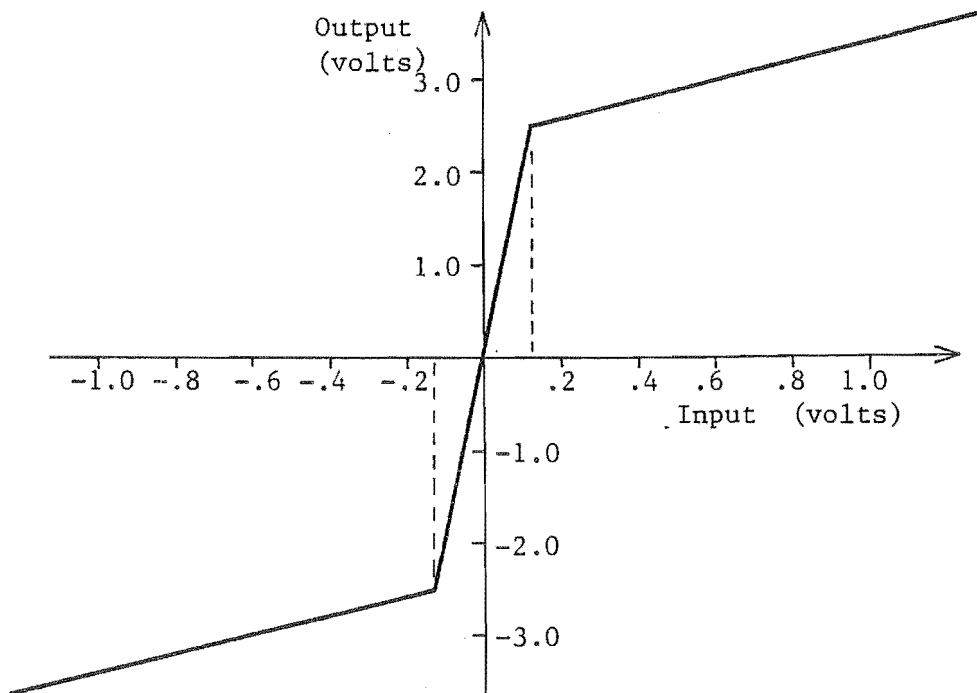


Figure 7.3 The gain characteristic of the non-linear gain stage.

The output of the non-linear gain stage is sampled and digitized at 1000 samples per second and with 12-bit precision. f_h is chosen to be 500 Hz to satisfy the sampling theorem (Raemer, 1969). Two commercial devices are used to perform the analogue-to-digital conversion (DATEL SHM-IC-1 sample-and-hold circuit and DATEL ADC-HZ12BMC analogue-to-digital converter). Both are connected according to the manufacturer's specifications (cf. Appendix 2). The effective resolution of the digital conversion is $0.093 \mu\text{V}$, referred to the electrode inputs, for the low level signals which receive maximum amplification. A V.S.C.S. signal of (say) $1 \mu\text{V}$ is therefore only spanning eleven quantization steps, but Diebold (1977) shows that the resolution of a quantized signal is improved by signal averaging. As a simple illustration, consider that the j th sample of the input signal in the averaging window is f_j and that $q < f_j < q + h$, where q and $q + h$ are adjacent quantizing levels. Although f_j may only have the digital value q or $q + h$ for each repetition, after N repetitions the averaged value \bar{f}_j may be q , $q + h$ or one of $N - 1$ values in between. The resolution after averaging is therefore h/N . Note that the finer resolution of the averaged signal is due to the presence of noise in the input signal (Diebold, 1977).

The 12 output lines of the analogue-to-digital converter are multiplexed into six lines by digital logic gates so that all of the data can be recorded by a 7-channel frequency multiplexed (F.M.) tape recorder (Electrodata 6500). The seventh recorder channel is used to record a two-level clock signal which also controls the multiplexing. When the clock signal is low, the least significant 6 bits of the analogue-to-digital converter output are recorded; when the clock signal is high, the most significant 6 bits are recorded (see Appendix 2). All seven signals are passed from the digital circuitry (battery powered - see below) to the recorder via Optron 12252 optical couplers. No direct connections occur between the instrumentation and the recorder. The recorder is operated at a tape speed of 9.5 cm/sec which corresponds to a frequency response of d.c. to 1250 Hz. The bandwidth is sufficient to allow perfect recovery of the recorded data when the tape is replayed and decoded (cf. §7.2.2).

The instrumentation from the preamplifier to the input side of the optical couplers is powered by a bank of seven rechargeable batteries. The batteries are 8 ampere-hour 6-volt Nickel-Cadmium units (Yuasa NP8-6). Three are used to provide a positive 15-volt regulated supply and three

more to provide a negative 15-volt regulated supply (cf. Appendix 2). The final battery provides a positive 5-volt supply via two forward biased power diodes in series (cf. Appendix 2). A common earth point is formed at the battery supply. Separate earth wires are taken from this point to the digital circuitry powered by the 5-volt supply and to the analogue circuitry powered by the 15-volt supplies. The shielding encasing all of the instrumentation (except the tape recorder) and cabling is connected to the analogue supply earth at the preamplifier (at the same point as the common-mode electrode). I found the text of Morrison (1967) useful in designing the shielding to minimise the sensitivity of the instrumentation to external sources of noise and to minimise crosstalk between the digital and analogue circuitry.

§7.2.2 Measurement protocol

In this sub-section I outline the manner in which measurements for NID are made with the instrumentation described in §7.2.1. I then review the material (both normal subjects and cardiac patients) that was studied to produce the results presented in Section 7.3.

The two measuring electrodes are positioned as shown in Figure 7.4.

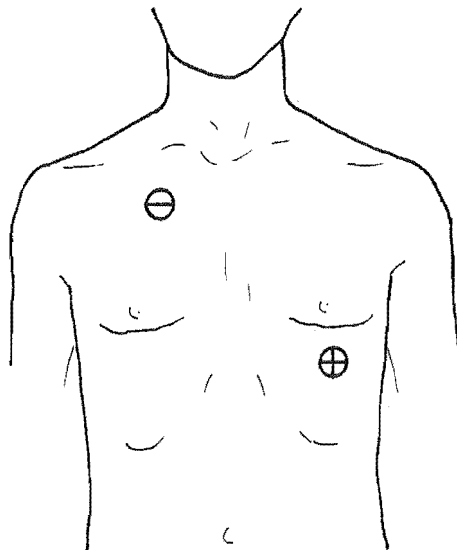


Figure 7.4 The approximate lead placement used in the study of NID reported here.

The positive electrode is in the V_4 position of the standard chest lead set (cf. §3.3.1). The negative electrode is at the right infraclavicular fossa. This bipolar lead is similar to that used by the majority of NID investigators (cf. Table 7.1). According to the modelling study presented in Section 6.3, the lead should receive a signal from the V.S.C.S. of the type shown in Figure 6.15. The position of the third (common-mode) electrode is not important. The site of each electrode is prepared as follows: 1) a vigorous rub with a pad of lint soaked in surgical alcohol and dusted with dental pumice powder; 2) a sponge with a clean alcohol-soaked pad; 3) a rub with a dry clean towel. An electrode of the disposable pre-gelled variety is then firmly applied after fastening on the electrode connecting wire. Several types of electrode were used and each was tested with an electrode impedance meter (Medical Physics Department, Christchurch Hospital). All the pre-gelled silver/silver chloride types that were tested gave a satisfactory performance although the Physio-Control Life-Patch electrodes consistently gave the lowest electrode/body/electrode impedance. It is possible to achieve an impedance of less than 500 ohms at 22 Hz in most subjects with the preparation outlined above. A low electrode impedance is necessary to minimise the reception of common-mode signals and noise from within the electrode interface and to maintain a stable electrode polarization voltage (cf. Geddes, 1972).

Of the 35 subjects studied, 15 were young fit normals in whom there was no evidence of cardiac disease. Each was studied in an electrostatically shielded room in which no mains-powered appliances were operating. Each normal subject was made comfortable in the supine position while the electrodes were applied. The battery-powered instrumentation was positioned alongside the subject inside the shielded room and the tape recorder was positioned outside the room. An oscilloscope was temporarily connected to the output of the non-linear gain stage of the instrumentation (cf. Figure 7.2) before making a recording, to check that the electrodes were making good contact to the subject and to check on the level of interference of skeletal muscle signals. This check frequently was necessary as a means of instructing subjects how best to relax the muscles in the chest and neck. The subject was then left in darkness and reasonable quiet for several minutes preceding and during the recording of data. The recording was made for at least 5 minutes with a tape speed of 9.5 cm/sec.

Twenty of the subjects studied were cardiac patients who were under the care of a consultant cardiologist at The Princess Margaret Hospital, Christchurch. All of the patients were either suspected of having a rhythm disorder or had a similar confirmed diagnosis. The rhythm disorders were tachyarrhythmias (12 patients), syncopal attacks (4) or long P-R intervals (4). A routine cardiac electrophysiology study (cf. §1.3.7; Narula, 1975) was performed on each patient. In 18 of the 20 patients a bipolar catheter was successfully manipulated through the tricuspid valve by a standard technique (Damato, 1969) to record the intracardiac His bundle electrogram. The H-V interval (defined to be the interval from the onset of the His bundle signal detected by the catheter to the onset of the ventricular activation detected by a simultaneous conventional E.C.G.) was measured in these patients for comparison with the NID results.

In five of the 20 patients, tape recordings of the surface electrocardiogram were made in exactly the same manner as described above for the normal subjects. The recordings were made as near as possible to the day of their electrophysiology study. In the other 15 patients, the tape recordings for NID purposes were made immediately before or during the electrophysiology study. In all of these latter cases the instrumentation and tape recorder were positioned alongside the patient in a catheterisation laboratory. Other equipment (mains-powered) was connected to the patient and the laboratory was not electrostatically shielded. In other respects (e.g. the electrode siting and preparation) the protocol for the measurements made on the patients in the catheterisation laboratory was identical to that used for the normal subjects.

§7.2.3 Signal processing

The tape recordings of digital data obtained by the measurement protocol outlined in §7.2.2 were decoded and analysed by a PDP 11/10 computer. The software I have developed for that purpose is outlined below. The description of the software is organised into four sections: data handling, QRS alignment, the basic averaging algorithm, and other algorithms.

The seven channels of digital data on the magnetic tape were replayed into the computer via a 16-bit digital I/O port (DR11-K). The input bit which received the clock signal (from tape channel 7) was

hardware-programmed to cause a processor interrupt on every transition of the clock signal. Six bits of data were input following each interrupt so that a full 12-bit data word was received for every complete clock period. The timing of this operation was arranged so that slight differences between the tape recorder channels (both in time skew and frequency response) did not cause errors in the decoded data. Thus the entire data transfer from the analogue-to-digital converter to the computer memory, including the tape transfer, was error free. The data was loaded from memory onto a cartridge 2.4M byte disk (RK05) to form a file 500 disk blocks (500×256 words) long. The file then contained 128 seconds of the sampled E.C.G. waveform. Each file was maintained only as long as that subject's data was needed for analysis since a permanent recording of the data existed on the magnetic tape.

During the analysis of a particular file of data, only four consecutive blocks of the file were resident in memory at any one time. A number of data handling subroutines allowed the file to be sequentially "rolled" through a buffer area in memory or a particular 4-block section to be brought into memory. Other routines displayed the current memory buffer contents on a Tektronix 4012 storage graphics screen. This software was designed to aid the development of analysis algorithms rather than to achieve high speed.

As discussed in Section 7.1, the accurate alignment of the ventricular activation in each beat is vital to the success of signal averaging for NID. In contrast to the methods used by other NID investigators, the alignment in my system is controlled by software with manual interaction. A typical QRS wave is selected from the first few blocks of the data file and three points (approximately on the Q, R and S waves respectively) are defined by positioning a vertical cursor on the graphics screen. These three points (specified in terms of their spacing in time and amplitude) form a "QRS template" for the detection of other QRS waves in the file. The vertical cursor is then used to define two time intervals near the template. One is a correlation ("C") interval, which includes the earliest sharp deflection of the QRS wave and which is less than or equal to 25 msec (i.e. 25 samples) in width. The other interval ("A") defines the window over which averaging is to be performed. The A interval contains a maximum of 128 samples (i.e. 128 msec). Once the manual definition of the intervals is completed, analysis may begin. During the analysis each QRS is detected, then aligned, in a two-stage process.

I define a "coincidence index" by the expression

$$\langle g(T) \cdot \omega \rangle = \frac{\sum_{i=0}^{M-1} (g(T+ih) - \omega(ih))^2}{\left[\sum_{i=0}^{M-1} (g(T+ih) - \omega(ih)) \right]^2} / M \quad (141)$$

where g and ω are functions of time with a sampling period of h , and ω is non-zero only over the first M samples. Note that this index, which is used several times below, is similar to the standard cross-correlation function except that the mean difference between the two waveforms is ignored and perfect coincidence results in an index of zero.

Each QRS wave is detected by stepping through the data file, five samples at a time, until the coincidence index of the QRS template with the corresponding three points of the data file drops below a preset threshold value. This completes the first stage of the QRS detection and derives an approximate reference time T' . In the second stage, the original data in the C interval, denoted f_C , is compared to the data of the new beat over the range of reference times $T' - 10h$ to $T' + 10h$ by calculating $\langle f(T) \cdot f_C \rangle$ at each step. I define the QRS reference time of a beat as the time T which gives the minimum $\langle f(T) \cdot f_C \rangle$.

The basic averaging algorithm used in this study uses equation (139) with $w_i(t)$ put equal to 1 over the A interval for all beats $i = 1$ to N . Thus the averaged waveform is

$$\bar{f}(t) = \sum_{i=1}^N f(t + T_i) \quad , \quad 0 \leq t \leq \tau \quad (142)$$

with the QRS reference times T_i derived as described above. As averaging proceeds, beat-by-beat, the averaged waveform is plotted on the graphics screen after every 10th additional beat. This allows an assessment to be made of when the addition of extra beats is not noticeably reducing the noise level on the signal. On occasions it is also possible to detect the existence of a beat which is so corrupted by noise that it ruins any chance of detecting small signals. An editing routine is used to remove such a beat from the data file. Generally, averaging is performed on groups of approximately 50 beats with satisfactory results. Comparing the averaged waveforms obtained from several exclusive groups of beats aids in the recognition of signal features. Clearly, such features appear on all averaged waveforms whereas features which result from residual noise are unlikely to do so.

In addition to the basic averaging algorithm, three other signal processing algorithms have been tried on the data collected for this NID study. The three algorithms are given the names "manual selection", "shift and correlate" and "R-R partitioning".

In the manual selection algorithm, each beat is displayed (i.e. the raw data) after the QRS detection but before inclusion in the basic averaging process. If an excessive amount of noise is observed during the A interval or at the onset of the ventricular activation (which may compromise the QRS alignment process), the beat may be discarded. Otherwise the manual selection algorithm is identical to the basic averaging algorithm.

The shift and correlate algorithm involves considerably more processing than the other algorithms (and is correspondingly slower). Initially, the basic averaging process is performed on a preset number of beats. Let the resulting averaged waveform be $\bar{f}_A(t)$ over the A interval. A second pass is made through the same data. For each beat the QRS reference time is corrected by finding ΔT such that $\langle f(T_1 + \Delta T), \bar{f}_A \rangle$ is a minimum, with ΔT in the range $-5h$ to $5h$. Averaging is then performed again with the corrected reference times and the result is displayed along with $\bar{f}_A(t)$. Because the shift and correlate process is degraded by any large noise pulse within the A interval, it is essential to carry out manual selection before this process is invoked.

The R-R partitioning algorithm attempts to distinguish the features in the averaged waveform which are associated with the activation of the atrial myocardium from the V.S.C.S. signals. Sinus arrhythmia (variation in rhythm associated with respiration; cf. §1.4.5) occurs in most people. During inspiration the heart rate increases (and therefore the R-R interval decreases) and the time taken for the excitory impulse to propagate through the A-V node increases slightly in most people. During expiration the reverse changes occur. The R-R partitioning algorithm selects for averaging only those beats which are preceded by a R-R interval within a manually specified range. A plot of the R-R intervals is provided to aid in the definition of the range. Otherwise this algorithm is the same as the basic averaging algorithm. Two or more groups of beats with exclusive R-R ranges are averaged and compared. If the R-R partitioning algorithm is successful, the averaged waveform features associated with the atrial myocardium (i.e. the last portions of the P wave) differ from group-to-group while the V.S.C.S. signal features remain the same.

7.3 RESULTS

In this section I summarize the results of my study of NID. The results are partitioned into the performance of the instrumentation, the success of the signal processing algorithms, the comparison of the measurements with the model predictions and finally the comparison of the NID measurements with the invasive measurements.

§7.3.1 Performance of the instrumentation

The overall internally generated noise of the instrumentation system is less than 1 μV r.m.s. referred to the input. When the instrumentation is connected to a subject in a screened room, as described in §7.2.2, no interference of mains origin can be discerned on the recorded data (decoded and displayed with the computer). The noise performance when operating the instrumentation in the (unscreened) catheter laboratory in the presence of mains-powered equipment is not noticeably different. Unwanted signals of muscular origin (I shall refer to this as physiological noise) do, however, occur at peak-to-peak amplitudes of up to 100 μV at the input, even on a "relaxed" subject. I found that it was impossible to reduce the level of such noise on three of the 35 subjects to a level which would make NID feasible. For example, Figure 7.5a shows a 1.024 second section of the "best" recording from one subject. The vertical scale shown applies to the central, high-gain region (recall that there is a non-linear amplifier in the instrumentation - §7.1.1). Fortunately most subjects can be relaxed sufficiently to reduce the physiological noise to a level which does not preclude the use of NID. In Figure 7.5b, an example is shown of data which has a low level of physiological noise.

The signals from the V.S.C.S. seem to be directly observable on the raw data of several of the subjects studied. This accords with what has been suggested by at least two previous investigators (Flowers *et al.*, 1981; Trethewie, 1977). For example, in Figure 7.6 the P-R segments of 10 consecutive beats of the raw data from one subject are plotted (numbered 1 to 10). The reference time of each beat is aligned vertically. The lowest waveform in Figure 7.6 is

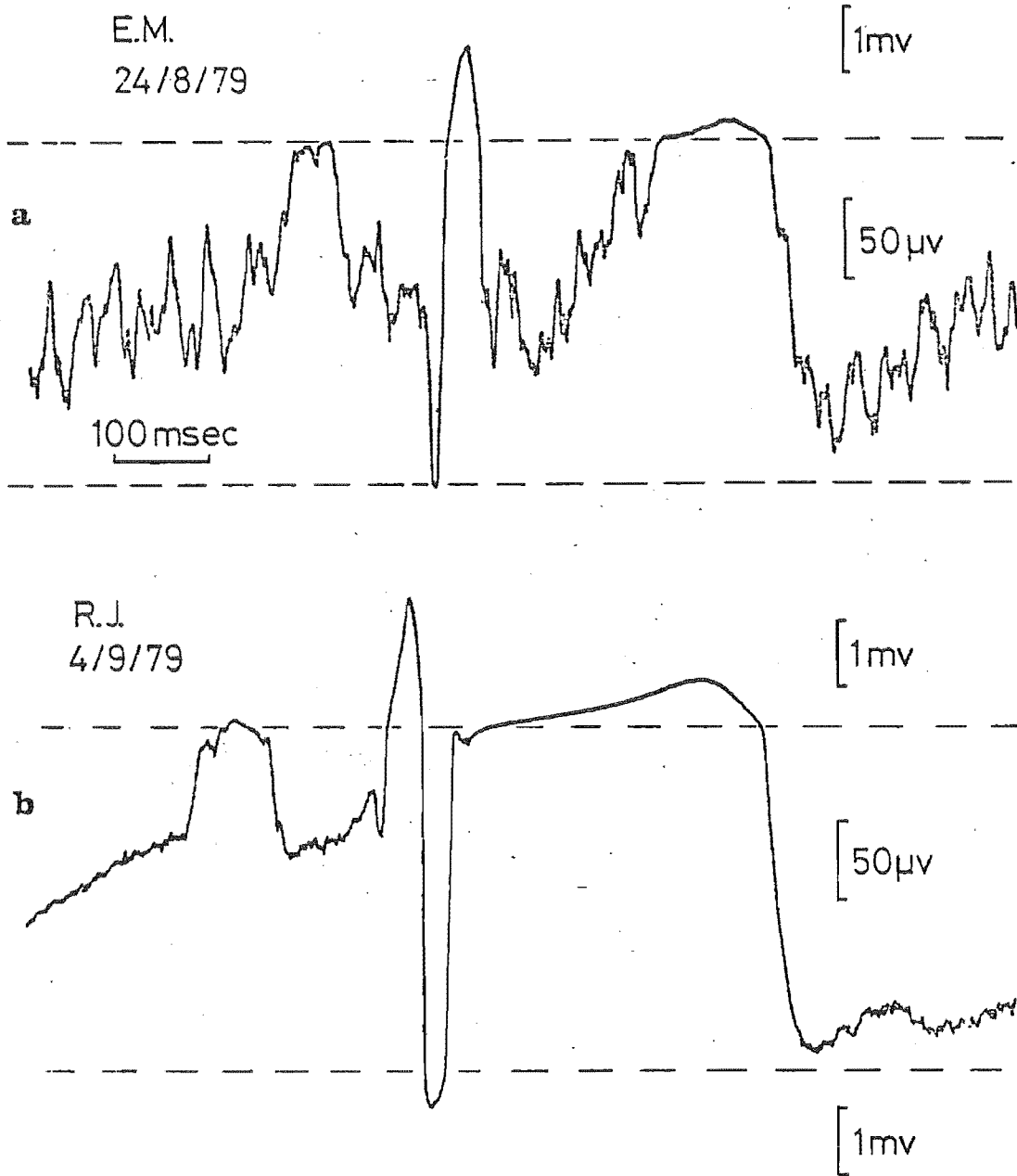


Figure 7.5 Examples of unprocessed data from two subjects showing a) high and b) low levels of physiological noise.

an averaged waveform (50 beats) from the same subject. The signal from the V.S.C.S. is underlined. Note that in several of the individual beats (cf. beats 1, 5 and 7 with \bar{f}) the same signal can be observed, while in the others it is obscured by noise. Clearly, reliable detection of the V.S.C.S signals from the raw data is difficult if not impossible unless the level of noise in the signal is extremely low.

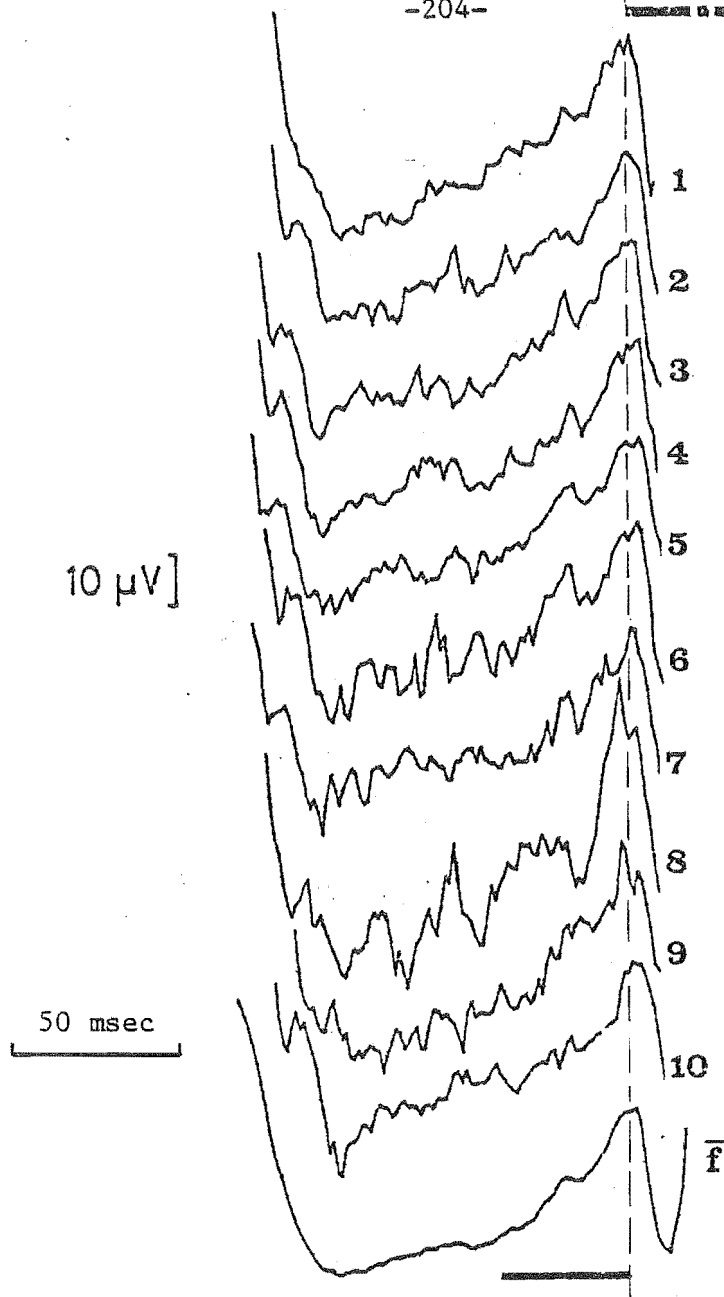


Figure 7.6 Direct observation of the V.S.C.S. signals. A plot of 10 consecutive beats and a 50-beat average from one subject.

§7.3.2 Signal processing

In 30 of the 35 subjects studied some V.S.C.S. signals were detected by the basic averaging algorithm. The averaged waveforms from several exclusive groups of beats (about 50 in each) were compared to distinguish signal features from residual noise. A selection of the basic averaged results for five subjects are shown in Figure 7.7. The onset of the QRS wave is aligned in each case to allow comparison between the waveforms. Only the last 10 msec of the P wave is shown in each case.

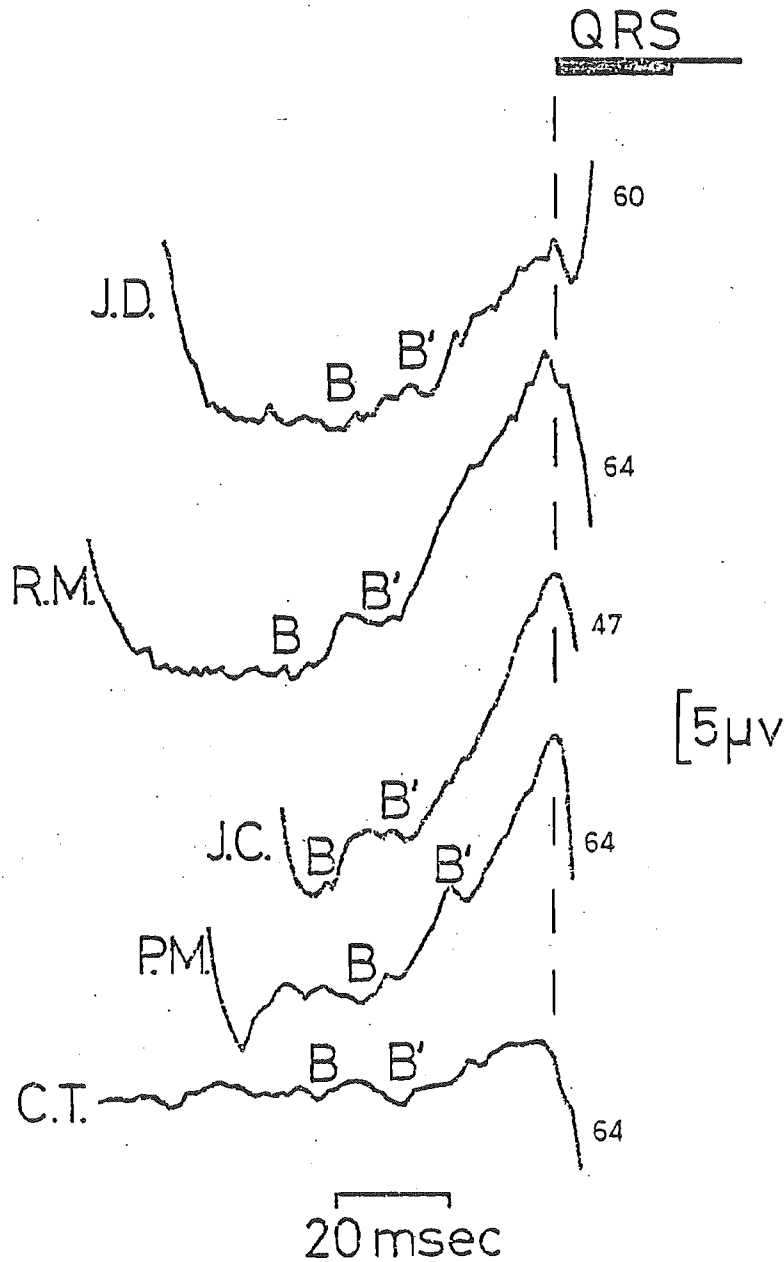


Figure 7.7 Averaged V.S.C.S. waveforms from five subjects. The number of beats averaged in each case is indicated on the right.

Two features in the V.S.C.S. signal are identified in Figure 7.7. The feature labelled B is the initial positive deflection of the waveform. B' is a second positive deflection, following a notch, which occurs at approximately one third of the interval between B and the onset of the QRS wave (cf. Figure 7.7). The averaged waveforms from all of the 30 subjects I studied successfully are similar to those in Figure 7.7. In eight subjects, however, it is not possible to distinguish one or both of the B and B' features from signals which arise from atrial activity, i.e. the P wave overlaps the V.S.C.S. waveform. The relationship of the B and B' features to the activation of the V.S.C.S. is discussed in §7.3.3 and §7.3.4.

It is difficult to determine the size of the V.S.C.S. signals from the averaged waveforms. Referring to Figure 7.7, the slope on the waveform near the onset of the QRS wave is probably only in part due to the V.S.C.S. activity. Atrial repolarisation and the effect of the high pass filter incorporated in the instrumentation (cf. §7.2.1) are both likely to contribute to the slope. However, it seems likely that the maximum amplitude of the V.S.C.S. signal is typically of the order of 5 μ V.

The manual selection, shift and correlate and R-R partitioning algorithms do not significantly improve the detection of V.S.C.S. signals in the subjects of this study, as compared to the basic averaging algorithm. The manual selection algorithm is useful in removing a small number of beats which are badly corrupted by noise. It is also useful in removing abnormal beats (e.g. ventricular ectopics) which have an altered stimulation sequence (and therefore an altered or missing V.S.C.S. signal). The shift and correlate algorithm proves to be very susceptible to low frequency information in the averaging window, some of which is probably unrelated to activity in the V.S.C.S. For example, if the end of the P wave extends slightly into the averaging window (as it frequently does), the shift and correlate algorithm tends to align that portion of the P wave rather than the V.S.C.S. signals. In many cases this algorithm degrades the averaging process. Finally, the R-R partitioning algorithm used in this study does not enable the P wave activity to be distinguished from the V.S.C.S. signals, despite the reported success of Ros (1980) with a similar technique. The algorithm is useful for partitioning the data into exclusive groups of beats (for comparison of the averaged results), but I find that the change in the P-R interval with respiration is too small to detect on the averaged recordings.

In five of the 30 subjects studied no V.S.C.S. signals were detected by any of the signal processing algorithms. In three of these, the failure was caused by the presence of a large amount of physiological noise (Figure 7.5a shows a beat from one of these subjects). In the other two, the reason for failure was undiscovered.

§7.3.3 Comparison of NID with invasive measurements

In 18 patients an intracardiac catheter was positioned to attempt to measure the activity of the bundle of His. The surface recordings from two of these patients contained such a high level of physiological noise that no NID was possible. In one other patient the existence of

an abnormality of impulse conduction (pre-excitation syndrome, cf. §1.4.5) prevented the detection of the V.S.C.S. signals by invasive or non-invasive means. In the remaining 15 patients, the H-V interval was measured from the invasive catheter signals (see §1.3.7) and NID was successfully performed by the basic averaging algorithm.

In Figure 7.8 the H-V intervals for the 15 patients are plotted against the corresponding intervals by the NID technique. Thus the B-V interval (filled circles) is the time from the B feature on the surface V.S.C.S. waveform to the onset of the ventricular activation, and the B'-V interval (open circles) is defined in the same way. In 10 out of 15 patients the B point occurred within ± 5 msec of the H point.

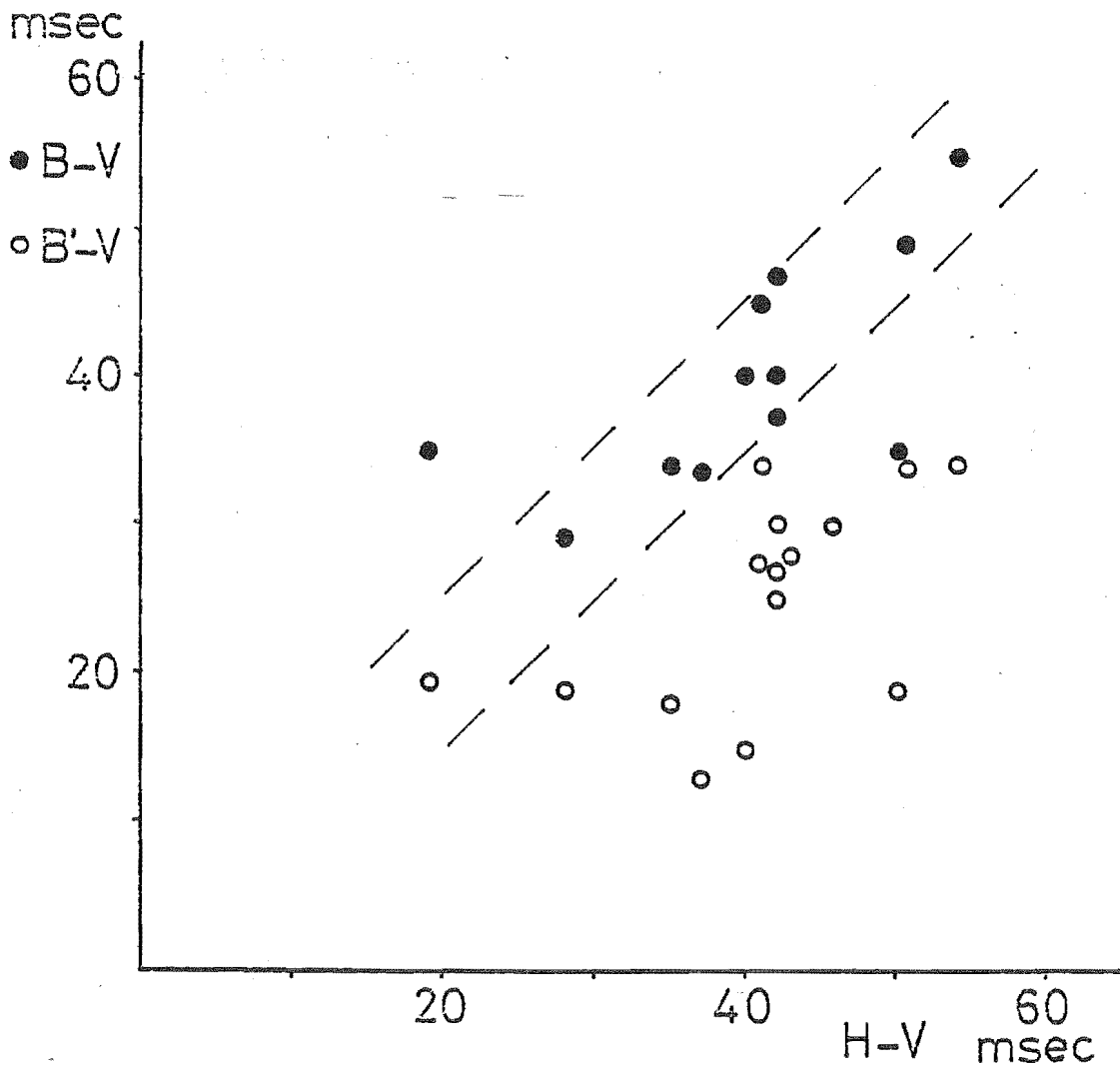


Figure 7.8 A comparison of the times of occurrence of the B and B' features (NID) and the His spike (catheter).

In my experience ± 5 msec is the approximate error bound for making measurements from catheter recordings (provided the His spike is correctly identified). For the case plotted most leftward in Figure 7.8, it is possible that the intracardiac catheter was incorrectly positioned and the activation of tissues lower in the V.S.C.S. than the bundle of His was detected. In three other patients, the P wave extended into the averaging window and prevented the detection of the B feature by NID. Only the B'-H interval is plotted for these patients.

§7.3.4 Comparison of the V.S.C.S. waveforms with the model predictions

The modelling presented in Section 6.3 predicts that the V.S.C.S. signal received by a bipolar lead (similar to that used in this experimental study) will look like the waveform in Figure 6.15. The waveform is relatively low-frequency in nature and is continuous, without zero crossings, throughout the V.S.C.S. activation. The model signal has an initial positive deflection corresponding to the initial activation of the bundle of His. A notch and a further positive deflection occurs when the activation (in the model) proceeds from the bundle of His into the bundle branches.

The resemblance of the waveform predicted by the model to those detected by NID (both in this study, and by Berbari *et al.*, 1979) is remarkable (compare Figure 6.15 with Figure 7.7 and Figure 7.1h). This close resemblance to the experimental data, coupled with the encouraging results in §7.3.3, suggests that the B and B' features are likely to be associated with the initial bundle of His activation and the movement of the activation into the bundle branches, respectively.

7.4 DISCUSSION

The success of NID is clearly dependent on the quality of the instrumentation used and on its method of use. This study suggests, however, that provided a critical threshold of performance is achieved with the instrumentation, electrode preparation, etc., then the success of NID is primarily dependent on factors which are external to the measuring system (these are discussed in following paragraphs). The critical performance specifications for NID (using signal averaging) are a total measuring system noise level of less than 2 μ V r.m.s. referred to the input and a bandwidth of 0.05 to 100 Hz. The noise level of the

measuring system may need to be even lower for direct observation of the V.S.C.S. signals.

This study indicates that the bandwidth I chose for my instrumentation (0.1 to 500 Hz) permits all significant signals to be recorded faithfully. A lower f_l will reduce the distortions apparent in the low frequency components of the waveforms (e.g. see Figure 7.5). However, lowering f_l will also have the undesirable effect of increasing the time for the signal to stabilize after any perturbation (such as that caused by a slight change in the polarization voltage of an electrode). There is little evidence that the V.S.C.S. signals have a significant spectral content at frequencies greater than 100 Hz (cf. Section 7.1). The choice of f_h is therefore a compromise between reducing the bandwidth to reduce noise and increasing the bandwidth to maintain an accurate time reference on the QRS wave.

The major factors which affect the success of NID in my study are physiological noise and interference from atrial signals. A secondary factor may be variations in the speed of propagation within the V.S.C.S. I found it necessary to encourage many of the subjects to relax and I left them several minutes in a comfortable position to reduce physiological noise. The use of a muscle relaxant may help to reduce this noise. It may also be possible to position the electrodes away from the skeletal muscles which are generating the unwanted signals. An alternative measurement scheme, which uses an array of electrodes to minimise physiological noise is discussed in Section 8.4.

The V.S.C.S. signals measured in my study of NID are distinctly different from the signals which are measured by intracardiac catheters, as predicted by the model of Section 6.3. The model shows that the catheter signals are generated by the activation of only a small region of the V.S.C.S., which is why the characteristic H "spike" is measured. On the other hand, it is clear that the surface field is generated by activation throughout the V.S.C.S. There is ample evidence (Sano, 1976; Spach and Barr, 1976) that the activation proceeds without break from the time that the bundle of His is activated until the ventricular myocardium is activated. Therefore, as the model predicts, there are no reasons for spikes to appear in the surface signals. Rather, smooth changes in the surface signal are produced by changes in the activation velocity and direction throughout the V.S.C.S. (Berbari *et al.*, 1979). Despite this, there are still investigators who report spikes obtained

by NID (Flowers *et al.*, 1981; Sciacca *et al.*, 1981). These spikes are clearly the result of filtering the V.S.C.S. signals (see Section 7.1) and it is probable that the signal filtering is deliberately designed to accentuate features of the V.S.C.S. waveform relative to the P wave. However, I feel that it is important not to alter the signal in this way. Since NID is performed in a similar manner to electrocardiography it is likely that physicians will apply the same interpretation method (see Section 3.1) and their interpretation will be in error. Moreover, the filtering is likely to cause errors in the apparent timing of the onset of V.S.C.S. activation (Berbari *et al.*, 1979). Several alternative methods of distinguishing the V.S.C.S. signals from the P wave are discussed in Section 8.4.

CHAPTER 8

CONCLUSIONS AND SUGGESTIONS FOR FUTURE WORK

Since Einthoven's work at the turn of the century, many medical and scientific workers have researched the science of electrocardiography. In Part I of this thesis their contributions are reviewed and background material is presented for the original work presented in Part II. In Chapter 2 the inverse solution for electrocardiography is shown to be non-unique. A *priori* knowledge of the source is required to interpret the E.C.G. measurements. Computer (or mathematical) modelling of the source (cf. Chapter 4) is one means of obtaining this a *priori* knowledge. Some conclusions and suggestions for future work on modelling the source are presented below in Section 8.1. In the standard E.C.G. interpretation schemes (Chapter 3) the source is assumed to be a single current dipole at a fixed position and attempts to find a more exact inverse solution have had only limited success. The effects of the body surface shape and the internal conductivity inhomogeneities on the E.C.G. field are not well understood and are likely to contribute to the difficulties of the inverse solution. The two new models presented in Chapters 5 and 6 enable the shape and inhomogeneity effects to be studied more conveniently than has hitherto been possible. Conclusions on the importance of the effects are made in Sections 8.2 and 8.3.

The advent of digital electronics has enabled the E.C.G. to be scrutinised more thoroughly for small signals. The study reported in Chapter 7 has achieved encouraging success in detecting the activation of the ventricular specialized conduction system. A number of conclusions and suggestions are made in Section 8.4 on the methods of measuring these signals and on the origin of the signal features.

8.1 MODELLING THE SOURCE OF THE E.C.G.

The potential field produced by a region of cells actively depolarising is discussed in Section 4.1. The numerical examples presented in §4.1.1 confirm that the field produced by the depolarisation of a bundle of fibres is similar to that of an "equivalent" dipole, even if the bundle forms a thin sheet of fibres (i.e. like the left bundle

branch of the V.S.C.S. - cf. §1.2.3). The equivalent dipole is positioned in the centre of the active region and it is perpendicular to the advancing depolarisation wavefront. The moment of the equivalent dipole is proportional to the area of the wavefront and to the total change in the transmembrane voltage during depolarisation (cf. equation (77)).

The characteristics of the field of a bundle of fibres, discussed in the previous paragraph, are not altered by the presence of the insulating body surface. This implies that the model presented in Section 6.3 for the body surface field arising from the activation of the V.S.C.S. is realistic. The model predicts that the surface potential is greatest on the lower left chest and least on the upper right chest and back. It also predicts that the potential varies only slowly with time. I therefore recommend using the electrode positions shown in Figure 6.15, and also instrumentation with the standard E.C.G. frequency response (0.05 Hz to 100 Hz), for detecting the body surface V.S.C.S. signals.

To date the studies of the non-invasive detection of the signals from the V.S.C.S. (NID - cf. Section 7.1) have concentrated on establishing the feasibility of detecting the signals. More model studies are required to establish what information can really be obtained from an inverse solution of the body surface measurements (cf. Section 2.2). For example, is it possible to measure the rate of impulse propagation along the V.S.C.S. tissues? Is it possible to locate an extra conducting pathway in patients with the pre-excitation syndrome? Other questions which need to be answered by modelling studies are: how many electrodes are required to perform an inverse solution and what signal-to-noise ratio must be achieved in the measurements? If it is established by modelling studies that a useful inverse solution can be constructed for the V.S.C.S. signals, it will be worthwhile attempting to perfect the NID methods to achieve the necessary signal-to-noise ratio.

The spherical cap double layer source of Frank (1953, cf. §4.1.2) is in my opinion the most realistic of the models suggested for the source during the activation of the myocardium. Although a single cap cannot accurately model the source in an abnormal heart, combining two or more of the spherical caps with the appropriate coordinate transformations (cf. Appendix 1) allows the incorporation of abnormalities into the model. For example, an otherwise normal ventricular myocardium with an infarcted region (cf. §1.4.1) is modelled by two spherical caps. One cap represents the depolarisation wavefront proceeding normally (as if the infarction is

not present) and the other represents the lack of activity in the infarcted region. The second spherical cap has a double layer strength of equal magnitude but opposite sign to the first and it is positioned so that its rim approximates the extent of the infarction. This extension of the Frank model needs to be tested computationally.

8.2 MODELLING THE EFFECT OF THE BODY SURFACE

The most significant point to come out of the work presented in Chapter 5 is that a surface admittance boundary condition can be used straightforwardly to model a change of body shape. While the shape modelled by a given admittance condition is theoretically dependent on the source distribution and internal inhomogeneities specified, it is in fact remarkably insensitive to these factors. Moreover, the admittance boundary condition can even model sharp boundary changes, as is illustrated by the model of a limb (in two dimensions) presented in Section 5.3. A difficulty with the admittance boundary condition is that the precise shape cannot be found analytically. Instead the shape is estimated by plotting the flow of current near the surface. The extended model discussed in Section 6.1 provides an alternative means of modelling the effect of the body surface shape. While an advantage of the extended model is that the outer boundary shape is specified exactly, a disadvantage is that a large number of integrals must be found numerically for each shape.

The results presented in Sections 5.2 and 5.3 show that the limbs and head can usually be neglected in considering the effect of the body surface. However the presence of a protrusion from the body surface decreases the gradient of the potential across the base of the protrusion and increases the gradient along the surface near the protrusion. Therefore the measurements made from an electrode positioned near a body protrusion should be interpreted as if the electrode is closer to the centre of the protrusion. Corrections for some electrode positions may be particularly important in performing an inverse solution for a complicated equivalent heart generator (cf. Sections 2.2 and 3.3). Some additional modelling is required to establish a simple formula for making these corrections.

8.3 MODELLING THE EFFECT OF INTERNAL INHOMOGENEITIES

The most significant effect of the inhomogeneities in conductivity that are studied in Chapters 5 and 6 is a change in the peak-to-peak amplitude of the potential field at the body surface. The inhomogeneities cause only minor changes to the form of the surface field. The surface field is insensitive to the exact shape of the internal inhomogeneities; it is sensitive only to their approximate locations relative to the source.

I feel that the "Brody effect" of the intracardiac blood (Brody, 1956; cf. §4.2.2) is less important than previous investigators have suggested. I base this conclusion on a model presented in Section 5.2 (cf. Figure 5.3) which I believe represents the relationship of the source to the conductivity variation in the heart region more realistically than does the Brody model. The peak-to-peak surface field amplitudes of a radial dipole and a tangential dipole (these orientations are relative to the highly conductive blood) in my model differ by only a few percent.

Another effect of the Brody type (but more significant) is associated with a region of low (or zero) conductivity lying outside the source region. If the low conductivity region is concentrated on one side of a source dipole, it affects the field of the dipole according to the dipole's orientation. If the dipole is oriented along a line which intersects the low conductivity region, the field is attenuated by its presence. If, however, the dipole is oriented tangentially to the low conductivity region, the field is amplified by its presence. This effect is most clearly demonstrated in Figure 6.7.

Future work should concentrate on two areas (at least). Firstly, the effects of tissue anisotropy need to receive more attention. There are indications in the literature (cf. Rush and Nelson, 1976; Geselowitz, 1980) that this is already happening. Secondly, and I believe most importantly, ways of correcting the E.C.G. field for the effects of the body shape and inhomogeneities must be investigated. While such corrections are important for all forms of inverse solution, I believe that most effort should be directed towards correcting the standard 12-lead E.C.G. measurements (since this system is used for the great majority of clinical interpretations of the E.C.G.). The corrections could be conveniently based on a simple set of measurements from standard chest radiographs. Alternatively, electrical impedance imaging (cf. Bates *et al.*, 1980) may in future be able to supply the appropriate information.

8.4 NON-INVASIVE DETECTION OF THE ACTIVATION OF THE V.S.C.S. (NID)

There is now no doubt that the activation of the V.S.C.S. produces an electrocardiographic field which can be measured in most subjects by the NID methods discussed in Chapter 7. However the success of NID is still compromised by the interference of signals from the atrial myocardium and from the skeletal muscles. In the following paragraphs I make some suggestions for improving NID.

I think that a reduction in the interference by skeletal muscle signals (and electrode noise) will be achieved by replacing each of the electrodes in a bipolar chest lead (cf. Figure 6.15) with an array of electrodes. Each array consists of a central electrode surrounded by (say) six equally-spaced electrodes arranged in a circle with a radius of (say) 8 cm. The electrodes in an array are each connected to a summing junction with a resistor of equal value and the two summed signals are connected to the first differential stage of the NID circuitry. Provided that the unwanted signals are uncorrelated (or only poorly correlated) while the V.S.C.S. signals are well correlated between the electrodes of each array, a significant improvement in the signal-to-noise ratio will be achieved. The method could be termed "spatial averaging". I cannot claim to be the first with this idea, because Flowers *et al.* (1981) have already reported using a number of amplifiers in parallel to achieve an improvement in the signal-to-noise ratio. To test the practicality of spatial averaging, I intend to measure the potential simultaneously at a number of positions on the body and see how well the skeletal muscle signals correlate between these positions.

There may be sufficient beat-to-beat variation in the V.S.C.S. signal and in the QRS wave to modify features in the averaged waveform. In particular, as outlined in Section 7.1, variation in the H-V interval will cause features in the waveform to be smoothed (cf. Ribeiro *et al.* 1980). It is generally believed that the H-V interval is constant, although much reliance has been placed on the results of one study by Scherlag *et al.* (1972). Some doubt has recently been expressed about the constancy of the H-V interval (Tonkin, 1981; Ishijima, 1978). I intend to perform NID using a simultaneous catheter recording of the His spike to provide a timing reference for averaging. Comparing the averaged V.S.C.S. waveform obtained in this way with that obtained with a QRS trigger (cf. §7.2.3) will indicate if variation in the H-V interval

affects the performance of NID significantly.

A number of schemes have been used, with only limited success, to distinguish the signals caused by the activation of the V.S.C.S. from those caused by the activation of the atria (cf. Section 7.1). In some patients with heart block (cf. §1.4.5) the V.S.C.S. activation commences after the end of the P wave, so that the V.S.C.S. signals can be detected within a clear "window" (cf. Takeda *et al.*, 1979). The same effect can be induced temporarily in other patients by administering a suitable drug (e.g. propranolol, cf. Narula, 1975). I suggest that such a minimal invasion will be acceptable (under close medical supervision) if this is the only way of achieving clinically useful data by NID.

One further method of minimising the interference of the P wave should be investigated. The depolarisation wavefront proceeds from right to left at the end of the P wave (cf. §1.3.3 and Figure 1.8) in most subjects whereas the V.S.C.S. activation proceeds in a more forward and downward direction. It may therefore be possible to place the electrodes (or electrode arrays) so as to minimise the atrial signals while retaining an acceptable sensitivity to the V.S.C.S. signals. An experimental study is needed to confirm this.

My final comments are on the future role of NID in the treatment of cardiac patients. It is possible that NID will replace catheterisation in assessing the need for a permanent pacemaker implantation in some elderly patients. I think that it is unlikely that NID will replace catheterisation in other patients, because a non-invasive means of pacing the heart (an essential part of most electrophysiological studies) is unlikely to be found. However, because NID can be readily repeated, without patient discomfort and at a low cost, it is ideally suited for checking patients after their electrophysiological study and for assessing the effectiveness of their treatment. Furthermore, future improvements may allow the NID methods to be extended to detecting activity in the sinus and A-V nodes and to detecting small signals from diseased cardiac cells (cf. Barbari *et al.*, 1978).

ACKNOWLEDGEMENTS

I first thank my wife, Jocelyn, for her substantial contribution to this thesis in accepting the solitude enforced by my work and in helping me through the bad times.

I sincerely thank my supervisor, Professor Richard Bates, for taking me in, pushing me through and pulling me out (a wiser man, I hope!). I count myself fortunate to have worked with such a stimulating thinker and taskmaster.

My associate supervisor, Dr Hamid Ikram, also deserves special thanks. I am grateful for Hamid's support and interest throughout this research and for our many stimulating discussions on topics connected with the work. I am also grateful to Dr David Hay and Professor Donald Beaven for their support in organising my registration for the degree. Others at the hospital who have helped in my research are William Chan, Andrew Maslowski, Jack Tait, Marie Flewellen, Sinclair Bennett, David Moore and Ross Raymond. My thanks to them.

Several other postgraduate students have contributed much in the way of ideas and have acted as a sounding board for some of my crazier notions. In particular I thank Graeme McKinnon, Andrew Seagar and Rick Millane.

Finally, I am grateful to the National Heart Foundation of New Zealand. I have received two project grants (one in conjunction with Dr William Chan) and a travel grant from the Foundation to aid in my research.

REFERENCES

- AKKER, T.J. van den, H.H. Ros, H.G. Goovaarts and H. Schneider.
Real-time method for noninvasive recording of His bundle activity
of the ECG. *Computers and Biomedical Research*, 9: 559, 1976.
- d'ALCHE, P., P. Ducimetiere and J. Lacombe. Computer model of cardiac
potential distribution in an infinite medium and on the human
torso during ventricular activation. *Circulation Research*, 34:
719, 1974.
- ARTHUR, R.M., D.B. Geselowitz, S.A. Brillner and R.F. Trost.
Path of the electrical centre of the human heart determined
from surface ECG's. *J Electrocardiology*, 4: 29, 1971.
- ARTHUR, R.M., D.B. Geselowitz, S.A. Brillner and R.F. Trost.
Quadrupole components of the human surface electrocardiogram.
American Heart J, 83: 663, 1972.
- ARZBAECHER, R.C. and D.A. Brody. The lead field: vector and tensor
properties. In Nelson, C.V. and D.B. Geselowitz. (Eds) *The
Theoretical Basis of Electrocardiography*. Oxford, Clarendon
Press, 1976, p 175.
- BAIRD, D.K. and J.B. Uther. Surgical management of supraventricular
tachycardia. In Kelly, D.T. (Ed) *Advances in the Management
of Arrhythmias*. Australia, Medical Telectronics, 1978, p 150.
- BAKER, B.B. and E.T. Copson. *Mathematical Theory of Huygens' Principle*.
2nd Ed. New York, Oxford, 1953.
- BAKER, C.M. and T.C. Pilkington. The use of time dependent models
in inverse electrocardiography. *I.E.E.E. Transactions*, BME-21:
460, 1974.
- BARNARD, A.C.L., I.M. Duck and M.S. Lynn. The application of
electromagnetic theory to electrocardiography. I. Derivation
of integral equations. II. Numerical solution of integral
equations. *Biophysical J*, 7: 443, 1967.
- BARNARD, A.C.L., J.H. Holt and J.O. Kramer. Models and methods in
inverse electrocardiography: the U.A.B. choice. In Nelson,
C.V. and D.B. Geselowitz. (Eds) *The Theoretical Basis of
Electrocardiography*. Oxford, Clarendon Press, 1976, p 323.

- BARR, R.C., T.C. Pilkington, J.P. Boineau and C.L. Rogers. An inverse electrocardiographic solution with an on-off model. I.E.E.E. Transactions, BME-17: 49, 1970.
- BARR, R.C., M. Spach and G. Herman-Giddens. Selection of the number and positions of measuring locations for electrocardiography. I.E.E.E. Transactions, BME-18: 125, 1971.
- BARR, R.C. and M.S. Spach. Inverse solutions directly in terms of potentials. In Nelson, C.V. and D.B. Geselowitz. (Eds) The Theoretical Basis of Electrocardiography. Oxford, Clarendon Press, 1976, p 294.
- BARR, R.C., M. Ramsey and M.S. Spach. Relating epicardial to body surface potential distributions by means of transfer coefficients based on geometry measurements. I.E.E.E. Transactions, BME-24: 1, 1977.
- BATES, R.H.T. and F.L. Ng. Polarisation-source formulation of electromagnetism and dielectric-loaded waveguides. Proceedings I.E.E., 119: 1568, 1972.
- BATES, R.H.T. Analytic constraints on electromagnetic field computations. I.E.E.E. Transactions, MTT-23: 605, 1975.
- BATES, R.H.T. and D.J.N. Wall. Null field approach to scalar diffraction (Parts I, II and III). Philosophical Transactions Royal Society, London, A, 287: 45, 1977.
- BATES, R.H.T. General introduction to the extended boundary condition. In Varadan, V.K. and V.V. Varadan. (Eds) Acoustic, Electromagnetic and Elastic Wave Scattering - Focus on the T-matrix Approach. U.K., Pergamon Press, 1980, p 21.
- BATES, R.H.T., G.C. McKinnon and A.D. Seagar. A limitation on systems for imaging electrical conductivity distributions. I.E.E.E. Transactions, BME-27: 418, 1980.
- BAULE, G.M. and R. McFee. Detection of the magnetic field of the heart. American Heart J, 66: 95, 1963.
- BAYLEY, R.H., J.M. Kalbfleisch and P.M. Berry. Changes in the body's QRS surface potentials produced by alterations in certain compartments of the non homogeneous conducting model. American Heart J, 77: 517, 1969.

- BEASLEY, M.D.R., J.H. Pickles, G. D'Amico, et al. Comparative study of three methods for computing electric fields. Proceedings I.E.E., 126: 126, 1979.
- BERBARI, E.J., R. Lazzara, P. Samet and B.J. Scherlag. Noninvasive technique for detection of electrical activity during the P-R segment. Circulation, 48: 1005, 1973.
- BERBARI, E.J., R. Lazzara, N. El-Sherif and B.J. Scherlag. Extracardiac recordings of His-Purkinje activity during conduction disorders and junctional rhythms. Circulation, 51: 802, 1975.
- BERBARI, E.J., B.J. Scherlag, N. El-Sherif, B. Befeler, J.M. Aranda and R. Lazzara. The His-Purkinje electrocardiogram in man. An initial assessment of its uses and limitations. Circulation, 54: 219, 1976.
- BERBARI, E.J., B.J. Scherlag, R.R. Hope and R. Lazzara. Recording from the body surface of arrhythmogenic ventricular activity during the S-T segment. American J Cardiology, 41: 697, 1978.
- BERBARI, E.J., R. Lazzara and B.J. Scherlag. The effects of filtering the His-Purkinje system electrocardiogram. I.E.E.E. Transactions on Biomedical Engineering, BME-26: 82, 1979.
- BERSON, A.S., W.K. Haisty and H.V. Pipberger. Electrode position effects on Frank lead electrocardiograms. American Heart J, 95: 463, 1978.
- BESOZZI, M., L. de Anbroggi, S. Devizzi, B. Taccardi and C. Viganotti. Analisi quantitativa d elettromappe cardiache normali. Bollettino della Societa Italiana di Cardiologia (Rome), 18: 748, 1973.
- BLACKBURN, H. (Ed). Measurement in Exercise Electrocardiography. Proceedings of the Ernst Simonson Conference. Illinois, Charles C. Thomas, 1969.
- BOINEAU, J.P., S.D. Blumenschein, M.S. Spach, D.C. Sabiston. Relationship between ventricular depolarisation and ECG in myocardial infarction. J Electrocardiology, 1: 233, 1968.
- BOINEAU, J.P. Panel discussion: Correlation of body surface potentials with heart potentials. Advances in Cardiology, Basel, 10: 139, 1974.

- BONES, P.J. The use of analogue-to-digital conversion and graphics facilities to perform vectorcardiography. *New Zealand Medical Physics and Bioengineering*, 3: 7, 1976.
- BRAUNWALD, E. *Heart Disease*. Philadelphia, Saunders, 1980.
- BRODY, D.A. and W.E. Romans. A model which demonstrates the quantitative relationship between the EMF of the heart and the extremity leads. *American Heart J*, 45: 263, 1953.
- BRODY, D.A. A theoretical analysis of intracavitary blood mass influence on the heart-lead relationship. *Circulation Research*, 4: 731, 1956.
- BRODY, D.A. and J.A. Hight. Test of an inverse electrocardiographic solution based on accurately determined model data. *I.E.E.E. Transactions, BME-19*: 221, 1972.
- BRORSON, L. and S.B. Olsson. Atrial repolarisation in healthy males. *Acta Medica Scandinavia*, 199: 447, 1976.
- BURGER, H.C. and J.B. van Milaan. Heart vector and leads. Part III. *British Heart J*, 10: 229, 1948.
- BURGER, H.C. and R. van Dongen. Specific electrical resistance of body tissues. *Physics in Medicine and Biology*, 5: 431, 1961.
- BURGESS, M.J., L.S. Green, K. Millar, R. Wyatt and J.A. Abildskov. The sequence of normal ventricular recovery. *American Heart J*, 84: 660, 1972.
- CASELLA, C. and B. Taccardi. The spread of excitation over short distances in heart muscle. *In International Symposium on the Electrophysiology of the Heart, Milan, 1963*. Edited by B. Taccardi and G. Marchetti. Oxford, Pergamon Press, 1965.
- CASTELLANOS, A. and R.J. Myerburg. The resting electrocardiogram. *In Hurst, J.W. (Ed) The Heart*. 4th Edition, U.S.A., McGraw-Hill, 1978, p 298.
- CHAPMAN, S. and J. Bartels. *Geomagnetism*. Oxford, Clarendon Press, 1951.
- CHOI, J. and T.C. Pilkington. Effects of geometric uncertainties on the E.C.G. *I.E.E.E. Transactions, BME-28*: 325, 1980.

- CORABOEUF, E. A review of cardiac electrophysiology. *American J Physiology*, 234: H101, 1978.
- CRONVICH, J.A., D.A. Ahlgren and G.E. Burch. Amplitude probability densities of electrocardiograms. *American Heart J*, 75: 510, 1968.
- CUFFIN, B.N. and D.B. Geselowitz. Studies of ECG using realistic cardiac and torso models. *I.E.E.E. Transactions, BME-24*: 242, 1977.
- CURRY, P.V.L. Fundamentals of arrhythmias: modern methods of investigation. In Krikler, D.M. and J.F. Goodwin. (Eds) *Cardiac Arrhythmias*. U.K., Saunders, 1975, p 39.
- DAMATO, A.N., S.H. Lau, R.H. Helfant, E. Stein, W.D. Berkowitz and S.L. Cohen. Study of atrioventricular conduction in man using electrode catheter recordings of His bundle activity. *Circulation*, 39: 287, 1969.
- DAVENPORT, W.B. and W.L. Root. *An Introduction to the Theory of Random Signals and Noise*. New York, McGraw-Hill, 1958.
- DEWHURST, D.J. *An Introduction to Biomedical Instrumentation*. 2nd Ed. U.K., Pergamon Press, 1976.
- DEY, A. and H.F. Morrison. Resistivity modelling for arbitrarily shaped three-dimensional structures. *Geophysics*, 44: 753, 1979.
- DIEBOLD, G.J. Effects of A/D converter resolution in signal averaging. *Review of Scientific Instrumentation*, 48: 1689, 1977.
- DURRER, D., R. Th. van Dam, G.E. Freud, M.J. Janse, F.L. Meijler and R.C. Arzbaecher. Total excitation of the isolated human heart. *Circulation*, 41: 899, 1970.
- EINTHOVEN, W., G. Fahr and A. de Waart. Über die Richtung und manifeste Grösse der Potentialschwankungen im menschlichen Herzen und über den Einfluss der Herzlage auf die Form des Elektrokardiograms. *Pflügers Archives des Physiologie*, 150: 275, 1913. (Translation, *American Heart J*, 40: 163, 1950.)
- FEIGENBAUM, H. *Echocardiography*. 2nd Ed. Philadelphia, Lea and Febiger, 1976.
- FISHER, J.D., H.E. Kulbertus and O. Narula. Panel discussion: The prognostic value of the H-V interval. *P.A.C.E.*, 1: 132, 1978.

- FLAHERTY, J.T., S.D. Blumenshein, A.W. Alexander, R.D. Gentzler, T.M. Gallie, J.P. Boineau and M.S. Spach. Influence of respiration on recording cardiac potentials, potential surface-mapping and VCG studies. *American J Cardiology*, 20: 21, 1967.
- FLOWERS, N.C. and L.G. Horan. Comparative surface potential patterns in obstructive and non-obstructive cardiomyopathy. *American Heart J*, 86: 196, 1973.
- FLOWERS, N.C., R.C. Hand, P.C. Orander, K.B. Miller, M.O. Walden and L.G. Horan. Surface recording of electrical activity from the region of the bundle of His. *American J Cardiology*, 33: 384, 1974.
- FLOWERS, N.C., L.G. Horan and J.C. Johnson. Anterior infarction changes occurring during mid and late ventricular activation detectable by surface mapping techniques. *Circulation*, 54: 906, 1976.
- FLOWERS, N.C., V. Shvartsman, B.M. Kennelly, G.S. Sohi and L.G. Horan. Surface recording of His-Purkinje activity on an every-beat basis without digital averaging. *Circulation*, 63: 948, 1981.
- FORBES, A.D. Forward and inverse solutions using distributed current sources. *Advances in Cardiology*, Basel, 10: 199, 1974.
- FOZZARD, H.A. and G.W. Beeler. The voltage clamp and cardiac electrophysiology. *Circulation Research*, 37: 403, 1975.
- FRANK, E. A comparative analysis of the eccentric double-layer representation of the human heart. *American Heart J*, 46: 364, 1953.
- FRANK, E. General theory of heart-vector projection. *Circulation Research*, 11: 258, 1954a.
- FRANK, E. The image surface of a homogeneous torso. *American Heart J*, 757, 1954b.
- FRANK, E. Analysis of R,L,F,B systems of spatial vectorcardiography. *American Heart J*, 51: 34, 1956a.
- FRANK, E. An accurate, clinically practical system for spatial vectorcardiography. *Circulation*, 13: 737, 1956b.
- FREYGANG, W.H. and W. Trautwein. The structural implications of the linear electrical properties of cardiac Purkinje strands. *J General Physiology*, 55: 524, 1970.

- FURNESS, A., G.P. Sharratt and P. Carson. The feasibility of detecting His-bundle activity from the body surface. *Cardiovascular Research*, 9: 390, 1975.
- GABOR, D. and C.V. Nelson. Determination of the resultant dipole of the heart from measurements on the body surface. *J Applied Physics*, 25: 413, 1954.
- GEDDES, L.A. *Electrodes and the Measurement of Bioelectric Events*. New York, Wiley, 1972.
- GELENTER, H.L. and J.C. Swihart. A mathematical-physical model of the genesis of the ECG. *Biophysical J*, 4: 285, 1964.
- GESELOWITZ, D.B. Multipole representation for an equivalent cardiac generator. *Proceedings I.R.E.*, 48: 75, 1960.
- GESELOWITZ, D.B. On bioelectric potentials in an inhomogeneous volume conductor. *Biophysical J*, 7: 1, 1967.
- GESELOWITZ, D.B. Determination of multipole components. In Nelson, C.V. and D.B. Geselowitz. (Eds) *The Theoretical Basis of Electrocardiography*. Oxford, Clarendon Press, 1976, p 202.
- GESELOWITZ, D.B. Representation of electric sources in anisotropic cardiac muscle. (Abstract). *I.E.E.E. Transactions, BME-27*: 528, 1980.
- GOLDBERGER, E. Simple, indifferent, electrocardiographic electrode of zero potential and technique of obtaining augmented, unipolar, extremity leads. *American Heart J*, 23: 483, 1942.
- GOLDMAN, M.J. *Principles of Clinical Electrocardiography*. 9th Edition, U.S.A., Lange Medical Publications, 1976.
- GRISHMAN, A. and L. Scherlis. *Spatial Vectorcardiography*. Philadelphia, W.B. Saunders Company, 1952.
- GROEBEN, J. van der, D.D. Fisher and J.G. Toole. Temporospacial frequency distribution of P, QRS and T in normal men and women. *American Heart J*, 75: 487, 1968.
- GUARDO, R., B. McA. Sayers and D.M. Monro. Evaluation and analysis of the cardiac multipole series based on a two-dimensional Fourier technique. In Nelson, C.V. and D.B. Geselowitz. (Eds) *The Theoretical Basis of Electrocardiography*. Oxford, Clarendon Press, 1976, p 213.

- GUYTON, A.C. Basic Human Physiology. Philadelphia, Saunders, 1971.
- HARRINGTON, R.F. Field Computation by Moment Methods. N.Y., Macmillan, 1968.
- HARTLINE, F.F. Biological applications for voltage sensitive dyes. Science, 203: 992, 1979.
- HELM, R.A. An accurate lead system for spatial vectorcardiography. American Heart J, 53: 415, 1957.
- HENDERSON, J.C. and C.C. Bowman. A cardiac surface potential acquisition system. New Zealand Medical Physics and Bio-medical Engineering, 5: 4, 1978.
- HILDEBRAND, F.B. Introduction to Numerical Analysis. 2nd Edition, U.S.A., McGraw-Hill, 1974.
- HISHIMOTO, Y. and T. Sawayama. Non-invasive recording of His bundle potential in man. Simplified method. British Heart J, 37: 635, 1975.
- HOBSON, E.W. The Theory of Spherical and Ellipsoidal Harmonics. Cambridge, University Press, 1930.
- HODGKIN, A.L. and A.F. Huxley. A quantitative description of membrane current and its application to conduction and excitation in nerve. J Physiology (London), 117: 500, 1952.
- HORAN, L.G. and N.C. Flowers. Recovery of the moving dipole from surface potential recordings. American Heart J, 82: 207, 1971.
- HORAN, L.G., R.C. Hand, N.C. Flowers, J.C. Johnson and D.A. Brody. The multipolar content of the human electrocardiogram. Annals of Biomedical Engineering, 4: 280, 1976.
- HURST, J.W. (Ed). The Heart. 4th Edition, U.S.A., McGraw-Hill, 1978.
- ISHIJIMA, M. Statistically compensated averaging method for noninvasive recording of His-Purkinje activity. Biomedical Sciences Instrumentation, 14: 129, 1978.
- IWA, T., T. Misaki, M. Ohira and M. Terananka. Electrical treatment of supraventricular tachycardias with implanted radiofrequency atrial pacemakers. In Kelly, D.T. (Ed) Advances in the Management of Arrhythmias. Australia, Medical Teletronics, 1978, p 118.

- JAMES, R.W. The Adams and Elsassser dynamo integrals. Proceedings Royal Society, London, A, 331: 469, 1973.
- JAMES, T.N. Anatomy of the conduction system of the heart. In Hurst, J.W. (Ed) The Heart. 4th Edition, U.S.A., McGraw-Hill, 1978, p 47.
- JAMES, T.N. and L. Sherf. Ultrastructure of the myocardium. In Hurst, J.W. (Ed) The Heart. 4th Edition, U.S.A., McGraw-Hill, 1978, p. 57.
- KAK, A.C. Computerised tomography with X-ray, emission and ultrasound sources. Proceedings I.E.E.E., 67: 1245, 1979.
- KINI, P.M., P. Ginefra and H.V. Pipberger. Day-to-day variation of the Frank ECG and VCG in heart disease. American Heart J, 88: 698, 1974.
- KNEPPO, P. and L.I. Titomir. Integral characteristics of the human cardiac electrical generator from electric field measurements by means of an automatic cylindrical coordinator. I.E.E.E. Transactions, BME-26: 21, 1979.
- KOOTSEY, J.M. and E.A. Johnson. Origin of the electrocardiogram: relationship between transmembrane potential and the electrocardiogram. In Nelson, C.V. and D.B. Geselowitz. (Eds) The Theoretical Basis of Electrocardiography. Oxford, Clarendon Press, 1976, p 21.
- KOSSMAN, C.E., D.A. Brody, G.E. Barch, *et al.* Recommendations for standardization of leads and of specifications for instruments in electrocardiography and vectorcardiography. Circulation, 35: 583, 1967.
- KRIKLER, D.M. and J.F. Goodwin (Eds). Cardiac Arrhythmias. U.K., Saunders, 1975.
- KULBERTUS, H.E., A.C. Arntzenius, P. Huisman, H.J. Ritsema van Eck and J. Robbins. Concept of left hemiblocks revisited. A histopathological and experimental study (with preliminary results on a computer simulation model of left fascicular blocks). Advances in Cardiology, Basel, 14: 126, 1975.
- KULBERTUS, H.E. and J-C. Demoulin. The conduction system: anatomical and pathological aspects. In Krikler, D.M. and J.F. Goodwin. (Eds) Cardiac Arrhythmias. U.K., Saunders, 1975, p 16.

- LANGER, G.A. and A.J. Brady (Eds). *The Mammalian Myocardium*.
New York, Wiley, 1974.
- LEPESCHKIN, E. Role of myocardial temperature, electrolyte and stress gradients in the genesis of the normal T-wave. *In* Schlant, R.C. and J.W. Hurst. (Eds) *Advances in Electrocardiography*.
New York, Grune and Stratton, 1976a, p 339.
- LEPESCHKIN, E. Physiologic basis of the U wave. *In* Schlant, R.C. and J.W. Hurst. (Eds) *Advances in Electrocardiography*.
New York, Grune and Stratton, 1976b, p 353.
- LEPESCHKIN, E. Physiological influences on transfer factors between heart currents and body-surface potentials. *In* Nelson, C.V. and D.B. Geselowitz. (Eds) *The Theoretical Basis of Electrocardiography*. Oxford, Clarendon Press, 1976c, p 135.
- LISTER, J.W., E. Stein, R.D. Kosowsky, S.H. Lau and A.N. Damato. Atrioventricular conduction in man. *American J Cardiology*, 16: 516, 1965.
- LUCCHESI, B.R. Electropharmacology of drugs used in the management of supraventricular tachyarrhythmias. *In* Kelly, D.T. (Ed) *Advances in the Management of Arrhythmias*. Australia, Medical Teletronics, 1978, p 97.
- LUX, R.L., C.R. Smith, R.F. Wyatt and J.A. Abildskov. Limited lead selection for estimation of body surface potential maps in electrocardiography. *I.E.E.E. Transactions, BME-25*: 270, 1978.
- LYNN, M.S., A.C.L. Barnard, J.H. Holt and L.T. Sheffield. A proposed method for the inverse problem in electrocardiography. *Biophysical J*, 7: 925, 1967.
- LYNN, M.S. and W.P. Timlake. The numerical solution of singular integral equations of potential theory. *Numerische Mathematik*, 11: 77, 1968.
- McFEE, R. and A. Parungao. An orthogonal lead system for clinical electrocardiography. *American Heart J*, 62: 93, 1961.
- McFEE, R. and S. Rush. Qualitative effects of thoracic resistivity variations on the interpretation of electrocardiograms: the low resistance surface layer. *American Heart J*, 76: 48, 1968.

- MARRIOT, H.J.L. and R.J. Myerburg. Recognition and treatment of cardiac arrhythmias and conduction disorders. In Hurst, J.W. (Ed) The Heart. 4th Edition. U.S.A., McGraw-Hill, 1978, p 637.
- MARRIOT, T.H., M.J. English and D.J. Wollons. A weighted signal averaging technique for E.C.G. analysis (Abstract). In Proceedings of the 20th Conference of the Biological Engineering Society, London, 1980, p 421.
- MARTIN, R.O. and T.C. Pilkington. Unconstrained inverse ECG: epicardial potentials. I.E.E.E. Transactions, BME-19: 276, 1972.
- MARTIN, R.O., T.C. Pilkington and M.N. Morrow. Statistically constrained inverse electrocardiography. I.E.E.E. Transactions, BME-22: 487, 1975.
- MASHIMA, S. On the determination and expressions of equivalent quadrupole of the cardiac generator. I.E.E.E. Transactions, BME-16: 69, 1969.
- MEIJLER, F.L., E.O. Robles de Medina and J.C. Helder. Future of computerised electrocardiography. British Heart J, 44: 1, 1980.
- METZ, W.C. and T.C. Pilkington. The utilisation of integral equations for solving 3-D, time-invariant, conservative fields. International J Engineering Science, 7: 183, 1969.
- MILLANE, R.P., P.J. Bones, H. Ikram and R.H.T. Bates. A computer model of cardiac conduction. Australasian Physical and Engineering Sciences in Medicine, 3: 205, 1980.
- MIRVIS, D.M., F.W. Keller and J.W. Cox. Experimental comparison of four inverse electrocardiographic constructs in the isolated rabbit heart. J Electrocardiology, 11: 57, 1978.
- MIRVIS, D.M. Body surface distribution of electrical potential during atrial depolarisation and repolarisation. Circulation, 62: 167, 1980.
- MITTRA, R. (Ed). Computer Techniques for Electromagnetics. Oxford, Pergamon Press, 1973.
- MOHAMMED-DJAFARI, A., F. Heron, R. Duperdu and J. Perrin. Noninvasive recording of the His-Purkinje system electrical activity by a digital system design. J Biomedical Engineering, 3: 147, 1981.

- MONRO, D.M., R. Guardo, P. Bourdillon and J. Tinker. A Fourier technique for simultaneous electrocardiographic surface mapping. *Cardiovascular Research*, 8: 688, 1974.
- MOORE, E.N. and J.F. Spear. Effect of autonomic activity on pacemaker function and conduction. In Wellens, H.J.J., K.I. Lie and M.J. Janse. (Eds) *The Conduction System of the Heart*. Netherlands, Stenfert Kroese, 1976, p 100.
- MORRISON, R. *Grounding and Shielding Techniques in Instrumentation*. New York, Wiley, 1967.
- MORSE, P.M. and H. Feshbach. *Methods of Theoretical Physics*. Vols 1 and 2. New York, McGraw-Hill, 1953.
- MYERS, G.H., Y.M. Kresh and V. Parsonnet. Characteristics of intracardiac electrograms. *P.A.C.E.*, 1: 90, 1978.
- NARULA, O.S. (Ed). *His Bundle Electrocardiography*. Philadelphia, F.A. Davis, 1975.
- NAYLOR, W.G. and D.M. Krikler. Depolarisation, repolarisation and conduction. In Krikler, D.M. and J.F. Goodwin. (Eds) *Cardiac Arrhythmias*. London, Saunders, 1975, p 1.
- NG, F.L. and R.H.T. Bates. Null-field method for waveguides of arbitrary cross section. *I.E.E.E. Transactions MTT-20*: 658, 1972.
- NOBLE, D. *The Initiation of the Heartbeat*. 2nd Edition. U.K., Clarendon Press, 1979.
- OKADA, R.H. The image surface of a circular cylinder. *American Heart J*, 489, 1956.
- OLSON, R.E. Physiology of cardiac muscle. In *Handbook of Physiology*, II. Circulation (Edited by W.F. Hamilton). Washington, American Physiological Society, 1962, 1: 199.
- PERNKOPF, E. *Atlas of Topographical and Applied Human Anatomy*. Philadelphia, Saunders, 1963.
- PEUCH, P. Atrioventricular block: the value of intracardiac recordings. In Krikler, D.M. and J.F. Goodwin. (Eds) *Cardiac Arrhythmias*. U.K., Saunders, 1975, p 81.

- PILKINGTON, T.C. and M.N. Morrow. The utilisation of spherical approximations to relate epicardial potentials to torso potentials. (Abstract). I.E.E.E. Transactions, BME-27: 528, 1980.
- PIPBERGER, H.V., M.J. Goldman, D. Littmann, G.P. Murphy, J. Cosma and J.R. Snyder. Correlations of the orthogonal ECG and VCG with constitutional variables in 518 normal men. Circulation, 35: 536, 1967.
- PLONSEY, R. The active fibre in a volume conductor. I.E.E.E. Transactions, BME-21: 371, 1974.
- PLONSEY, R. Laws governing current flow in the volume conductor. In Nelson, C.V. and D.B. Geselowitz. (Eds) The Theoretical Basis of Electrocardiography. Oxford, Clarendon Press, 1976, p 165.
- RAEMER, H.R. Statistical Communication Theory and Applications. New Jersey, Prentice-Hall, 1969.
- RIBEIRO, J.E., A. Caprihan, A. Gianella Neto, N.G. Wiederehecker and A.F.C. Infantosi. Theoretical analysis of error during signal averaging for detection of His-bundle activity. I.E.E.E. Transactions BME-27: 473, 1980.
- RIJLANT, P. Electrogenese global du coeur chez l'homme. Electrocardiographie vectorielle et. vectorcardiographie. Acta Cardiologia, 13: 349, 1958.
- ROGERS, C.L. and T.C. Pilkington. The solution of overdetermined linear equations as a multistage process. I.E.E.E. Transactions, BME-15: 179, 1968a.
- ROGERS, C.L. and T.C. Pilkington. Free-moment current dipoles in inverse electrocardiography. I.E.E.E. Transactions, BME-15: 312, 1968b.
- ROS, H.H. His bundle activity detection using P-R interval variations. (Abstract). In Proceedings of the 20th Conference of the Biological Engineering Society, London, 1980, p 279.
- ROSENBAUM, M.B. The hemiblocks: diagnostic criteria and clinical significance. Modern Concepts of Cardiovascular Disease, 39: 141, 1970.

- ROSS, D.L., J. Farre, F.W. Bar, E.J. Vanagt, W.R.M. Dassen, I. Weiner and H.J.J. Wellens. Comprehensive clinical electrophysiologic studies in the investigation of documented or suspected tachycardias. *Circulation*, 61: 1010, 1980.
- RUDY, Y. and R. Plonsey. The eccentric spheres model as the basis for a study of the role of geometry and inhomogeneities in electrocardiography. *I.E.E.E. Transactions, BME-26*: 392, 1979.
- RUSH, S., J.A. Abildskov and R. McFee. Resistivity of body tissues at low frequencies. *Circulation Research*, 12: 40, 1963.
- RUSH, S. An inhomogeneous anisotropic model of the human torso for ECG studies. *Medical and Biological Engineering*, 9: 201, 1971.
- RUSH, S. and C.V. Nelson. The effects of electrical inhomogeneity and anisotropy of thoracic tissues on the field of the heart. In Nelson, C.V. and D.B. Geselowitz. (Eds) *The Theoretical Basis of Electrocardiography*. Oxford, Clarendon Press, 1976, p 323.
- RUSH, S. Relationships among Green's Theorem, Helmholtz' Theorem and integral equation methods of solving the forward E.C.G. problem. *I.E.E.E. Transactions, BME-25*: 283, 1978.
- RUSHMER, R.F. *Cardiovascular Dynamics*. 2nd Edition. U.S.A., Saunders, 1961.
- RUTTKAY-NEDECKY, I. Effects of respiration and heart position on the cardiac electric field. In Nelson, C.V. and D.B. Geselowitz. (Eds) *The Theoretical Basis of Electrocardiography*. Oxford, Clarendon Press, 1976, p 120.
- SALU, Y. and M.L. Marcus. Computer simulation of the precordial QRS complex: effects of simulated changes in ventricular wall thickness and volume. *American Heart J*, 92: 758, 1976.
- SALU, Y., D. Laughlin, J. Rogers and M. Marcus. Effects of the volume conduction on the apparent orientation of a known cardiac dipole. *J Electrocardiology*, 11: 143, 1978.
- SANO, T. Conduction in the heart. In Nelson, C.V. and D.B. Geselowitz. (Eds) *The Theoretical Basis of Electrocardiography*. Oxford, Clarendon Press, 1976, p 70.
- SCHAMROTH, L. *The Disorders of Cardiac Rhythm*. Great Britain, Blackwell, 1971.

- SCHAMROTH, L. The Electrocardiology of Coronary Artery Disease. Great Britain, Blackwell, 1975.
- SCHER, A.M., W.W. Ohm, W.G. Kerrick, S.M. Lewis and A.C. Young. Effects of body surface boundary and tissue inhomogeneity on the ECG of the dog. *Circulation Research*, 29: 600, 1971.
- SCHER, A.M. Excitation of the heart. In Nelson, C.V. and D.B. Geselowitz. (Eds) *The Theoretical Basis of Electrocardiography*. Oxford, Clarendon Press, 1976, p 21.
- SCHERLAG, B.J., P. Samet and R.H. Helfant. His-bundle electrograms. *British Heart J*, 33: 633, 1972.
- SCHMITT, O.H. and E. Simonson. The present status of vectorcardiography. *Archives Internal Medicine*, 96: 574, 1955.
- SCHMITT, O.H. Lead vectors and transfer impedance. In *The Electrophysiology of the Heart*. (Edited by H.H. Hecht.) *Annals of the New York Academy of Sciences*, Vol 65, 1957, p 1092.
- SCHMITT, O. The biophysical implications of orthogonal lead electrocardiology. *Advances in Cardiology*, Basel, 16: 62, 1976.
- SCHWAN, H.P. and C.F. Kay. The conductivity of living tissues. In *The Electrophysiology of the Heart*. (Edited by H.H. Hecht.) *Annals of the New York Academy of Sciences*, Vol 65, 1957, p 1007.
- SCIACCA, A., G. Baciarello, G. Carmenini, F.Di Maio, S. Vittatico Campbell and D. Leonari. Non invasive recording of His bundle potentials. (Abstract). *P.A.C.E.*, 4: A-8, 1981.
- SELVESTER, R.H., R. Kataba, C.R. Collier, R. Bellman and H. Kagiwada. A digital computer model of the vectorcardiogram with distance and boundary effects: simulated myocardial infarction. *American Heart J*, 74: 792, 1967.
- SELVESTER, R.H. and R.B. Pearson. High-gain averaged atrial VCGs. In *Proceedings of the XIth Symposium on Vectorcardiography*. (Edited by I. Hoffman.) Netherlands, North-Holland, 1971, p 689.
- SIMONSON, E. Differentiation Between Normal and Abnormal in Electrocardiography. St Louis, C.V. Mosby, 1961.
- SOLOMON, J.C. and R.H. Selvester. Current dipole moment density of the heart. *American Heart J*, 81: 351, 1971.

- SOLOMON, J.C. and R.H. Selvester. Myocardial activation sequence simulation. *In Proceedings of the XIth Symposium on Vectorcardiography.* (Edited by I. Hoffman.) Netherlands, North-Holland, 1971, p 175.
- SOLOMON, J.C. and R.H. Selvester. Simulation of measured activation sequence in the human heart. *American Heart J*, 85: 518, 1973.
- SPACH, M.S., T.D. King, R.C. Barr, D.E. Boaz, M.N. Morrow and S. Herman-Giddens. Electrical potential distribution surrounding the atria during depolarisation and repolarisation in the dog. *Circulation Research*, 24: 857, 1969.
- SPACH, M.S. and R.C. Barr. Cardiac anatomy from an electrophysiological viewpoint. *In Nelson, C.V. and D.B. Geselowitz. (Eds) The Theoretical Basis of Electrocardiography.* Oxford, Clarendon Press, 1976, p 3.
- SPACH, M.S., R.C. Barr, R.B. Warren, D.W. Benson, A. Walston and S.B. Edwards. Isopotential body surface mapping in subjects of all ages: emphasis on low-level potentials with analysis of the method. *Circulation*, 59: 805, 1979a.
- SPACH, M.S., R.C. Barr, D.W. Benson, A. Walston, R.B. Warren and S.B. Edwards. Body surface low-level potentials during ventricular repolarization with analysis of the S-T segment. Variability in normal subjects. *Circulation*, 59: 822, 1979b.
- STRATTON, J. *Electromagnetic Theory.* New York, McGraw-Hill, 1941.
- SWIHART, J.C. Numerical methods for solving the forward problem in electrocardiography. *In Nelson, C.V. and D.B. Geselowitz. (Eds) The Theoretical Basis of Electrocardiography.* Oxford, Clarendon Press, 1976, p 257.
- TACCARDI, B., L. de Ambroggi and C. Viganotti. Body-surface mapping of heart potentials. *In Nelson, C.V. and D.B. Geselowitz. (Eds) The Theoretical Basis of Electrocardiography.* Oxford, Clarendon Press, 1976, p 436.
- TAKEDA, H., K. Kitamura, T. Takanashi, T. Tokuoka, H. Hamamoto, T. Katoh, I. Niki and Y. Hishimoto. Noninvasive recording of His-Purkinje activity in patients with complete atrioventricular block. *Circulation*, 60: 421, 1979.

- TONKIN, A.M. Personal communication, 1981.
- TOYOSHIMA, H., A. Ito, J. Toyama and K. Yamada. Effects of torso shape and change of dipole location on ECG and VCG lead vectors in a homogeneous torso model. *J Electrocardiology*, 12: 307, 1979.
- TRANCHESTI, J., V. Adelardi and J.H. de Oliveira. Atrial repolarisation - its importance in clinical electrocardiography. *Circulation*, 12: 635, 1960.
- TRETHERWIE, E.R. Simplified electrocardiography. Melbourne, 1953.
- TRETHERWIE, E.R. Constancy of the H-V interval and contour in Lead A: surface His's bundle E.C.G. *Medical J Australia*, 2: 230, 1977.
- VINCENT, R., N.P. Shroud, R. Jenner, M.J. English, D.J. Woollons and D.A. Chamberlain. Noninvasive recording of electrical activity in the P-R segment in man. *British Heart J*, 40: 124, 1978.
- WAIT, J.R. Electromagnetic surface waves. *Advances in Radio Research*, New York, Academic Press, 1: 157, 1964.
- WAIT, J.R. Exact surface impedance for a cylindrical conductor. *Electronics Letters*, 15: 659, 1979.
- WAJSZCZUK, W.J., M.J. Stopczyk, M.S. Moskowitz, R.J. Zochowski, T. Bauld, P.L. Dabos and M. Rubenfire. Noninvasive recording of His-Purkinje activity in man by QRS-triggered signal averaging. *Circulation*, 58: 95, 1978.
- WATERMAN, P.C. Matrix methods in potential theory and electromagnetic scattering. *J Applied Physics* 50: 4550, 1979.
- WEBER, E. *Electromagnetic Fields, Theory and Applications*. New York, Wiley, 1950.
- WEST, T.C. Electrophysiology of the sinoatrial node. In De Mello, W.C. (Ed) *Electrical Phenomena in the Heart*. New York, Academic Press, 1972.
- WILSON, F.N., F.D. Johnston, A.G. Macleod and P.S. Barker. Electrocardiograms that represent the potential variations of a single electrode. *American Heart J*, 9: 447, 1934.
- WILSON, F.N., F.D. Johnston and C.E. Kossmann. The substitution of a tetrahedron for the Einthoven triangle. *American Heart J*, 33: 594, 1947.

WILSON, F.N., C.E. Kossmann, G.E. Burch, *et al.* Recommendations for standardisation of electrocardiographic and vectorcardiographic leads. *Circulation*, 10: 564, 1954.

WITHAM, A.C. A System of VCG Interpretation. U.S.A., Year Book Med. Publishers, 1975.

WYNDHAM, C.R., R. Dhingra, F. Amat-Y-Leon and K.M. Rosen. Sinus node disease. State of the art. *In Advances in the Management of Arrhythmias*. Australia, Telectronics Pty. Ltd, 1978, p 408.

WYNNE, D.J. and L.C. Westphal. A thoracic isopotential mapper for use in a clinical environment. *In Proceedings I.R.E.E. International Convention*, Sydney, Australia, 1979, p 287.

ZABLOW, L. An equivalent cardiac generator which preserves topography. (Letter). *Biophysical J*, 6: 535, 1976.

APPENDIX 1

FORMULAE

§A.1.1 Spherical harmonic functions

The normalized spherical harmonic functions $Y_{nm} = Y_{nm}(\theta, \phi)$, where θ and ϕ are the polar and azimuthal angles of the spherical coordinate system, are defined by

$$Y_{nm}(\theta, \phi) = (-1)^m \left[(2n+1) \frac{(n-m)!}{(n+m)!} \right]^{\frac{1}{2}} P_n^m(\cos\theta) e^{im\phi}$$

and

$$Y_{n,-m}(\theta, \phi) = (-1)^m \overline{Y_{nm}}, \quad n = 0, 1, 2, \dots, m = 0, 1, \dots, n,$$

where $i = \sqrt{-1}$ and $\overline{\quad}$ denotes the complex conjugate (James, 1973).

The $P_n^m(\cos\theta)$ are the Associated Legendre Functions in Neumann's form (Morse and Feshbach, 1953) and are defined by

$$P_n^m(\cos\theta) = \sin^m\theta d^m P_n(\cos\theta)/d(\cos\theta)^m, \quad m \geq 0,$$

where the $P_n(\cos\theta)$ are the Legendre Functions of the First Kind (also called the Legendre Polynomials). Note that the $P_n^m(\cos\theta)$ defined above (Morse and Feshbach, 1953) are identical to $P_{n,m}(\cos\theta)$ as defined in Chapman and Bartels (1951) and to $(-1)^m P_n^m(\cos\theta)$ as defined in Hobson (1930). The reader is referred to Morse and Feshbach (1953, pp. 1325-27), Chapman and Bartels (1951, pp. 622-3) and Hobson (1930, Chapter 3) for recursive formulae relating the $P_n^m(\cos\theta)$.

The Y_{nm} are orthonormal over a closed surface, i.e.

$$(4\pi)^{-1} \int_0^{2\pi} \int_0^\pi Y_{nm}(\theta, \phi) Y_{uv}(\theta, \phi) \sin\theta d\theta d\phi = 1, \quad n = u \quad \text{and} \quad m = v,$$

$$= 0, \quad n \neq u \quad \text{or} \quad m \neq v.$$

§A.1.2 Green's Function

The Green's Function for potential in an infinite homogeneous region is $(4\pi R)^{-1}$, where $R = |\underline{x} - \underline{x}'|$, \underline{x}' is a source point and \underline{x} is a field point (Stratton, 1941; Morse and Feshbach, 1953; see Figure A.1).

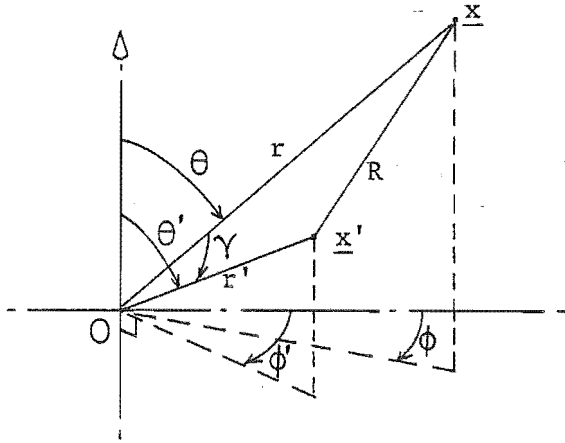


Figure A.1 Geometrical relationships involved in deriving the spherical harmonic expansion of the Green's Function.

The Cosine Rule gives

$$R^{-1} = (r^2 + r'^2 - 2 r r' \cos\gamma)^{-\frac{1}{2}}$$

which is expressed by the absolutely and uniformly convergent series

$$R^{-1} = \sum_{n=0}^{\infty} r^n r'^{-n-1} P_n(\cos\gamma) \quad , \quad r < r'$$

(Hobson, 1930, §90). Now the Addition Theorem for Legendre Functions (Hobson, 1930, §90) gives $P_n(\cos\gamma)$ in terms of functions of $\theta, \phi, \theta', \phi'$.

Thus

$$P_n(\cos\gamma) = P_n(\cos\theta) P_n(\cos\theta') + 2 \sum_{m=1}^{m=n} \frac{(n-m)!}{(n+m)!} P_n^m(\cos\theta) P_n^m(\cos\theta') \cos m(\phi - \phi')$$

Combining these expressions and substituting the normalized spherical harmonic functions for the $P_n^m(\cos\theta)$, the Green's Function is finally expressed by

$$\begin{aligned} (4\pi R)^{-1} &= (4\pi)^{-1} \sum_{n,m} (2n+1)^{-1} r^n Y_{nm}(\theta, \phi) r'^{-n-1} Y_{nm}(\theta', \phi') \quad , \quad r < r' \quad , \\ &= (4\pi)^{-1} \sum_{n,m} (2n+1)^{-1} r'^n Y_{nm}(\theta', \phi') r^{-n-1} Y_{nm}(\theta, \phi) \quad , \quad r > r' \quad . \end{aligned}$$

Recall that $\sum_{n,m}$ infers

$$\sum_{n=0}^{\infty} \sum_{m=-n}^n \dots$$

The functions $r^n Y_{nm}(\theta, \phi)$ (regular at the origin) and $r^{-n-1} Y_{nm}(\theta, \phi)$ (regular at infinity) are known as the "solid" spherical harmonic functions (Hobson, 1930).

§A.1.3 Coordinate transformations

Formulae are given below to express the solid spherical harmonic functions in terms of a new coordinate system (see Figure A.2).

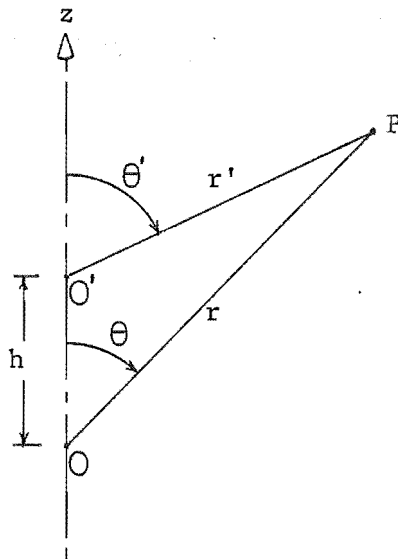


Figure A.2 Transformation of the origin of coordinates from O to O'.

The new origin O' lies at the point $z = h$ of the original system with origin O (the z axis is colinear with $\theta = 0$) and $\phi' = \phi$. The formulae are based on those given in Hobson (1930, §89), though corrected and extended. Note that two formulae are necessary for the solid spherical harmonics which are regular at infinity.

The formulae are

$$r^n Y_{nm}(\theta, \phi) = \sum_{u=m}^n \left[\frac{(2n+1)(n-m)!(u+m)!}{(2u+1)(n+m)!(u-m)!} \right]^{\frac{1}{2}} r'^u h^{n-u} \frac{(n+m)!}{(n-u)!(u+m)!} Y_{um}(\theta', \phi'),$$

$$r^{-n-1} Y_{nm}(\theta, \phi) = \sum_{u=n}^{\infty} \left[\frac{(2n+1)(n-m)!(u+m)!}{(2u+1)(n+m)!(u-m)!} \right]^{\frac{1}{2}} (-1)^{u-n} r'^{-u-1} h^{u-n} \frac{(u-m)!}{(u-n)!(n-m)!} Y_{um}(\theta', \phi'),$$

$r' > h$

$$r^{-n-1} Y_{nm}(\theta, \phi) = \sum_{u=m}^{\infty} \left[\frac{(2n+1)(n-m)!(u+m)!}{(2u+1)(n+m)!(u-m)!} \right]^{\frac{1}{2}} (-1)^{u+m} r'^u h^{-n-u-1} \frac{(n+u)!}{(u+m)!(n-m)!} Y_{um}(\theta', \phi'),$$

$r' < h$.

The Addition Theorem for Legendre Functions (Hobson, 1930, §90) is used to carry out a rotation of the coordinate system.

APPENDIX 2

INSTRUMENTATION

§A.2.1 References to equipment manufacturers

1. Analog Devices Conversion Products Catalogue.
Analog Devices, U.S.A., 1977.
2. Datel ADC H-Z Series Application Notes.
Datel Systems Inc., Massachusetts, 1977.
3. D.E.C. PDP-11 Processor and Peripherals Handbooks.
Digital Equipment Corp., Massachusetts, 1975.
4. Electrodata 6500 Instrumentation Recorder Manual.
Electrodata Associates Pty. Ltd., New South Wales,
Australia, 1978.
5. Tektronix 4012 Operation and Maintenance Manuals.
Tektronix Inc., Oregon, 1973.

§A.2.2 Circuit diagram

Overleaf, a complete circuit diagram is shown of the instrumentation used in the study reported in Chapter 7.

